



# UNIVERSITY OF LEICESTER

DEPARTMENT OF PHYSICS AND ASTRONOMY

Radio and Space Plasma Physics Group

---

## **Raman spectroscopy using miniaturised spectrometers in preparation for the 2020 ExoMars rover mission**

---

Liam Vincent Harris

*Submitted in accordance with the requirements for the degree of Doctor of Philosophy.*

Under the supervision of Dr Ian B. Hutchinson and Dr Richard Ingley at the University  
of Leicester.

June 2018

The candidate confirms that the work submitted is his own and that appropriate credit has been given  
where reference has been made to the work of others.

This copy has been supplied on the understanding that it is copyright material and that no quotation from  
the thesis may be published without proper acknowledgement.

# **Portable Raman spectroscopy in preparation for the 2020 ExoMars rover mission**

**Liam Vincent Harris**

## **ABSTRACT**

Over the past two decades, the potential of Raman spectroscopy as a tool for planetary exploration has been explored in detail and greatly advocated. It is ideally suited for in situ measurement as it provides rapid, non-destructive, unambiguous molecular identification, without any need for mechanical or chemical sample preparation. Developments in the miniaturisation of lasers, charge-coupled device detectors and other instrument components has, for the first time, enabled the development of Raman instruments for space missions.

The first to be deployed on another planet will be the Raman Laser Spectrometer instrument onboard the ExoMars rover, a joint mission between the European Space Agency and the Roscosmos State Corporation for Space Activities, which will be launched in 2020. Two further Raman instruments, SuperCam and SHERLOC, will be included in the payload of NASA's Mars 2020 rover. Prior to the deployment of these instruments, it is necessary to conduct analogue studies using flight-representative hardware in order to optimise instrument configuration, mode of operation, data extraction and analysis protocols. The programme of research presented in this thesis constitutes a series of such studies.

The capabilities of two flight-representative, portable Raman spectrometers, one using 532 nm excitation and the other 785 nm, have been evaluated through a series of Mars analogue studies. Spectra have been acquired from a range of relevant target materials, including silica, haematite and calcium sulphate of varying levels of hydration. Caution is urged in the interpretation of spectra from portable Raman systems, since limitations introduced by their miniaturisation make band misassignment possible. As a result of

this research, it is recommended that instruments are designed with a minimum spectral range from 100 to 4000  $\text{cm}^{-1}$  and a spectral resolution of at least 3  $\text{cm}^{-1}$ , in order to avoid the misinterpretation of spectra.

Several sets of analogue samples that are rich in reduced carbon have also been studied. It has been demonstrated that reduced carbon can not only be detected in concentrations as low as 0.08%, but distinct carbon populations can be differentiated by the measurement of certain spectral parameters. Furthermore, this analysis enables the qualitative comparison of the thermal maturity of different samples containing reduced carbon. These analytical techniques will be highly valuable when analysing spectra returned by planetary instruments.

# Acknowledgements

There are a great number of people who without their continuous support, advice, feedback, constructive criticism, pub companionship and baked goods, I absolutely could not have carried out the kind of work that I'm proud of, much less completed the thesis that you're about to read. I want to give proper thanks to each and every one of them, so please bear with me.

Firstly, I cannot give enough thanks to my supervisors, **Ian Hutchinson** and **Richard Ingley**. They initially gave me the chance to study for my doctorate here at Leicester, and since then have given me the guided tour of the world of academia. They've trained me in all aspects of research, given me a lot of great ideas, introduced me to collaborators, contributed significantly to my caffeine habit and put up with the full spectrum of my emotional states (which at times I imagine was a nightmare!), so for all of that I will forever be extremely grateful.

Next, I want to thank the members of my research team, **Melissa McHugh**, **Arthur Smalley**, **Peter Edwards**, **Cédric Malherbe** and **Hannah Lerman**, who along with Ian and Richard have all contributed to four of the most enjoyable years of my life so far. We've worked together, drank together, travelled the world together and watched *The Great British Bake Off* together, and I can't think of a group of people I'd more like to spend most of my time with.

I also want to thank my mum **Carol Tyler-Harris**, my dad **Richard Harris** and my brother **Jamie Harris**. My family supported my decision to pursue an academic career, instead of getting "one of those high paying jobs that physics graduates get", listened to my stresses when my research wasn't going so smoothly and got more excited than

## Acknowledgements

---

even I did about conference awards and published papers. I genuinely couldn't ask for a more supportive family and I hope that I've made them proud.

Of course, distractions from work are sometimes required to keep morale high whilst doing research and writing a thesis, and there are several people that I'd like to acknowledge for their help with this. Thanks go to **Michael Perry** for his masterful storytelling and for being almost as keen for a friendly argument as I am, **James Blake** for sharing with me much of the internet's wealth of amusing videos, **Alex Webb** for his special interests in ancient stonework, Norse gods and penmanship, **Matthew Grant** for providing entertainment during MPAGS courses back in the distant past at the beginning of our PhDs, and **Peter Somkuti** for showing me that there's a time and a place for even the most vicious of mockery. I'd also like to thank my surrogate family in Leicester, **Jane McHugh**, **Wayne McHugh** and **Kate McHugh**, who've provided me with laughs, music and tasty food on a multitude of occasions.

Last and most importantly, I'd like to once again thank **Melissa McHugh**, who is not only a wonderful friend and colleague, but is also the love of my life. I know it sounds cliché, but I would be nothing without her. Mel is the most optimistic person I've ever met: she's the first to celebrate when I succeed, to advise me when I'm lost and to encourage me when I lack motivation, and somehow she has done all of that whilst working on her own PhD. She also makes the best Cheddar Bay Biscuits you've ever tasted (no really!). I love Melissa for every little thing that she does to make my life perfect, which has definitely made writing this thesis easier, so I'd like to thank her most of all.

# Contents

<b>Acknowledgements</b>	<b>iii</b>
<b>List of Tables</b>	<b>xi</b>
<b>List of Figures</b>	<b>xii</b>
<b>List of Acronyms and Abbreviations</b>	<b>xvii</b>
<b>Publications</b>	<b>xxi</b>
<b>Personal Contribution</b>	<b>xxiii</b>
<b>Preface</b>	<b>1</b>
<b>1 Introduction</b>	<b>4</b>
1.1 The exploration of Mars	4
1.1.1 The history of Mars exploration	5
1.1.1.1 Mariner 4	7
1.1.1.2 Viking programme	8
1.1.1.3 Mars Global Surveyor	11
1.1.1.4 Mars Pathfinder	13
1.1.1.5 Mars Express and Beagle 2	14
1.1.1.6 Mars Exploration Rovers	16

1.1.1.7	Mars Reconnaissance Orbiter	18
1.1.1.8	Phoenix	19
1.1.1.9	Mars Science Laboratory	21
1.1.2	The Mars environment	23
1.1.2.1	Perchlorates on Mars	23
1.1.2.1.1	Reanalysis of past mission data	24
1.1.3	Historical martian conditions	24
1.1.4	Geology of Mars	25
1.2	Astrobiology	25
1.2.1	Extremophilic life on Earth	26
1.2.2	Biomarkers	27
1.2.2.1	Terrestrial analogue samples	28
1.2.2.2	Terrestrial analogue sites	29
1.3	Raman spectroscopy	29
1.3.1	The history of Raman spectroscopy	29
1.3.2	Theory of Raman scattering	30
1.3.2.1	Group theory	31
1.3.2.2	Typical wavenumbers ranges	31
1.3.2.3	Quantitative and qualitative analysis	32
1.3.3	Challenges and possible solutions	33
1.3.3.1	Fluorescence and scattering	33
1.3.3.2	Excitation wavelength dispersive Raman bands	34
1.3.3.3	Mass budget	34
1.3.3.4	Volume budget	35
1.3.3.5	Power budget	35
1.3.3.6	Technology readiness level	35
1.3.3.7	Comparing space and laboratory instruments	36
1.3.4	Raman spectroscopy for planetary exploration	37
1.3.4.1	Mars exploration with a Raman spectrometer	38
1.3.5	Basic Raman spectrometer	38
1.3.5.1	Laser	39
1.3.5.2	Sample	40
1.3.5.3	Filter	40

1.3.5.4	Slit	41
1.3.5.5	Diffraction grating	41
1.3.5.6	Detector	42
1.3.5.6.1	Cooling	42
1.3.6	Advanced Raman techniques	43
1.3.6.1	Resonance Raman	43
1.3.6.2	Raman imaging	44
<b>2</b>	<b>Instrumentation</b>	<b>45</b>
2.1	ExoMars programme	45
2.1.1	ExoMars 2016 mission	46
2.1.1.1	Trace Gas Orbiter	46
2.1.1.1.1	CaSSIS	47
2.1.1.1.2	FREND	47
2.1.1.2	Entry, Descent and Landing Demonstrator Module	48
2.1.2	ExoMars 2020 mission	48
2.1.2.1	Target selection	50
2.1.2.2	Sample acquisition	51
2.1.2.3	Sample Preparation and Distribution System	51
2.1.2.4	Analytical Laboratory Drawer	51
2.1.2.4.1	MicrOmega	52
2.1.2.4.2	RLS	52
2.1.2.4.3	MOMA	53
2.1.2.4.4	Instrument complementarity	54
2.2	The specific case of Mars	54
2.2.1	The Martian radiation environment	55
2.2.1.1	Measurements of Martian radiation	55
2.2.1.2	Impact on environmentally preserved biomarkers	56
2.2.1.3	Impact on Raman spectrum	57
2.2.2	Sample crushing	57
2.3	Raman spectroscopy on future missions	58
2.3.1	SuperCam	58
2.3.2	SHERLOC	58

2.3.3	Future missions	59
2.4	Raman spectrometers used in this thesis	59
2.4.1	532 nm benchtop spectrometer	59
2.4.2	785 nm handheld spectrometer	60
2.4.3	UK ExoMars RLS breadboard	60
2.4.4	Comparison with RLS specifications	60
2.5	Data analysis methods	61
2.5.1	Extraction of data from a CCD	61
2.5.2	Wavenumber calibration	63
2.5.2.1	Instrument calibration throughout this thesis	64
2.5.3	Noise limitations	65
2.5.4	Signal-to-noise ratio	66
2.5.5	Background subtraction	67
2.5.6	Band identification	68
2.5.7	Measurement of band centroids	69
<b>3</b>	<b>Avoiding misassignment of Raman bands in planetary spectra</b>	<b>71</b>
3.1	Preparation for the ExoMars rover mission	72
3.1.1	Reduction in performance for flight	73
3.2	Partially oxidised carbonaceous mudstone	73
3.2.1	Relevance to Mars exploration	74
3.2.2	Acquisition of Raman spectra	74
3.2.3	Results	75
3.3	Desert varnish	77
3.3.1	Relevance to Mars exploration	77
3.3.2	Acquisition of Raman spectra	78
3.3.3	Results	79
3.4	Hydrated calcium sulphates	82
3.4.1	Relevance to Mars exploration	82
3.4.2	Acquisition of Raman spectra	83
3.4.3	Results	83
3.5	Bacterially colonised evaporite	84
3.5.1	Relevance to Mars exploration	85

3.5.2	Acquisition of Raman spectra	85
3.5.3	Results	86
3.6	Discussion	87
3.6.1	Partially oxidised carbonaceous mudstone	87
3.6.2	Desert varnish	88
3.6.3	Hydrated calcium sulphates	89
3.6.4	Bacterially colonised evaporite	90
3.6.5	Recommendations	91
3.7	Future work	92
3.8	Summary	92
<b>4</b>	<b>Differentiation of distinct populations of reduced carbon</b>	<b>94</b>
4.1	Forms of carbon	94
4.1.1	Diamond	95
4.1.2	Graphite	95
4.1.3	Amorphous carbon	96
4.1.4	Reduced carbon	97
4.1.4.1	Relevance to the search for life	98
4.1.4.2	Raman spectrum	98
4.2	Modelling the uncertainty in spectra measurements	99
4.3	Nakhla meteorite analogue	101
4.3.1	Rock sample	101
4.3.2	Acquisition of Raman spectra	102
4.3.3	Reduced carbon analysis	102
4.4	Carbon-rich shale samples	105
4.4.1	Rock samples	105
4.4.2	Acquisition of Raman spectra	107
4.4.3	Results	108
4.4.4	Raman analysis of thermal maturity	110
4.5	Summary	113

<b>5</b>	<b>Comparison of 532 and 785 nm excitation for Raman spectroscopy of reduced carbon</b>	<b>116</b>
5.1	Analogue samples	117
5.1.1	Archean chert	117
5.1.2	Geological setting	117
5.1.3	Relevance to Mars exploration	118
5.2	Raman spectroscopic study	118
5.2.1	Acquisition of Raman spectra	119
5.2.2	Spectroscopic results	120
5.2.3	Reduced carbon analysis	121
5.3	Comparison of 532 nm and 785 nm Raman spectroscopy	124
5.3.1	Recommendations	125
5.3.2	UV Raman study of reduced carbon	128
5.4	Summary	128
<b>6</b>	<b>Summary, conclusions and future work</b>	<b>130</b>
6.1	Differentiation of reduced carbon populations	130
6.2	Recommendations for future instrument design	131
6.3	Complementary instruments	133
6.4	Suggestions for future work	134
6.5	Concluding remarks	135
	<b>Glossary</b>	<b>136</b>
	<b>References</b>	<b>138</b>

# List of Tables

1.1	Comparison of the specifications of NASA's Mars rovers	22
1.2	Technology readiness level attainment criteria	36
1.3	Comparison of the specifications of the Renishaw inVia Qontor laboratory Raman spectrometer and the RLS instrument	37
4.1	Details of carbonaceous shales from Caithness, Northern Scotland	109
5.1	Comparison of the detection rate of reduced carbon in Archean cherts using 532 and 785 nm Raman spectroscopy	126

# List of Figures

1.1	Timeline of Mars exploration missions	6
1.2	Artist's impression of the Mariner 4 satellite	7
1.3	Orbital photograph of Sirenum Fossae, taken by Mariner 4	8
1.4	Photograph of a model of the Viking landers	9
1.5	Artist's impression of the Mars Global Surveyor orbiter	12
1.6	Topographical map of Mars, generated using Mars Orbiter Laser Altimeter data	12
1.7	Photographs of the Pathfinder lander and Sojourner rover	13
1.8	Artist's impression of the Mars Express orbiter and photograph of a model of the Beagle 2 lander	14
1.9	Orbital photograph of the Beagle 2 landing site, taken using the HiRISE instrument onboard the Mars Reconnaissance Orbiter	15
1.10	Artist's impression of the Mars Exploration Rovers	17

## List of Figures

---

1.11	Artist's impression of the Mars Reconnaissance Orbiter	18
1.12	Orbital photograph of Sirenum Fossae, taken using the HiRISE instrument onboard the Mars Reconnaissance Orbiter	19
1.13	Artist's impression of the Phoenix lander	20
1.14	Self-portrait of the Curiosity rover, taken using the Mars Hand Lens Imager	21
1.15	Microscope image of an OU-20 bacterium	27
1.16	Photograph of a microbially colonised, iron-rich Mars analogue from Antarctica	28
1.17	Energy level diagram of Raman scattering	30
1.18	Classical depiction of some possible molecular vibrational modes	31
1.19	Photographs of a Renishaw inVia Qontor Raman spectrometer and the RLS Spectrometer Unit	37
1.20	Component diagram of a simple Raman spectrometer	39
1.21	Diagram showing the effect of a blazed diffraction grating	42
2.1	Artist's impression of the ExoMars rover	46
2.2	Artist's impression of the ExoMars rover deploying its drill	49
2.3	Grain size distribution produced by the ExoMars Sample Preparation and Distribution System	52

## List of Figures

---

2.4	CAD drawing of the Raman Laser Spectrometer instrument	53
2.5	CCD image showing spectral orders from a Raman system	62
2.6	Diagram explaining the readout of a CCD to produce a Raman spectrum	62
2.7	Raman spectrum of a polystyrene calibration standard	65
2.8	Diagram showing a Raman spectrum, before and after background reduction using Fourier transformation	68
3.1	Photograph of a partially oxidised sample of carbonaceous mudstone	73
3.2	Raman spectra of reduced carbon and haematite, acquired from a partially oxidised sample of carbonaceous mudstone	75
3.3	Photograph and microscope image of a rock sample coated with a desert varnish	77
3.4	Raman spectra acquired from desert varnish samples	80
3.5	Modelled Raman spectrum showing the superposition of the anatase and haematite spectra, acquired using a poor resolution system	82
3.6	Photographs of calcium sulphates of varying levels of hydration	83
3.7	Raman spectrum of gypsum	83
3.8	Photograph of a microbially colonised hypersaline evaporite	84

## List of Figures

---

3.9	Raman spectra of different coloured carotenoid molecules	86
3.10	Molecular structure of $\beta$ -carotene	90
4.1	Molecular structure and Raman spectrum of diamond	95
4.2	Molecular structure of graphite	96
4.3	Schematic of C-C stretching in a graphite ring and the Raman spectrum of the associated carbon G band	96
4.4	Molecular structure of amorphous carbon	97
4.5	Molecular structure of reduced carbon	97
4.6	Schematic of the breathing mode of aromatic carbon and the Raman spectrum of the associated carbon D band	99
4.7	Model Raman spectrum and close-up of a Raman band following background subtraction	100
4.8	Uncertainty in measurements of Raman band width and position, as functions of signal-to-noise ratio	100
4.9	Photograph of a basaltic Mars analogue from Helen's Bay, Northern Ireland	101
4.10	Raman spectra of reduced carbon, haematite, calcite and silica, acquired from the Helen's Bay basalt	103
4.11	Comparison of the carbon G band in Raman spectra acquired from different areas on the surface of the Helen's Bay basalt	104

## List of Figures

---

4.12	Cross-plot of carbon G band width against spectral position in Raman spectra acquired from different areas on the surface of the Helen's Bay basalt	105
4.13	Map of the Orcadian Basin, Northern Scotland	106
4.14	Map of shale sample sites in Caithness, Northern Scotland	107
4.15	Raman spectrum of reduced carbon, silica and anatase, acquired from a Caithness shale and a comparison of the carbon G band in spectra acquired from two shales	110
4.16	Cross-plot of carbon G band width against spectral position in Raman spectra acquired from the Caithness shales	111
4.17	Extractable carbon fraction against carbon <i>G</i> band position in Raman spectra acquired from the Caithness shales	113
5.1	Raman spectrum of silica, acquired from an Archean chert sample	120
5.2	Photograph of Archean chert sample AC1 and Raman spectrum of a carotenoid molecule, acquired from its surface	121
5.3	Raman spectrum of haematite, acquired from an Archean chert	122
5.4	Reduced carbon and silica spectrum from an Archean chert	122
5.5	Cross-plot of carbon G band width against spectral position in Raman spectra acquired from the Archean cherts	123
5.6	Comparison of Raman spectra of reduced carbon, acquired from Archean chert sample DFM1 using 532 and 785 nm excitation	125

# List of Acronyms and Abbreviations

<b>ACS</b>	Atmospheric Chemistry Suite
<b>ALD</b>	Analytical Laboratory Drawer
<b>AMELIA</b>	Atmospheric Mars Entry and Landing Investigation and Analysis
<b>APXS</b>	Alpha particle X-ray spectroscopy
<b>CARS</b>	Coherent anti-Stokes Raman spectroscopy
<b>CaSSIS</b>	Colour and Stereo Surface Imaging System
<b>CCD</b>	Charge-coupled device
<b>CIRS</b>	Compact Integrated Raman Spectrometer
<b>CLUPI</b>	Close-Up Imager
<b>CMOS</b>	Complementary metal-oxide semiconductor
<b>CW</b>	Continuous wave
<b>DECA</b>	Entry and Descent Module Descent Camera

## List of Abbreviations

---

<b>DREAMS</b>	Dust Characterisation, Risk Assessment, and Environment Analyser on the Martian Surface
<b>DUV</b>	Deep-ultraviolet
<b>EDM</b>	Entry, Descent and Landing Demonstrator Module
<b>EM</b>	Electromagnetic
<b>ESA</b>	European Space Agency
<b>FREND</b>	Fine Resolution Epithermal Neutron Detector
<b>GC-MS</b>	Gas chromatography-mass spectrometry
<b>GCR</b>	Galactic cosmic ray
<b>GEx</b>	Gas Exchange
<b>HiRISE</b>	High Resolution Imaging Science Experiment
<b>IKI</b>	Russian Space Research Institute
<b>IR</b>	Infrared
<b>ISEM</b>	Infrared Spectrometer for ExoMars
<b>ISS</b>	International Space Station
<b>LD-MS</b>	Laser desorption-mass spectrometry
<b>LIBS</b>	Laser induced breakdown spectroscopy
<b>LR</b>	Labelled Release
<b>Ma_MISS</b>	Mars Multispectral Imager for Subsurface Studies
<b>MER</b>	Mars Exploration Rover

## List of Abbreviations

---

<b>MGS</b>	Mars Global Surveyor
<b>MMRS</b>	Mars Microbeam Raman Spectrometer
<b>MOLA</b>	Mars Orbiter Laser Altimeter
<b>MOMA</b>	Mars Organic Molecule Analyser
<b>MRO</b>	Mars Reconnaissance Orbiter
<b>MSL</b>	Mars Science Laboratory
<b>NASA</b>	National Aeronautics and Space Administration
<b>NIR</b>	Near-infrared
<b>NOMAD</b>	Nadir and Occultation for Mars Discovery
<b>PanCam</b>	Panoramic Camera
<b>PI</b>	Principal Investigator
<b>PR</b>	Pyrolytic Release
<b>QE</b>	Quantum efficiency
<b>RLS</b>	Raman Laser Spectrometer
<b>Roscosmos</b>	Roscosmos State Corporation for Space Activities
<b>RTG</b>	Radioisotope thermoelectric generator
<b>SAGE</b>	Surface and Atmosphere Geochemical Explorer
<b>SEP</b>	Solar energetic particle
<b>SERS</b>	Surface enhanced Raman spectroscopy

## List of Abbreviations

---

<b>SHERLOC</b>	Scanning Habitable Environments with Raman & Luminescence for Organics & Chemicals
<b>SNC</b>	Shergottite, Nakhlite and Chassignite
<b>SNR</b>	Signal-to-noise ratio
<b>SPDS</b>	Sample Preparation and Distribution System
<b>TEC</b>	Thermoelectric cooler
<b>TES</b>	Thermal Emission Spectrometer
<b>TGO</b>	Trace Gas Orbiter
<b>TRL</b>	Technology Readiness Level
<b>UKBB</b>	UK ExoMars RLS breadboard
<b>UV</b>	Ultraviolet
<b>WISDOM</b>	Water Ice and Subsurface Deposit Observation On Mars
<b>XRD</b>	X-ray diffraction

# Publications

The research presented in Chapter 3 has also been published in the following paper:

**Harris, L.V.**, McHugh, M., Hutchinson, I.B., Ingley, R., Malherbe, C., Parnell, J., Olcott Marshall, A. and Edwards, H.G.M. (2015b) Avoiding misidentification of bands in planetary Raman spectra. *J. Raman Spectrosc.* 46:863-872.

The research presented in Chapter 4 has been published in the following two papers:

Parnell, J., McMahon, S., Blamey, N.J., Hutchinson, I.B., **Harris, L.V.**, Ingley, R., Edwards, H.G.M., Lynch E. and Feely, M. (2014) Detection of reduced carbon in a basalt analogue for martian nakhlite: a signpost to habitat on Mars. *Int. J. Astrobiol.* 13:124-131.

Hutchinson, I.B., Parnell, J., Edwards, H.G.M., Jehlička, J., Marshall, C.P., **Harris, L.V.** and Ingley, R. (2014a) Potential for analysis of carbonaceous matter on Mars using Raman spectroscopy. *Planet. Space Sci.* 103:184-190.

The research presented in Chapter 5 has also been published in the following paper:

**Harris, L.V.**, Hutchinson, I.B., Ingley, R., Marshall, C.P., Olcott Marshall, A. and Edwards, H.G.M. (2015a) Selection of portable spectrometers for planetary exploration: a comparison of 532 nm and 785 nm Raman spectroscopy of reduced carbon in Archean cherts. *Astrobiology* 15:420-429.

Finally, I also co-authored the following two papers whilst conducting the research presented throughout this thesis:

## Publications

---

Hutchinson, I.B., Ingle, R., Edwards, H.G.M., **Harris, L.V.**, McHugh, M., Malherbe, C. and Parnell, J. (2014b) Raman spectroscopy on Mars: identification of geological and bio-geological signatures in Martian analogues using miniaturized Raman spectrometers. *Phil. Trans. R. Soc. A* 372, doi:10.1098/rsta.2014.0204.

Malherbe, C., Ingle, R., Hutchinson, I.B., Edwards, H.G.M., Carr, A.S., **Harris, L.V.** and Boom, A. (2015) Biogeological analysis of desert varnish using portable Raman spectrometers. *Astrobiology* 15:442-452.

## Personal Contribution

All of the data presented in this thesis were acquired and analysed by myself, except where noted below. I also developed the software tools that were used in their analysis. Finally, all of the conclusions drawn from this research are my own, following discussions with my supervisors and collaborators.

I led the preparation of the paper that Chapter 3 is based upon and also performed the study of the mudstone samples, which were provided by John Parnell. The desert varnish samples were acquired by Andrew Carr and Arnoud Boom and studied by Cédric Malherbe, who also produced Figure 3.3. The hydrated calcium sulphate study was carried out by Ian Hutchinson, who was also responsible for the Raman spectrum of gypsum in Figure 3.4. Lastly, Jan Jehlička obtained the microbially colonised gypsum samples that were studied by Melissa McHugh, who also generated Figure 3.5.

The data presented in Chapter 4 were acquired and analysed by myself, except for the total organic carbon concentrations and extractable carbon fractions presented in Table 4.1, which were provided by John Parnell. John also acquired the shale samples studied in the chapter and provided their original locations for the map in Figure 4.6. The first half of Chapter 4 is based on a paper by Parnell *et al.* (2014), to which I contributed text and the Raman data and analysis that also appear in the chapter. The second half of the chapter is based on a paper by Hutchinson *et al.* (2014), to which I contributed all of the data, analysis and figures.

The Archean chert samples studied in Chapter 5 were obtained by Craig Marshall and Alison Olcott Marshall, who both also provided excellent advice and information regarding the samples during the study.

# Preface

With the inclusion of three different Raman instruments in the payloads of upcoming missions to Mars, a great deal of preparatory work is necessary to assess the potential quality of the data that they will return and to develop the most appropriate methods of analysis. The first of these instruments to be deployed on Mars will be the Raman Laser Spectrometer (RLS), an internal Raman spectrometer with a fibre-coupled optical head and a 532 nm excitation source. RLS is to be included in the Analytical Laboratory Drawer (ALD) of the ExoMars rover, which is due for launch in July 2020. ExoMars is a joint mission between the European Space Agency (ESA) and the Roscosmos State Corporation for Space Activities (Roscosmos; formerly the Russian Federal Space Agency), whose primary objective is to search for signs of either extinct or extant life on Mars.

Two additional instruments, SuperCam and SHERLOC (Scanning Habitable Environments with Raman & Luminescence for Organics & Chemicals), have been selected for inclusion in the payload of the NASA (National Aeronautics and Space Administration) Mars 2020 rover, which as its name suggests is due for launch in 2020. SuperCam incorporates a 532 nm stand-off Raman spectrometer, which is able to perform Raman spectroscopy at distances of up to 12 m from the rover. The instrument is also capable of stand-off laser induced breakdown spectroscopy (LIBS) and remote micro-imaging. SHERLOC is an ultraviolet (UV) Raman imaging spectrometer that will be mounted on the rover's robotic arm, enabling it to scan rock surfaces to produce Raman maps.

Prior to the deployment of these instruments, their capabilities must be assessed through laboratory and field operation of flight-representative and prototype instrumentation.

This usually takes the form of analogue studies, which involve Raman characterisation of analogue samples. These are terrestrial rock samples with mineralogical, chemical or geological similarities to the destination of the mission in preparation, which in this case is the planet Mars. Such studies make it possible to establish the limitations of miniaturised instruments and what they will be able to achieve in terms of the materials that will be discernible, their lowest detectable concentrations and the level of quantitative analysis that will be possible. Analogue studies also facilitate the development and optimisation of analysis algorithms and methodologies, in order to maximise the return from these inherently impaired instruments. For example, these might include strategies for dealing with the fluorescence and scattering background signal, or for measuring spectral parameters of Raman bands. Finally, such work informs future instrument development, leading to recommendations for optimum instrument design for particular applications, targets of interest or science requirements.

The research presented in this thesis is focused on preparations for the launch and deployment of RLS on the ExoMars rover. The instrument is to be used for both mineralogical characterisation and in the search for signs of life, therefore both applications are explored in detail and optimum modes of operation for data acquisition and analysis are suggested. The thesis is organised as follows:

- Chapter 1 provides the necessary background information for the research presented in the thesis and review of the current literature, covering three broad topics:
  - Mars science and a history of Mars exploration, focusing on technologies and results that have significantly affected our understanding of Mars and its environment, and continue to have an impact on current mission design.
  - A brief overview of the field of astrobiology, the lessons that can be learned from studying extremophilic life on Earth and how signs of life on another planet might be detected and recognised.
  - The physics of Raman scattering and the capabilities and limitations of Raman spectroscopy. The requirements of a basic Raman spectrometer are given and the trade-offs that must be performed during instrument development are explored.

- Chapter 2 describes the instrumentation and general analysis methods that have been used throughout this thesis to obtain and interpret data. Details regarding the ExoMars mission and the RLS instrument are also given, in order to provide context for this work and the choices made therein.
- Chapter 3 demonstrates the limitations of miniaturised Raman spectrometers and the challenges faced when interpreting data obtained using them. Caution is urged in the assignment of bands in such spectra, and several case studies are presented that highlight areas in which there is the potential for the misassignment of Raman bands in planetary spectra. Strategies are provided for avoiding this and minimum instrument operating parameters are recommended.
- Chapter 4 explores the detection and characterisation of reduced carbon in Mars analogue samples. It is demonstrated that not only can reduced carbon be successfully detected at low concentrations using flight-representative Raman spectrometers, but distinct carbon populations can be distinguished through careful measurement of spectral parameters. This is made possible due to differences between their thermal histories, which also means that Raman spectroscopy can be used to make qualitative statements about the level of thermal maturity of carbonaceous samples.
- Chapter 5 is a continuation of the reduced carbon work in Chapter 4, reporting on the study of a set of carbonaceous Archean cherts. This research was conducted using two portable spectrometers, one equipped with a 532 nm excitation source and the other a 785 nm source. It was determined that 785 nm excitation is more appropriate when seeking to detect and characterise reduced carbon. The case is made for strongly considering a 785 nm instrument for future missions that aim to detect and characterise organic material.
- The final chapter provides a summary of the work presented and a recap of the conclusions drawn from the data. Possibilities for future work are also discussed, since a great deal of research is still necessary prior to the deployment of RLS on Mars in 2021.

# Chapter 1

## Introduction

---

### 1.1 The exploration of Mars

For over five decades, Mars has been the focus of intense robotic exploration, both remotely and in situ. This high level of concentrated activity has been motivated primarily by the search for signs of either past or present life (Klein, 1979; McKay, 1997; Cabane *et al.*, 2004). However, such a search requires a comprehensive understanding of the Martian environment in terms of its geochemistry, climate and radiation environment (Horneck, 2000), all of which are worthwhile subjects of study themselves and the main objectives of numerous missions to Mars have been to investigate one or more of them.

It has long been suggested that the Martian climate was once much warmer and wetter than it is today (Pollack *et al.*, 1987; Craddock and Howard, 2002), a theory corroborated by the discovery of suspected ancient streambeds (Williams *et al.*, 2013) and lakes (Grotzinger *et al.*, 2014) on Mars by the Mars Science Laboratory (MSL) Curiosity rover. If Mars did indeed host liquid water on its surface for an extended period of its history, it is conceivable that life could have developed there. If living organisms existed on Mars in the past, markers of their presence may persist in the geological record that could be detectable today (Farmer and Des Marais, 1999). There is also the distinct possibility that such organisms could have adapted to changing Martian conditions, in the same way that life has adapted to survival in extreme or hostile environments here on Earth (Rothschild and Mancinelli, 2001), and so may

survive to this day in protected environmental niches and therefore be detectable by carefully conceived missions to Mars.

As a result of the extensive exploration of Mars, a great deal is already known about typical Martian geology and some of the most interesting features of the planet. However, given the difficulties associated with conducting a Mars sample return mission (Stephenson and Willenberg, 2006), the only available direct sources of information regarding the composition of Mars are the Shergottite, Nakhlite and Chassignite (SNC) meteorites. The SNC meteorites are all basaltic (Longhi *et al.*, 1992), so consist primarily of feldspars, olivine and pyroxenes. Considering what is known of the volcanic history of Mars (Mouginis-Mark *et al.*, 1992; Wilson and Head III, 1994) and its primordial internal structure (Zuber *et al.*, 2000) and given the composition of the SNC meteorites, it seems reasonable to surmise that Mars is largely igneous. Nevertheless, there is also evidence for the formation of sedimentary rocks on Mars, certainly via aeolian processes (Greeley *et al.*, 1992), and also possibly by fluvial (e.g. Fassett and Head III, 2005) and lacustrine (Ehlmann *et al.*, 2008) processes as well.

### 1.1.1 The history of Mars exploration

Since 10 October 1960, the date of the attempted launch of the Soviet Union's first M1 spacecraft (Varfolomeyev, 1993), there have been a total of 43 missions to Mars or its moons<sup>1</sup>, making it one of the most extensively explored bodies in the Solar System (see Figure 1.1 for a timeline of key Mars missions). Of these 43 missions, 18 were considered successful and a further 2 were a partial success, with at least one mission element completing its primary objectives. Reasons for mission failure include spacecraft that failed to launch or reach Earth orbit, craft that failed to leave Earth orbit or missed their target and never achieved Mars orbit, malfunctioning radio systems and some unexplained losses. Even a failed mission is not entirely negative however, as a great deal of data is acquired that can be used to improve mission design and prevent similar failures in the future. It is the case that mission failure has been much less common in the last 15 years and this is at least partly the result of lessons learned from past missions.

---

<sup>1</sup> <http://mars.nasa.gov/programmissions/missions/log/> [Accessed: 10 November 2015].

## 1.1 The exploration of Mars

Several different types of unmanned spacecraft have been used successfully to explore Mars, acquiring and returning data. The earliest missions to Mars were flybys, as such craft did not need to carry the additional fuel required for orbital insertion, but instead acquired photographs and scientific data as they passed close to the planet. Since then there have been numerous Mars orbiters, equipped with high-resolution cameras and scientific instruments for imaging and studying the Martian surface and atmosphere, as well as communication systems for relaying data back to Earth and transmitting instructions to surface vehicles. There have also been a number of Mars landers, capable of performing a soft landing and then conducting experiments using onboard scientific instrumentation. Finally, NASA have had great success in sending rovers to Mars that carry suites of analytical instruments like landers, but are also capable of traversing the Martian terrain in order to explore larger areas of the planet. In addition, there have been two failed attempts at deploying penetrators on Mars, designed to ballistically drop to the planet's surface, slamming into it and becoming embedded at depths of several metres, enabling subsurface investigation using onboard instrumentation (Surkov and Kremnev, 1998; Smrekar *et al.*, 1999). There have also been attempts to radically redesign how a planetary surface vehicle might travel, for example with the proposed Mars Hopper (Howe *et al.*, 2011).

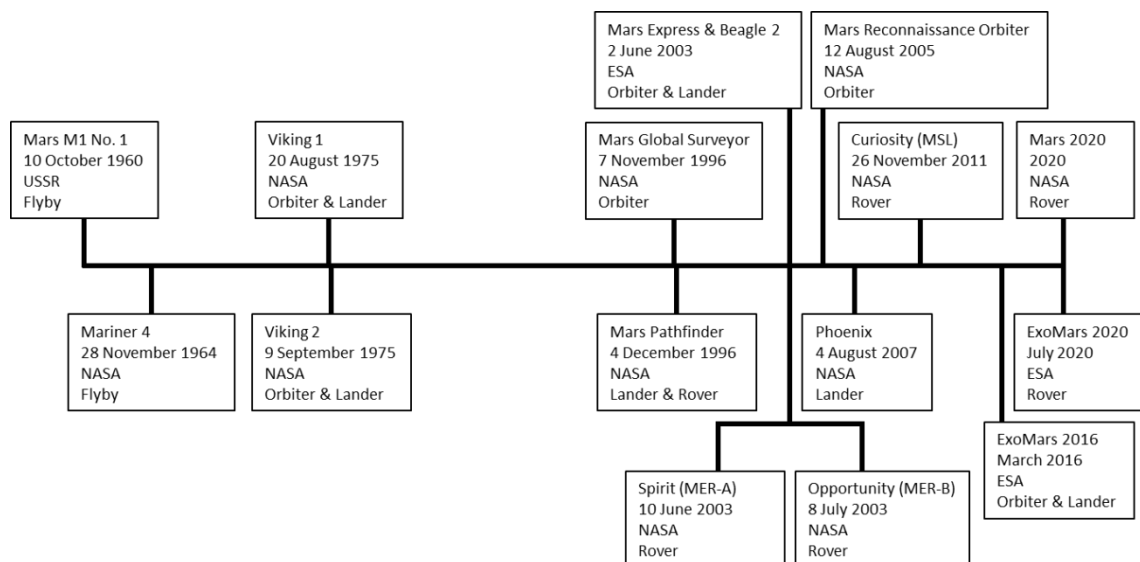


Figure 1.1: A timeline of key Mars exploration missions, giving each mission's name, launch date, operator and mission type.

The following subsections provide details about a selection of missions that have had a large impact on our understanding of Mars and its environment. A description of the key objectives of each mission is given, followed by a discussion of the scientific data

acquired, the main findings of each mission and their relevance to current and future exploration missions. This will help to provide appropriate context for the ExoMars missions and for the studies presented in this thesis.

### 1.1.1.1 Mariner 4

Mariner 4 (Figure 1.2) was a NASA space probe, launched on 28 November 1964, whose primary mission was to perform a flyby of Mars, acquire images and scientific observations of the planet at its closest approach and transmit them back to Earth (Schneiderman, 1967). Its secondary objectives were to make measurements of the magnetic field and energetic particles in interplanetary space, both before and after its encounter with Mars.



Figure 1.2: An artist's impression of the Mariner 4 space probe. Image credit: NASA/JPL-Caltech.

Mariner 4 was equipped with a cosmic ray telescope for detecting extrasolar high energy alpha particles and protons, a cosmic dust detector with which to investigate interplanetary dust, a trapped radiation detector for studying low energy particles, an ionisation chamber to measure charged particle densities, a plasma probe for observing solar plasma flux and a magnetometer for making magnetic field measurements. The probe also carried a television camera that was to be used to image the surface of Mars (Reiff, 1966).

On 14 July 1965, 7½ months after launch, the Mariner 4 probe provided the first close-up images of the Martian surface (e.g. Figure 1.3). These pictures were largely responsible for a change in common opinion about Mars, as it was considered extremely unlikely that the dusty, cratered world seen in them could harbour life. Data acquired by Mariner 4 also had a great impact on our understanding of the interplanetary magnetic field and its interaction with the solar wind (e.g. Siscoe *et al.*, 1968), the Martian atmosphere (Fjeldbo *et al.*, 1966) and asteroidal bombardment throughout the history of the Solar System (Chapman *et al.*, 1969).

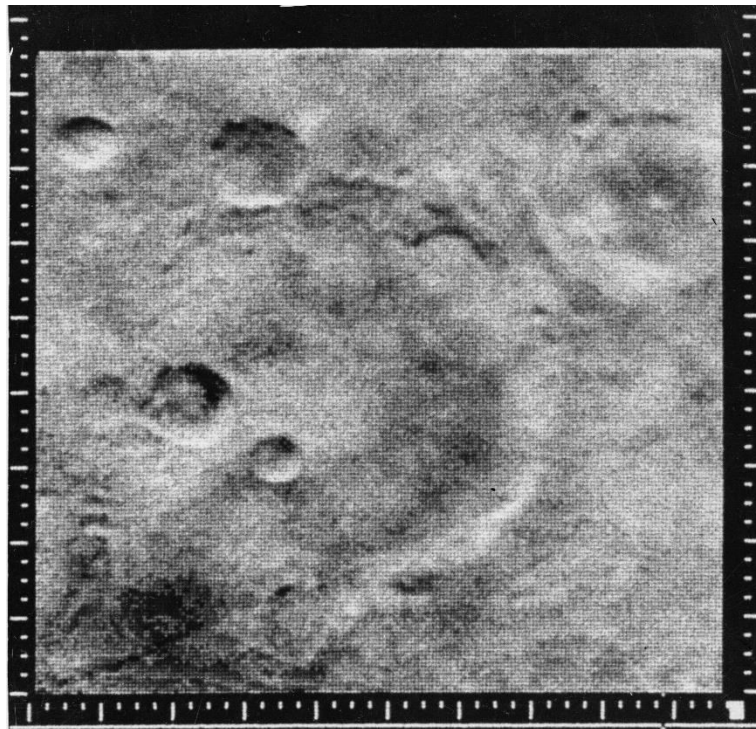


Figure 1.3: Photograph of part of Sirenum Fossae, taken from an altitude of around 12,600 km by the Mariner 4 space probe. The image covers an area of 250 by 254 km, is centred at 32.7°S 162.7°W and clearly shows the cratering on the surface of Mars. The large, heavily eroded crater that takes up the bottom left portion of the photograph is the probe's namesake, the Mariner crater. Image credit: NASA/JPL-Caltech.

### 1.1.1.2 Viking programme

Throughout the late 60s and early 70s, NASA achieved further successes with the Mariner 6 and 7 flyby probes and the Mariner 9 orbiter. The Mariner programme's successor, the Viking programme, was considerably more ambitious, aiming to perform the first successful soft landing on Mars. The Viking 1 and 2 spacecraft were launched on 20 August and 9 September 1975 respectively, each consisting of an orbiter and a lander. Viking 1 achieved an orbit around Mars on 19 June 1976 and after around a month in orbit, once a landing site had been identified, released its lander (Figure 1.4),

which performed the first successful soft landing on the surface of Mars on 20 July. Viking 2 followed behind, arriving at the planet on 7 August and depositing its lander on 3 September.



Figure 1.4: A model of the Viking landers. Image credit: NASA/JPL-Caltech/University of Arizona.

The science objectives of the programme were to return high-resolution photographs directly from the Martian surface, determine the composition of both the planet and the atmosphere and finally to search for signs of life on Mars. In order to complete some aspects of these objectives, each of the orbiters carried two high-resolution cameras for capturing photographs of the surface from orbit, an infrared (IR) spectrometer for mapping the water vapour in the Martian atmosphere and an IR radiometer for producing thermal maps of the Martian surface.

The landers were each equipped with a 360° panoramic mast camera, an instrument for performing gas chromatography-mass spectrometry (GC-MS), a suite of biology experiments, a retarding potential analyser for the analysis of charged particles in the upper atmosphere during entry, an array of meteorological sensors, a miniature seismometer, arm-mounted magnets for contact experiments with the Martian regolith, a variety of sensors for the acquisition of physical data (e.g. images of the lander footpads, mechanical resistance of the surface, lander temperature, etc.) and finally a

communication radio that could also be used for a number of science investigations (Soffen and Young, 1972).

Of particular scientific interest were the results of the three biological experiments onboard the Viking landers (Brown *et al.*, 1978). The first was the Pyrolytic Release (PR) experiment, which involved exposing a sample of Martian regolith to a CO and CO<sub>2</sub> atmosphere, in which all of the carbon atoms were in fact radioactive carbon-14 (<sup>14</sup>C). If photosynthetic organisms were present, it was thought that some <sup>14</sup>C would be incorporated by them into organic molecules that would be vaporised upon heating and therefore be detectable by their inherited radioactivity, providing evidence for the presence of photosynthetic life. The second experiment was called Labelled Release (LR) and was quite similar to pyrolytic release. In the labelled release experiment, a small amount of aqueous nutrient solution containing <sup>14</sup>C was introduced to a sample of Martian regolith. If microbial life was present, it would metabolise the nutrients in the solution, evolving radioactive <sup>14</sup>CO<sub>2</sub> that could be detected, providing evidence for the presence of microbial life. The final biological experiment was the Gas Exchange (GEx) experiment, which involved isolating a regolith sample in an incubation chamber with nutrients and water and using the lander's onboard GC-MS instrument to periodically measure the concentrations of certain gasses in the chamber, including hydrogen, methane, CO<sub>2</sub>, oxygen and nitrogen. The hypothesis was that if living organisms were present, these concentrations would be observed to change in a closed environment such as this.

The results of the Viking biological experiments were contradictory, however Klein (1978) concluded that abiotic explanations could be given for all of the data if taken as a whole. The results of the GEx experiment pointed convincingly towards an abiotic cause, largely because heating samples of Martian regolith to temperatures that should result in sterilisation appeared to have no effect on the outcome of the experiment. Klein postulated that the presence of superoxides, combined with a secondary oxidant such as gamma phase iron(III) oxide ( $\gamma$ -Fe<sub>2</sub>O<sub>3</sub>), would completely explain the GEx results. The LR experiment had a positive result, with significant quantities of radioactively labelled CO<sub>2</sub> developed following introduction of the aqueous nutrient solution. Unlike the GEx experiment, this reaction was inhibited by heating, potentially suggesting a biological cause. However, Klein calculated that a particularly high concentration of biological cells would be required to drive the observed rate of CO<sub>2</sub> production. This was at odds

with the GEx results, so Klein offered an alternative explanation. It was hypothesised that the results of the LR experiment could be explained by the presence of a third, more thermally sensitive oxidant in the Martian regolith, such as hydrogen peroxide ( $\text{H}_2\text{O}_2$ ), whose presence on Mars had already been postulated. The results of the PR experiment were the most ambiguous, with as many likely abiotic explanations as biotic. Given the conclusions drawn from the results of the other two experiments, Klein also gave an abiotic explanation for the results of the PR experiment.

Of course, the data acquired by the Viking landers have been repeatedly scrutinised over the last 40 years and various different interpretations have been offered (e.g. Houtkooper and Schulze-Makuch, 2007) and see §1.1.2.1 later in this chapter for a discussion of the most convincing evidence that the results of the Viking biological experiments requires further, additional investigation.

A great deal of data were acquired by the Viking orbiters and landers in addition to those obtained from the landers' biological experiments. Analysis of these data vastly improved knowledge of the temperature profile and weather on Mars (Kieffer *et al.*, 1977), the planet's geology (Binder *et al.*, 1977; Mutch *et al.*, 1977) and the abundance of hygroscopic minerals in the regolith (Clark, 1978).

### 1.1.1.3 Mars Global Surveyor

The overall null result of the Viking landers' biological experiments resulted in a temporary loss of interest in the exploration of Mars. In 1988, the Soviet Union launched its Phobos missions to explore the Martian moons Phobos and Deimos, however both missions ended in failure. It was not until 1992 that a new mission to Mars was attempted, with NASA's Mars Observer orbiter, also lost prior to its arrival at the Martian system. The next successful Mars mission was in 1996.

The Mars Global Surveyor (MGS), seen in Figure 1.5, was launched on 7 November 1996 and had six formal scientific objectives, many of which it inherited from the failed Mars Observer. They were to study the morphology of the surface of Mars, map surface composition in terms of key minerals, rocks and ices, map global topography in relation to gravitational field strength, determine the nature of the planetary magnetic field, monitor Martian weather and finally investigate the interaction between the atmosphere and surface by observing features such as the polar ice caps (Albee *et al.*, 2001).



Figure 1.5: Artist's impression of the Mars Global Surveyor orbiter. Image credit: NASA/JPL-Caltech.

The MGS payload included a number of science instruments with which to achieve its objectives. These were the Mars Orbiter Camera (MOC), the Thermal Emission Spectrometer (TES), the Mars Orbiter Laser Altimeter (MOLA), the Ultrastable Oscillator (USO/RS), the Magnetometer/Electron Reflectometer (MAG/ER) and the Mars Relay (MR) (Albee *et al.*, 2001). Of these it is MOLA that has had the greatest, longest lasting impact on Mars science (Smith *et al.*, 2001). It was used to generate complete topographical maps of Mars (Figure 1.6), using measurements of the time-of-flight of IR pulses to precisely measure distances to the surface. The maps have been used to perform detailed studies of regions of particular interest, for example the polar caps (Zuber *et al.*, 1998), and candidates for ancient oceans (Head III *et al.*, 1999).

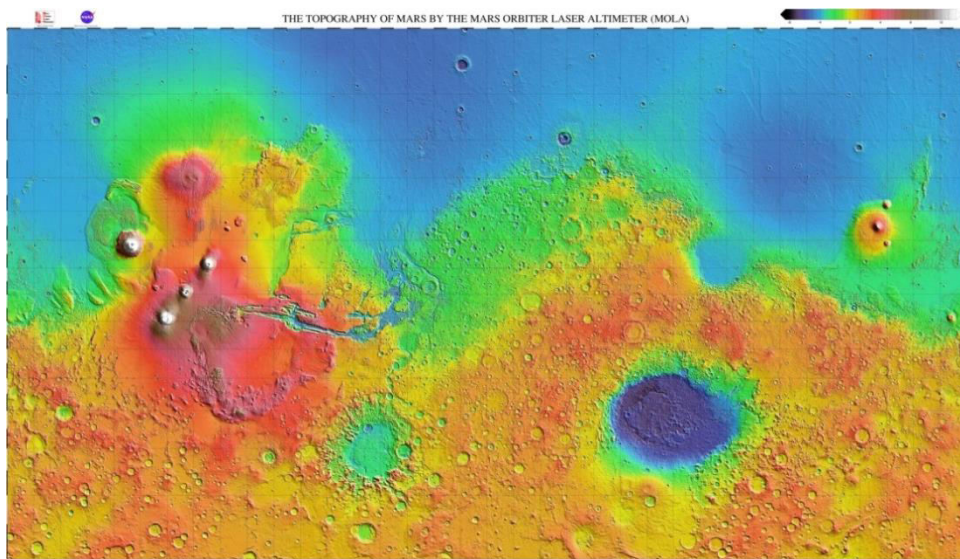


Figure 1.6: Colour-coded topography map of Mars, generated using data from the Mars Orbiter Laser Altimeter instrument onboard the Mars Global Surveyor orbiter. Image credit: NASA/JPL-Caltech.

In addition to its contribution to the study of Martian topography, the MGS was instrumental in the discovery of Mars' remnant crustal magnetic field (Acuña *et al.*, 1999), provided the first observations of the polar seasonal cycle (Kieffer and Titus, 2001) and has been used in the analysis of potential landing sites for future missions, such as the Phoenix lander (Mellon *et al.*, 2008a; Mellon *et al.*, 2008b) and the Curiosity rover (Golombek *et al.*, 2012).

### 1.1.1.4 Mars Pathfinder

NASA's subsequent mission, Mars Pathfinder, was launched on 4 December 1996 (Golombek *et al.*, 1997). It was the first Mars surface mission attempted since the Viking programme and consisted of a lander, which was later renamed the Carl Sagan Memorial Station, and a rover named Sojourner, the first rover to be deployed on Mars (Figure 1.7). The mission was primarily intended to be the first demonstration of rover exploration on Mars, as well as proof that rapid, low-cost spacecraft development was feasible. In fact, the Sojourner rover took only three years to design and build, costing only \$25m, which was more than an order of magnitude less than any other interplanetary spacecraft deployed at the time (Stone, 1996). In addition, Pathfinder also provided the first demonstration of an airbag landing on Mars (Cadogan *et al.*, 2002).

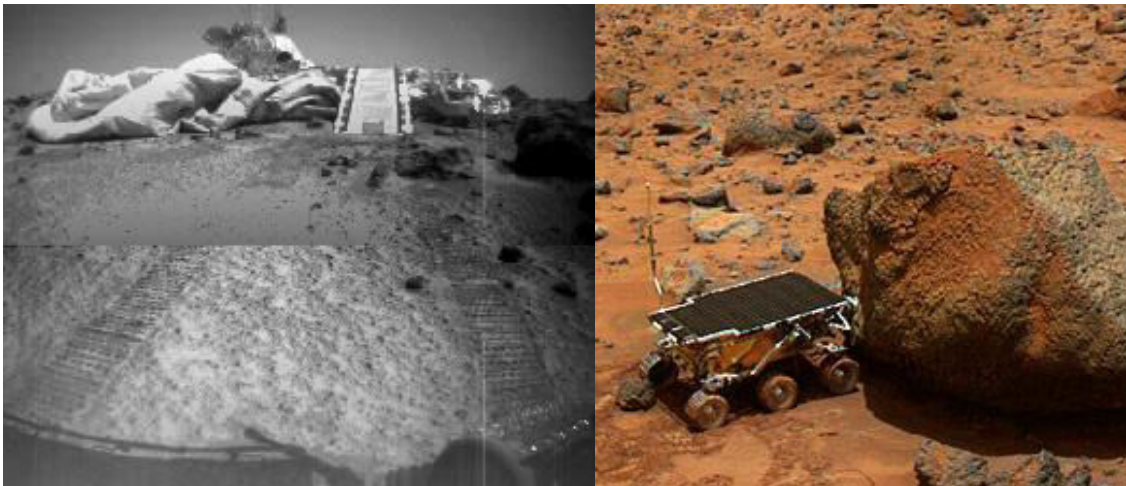


Figure 1.7: Left: A photograph of the Pathfinder lander, also known as the Carl Sagan Memorial Station, taken using the rear camera onboard the Sojourner rover. Right: A photograph of Sojourner investigating a Martian rock, taken by the lander. Image credit: NASA/JPL-Caltech.

In addition to the mission technological objectives the lander and rover carried science payloads. The lander was equipped with an imaging system and a suite of meteorological sensors, whilst the rover's payload included its own imaging system, a hazard detection and avoidance system, a spectrometer for alpha particle X-ray

spectroscopy (APXS), a wheel abrasion experiment, a materials adherence experiment and several accelerometers. The mission made significant contributions to the understanding of Martian weather and atmosphere (Schofield *et al.*, 1997), as well as the interior structure of Mars (Folkner *et al.*, 1997).

### 1.1.1.5 Mars Express and Beagle 2

Mars Express (Figure 1.8) is an ESA Mars orbiter that was launched on 2 June 2003. It was designed to perform further remote study of the Martian atmosphere and surface, focusing particularly on the evaluation of the water inventory on Mars (Chicarro *et al.*, 2004). It carried with it the British lander Beagle 2 (Figure 1.8), whose primary objective was to search for signs of past or present life on Mars. Contact was lost with Beagle 2 during the descent phase and that element of the mission was declared a failure. However, on 16 January 2015 it was announced that Beagle 2 had been observed in high resolution photographs taken by the High Resolution Imaging Science Experiment (HiRISE) camera onboard NASA's Mars Reconnaissance Orbiter (MRO)<sup>2</sup>. These photographs (Figure 1.9) showed that Beagle 2's solar panels failed to unfurl completely, preventing a communication link with the lander from being established.

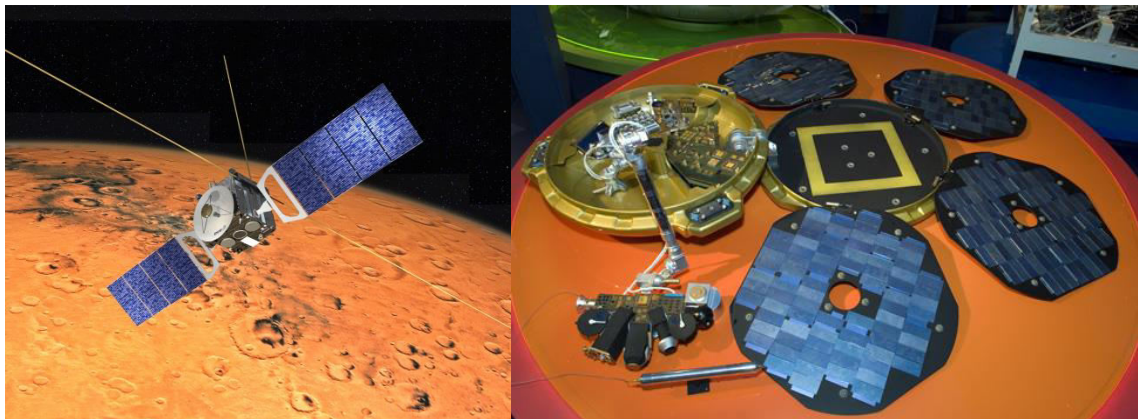


Figure 1.8: Left: Artist's impression of the Mars Express orbiter above the surface of Mars. Image credit: ESA. Right: Replica model of the Beagle 2 lander with its solar panels fully deployed. Image credit: Science Museum/Science & Society Picture Library.

As with NASA's Pathfinder mission, ESA's Mars Express (including the Beagle 2 lander) attempted to consolidate the view that low-cost planetary exploration was not only possible, but programmatically preferable. The initial mission cost cap was €150m, which by 2003 had increased to €203m in line with inflation rates, making it half as

---

<sup>2</sup> <http://www.nasa.gov/jpl/lost-2003-mars-lander-found-by-mars-reconnaissance-orbiter/> [Accessed: 17 December 2015].

expensive as similar missions (Schmidt, 2003). In order to accomplish this, the mission had a very modest mass budget, extending to a maximum mass for the Beagle 2 lander of just 69 kg (Pullan *et al.*, 2004). By comparison, the Pathfinder lander had a mass of 264 kg. This extremely low mass was achieved with a number of innovative design features and an almost complete lack of redundancy.

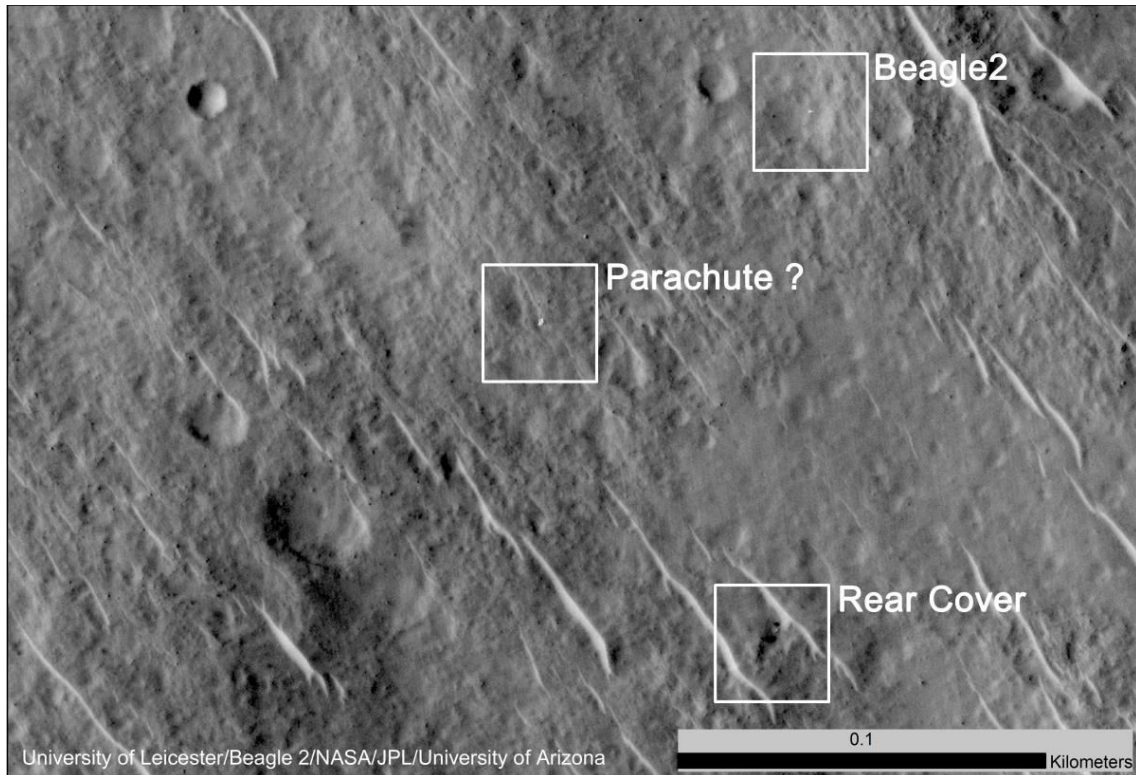


Figure 1.9: Annotated photograph taken by the HiRISE camera onboard NASA's Mars Reconnaissance Orbiter, showing the final location of the Beagle 2 lander, its successfully detached rear cover and possibly its parachute. Image credit: NASA/JPL-Caltech/Univ. of Arizona/University of Leicester.

Despite the loss of Beagle 2, Mars Express has been an extremely successful mission and continues to operate today. The orbiter's payload includes the High Resolution Stereo Camera (HRSC) for imaging the surface of Mars, the Visible and IR Mineralogical Mapping Spectrometer (OMEGA) for determining the composition of the Martian atmosphere and surface in order to elucidate the CO<sub>2</sub> and H<sub>2</sub>O cycles on Mars, the Planetary Fourier Spectrometer (PFS) for measuring atmospheric pressure and temperature, the UV and IR Atmospheric Spectrometer (SPICAM) for determining the elemental composition of the atmosphere, the Subsurface-Sounding Radar/Altimeter (MARSIS) for detecting and mapping subsurface water (both liquid and solid) and the Analyser of Space Plasmas and Energetic Atoms (ASPERA) for studying plasmas at the interface between Mars' upper atmosphere and the interplanetary medium (Chicarro *et*

*al.*, 2004). Mars Express is also equipped with a Visual Monitoring Camera, which was used to image the separation of the orbiter and the Beagle 2 lander, and a communication array that was intended to provide a link with Beagle 2, but has instead been used to provide support to NASA's Mars Exploration Rover (Edwards, Jr. *et al.*, 2006) and Phoenix (Edwards, Jr. *et al.*, 2010) missions.

Data acquired using the instruments onboard the Mars Express orbiter have been used, amongst other things, to derive new information about Mars' water history (Bibring *et al.*, 2006) and to gain an understanding of how the Martian atmosphere is eroded by the solar wind (Lundin *et al.*, 2004).

### 1.1.1.6 Mars Exploration Rovers

The Mars Exploration Rover (MER) mission is a NASA Mars exploration mission that consisted of a pair of rovers (Figure 1.10), designated Spirit (MER-A) and Opportunity (MER-B) (Crisp *et al.*, 2003). They were launched on 10 June and 7 July 2003 respectively, with a set of joint primary science objectives that were aimed at determining the past and present habitability of Mars. These were to investigate landing sites that are likely to retain evidence for the action of water, to identify and analyse surface material that provides clues to past water activity, to determine at what point in time liquid water was present and assess whether the environment could have supported life. Further objectives included investigating the geological composition of the landing sites and the geochemical processes that must have resulted in such composition, in order to provide a comparison with remote sensing data. Spirit and Opportunity arrived on Mars on 4 and 25 January 2004 respectively, making a soft landing utilising airbag systems similar to the one first tested by the Pathfinder mission.

Spirit and Opportunity each carry the Athena science payload (Squyres *et al.*, 2003). This suite of scientific instruments includes the Panoramic Camera (PanCam) and Miniature Thermal Emission Spectrometer (Mini-TES), which are co-pointed and mounted on the rover masts. The rest of the instruments are mounted on a robotic arm and comprise a microscopic imager, an APXS instrument, a Mössbauer spectrometer and a rock abrasion tool for removing the outer surface of rocks, exposing their interior for study. Finally, each rover is equipped with a number of magnets with which to conduct a magnetic properties experiment with material recovered from the Martian surface.



Figure 1.10: An artist's impression of NASA's Mars Exploration Rovers. Image credit: NASA/JPL-Caltech.

The MER rovers are one of the greatest successes in Mars exploration to date, having completely exceeded all expectations of the mission in every possible way. On 1 May 2009, Spirit became stuck in the Martian regolith and despite the best efforts of NASA engineers it was impossible to free. After a short period as a stationary science platform, communication was completely lost with the rover and on 24 May 2011 its mission was officially ended. Spirit was operational for 2208 sols, over 20 times its originally planned 90 sol mission timescale, having travelled 7.73 km, considerably further than the original mission requirement of 600 m. In this time, Spirit transmitted over 128,000 raw images and a wealth of other scientific information. Opportunity has enjoyed even greater longevity and is still operational, having travelled an impressive 42.65 km in 4228 sols as of 15 December 2015<sup>3</sup>.

One of the highlights of the MER mission so far is the rovers' huge contribution to our ever increasing understanding of the water environment on Mars. This involved the detection of sulphate salts and jarosite in Martian rocks, both examples of minerals that require liquid water to form on Earth. The MER rovers have also been used to observe transits of both Phobos and Deimos across the Sun and, in combination with the TES

---

<sup>3</sup> [http://mars.nasa.gov/mer/mission/status\\_opportunityAll.html](http://mars.nasa.gov/mer/mission/status_opportunityAll.html) [Accessed: 19 December 2015].

instrument onboard the MGS orbiter, helped to generate the first complete temperature profile of the Martian atmosphere.

### 1.1.1.7 Mars Reconnaissance Orbiter

NASA's MRO, an artist's impression of which can be seen in Figure 1.11, was designed to be a versatile satellite with an array of scientific instruments for analysing the surface and returning more data than any previous mission (Bibring, 2011), monitoring Martian weather and imaging potential landing sites for future surface missions. It was launched on 12 August 2005 and following a 7 month transit, achieved a stable orbit around Mars on 10 March 2006.



Figure 1.11: An artist's impression of NASA's Mars Reconnaissance Orbiter in orbit above Mars. Image credit: NASA/JPL-Caltech.

The MRO is equipped with six science instruments, as well as a suite of engineering tools and instrumentation. The science instruments include the Context Camera (CTX) to provide context images for the other instruments, the HiRISE camera, a 0.5 m reflector telescope and camera system capable of capturing images of the Martian surface with a resolution of around 0.3 m, the Mars Colour Imager (MARCI) for mapping atmospheric water vapour and ozone, the Compact Reconnaissance Imaging Spectrometer for Mars (CRISM), a visible and near IR spectrometer designed to map

surface mineralogy, the Mars Climate Sounder (MCS) for measuring climate parameters and finally the Shallow Subsurface Radar (SHARAD) for studying the polar ice caps.

The HiRISE camera has provided an unprecedented view of the surface of Mars at an extremely high spatial resolution of 0.3 m. Figure 1.12 shows a HiRISE image in the Sirenum Fossae region, the same area as seen in the Mariner 4 photograph in Figure 1.3. HiRISE has enabled surface features to be studied in great detail, by both researchers worldwide and by citizen science projects, and has also been used to acquire images of every Mars surface mission (including the ill-fated Beagle 2 lander, as discussed in §1.1.1.5). The CRISM instrument has also made a significant contribution to Mars science, having been used to map out surface minerals that provide information about the Martian water environment (such as oxides, phyllosilicates and carbonates). This is particularly important when searching for potential habitats, or even direct signs of extant life on Mars.

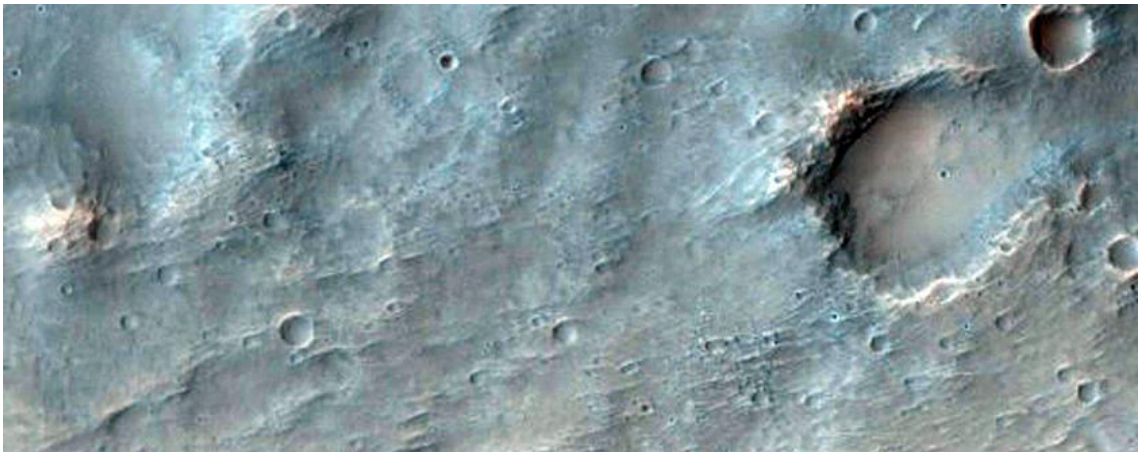


Figure 1.12: HiRISE image centred at 32.611S 211.364E, showing cratering in the Sirenum Fossae region of Mars. Image credit: NASA/JPL/University of Arizona.

### 1.1.1.8 Phoenix

Phoenix was a NASA lander mission to the Martian north pole that was launched on 4 August 2007. The Phoenix lander (Figure 1.13) was equipped with a science payload with objectives to investigate the polar water history to resolve climate change, and evaluate past and present habitability of the polar subsurface ice. The lander's payload included (Shotwell, 2005):

- a robotic arm for sample acquisition from up to 0.5 m below the surface

- several camera systems, including one mounted on the arm, one on a mast and a rear facing system for imaging the descent of the lander
- the Thermal and Evolved Gas Analyser (TEGA) for heating samples of surface material and analysing the evolved gas via mass spectrometry
- the Microscopy, Electrochemistry, and Conductivity Analyser (MECA)
- a suite of experiments including optical and atomic force microscopes and a wet chemistry laboratory
- the Thermal and Electrical Conductivity Probe (TECP), and
- a Meteorological station

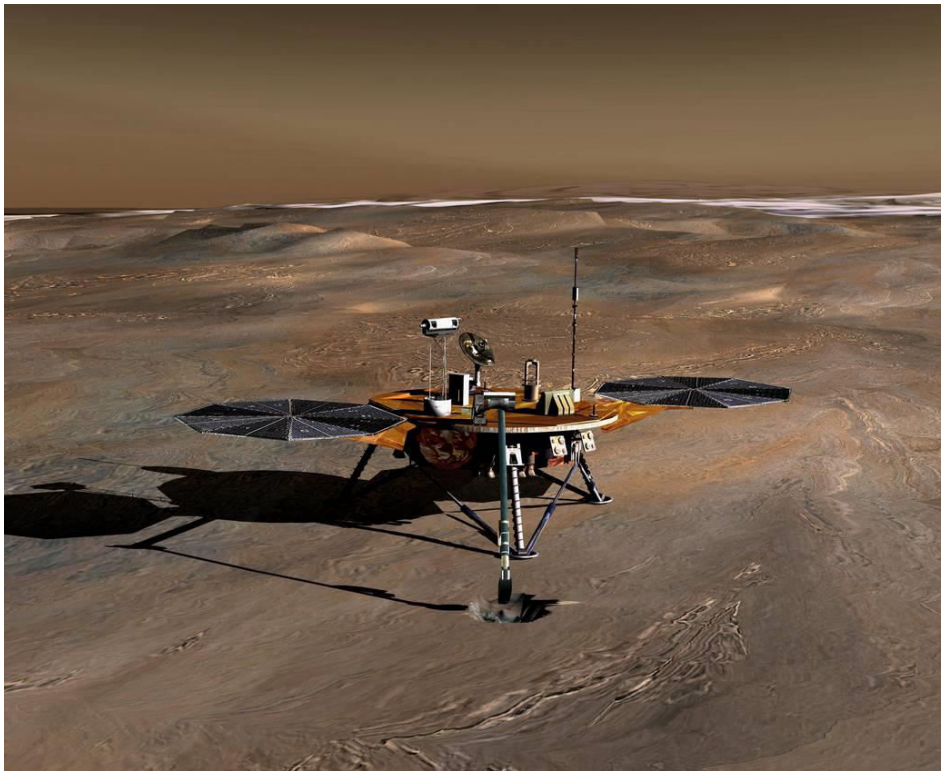


Figure 1.13: An artist's impression of the Phoenix lander on the surface of Mars. Image credit: NASA/JPL-Caltech.

During the 157 sols for which the Phoenix lander was in operation, it successfully completed all of its primary objectives. It provided direct evidence for the presence of water ice just below the surface at the Martian north pole, something that had previously only been inferred from remote sensing data. It also made the first observation of snow cirrus clouds on Mars, improving our understanding of Martian weather. Consistent with the findings of the Viking landers, Phoenix found no evidence of organic chemistry, although it did discover an abundance of perchlorate salts in the Martian regolith (Hecht *et al.*, 2009). It was hypothesised that the presence of perchlorate salts in

any heated sample could destroy any organics present in the sample, producing null results from many decades of organic detection experiments. This discovery, and its impact upon the interpretation of data acquired by past Mars missions, is fully discussed in §1.1.2.1.

### 1.1.1.9 Mars Science Laboratory

MSL is an ongoing NASA Mars mission that succeeded in landing the Curiosity rover (Figure 1.14) on the surface of Mars, in Gale crater at the foot of Mount Sharp. Curiosity launched on 26 November 2011 with the primary objective to assess the past habitability of Gale crater by analysing the geology, climate and water environment, evaluating whether conditions were ever suitable for supporting bacterial life. Much of this research is also good preparation for potential future human exploration of Mars.

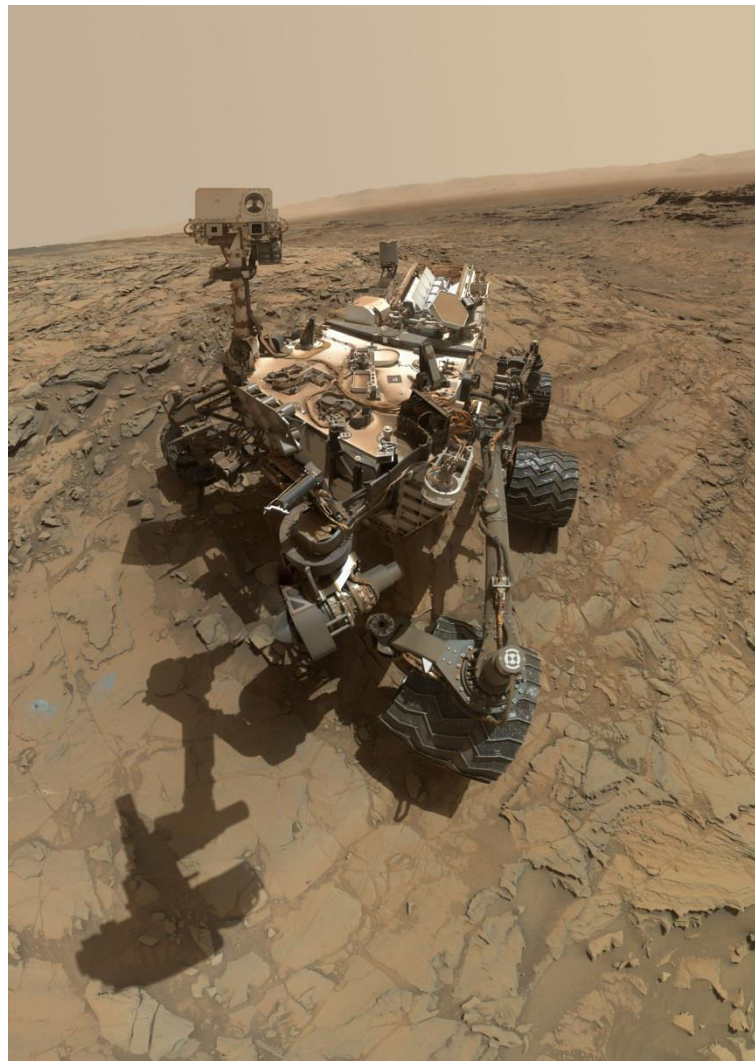


Figure 1.14: A self-portrait of NASA's Curiosity rover on the surface of Mars, acquired on sol 1126 of its mission, or 6 October 2015, using the Mars Hand Lens Imager camera that is mounted on the rover's robotic arm. Image credit: NASA/JPL-Caltech/MSSS.

## 1.1 The exploration of Mars

---

The Curiosity rover is larger, heavier and requires more power than any of NASA's previous Mars rovers. It is the size of a small car and equipped with a radioisotope thermoelectric generator (RTG) to meet its power requirements. Table 1.1 gives a comparison of NASA's three models of Mars rover.

Table 1.1: A comparison of NASA's three models of Mars rover.

	<b>Sojourner</b>	<b>Mars Exploration Rover</b>	<b>Curiosity</b>
<b>Mass (kg)</b>	11.5	185	899
<b>Dimensions (m)</b>	0.65 long x 0.48 wide x 0.30 tall	1.6 long x 2.3 wide x 1.5 tall	2.9 long x 2.7 wide x 2.2 tall
<b>Power (W)</b>	16.5 on Mars at noon	140 for four hours per sol	125 continuously

Curiosity's science payload includes the Mast Camera (MastCam) system, a pair of true-colour cameras that are also capable of performing reflectance spectroscopy, the Chemistry and Camera complex (ChemCam; a remote LIBS instrument), four navigation cameras (NavCams), eight hazard avoidance cameras (HazCams), the Rover Environmental Monitoring System (REMS) for making meteorological measurements, the Mars Hand Lens Imager (MAHLI), a camera that is mounted on the rover's robotic arm for microscopic and fluorescent imaging of rock samples, an APXS instrument, the Chemistry and Mineralogy experiment (CheMin) which is an X-ray powder diffractometer, the Sample Analysis at Mars experiment (SAM) which incorporates a quadrupole mass spectrometer, a gas chromatograph and a tunable laser spectrometer, a Dust Removal Tool (DRT), a Radiation Assessment Detector (RAD), the Dynamic Albedo of Neutrons experiment (DAN) and finally the Mars Descent Imager (MARDI) for acquiring photographs during the rover's landing (Grotzinger *et al.*, 2012).

Like the other Mars missions discussed throughout §1.1.1, the Curiosity rover has contributed a great deal to our knowledge and understanding of Mars and the Martian environment (e.g. Mahaffy *et al.*, 2013; Grotzinger. 2014; Webster *et al.*, 2015). One of the most significant results from the mission so far is the discovery of all of the elemental "building blocks" required for life in rocks on Mars, which are carbon, hydrogen, oxygen, phosphorus and sulphur. Curiosity made the first detection of biologically useful nitrogen on Mars (Stern *et al.*, 2015). Other important results include the discovery of evidence of historical flowing water, in the form of what appear to be ancient stream beds (Williams *et al.*, 2013), and the monitoring of the dangerous levels

of radiation on the surface of Mars, which would pose a significant risk for any human explorers on Mars in the future (Zeitlin *et al.*, 2013; Hassler *et al.*, 2014).

### 1.1.2 The Mars environment

As a result of the extensive exploration of Mars, summarised in §1.1.1, the present Martian surface environment is well understood and much about Mars' past has also been inferred. Current conditions are not especially conducive to life, although terrestrial extremophilic life, as will be discussed in detail in §1.2, provides many examples of living organisms that are capable of survival in extreme environments similar to those found on Mars.

Mars has a tenuous atmosphere with an average surface pressure of 0.6 kPa, less than 1% of that of Earth, composed almost entirely of CO<sub>2</sub> (Barlow, 2008). Combined with Mars' distance from the Sun, this results in an average surface temperature of -55 °C, with a minimum of around -153 °C and a maximum of around 20 °C. The majority of Mars' water is therefore frozen, presenting steep challenges for microbial life, though Ojha *et al.* (2015) recently confirmed the existence of seasonal flows of briny, liquid water on the Martian surface.

In addition to the unfavourable climatic conditions, the Martian regolith is also unsuited to supporting unadapted living organisms. It contains a number of powerful oxidants (Benner *et al.*, 2000) and is highly desiccating due to its high salt concentrations (Mancinelli *et al.*, 2004). Finally, the presence of perchlorate salts in the Martian regolith, as detected by NASA's Phoenix lander, would likely be extremely inhibitive to the survival of living organisms.

#### 1.1.2.1 Perchlorates on Mars

A perchlorate salt is any ionic salt that forms from the ClO<sub>4</sub><sup>-</sup> perchlorate ion. Although several perchlorate species are naturally occurring in small quantities on Earth, it is thought that the most common species in the Martian regolith are MgClO<sub>4</sub> and NaClO<sub>4</sub>, however Ca(ClO<sub>4</sub>)<sub>2</sub> is also considered likely. It has been suggested that perchlorates form naturally in arid environments as a result of the oxidation of chlorine compounds by ozone and its photochemical products, a process that may be responsible for the abundance of perchlorates on Mars (Catling *et al.*, 2010).

### **1.1.3 Historical Martian conditions**

---

The presence of significant concentrations of perchlorates in the Martian regolith has a number of consequences. Of particular relevance are i) water will freeze at lower temperatures, increasing the stability of water on the surface of Mars with significant implications for life (Zorzano *et al.*, 2009), and ii) in sufficient concentration, perchlorates are toxic to humans, complicating any future human exploration or habitation of Mars (Davila *et al.*, 2013).

#### **1.1.2.1.1 Reanalysis of past mission data**

The detection of perchlorates on Mars also has a number of implications for the conclusions drawn from some of the data acquired by past Mars missions, so there have been a number of attempts at reinterpreting data in order to draw new conclusions from previous missions in light of their presence. It has been shown that when organic-rich soils are heated, as the Martian regolith was during the Viking biological experiments, in the presence of perchlorate, all organic material is entirely decomposed into carbon dioxide and water (Navarro-González *et al.*, 2010). This means that the experiments onboard the Viking landers may have inadvertently destroyed any organics that were indeed present in the samples of the Martian regolith that they were interrogating, explaining why they were not detected. Navarro-González *et al.* modelled the concentration of organic carbon that may have been present at the Viking landing sites, estimating that it could be between 1.5 and 6.5 ppm at site 1 and between 0.7 and 2.6 ppm at site 2.

### **1.1.3 Historical Martian conditions**

As stated earlier, it is theorised that conditions on Mars have changed drastically over geological timescales and that at some point in its history, the climate was much warmer and therefore wetter than it is currently (Pollack *et al.*, 1987; Craddock and Howard, 2002). If this hypothesis is true, and given the weakness of the young Sun, early Mars must have had a much thicker, more heat retentive atmosphere. Modelling has suggested that it may have been possible for Mars to have retained an atmosphere with pressures of up to 1 bar until after the late heavy bombardment (Carr, 1999).

Following this period, Mars' primordial atmosphere was most likely eroded by the solar wind, which was made possible due to the planet's low gravitational field strength and the lack of sufficient renewal of atmospheric gases (Perez-de-Tejada, 1992).

**1.1.4 Geology of Mars**

As with other rocky planetary bodies, the geology of Mars is quite complex. It is dominated by igneous basalts that result from the planet's primordial volcanism and internal dynamism. This makes much of the rock on Mars relatively old, as the planet is no longer volcanically active and magnetic field measurements show that it no longer has a fluidic core or mantle. There is a small proportion of sedimentary rock on Mars, which has largely formed as a result of aeolian deposition, although there is also some evidence for fluvial and lacustrine sedimentary deposits. This is of great importance for missions to Mars for two reasons: firstly, sedimentary rocks can provide ideal habitats for microbial life, and secondly, aeolian processes are essential in the formation of desert varnishes, which are possibly of biological origin (Dorn and Oberlander, 1981). There is also some metamorphism on Mars that occurs as a result of pressure and thermal processing following the burying of material.

Of particular interest to Mars exploration missions are minerals that either require water for formation, or are highly hygroscopic and so contain water bound in their molecules. Good examples of these are hydrated sulphates such as gypsum or jarosite, or clay minerals such as montmorillonite, which have all been detected in some abundance by past Mars missions (e.g. Squyres *et al.*, 2004; Langevin *et al.*, 2005; Poulet *et al.*, 2005).

There is also a significant quantity of calcium carbonate on Mars. This is of interest due to the link between certain polymorphs and marine life on Earth, which means that future missions to Mars must be able to distinguish between polymorphs of calcium carbonate. There are also a great number of microbial species on Earth that precipitate calcium carbonate following the metabolism of calcium, which means that carbonate deposits represent potential habitats (Hammes and Verstraete, 2002).

**1.2 Astrobiology**

Astrobiology is a broad, multidisciplinary field that encompasses the study of the genesis and evolution of terrestrial life, the search for life on other worlds and the future of life in the Universe (Des Marais *et al.*, 2008). This currently takes the form of the identification of potential extraterrestrial habitats, the determination of adaptations required by living organisms to survive, and even thrive, in such environments and the design of experiments and space missions capable of detecting those organisms. The

first stage of this research is the study of terrestrial life that has adapted to survival in the harshest, most life-limiting conditions on Earth. By investigating the mechanisms that facilitate their survival it is possible to extrapolate, or in some cases even directly experiment, to establish whether life could survive on another planet. The field of astrobiology also seeks to elucidate the origins of life, an endeavour that would be supported by the discovery of an entirely independent branch of life in the Solar System, but also one that will improve our ability to locate suitable habitats for life and therefore enable such a discovery.

In the context of Mars exploration, astrobiologists seek to evaluate both the past and present habitability of the Martian environment and search for signs of either extinct or extant life. In the case of extinct life, the goal is to find unequivocal fossil evidence that Mars hosted life at some point in its history. This is not a trivial challenge, but is tied inextricably to the search for the earliest life on Earth and the definition of sufficient evidence for the existence of ancient living organisms. In the case of extant life, the aim is to detect chemical or geological biomarkers that have no plausible abiotic origin (Edwards *et al.*, 2014).

### **1.2.1 Extremophilic life on Earth**

Over the past few decades it has been observed that life has adapted to survive in almost every environment on Earth, no matter how severe, so long as liquid water is present (Rothschild and Mancinelli, 2001). Extremophiles are living organisms that are highly adapted for survival in harsh conditions, for example cryophiles, which can survive and reproduce at very low temperatures (e.g. Cavicchioli *et al.*, 2002), xerophiles, which can withstand especially dry conditions (e.g. Direito *et al.*, 2011), and halophiles, which flourish in high salt concentrations (e.g. Oren, 2002). Each of these adaptations would be extremely beneficial to any living organisms attempting to survive on Mars.

A study by Cockell *et al.* (2011), which utilised ESA's EXPOSE-E facility (Rabbow *et al.*, 2009) on the exterior of the International Space Station (ISS), found that one particular cyanobacterium, which they designated OU-20 (Figure 1.15), was capable of survival when exposed to space conditions for at least 548 days. The bacterium, which is extremely similar to the cyanobacterium *Gloeocapsa*, was cultured from rocks taken from the cliffs at Beer, Devon, UK. It is adapted to endure the extreme desiccation and UV exposure that it suffers in its native environment, also helping it to survive space

exposure. It manages this by synthesising protective molecules such as carotenoids, which both absorb UV radiation to prevent damage and act as antioxidants, reacting with UV-generated free radicals, to prevent any further damage. This is pertinent for astrobiology on Mars, as not only is this an example of a living organism that could conceivably survive on the planet, but the chemical protectants produced by extremophiles such as OU-20 could be used as biomarkers and if detected on Mars, could indicate the presence of life.

### 1.2.2 Biomarkers

The search for signs of past or present life on a planetary body is more accurately the search for biomarkers (Edwards *et al.*, 2014). A biomarker is defined as any chemical compound or geological feature whose only possible source is biotic. Biomarkers therefore either indicate the presence of extant life or act as a record of ancient, extinct life. It is important to completely understand an environment in order to appreciate whether a suspected biomarker could have an abiotic source, or whether it truly represents the activity of living organisms.



Figure 1.15: Microscopy image of a single cell of the bacterium designated OU-20, a cyanobacterium capable of survival in space conditions for at least 548 days. OU-20 closely resembles the cyanobacterium *Gloeocapsa*. Image credit: OU/PSSRI.

Many biomarkers are chemical compounds that are synthesised by extremophilic organisms as part of survival mechanisms in harsh environments (Edwards *et al.*, 2014). These include carotenoids such as  $\beta$ -carotene (Vítek *et al.*, 2009), bacterioruberin and salinixanthin (Jehlička *et al.*, 2013), all of which are efficient UV absorbers and powerful antioxidants. Scytonemin is also synthesised by organisms for UV protection and is therefore a useful biomarker (Varnali *et al.*, 2009).

Other biomarkers are in the form of geological or environmental changes that are caused by living organisms. One example of this is the mobilisation of iron oxide by Antarctic endoliths to create a protected environment (Jorge Villar *et al.*, 2005). This produces a distinctive banding in a colonised rock (Figure 1.16) that if detected,

possibly using a Raman imaging system, would indicate that at some point the rock had hosted living organisms.

Figure 1.16: Mars analogue rock sample taken from Antarctica. The darker bands are iron oxide that have been mobilised out of the light coloured band, which is colonised by endolithic extremophiles. Image taken from Jorge Villar *et al.* (2004).



### 1.2.2.1 Terrestrial analogue samples

From the earliest conceptual stages of a planetary exploration instrument programme, it is necessary to test, verify and sometimes redesign the instrument concept in order to ensure it will meet its scientific objectives. There are some applications where detailed modelling and use of prototypes against calibration targets suffices for this purpose. However, in the case of a Raman spectrometer performing in-situ measurements on a diverse range of complex and inhomogeneous geological targets, it is not possible to analytically or numerically model the instrument response satisfactorily. A thorough set of measurements of geological analogue target samples, using flight-representative prototypes is required, in order to retire the risk of mission failure due to unforeseen instrument behaviour following deployment. The analogue samples used are rock specimens from Earth that are geologically or chemically similar to the sort of samples that will be encountered by the mission. Analogue samples do not necessarily need to be perfect representations of potential mission targets, however a particular feature of interest that is to be examined should be representative, for example the abundance of a given mineral or the occurrence of a particular process or reaction.

Analogue studies are useful for making predictions about the science that an instrument will be capable of. They also enable the determination of optimum operating modes and analysis methodologies for maximising science return. Finally, the study of analogue samples makes it possible to make recommendations regarding the design of future instruments (e.g. Tucker *et al.*, 2008; Lopez Reyes *et al.*, 2013; Harris *et al.*, 2015).

**1.2.2.2 Terrestrial analogue sites**

A terrestrial analogue site is a location on Earth that exhibits some of the same conditions as another planetary body. There are many analogue sites of Mars around the world that are used for acquiring analogue samples and testing flight-like instrumentation in the field. One such site is the Atacama Desert in South America, where the soil contains extremely low concentrations of organic material, comparable to the Martian regolith, and in some places almost no detectable living organisms (Wierzchos *et al.*, 2006). Another good analogue site is the region around the Río Tinto river in Andalusia, Spain. The river water is extremely acidic (with an average pH of 2) and the rocks in the area possess high concentrations of sulphides and iron minerals, providing iron and sulphur metabolising extremophiles with a source of energy (Mangold *et al.*, 2011). Given that these conditions are comparable with the Martian subsurface, the Río Tinto river makes an excellent analogue of potential Martian habitats (Fernández-Remolar *et al.*, 2004; Fernández-Remolar *et al.*, 2005; Amils *et al.*, 2007).

**1.3 Raman spectroscopy**

**1.3.1 The history of Raman spectroscopy**

Raman scattering in liquids was first observed in 1928 by Raman and Krishnan (1928a; see also Raman and Krishnan, 1928b; Raman and Krishnan, 1929; Raman, 1929). In their experiments, they focussed monochromatically filtered sunlight through clear liquids, observing a shift in the wavelength of a small component of the scattered light. Around the same time, the effect was independently observed in solid crystals by Landsberg and Mandelstam (1928), but due to their publication in the German-language journal *Naturwissenschaften*, it was Raman who was awarded the Nobel Prize in Physics in 1930 for its discovery. As a result, the effect also bears Raman's name, however in Russian scientific literature it is often described as combination scattering. Prior to its experimental discovery, Raman scattering had been theoretically predicted by Smekal (1923), so in German-language literature it is sometimes called the Smekal-Raman effect.

Throughout the subsequent 85 years much research has been conducted in the field of Raman spectroscopy, resulting in its widespread use for a variety of applications. These

include pharmaceutical analysis (e.g. Henson and Zhang, 2006), artwork validation and dating by the identification of specific pigments (e.g. Castro *et al.*, 2004) and by security forces for the detection of narcotics and explosive materials (e.g. Eliasson *et al.*, 2007).

### 1.3.2 Theory of Raman scattering

Raman scattering is a type of inelastic scattering, which causes a shift in the wavelength of light following its interaction with molecular matter. When light is incident on a material sample (in any phase or state of matter), the interaction between the electric field associated with the electromagnetic (EM) radiation, and the molecules in the sample, causes the deformation or polarisation of the molecular electron clouds. This results in the formation of virtual molecular excitation states (Figure 1.17) that are extremely unstable and therefore short-lived, leading to their almost immediate decay and the reemission of photons (Smith and Dent, 2005).

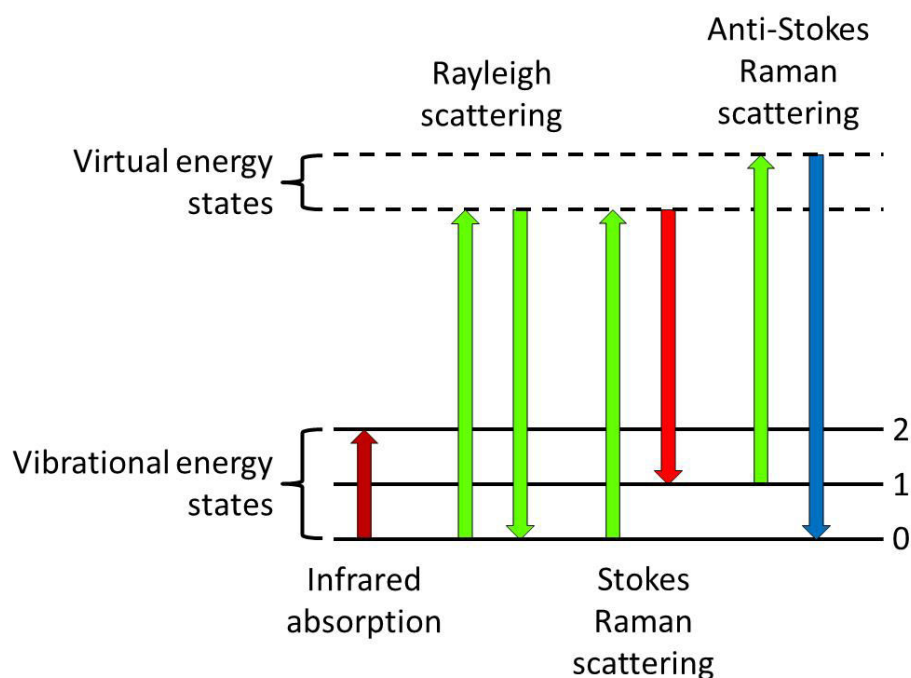


Figure 1.17: Energy level diagram showing possible modes of excitation and relaxation, to and from virtual energy states.

The vast majority of molecules excited in this manner return to their ground state following relaxation. This elastic process, known as Rayleigh scattering, produces photons of exactly the same wavelength as the excitation source. However, approximately 1 photon in every  $10^6$ - $10^8$  undergoes inelastic Raman scattering. In this case, an excited molecule relaxes to a state other than its initial one, emitting a photon

with different energy than the incident photons, equal to the difference in energy between the two states (Harris and Bertolucci, 1978). This change in energy is equivalent to a shift in wavelength. The classical description of this process is that vibrational modes of the interatomic bonds in a molecule are excited by the incident light (Figure 1.18). The precise frequency of a vibrational mode is completely dependent on the structure of the molecule causing the scattering, so the spectrum of the scattered light can be interpreted like a “fingerprint” to identify the molecules in a sample with unknown composition.

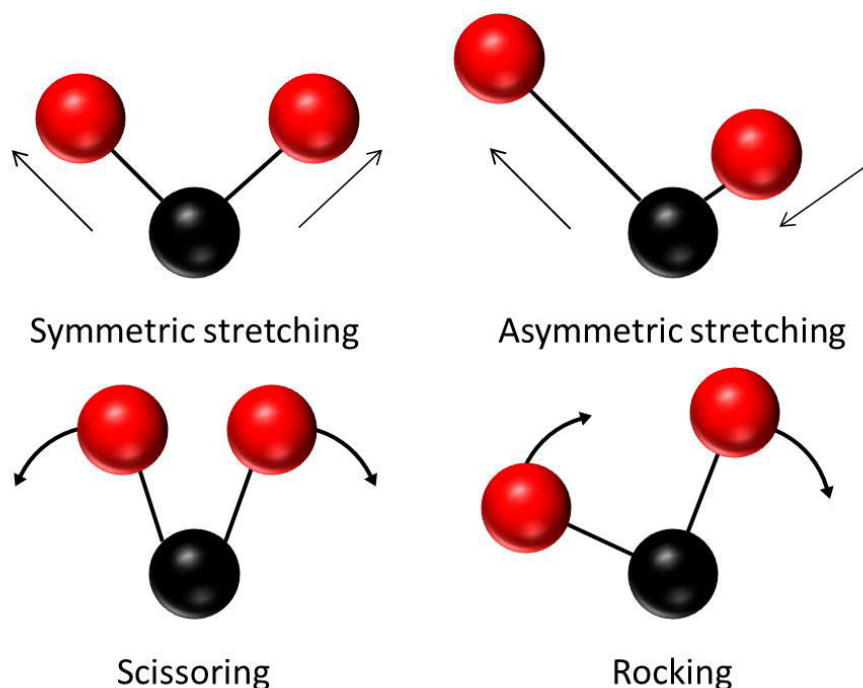


Figure 1.18: Classical representation of some of the possible modes of molecular vibration.

### 1.3.2.1 Group theory

Group theory is a branch of abstract algebra that involves the study of groups, algebraic structures that describe sets of elements and the operations that can be performed on them. Certain groups can be used to model molecules and therefore can provide insight into their properties and behaviour. By augmenting a simple group with additional operations, predictions can be made about which vibrations a molecule will undergo and therefore what its Raman spectrum should look like (Xin, n.d.).

### 1.3.2.2 Typical wavenumber ranges

Through mathematical modelling it is possible to identify wavenumber ranges in which particular kinds of vibrations will occur. This is important, as it provides a solid

foundation when attempting to identify bands in an unknown spectrum. Double bond (e.g. C=O, C=N and C=C) vibrations tend to occur between 1500 and 2000  $\text{cm}^{-1}$ , the region from 2000 to 2500  $\text{cm}^{-1}$  includes vibrations involving multi-bond groups (e.g. N=C=O) and single bond (e.g. C-H) vibrations occur between 2500 and 4000  $\text{cm}^{-1}$  (Smith and Dent, 2005). The region below 1500  $\text{cm}^{-1}$  is referred to as the fingerprint region. This is where an array of bands resulting from the vibration of complex groups such as nitro groups (O=N=O) occur. At even lower Raman shifts, below 650  $\text{cm}^{-1}$ , bands arising from inorganic groups, metal-organic groups and lattice vibrations occur.

In addition to the molecular vibrations that have been discussed thus far, macromolecular structures such as crystals and highly ordered solids like silicon and carbon can exhibit lattice vibrational modes. These are excited in the same manner as stretches and rotations, but involve the induction of vibrations throughout the whole lattice. The Raman bands that results from lattice vibrations can be quite broad, as there are often several possible vibrational energies within the lattice. The exact Raman shift and band width are usually functions of lattice parameters such as crystal size and level of order, allowing Raman spectroscopy to be used to probe these parameters.

### **1.3.2.3 Quantitative and qualitative analysis**

Raman spectroscopy is useful in both qualitative and quantitative applications. In its simplest qualitative form, Raman shifts that are specific to a molecule or material can be determined and used to identify that target at a particular spot. If many spectra can be acquired from different locations across a sample, the distribution of materials across a sample can be determined. This is the basis of Raman imaging, which is discussed in more detail in §1.3.6.2.

If quantitative information is required, this can be acquired via the meticulous measurement of certain spectral parameters. For specific Raman bands, precise measurement of their Raman shift and width can yield molecular structural data, which can provide information about the material under scrutiny. This kind of analysis can be used to differentiate between different populations of reduced carbon, which will be discussed further in Chapter 4. Another method of acquiring quantitative data using Raman spectroscopy is by carefully determining the relative intensities of bands in a spectrum. Care must be taken, because there are a number of factors that can alter the intensity of a Raman band, including laser power, temperature, sample orientation,

polarisation and grain size. Furthermore, if it is desirable to obtain quantitative information from a single Raman band, the accuracy of the instrument will be limited by the accuracy to which the response of each instrument subsystem to light is known. For example, the quantum efficiency (QE) of the detector (as a function of wavelength), throughput of optics in the optical head, spectrograph and any fibres (as a function of wavelength and polarisation), and laser power all have uncertainties associated with them, which combine to limit the accuracy to which the final Raman scattering efficiency at a particular wavelength shift is known. It is possible to constrain and measure all of these parameters sufficiently to perform useful numerical analysis, for example measuring the relative intensities of Raman bands to determine the relative abundances or concentrations of materials in a sample. However, if only the wavelength positions of Raman bands are required (as is the case for ExoMars RLS), the instrument can be much simpler.

### **1.3.3 Challenges and possible solutions**

The following subsections provide a discussion of the various challenges that must be overcome in order to acquire and accurately analyse Raman spectra. Some of the issues can be solved, or at least mitigated, through hardware improvements, whereas others require the application of innovative post-processing techniques. The development of flight instrumentation for space missions introduces additional, more specific challenges that must also be considered.

#### **1.3.3.1 Fluorescence and scattering**

One of the greatest challenges associated with Raman spectroscopy is the high level of background signal that results from fluorescence and scattering effects generally observed when illuminating a sample with high intensity light. Fluorescence occurs following the exposure of a material to EM radiation and the excitation of electrons in the molecules of the material. When excited electrons relax, light is emitted producing a continuum, which can dominate the spectrum and obscure Raman features.

There are a number of ways in which the problems caused by background effects can be alleviated, for example software may be employed to subtract the background post-acquisition. The simplest way of doing this is to fit a high-order polynomial to the background by manually selecting points to fit to that are away from bands, then

subtracting the fit from the spectrum. This process however can introduce artefacts in the data or smooth over scientific information and may require more computing power than is available onboard a planetary rover. Background subtraction also introduces a new source of noise, which may be undesirable when analysing low signal-to-noise ratio (SNR) spectra. A number of specialist Raman techniques could be used to increase the strength of the Raman signal, such as surface enhanced Raman spectroscopy (SERS) and coherent anti-Stokes Raman spectroscopy (CARS), both of which will be discussed in §1.3.6. These techniques work very well under laboratory conditions, however they are beyond the current capabilities of space mission instrumentation.

The final option is to carefully select the excitation wavelength of the instrument used in order to either reduce the fluorescence effect or increase the strength of the Raman scattering. The selection of an appropriate excitation wavelength is discussed fully in §1.3.5.1.

### 1.3.3.2 Excitation wavelength dispersive Raman bands

Particular bands in the Raman spectra of a small number of materials are excitation wavelength dispersive. This means that their Raman shifts are dependent on the wavelength of the excitation source, or more precisely on the energy of the incident photons. Excitation wavelength dispersion occurs in metallic crystals and crystal-like materials, which possess many possible Raman-active phonon states with similar but distinct energies, each of which is excited by a different incident photon energy (e.g. Saito *et al.*, 2002). Dispersive Raman bands have been observed in a number of materials, including disordered carbon (Ferrari and Robertson, 2001; Olcott Marshall *et al.*, 2012), Cu<sub>2</sub>O (Peter and Shen, 1974) and AgBr (Windscheif *et al.*, 1977).

### 1.3.3.3 Mass budget

Flight instruments must adhere to strict mass budgets due to the limited mass that can be accommodated by a launch vehicle. The total mass budget of a space mission depends on the astrodynamics of the launch window and the launch vehicle being used. The mass of a Raman instrument can be minimised by keeping it as simple as possible and by carefully selecting the materials from which it is constructed, although some elements of a Raman spectrometer do necessitate the use of higher mass components. Typically the mass of an instrument is dominated by the laser and detector cooling

systems, as well as the need for multiple optical elements such as lenses, which are usually made out of high density materials such as BK7 glass or fused silica. Reducing the mass of an optical bench or instrument housing is limited by the need to maintain thermal gradients, stiffness, strength and fundamental vibrational frequencies.

### **1.3.3.4 Volume budget**

As with mass, the volume of flight instruments must be strictly controlled. This is partly to enable accommodation by the launch vehicle, but also to fit within the mission vehicle along with other instruments and hardware. The volume budget allocated to a given instrument may depend on where it is to be located, for example whether it is an internal instrument or to be mounted on an external robotic arm. Volume is usually dominated by electronics packages and optical systems, which is certainly the case for Raman instruments. In order to minimise the volume envelope of an instrument, innovative space management solutions must be sought.

### **1.3.3.5 Power budget**

The total power budget of a space mission is determined by the power that the mission vehicle can generate, which depends on the means by which its power is produced. Space missions usually generate power using either solar panels, which provide a large amount of energy but only for a few hours per day, or using an RTG, which provides a constant source of energy. The power requirements of a Raman instrument depend upon its electrical components, including the laser, detector and supporting electronics. Each of these can be designed to require a minimal power supply. As an example, the RLS instrument will have a total power consumption of around 30 W.

### **1.3.3.6 Technology Readiness Level**

The Technology Readiness Level (TRL) of a component, system or entire instrument is a measure of how mature that system is in terms of how ready it is for space flight. NASA have defined nine grades of TRL (Mankins, 1995), the requirements for which are detailed in Table 1.2. Other space agencies have slightly different TRL definitions, but NASA's system provides an insight into the typical requirements on flight instruments.

As a result of the TRL system, the heritage of instruments and instrument components is important. If a particular component, such as a detector or a laser, has been flown on a previous mission, it is already TRL 9, making its inclusion in a future instrument extremely favourable. At the outset of the development of a Raman instrument, the majority of subsystems are at TRL 4, and during development this will be increased to TRL 5 or 6.

Table 1.2: NASA’s requirements for attaining each technology readiness level.

<b>Technology Readiness Level, TRL</b>	<b>Requirements</b>
1	Scientific principal studied
2	Technological application formulated
3	Proof-of-concept demonstration performed
4	Breadboard system validated in laboratory environment
5	Breadboard system validated in relevant environment
6	Prototype system operated in relevant environment
7	Prototype system operated in space environment
8	Final system built and flight qualified
9	Final system proven through mission operation

**1.3.3.7 Comparing space and laboratory instruments**

In order to overcome the challenges described in §1.3.3.3-1.3.3.6, certain trade-offs must be made that will result in impaired performance. The most powerful laboratory instruments, such as the Renishaw inVia Qontor (Figure 1.19), would exceed mass, volume and power budgets imposed by space missions, and would also include numerous low TRL components.

Table 1.3 provides a comparison of the physical characteristics of the Qontor and the RLS instrument, as well as some of their key performance parameters. RLS is clearly less massive, smaller and not as power hungry as the laboratory instrument. However, as a result it also has reduced spectral resolution and spectral range. Although the final spatial resolution of RLS is not yet known, its proposed laser spot size is 200 times

larger than the spatial resolution of the Qontor, indicating that its spatial resolution will also be much greater.

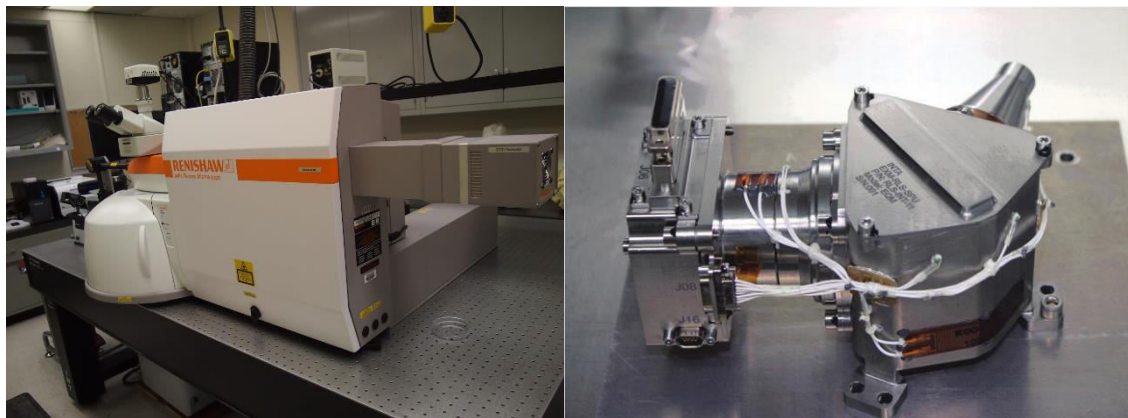


Figure 1.19: Left: A Renishaw inVia Qontor, an example of a laboratory micro Raman spectrometer. Image credit: Stony Brook University. Right: The RLS Spectrometer Unit. Image credit: Rull *et al.*, 2017

Table 1.3: Comparison of the physical characteristics and performance parameters of a Renishaw inVia Qontor and the RLS instrument. Values for the Qontor obtained from renishaw.com, 01/12/2017.

Parameter	Renishaw inVia Qontor	RLS instrument
Mass (kg)	90 + laser mass	2.5
Dimensions (m)	1.6 x 0.61 x 1.12	~0.26 x 0.18 x 0.13
Volume (m <sup>3</sup> )	1.09	0.006
Power consumption (W)	150 + laser power consumption	30
Spectral resolution (cm <sup>-1</sup> )	0.3	6-8
Spectral range (cm <sup>-1</sup> )	5-30,000	150-3,800
Spatial resolution (μm)	0.25	
Laser spot size (μm)		50

### 1.3.4 Raman spectroscopy for planetary exploration

The Raman technique has a number of features that make it a powerful tool for remote planetary geology and astrobiology (Jorge Villar and Edwards, 2006). These include:

- Sensitivity to the precise structure of molecules, which means that Raman can be used to differentiate between isomorphs and polymorphs of the same compound.
- The ability to detect both organic and inorganic molecules.
- No requirement for physical or chemical sample preparation prior to analyses.
- Raman is usually a non-destructive technique.
- Spectral acquisition is extremely rapid, typically requiring acquisition times of only a few seconds.

Each of these features is highly advantageous, making Raman spectroscopy an ideal analytical technique for the initial investigation of samples, on a remote robotic planetary exploration mission.

### 1.3.4.1 Mars exploration with a Raman spectrometer

In preparation for the deployment of the first Raman spectrometer on Mars, it is necessary to build a database of Raman spectra that will assist in the identification of materials encountered by the mission. The process of building such a database will demonstrate the quality of data achievable by the flight instrument and also facilitate the development of optimum analysis techniques.

A great deal of progress has already been made in this process. It has been demonstrated that Raman spectroscopy can be used to distinguish between carbonates of calcium and magnesium, which may be of relevance in the search for signs of life (Edwards *et al.*, 2005a). Raman is also useful for distinguishing between the hydrated calcium sulphates gypsum and bassanite, and their anhydrous counterpart anhydrite (Liu *et al.*, 2009). Detection of these minerals on Mars, as well as hydrated magnesium sulphates (Wang *et al.*, 2006) makes it possible to map ancient surface water, due to its requirement for their formation. The majority of the preparatory work that has been conducted so far has been focused on the detection and analysis of biochemical biomarkers (e.g. Wynn-Williams and Edwards, 2000; Edwards *et al.*, 2005b; Edwards *et al.*, 2005c).

### 1.3.5 Basic Raman spectrometer

Modern Raman spectroscopy is usually carried out using a laser as the monochromatic excitation light source. Figure 1.20 shows a simplified diagram of a Raman spectrometer that illustrates its primary elements. The laser is focused onto the sample and as much of the scattered light is collected as possible, filtering out the component with the same wavelength as the laser and therefore the elastically or Rayleigh scattered light. This leaves only the light which has undergone a wavelength shift, which is transmitted through or reflected off a diffraction grating, dispersing it before it is collected by a detector, usually a charge-coupled device (CCD). If the CCD is wavelength-calibrated correctly, the position of each band on the CCD can be related to wavelength and a spectrum can be read out.

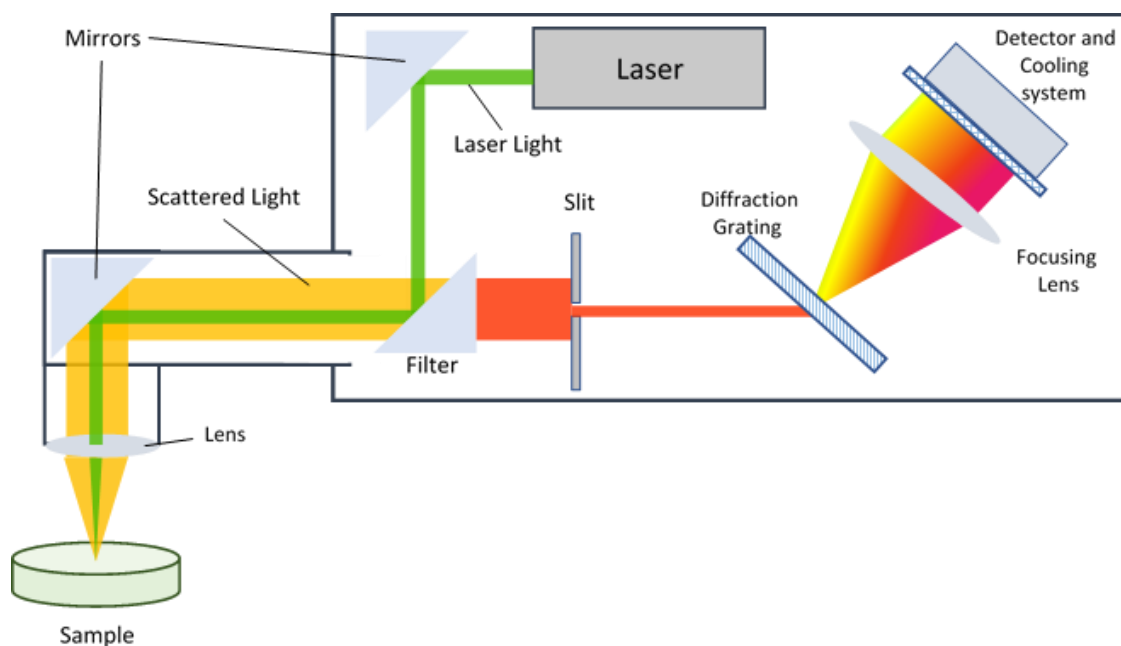


Figure 1.20: Component diagram of a simple Raman spectrometer. Green light leaves the laser, which is discussed in §1.3.5.1, and is introduced to the sample, discussed in §1.3.5.2. The orange section represents scattered light, including Raman and Raleigh, which is collected and passed through a filter, considered in §1.3.5.3. The redshifted filtered light, depicted in red, is passed through a slit, discussed in §1.3.5.4, and introduced to a diffraction grating, the subject of §1.3.5.5. The light is dispersed by wavelength by the grating, before being focussed onto a cooled detector, discussed in §1.3.5.6.

### 1.3.5.1 Laser

The key consideration regarding the selection of a laser for use in a Raman system is its wavelength. This is important, as Raman scattering intensity is dependent on the wavelength of the laser, according to the relation in Equation 1.1.

$$I_{Raman} \propto \lambda^{-4} \quad (1.1)$$

Where  $I_{Raman}$  is the intensity of the Raman scattering and  $\lambda$  is the excitation wavelength. According to Equation 1.1, reducing the wavelength of the monochromatic light source in the instrument will significantly increase the strength of the Raman features in a spectrum. Using UV excitation increases the Raman scattering strength. Additionally, fluorescence occurs across a particular range of wavelengths, whereas the wavelengths of Raman photons are relative to the excitation wavelength. As a result, Raman bands are spectroscopically separated from fluorescence in UV Raman spectra. However, UV lasers and the optics required to focus them are much more expensive than their optical counterparts. Furthermore, there is a much greater risk of causing burning or degradation of samples when using more energetic wavelengths like UV,

especially with organic samples. UV optics are also more susceptible to blackening under exposure to radiation during cruise to Mars.

Alternatively, an IR excitation wavelength could be used as almost no fluorescence occurs under infrared, however due to the relation in Equation 1.1, this results in very weak Raman scattering intensity. If the spectra acquired are likely to have low SNRs, this reduction in Raman signal could make identifying minerals by their Raman spectra extremely difficult, and would likely make quantitative analysis impossible.

Yet another method of reducing the impact of fluorescence is to make use of resonance effects to increase the strength of the Raman signal. If the laser wavelength is at or near the energy of electronic transitions within the molecules that are being targeted with the technique, resonance occurs which vastly increases the strength of the scattering. This is the reason that a green, 532 nm laser has been selected for the RLS instrument on ExoMars, as this will induce resonance in the biological pigments such as the carotenoids that the instrument will be looking for.

#### 1.3.5.2 Sample

The nature of the sample being studied can affect the Raman spectrum that is acquired and can place constraints on the required instrumentation. Fundamentally, the technique is effective on samples in any phase, however fluid samples must be contained, introducing an additional spectral component resulting from the container which must be removed or ignored during analysis. The colour and opacity of a solid sample is significant, as a laser of a particular wavelength may be required to successfully acquire a spectrum, or the power may have to be carefully considered in order to prevent thermal degradation of the sample. Finally, although no sample preparation is required, if any is performed this can alter its spectrum. As a sample is crushed more finely, its surface area to volume ratio is increased, which enhances scattering effects and adds to the background continuum, potentially complicating band identification.

#### 1.3.5.3 Filter

There are three main methods of filtering Rayleigh scattered light out of the total light collected by a spectrometer. These are with an edge filter, a holographic notch filter or using a tunable filter spectrometer.

An edge filter is a longpass optical filter, with an extremely steep cut-off between its absorption and transmission regions. It absorbs all light up to a particular wavelength, efficiently transmitting the remaining light. The cut-off is selected slightly above the laser wavelength, resulting in a small region of the spectrum that is also filtered. At best this might be around  $70\text{ cm}^{-1}$ , however at worst this could be up to  $200\text{ cm}^{-1}$ , although edge filters have almost infinite lifetimes due to their environmental stability.

A holographic notch filter has a narrow absorption range, usually centred on the instrument laser wavelength. This is often only a few hundred wavenumbers wide which wouldn't enable the detection of high wavenumber bands, however using a notch filter allows the detection of anti-Stokes scattered light at negative wavenumbers, unlike an edge filter. Notch filters do have finite lifetimes and therefore must be periodically replaced, making them unsuitable for long-duration space missions.

Finally, a tunable filter spectrometer works by dispersing the light scattered from a sample and removing the laser line by physically blocking it from the dispersed light. The remaining light is recombined, then passed through a spectrometer for analysis. Only the first  $5\text{ cm}^{-1}$  of the spectrum is occluded, giving unprecedented wavenumber coverage, however it is an extremely specialist technique that requires careful calibration, as well as additional hardware compared with regular Raman techniques, making it somewhat unsuitable for a flight instrument.

#### **1.3.5.4 Slit**

A slit is necessary in a Raman spectrometer to vignette the filtered light, parallelising it before it is collimated onto the diffraction grating. The slit used will influence the throughput and resolution of the spectrometer. If a large slit is used, the throughput will be good but the resolution will suffer. Using a very narrow slit will improve the resolution of the system, however the throughput will be lower, which could result in insufficient light reaching the detector.

#### **1.3.5.5 Diffraction grating**

A diffraction grating is used to wavelength disperse the Raman scattered light so that it can be analysed. There are two main types of basic diffraction grating: ruled and holographic gratings. Ruled gratings are manufactured by etching parallel grooves onto either a reflective or transmissive material, whereas a holographic grating is made of

glass that has a sinusoidally varying index of refraction, created by interfering two UV beams. Holographic gratings are generally less efficient than their grooved equivalent, however they have a much more uniform response (Palmer and Loewen, 2005).

Groove frequency must be considered when selecting a diffraction grating for inclusion in a Raman spectrometer. Increasing groove frequency will improve spectral resolution, however it will also increase dispersion, which means that a larger detector will be required in order to image the entire spectral order. A blazed grating can also be used, with grooves that have a non-perpendicular facet angle (see Figure 1.21 for an illustration). If the blaze angle is calculated correctly, this can be used to maximise the efficiency of the grating around the laser wavelength.

### 1.3.5.6 Detector

The detector is the element of a Raman spectrometer that images and records the dispersed, scattered light. If calibrated correctly, this enables wavelength analysis of the light and therefore the generation of recognisable spectra. The main types of detector used for Raman spectroscopy are CCDs and complementary metal-oxide semiconductor (CMOS) detectors.

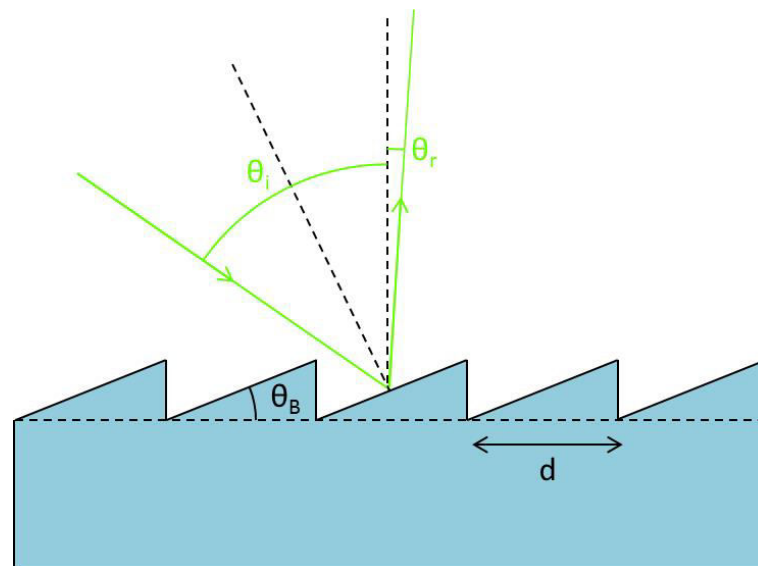


Figure 1.21: Diffraction at the surface of a blazed reflective diffraction grating.  $\theta_B$  is the blaze angle,  $d$  is the grating line spacing,  $\theta_i$  is the angle of incidence of the incoming light and  $\theta_r$  is its angle of reflection.

### 1.3.5.6.1 Cooling

Although cooling the detector in a Raman spectrometer is not an absolute requirement, cooling can be employed to decrease dark current, improving potential SNR and so

therefore the detection limits of the system. The most common method is to use a thermoelectric cooler (TEC), which utilises the Peltier effect to create a step in temperature across the junction between two semiconductor materials. By placing the detector on the cold side of the TEC, heat can be removed from the system by passing a coolant (e.g. water or a cryogenic fluid) across its hot side. A typical TEC might be able to achieve a temperature step between its hot and cold sides ( $\Delta T$ ) of 75 K with a hot side temperature of 323 K, sinking 25 W of heat.

#### 1.3.6 Advanced Raman techniques

The SERS technique works by introducing a sample onto a surface of a material such as silver or gold and using an excitation source with a wavelength which resonates with plasmons in the surface material (Campion and Kambhampati, 1998). The subsequent excitation of those plasmons causes an increase in both the Raman scattering intensity and the incident light. The increase in the incident light intensity causes a further increase in the strength of the Raman scattering.

CARS uses two lasers to pump electrons from the ground state to a vibrational excitation state and a third laser to induce anti-Stokes Raman scattering. This results in negative Raman shifts as the light from the third laser is shifted to lower wavelengths and since no fluorescence occurs at these wavenumbers, Raman features are much more easily observed.

##### 1.3.6.1 Resonance Raman

Resonance Raman scattering occurs when the excitation wavelength is close to that of an electronic transition in a molecule being illuminated. The ideal method of achieving this by design is using a tunable laser, however careful selection of a fixed laser wavelength is also viable for some applications. Excitation of a molecule to a higher energy electronic state increases its polarizability, therefore increasing Raman scattering intensity by up to a factor of  $10^6$ . This is highly beneficial due to the large increase in SNR.

Inclusion of a tunable laser on a flight instrument for a space mission is not practical, however careful selection of laser wavelength can be advantageous. For example, a 532 nm laser was selected for RLS to take advantage of resonances in biological pigments such as carotenoids (Edwards *et al.*, 2012).

1.3.6.2 Raman imaging

Raman imaging is the process of mapping sample surfaces according to the intensity of specific Raman bands. This is achieved by acquiring spectra from a raster of points, either by scanning the optical head/sample stage, or by using a laser line instead of a spot to build a Raman “image”. Each pixel in the image represents a Raman spectrum at that spot, and the colour of the pixel is determined by measuring the intensity of a band or bands of interest in those spectra and applying a colour map to those measured intensities. Raman imaging yields a great deal of spatial information that can be used to identify features in a sample, some of which may be relevant to the search for signs of life. Potential microbial habitats could be identified by mapping the location of relevant minerals, and in some cases evidence of the environmental influence of living organisms has a spatial component. For example, Edwards *et al.* (2005b) studied Antarctic sandstone that exhibited stratification of iron (III) oxide, caused by the colonisation of the microhabitat by symbiotic lichen and cyanobacteria.

Raman imaging could be performed by a Raman spectrometer mounted inside a rover, with a two dimensional translation stage to enable scanning. Alternatively, a Raman instrument could be mounted on a robotic arm on the outside of a mission vehicle, allowing it to be passed over a sample, acquiring many spectra during each transect scan. This latter option is the mode of operation for SHERLOC, a UV Raman instrument that has been included on the payload of NASA’s Mars 2020 rover (Beegle *et al.*, 2014). SHERLOC is discussed in more detail in Chapter 2.

# Chapter 2

## Instrumentation

---

### 2.1 ExoMars programme

ExoMars is a programme of Mars exploration missions, operated jointly by ESA and Roscosmos. It consists of two missions, the first of which was successfully launched from the Baikonur Cosmodrome in Kazakhstan in March 2016, with the second mission due for launch in July 2020. The 2016 mission consists of the Trace Gas Orbiter (TGO), a satellite equipped with instrumentation for monitoring the tenuous Martian atmosphere and detecting trace gases, and the Entry, Descent and Landing Demonstrator Module (EDM), which will provide a test of ESA's landing technology and will also be used to measure various atmospheric parameters as a function of altitude. The 2020 mission will be entirely devoted to deploying the ExoMars rover (Figure 2.1) on the surface of Mars, which will employ the first core drill on Mars to acquire rock cores from up to 2 m below the surface, studying them with a suite of scientific instruments, including one of the first Raman spectrometers to be included on a space mission (Vago *et al.*, 2013).

The ExoMars programme has three primary scientific objectives. These are to search for signs of either extinct or extant life on Mars, to study the geochemical and water environments of the Martian subsurface and to investigate the sources of trace gases in the Martian atmosphere (Vago *et al.*, 2015a). Additional goals of the programme are to continue to explore Mars and identify potential hazards for future human exploration, to

evaluate the habitability of the Martian subsurface and to conduct preparatory work for a potential future sample return mission.

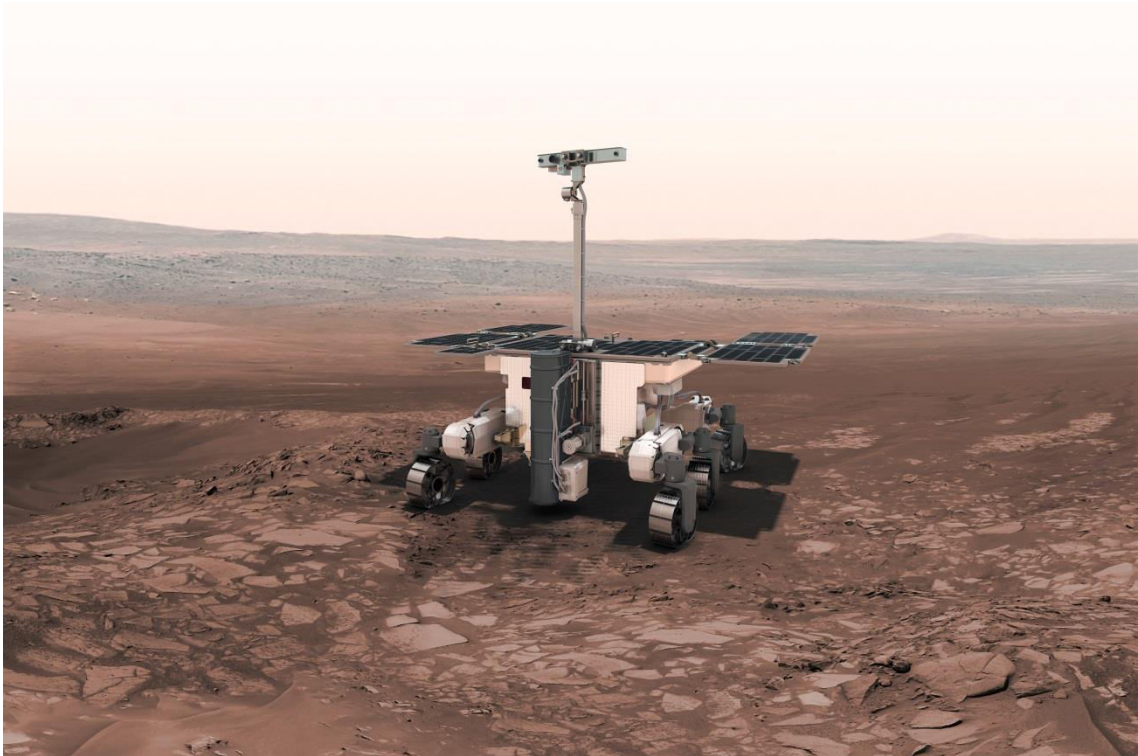


Figure 2.1: An artist's impression of the ExoMars rover on the surface of Mars. Image credit: ESA.

### 2.1.1 The ExoMars 2016 mission

The ExoMars 2016 mission will be made up of two elements: the TGO and the EDM, as described in §2.1. The primary objective of the mission is to make measurements of the Martian atmosphere, specifically looking for trace gasses that could be related to ongoing geological or biological processes on Mars. It will also provide the opportunity to test ESA's landing capability with the EDM and gather valuable telemetry in preparation for the 2020 mission landing. Additionally, the TGO will provide support for the 2020 rover mission, both by providing preparatory surface and landing site analysis and by acting as a communications relay.

#### 2.1.1.1 Trace Gas Orbiter

The TGO is equipped with four scientific instruments, two of which will monitor the atmosphere of Mars, whilst the other two study its surface. The orbiter will also provide a communication link with both the EDM and the ExoMars rover, and is capable of supporting future surface missions as well.

Two of the TGO's instruments, NOMAD (Nadir and Occultation for Mars Discovery) and ACS (Atmospheric Chemistry Suite), will be used to search the tenuous Martian atmosphere for trace gasses that might be indicative of biological processes. NOMAD is a solar spectrometer with very broad wavelength coverage from IR to UV, which will measure the spectrum of sunlight passing through and reflecting off the Martian atmosphere. This will enable the identification and mapping of atmospheric gasses such as methane (Vandaele *et al.*, 2011). ACS is also a nadir and occultation solar spectrometer, however it only operates at IR wavelengths for increased resolution in this wavelength range (Korablev *et al.*, 2014).

The TGO's remaining two instruments, CaSSIS (Colour and Stereo Surface Imaging System) and FREND (Fine Resolution Epithermal Neutron Detector), are described in greater detail in the following two subsections. Such a detailed description is relevant to this thesis, as in addition to their scientific outputs, these instruments will be used to support the 2020 rover mission. This support will take the form of landing site characterisation and the identification of features of interest for in situ investigation.

### 2.1.1.1 CaSSIS

CaSSIS is a high resolution, telescopic camera system that will be pointed at the surface of Mars (Thomas *et al.*, 2017). Images of the planet's surface acquired using CaSSIS will have maximum horizontal and vertical resolution of 5 and 6 m respectively. The instrument's primary function will be to image surface sites that could potentially contain sources of trace gasses identified using NOMAD and ACS. This will highlight large-scale, geological processes, such as erosion and sublimation, which could potentially contribute gasses to the atmosphere.

CaSSIS will also be used to image the landing site that is ultimately selected for the 2020 rover mission, characterising slope gradients, large obstacles and other potential hazards. This support will continue throughout the duration of the 2020 mission.

### 2.1.1.2 FREND

FREND is a neutron detection experiment onboard the TGO (Mitrofanov *et al.*, 2016). Neutrons are continuously created in the upper 2 m of the Martian regolith, following the interaction between regolith material and incident cosmic rays. FREND will produce fine resolution maps of neutron flux and velocity, which will provide a great

deal of information regarding the materials in the regolith, especially any hydrogen that is present. Hydrogen has been shown to significantly affect epithermal neutron velocity (Boynton *et al.*, 2002), enabling the production of hydrogen maps that can be correlated with the abundance of water in the shallow subsurface.

### 2.1.1.2 Entry, Descent and Landing Demonstrator Module

Development of the EDM, also named Schiaparelli after the 19<sup>th</sup> century Italian astronomer Giovanni Schiaparelli, has provided ESA and Roscosmos with the necessary technology for payload delivery to the surface of Mars. Deployment of the EDM on the Martian surface will also provide a chance to gather valuable engineering and atmospheric telemetry, which will be of use during the deployment of the ExoMars rover in 2021.

During the landing of the EDM, the Entry and Descent Science Team will follow the Atmospheric Mars Entry and Landing Investigation and Analysis (AMELIA) programme (Ferri *et al.*, 2012). This is a set of protocols for monitoring and analysing the lander's engineering data, in order to evaluate atmospheric conditions and reconstruct the landing trajectory. The EDM is also fitted with a camera system called DECA (Entry and Descent Module Descent Camera), which will be operated during landing<sup>1</sup>.

Once on the surface, the EDM has enough charge in its onboard battery to operate for 4 sols. For the duration of its lifetime, the surface payload DREAMS (Dust Characterisation, Risk Assessment, and Environment Analyser on the Martian Surface) will be used to make environmental measurements. DREAMS is a suite of meteorological sensors capable of measuring wind, humidity, pressure, temperature, atmospheric dust concentration and the atmospheric electric field (Esposito *et al.*, 2014).

### 2.1.2 The ExoMars 2020 mission

The sole purpose of the 2020 launch is to deliver the ExoMars rover to Mars. The rover will be solar powered and its initial mission lifetime is expected to be 218 sols, however this could be extended if the initial mission is successful. It will be equipped with a 2 m long drill (Figure 2.2), the first to be deployed on Mars, which will acquire rock cores

---

<sup>1</sup> [exploration.esa.int/mars/54333-deca-the-descent-camera-on-schiaparelli](http://exploration.esa.int/mars/54333-deca-the-descent-camera-on-schiaparelli) [Accessed: 08/12/2017].

from below the surface for analysis with onboard analytical instrumentation. This is important due to the influence of solar radiation and cosmic rays on the upper regolith. Only very specialised living organisms could survive in such an environment and biomarkers are unlikely to persist. Retrieving samples from the subsurface will maximise the probability of detecting signs of life, whether extant or extinct, and will also enable characterisation of Martian geochemistry less affected by radiation.

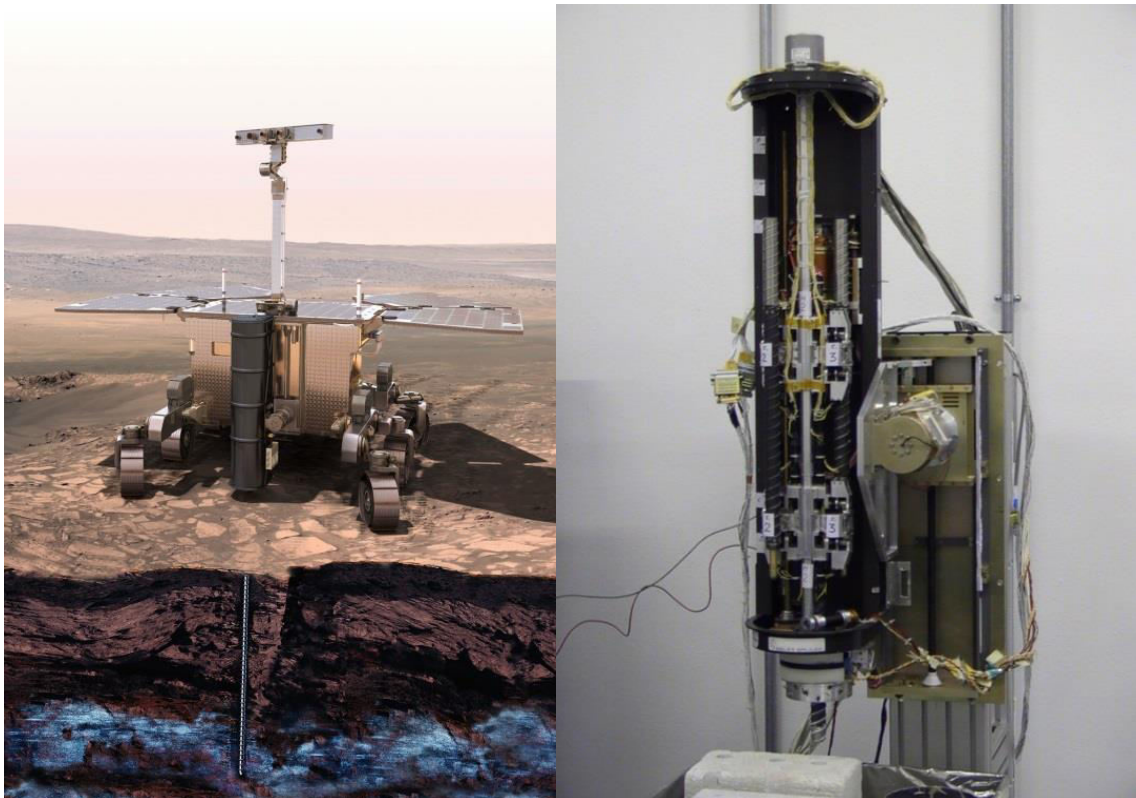


Figure 2.2: Left: An artist's impression of the ExoMars rover, deploying its drill. Image credit: ESA. Right: Photograph of the ExoMars rover drill prototype. Image credit: SELEX Galileo.

The ExoMars rover is due to land on Mars in 2021. Following a selection process (Vago *et al.*, 2015b), a landing site at Oxia Planum, a clay-rich plain close to the Martian equator, has been recommended for the mission. The apparent abundance of clays rich in iron and magnesium in this area suggest a prevalence of ancient water, something of significant interest when searching for signs of life, and they also may help to preserve buried biomarkers by offering shielding from cosmic radiation. Following the postponement of the mission launch until the next window of opportunity, in July 2020, two more landing sites at Mawrth Vallis and Aram Dorsum will also be considered. The former is located near to the proposed site at Oxia Planum and is similarly clay-rich, whereas the latter is dominated by alluvial sedimentary deposits.

Once on the surface of Mars, the ExoMars rover will image its surroundings using a pair of stereo navigation and hazard avoidance cameras mounted on its mast. Using these images, navigation solutions will be calculated using only the rover's onboard computers, enabling it to automatically plot and travel the safest course from one location to another, covering up to 100 m per sol.

The following subsections provide details about the scientific payload of the ExoMars rover, the particular roles of each of its instruments and how they can be used in conjunction to achieve the mission's scientific objectives.

### 2.1.2.1 Target selection

The ExoMars rover is equipped with a number of instruments that will help to remotely select targets, either on the surface or below the ground, for more detailed study using the rover's onboard suite of analytical instruments. The first of these is PanCam (Panoramic Camera), a mast-mounted camera system that incorporates two wide angle cameras, each fitted with 12 different spectral filters, and a high resolution colour camera. PanCam can be used to gain both textural and multispectral information about rock surfaces, all without moving the rover, enabling the identification of sites of interest for more detailed in situ investigation (Coates *et al.*, 2015).

ISEM (Infrared Spectrometer for ExoMars) is a remote IR acousto-optical tunable filter spectrometer (Korablev *et al.*, 2017). ISEM will be used in conjunction with PanCam to remotely identify interesting targets. It will be able to add additional mineralogical information to that acquired by PanCam, particularly regarding the presence of hydroxides such as jarosite, and hydrated minerals such as gypsum.

WISDOM (Water Ice and Subsurface Deposit Observation On Mars) is a radar system, mounted on the underside of the rover pointing at the ground (Ciarletti *et al.*, 2011). It will be used to remotely explore the Martian subsurface, performing a search for deposits of water ice and interesting stratigraphy worthy of closer investigation using the rover's drill. The size and nature of potential drill targets can be determined using WISDOM, whilst possible hazards that could cause damage to the drill can be avoided. WISDOM will work in conjunction with Adron, a neutron spectrometer that will operate in a similar way to the FRENDS instrument on the TGO. It will be used to

investigate subsurface hydration and to confirm identifications of water ice made by WISDOM.

### 2.1.2.2 Sample acquisition

Rock cores, with diameters and lengths of 1 and 3 cm respectively, will be acquired using the ExoMars drill unit. The drill will be able to achieve a maximum depth of a little over 2 m by adding up to three 0.5 m extension rods to its initial 0.7 m drill bit. It is anticipated that the drill will be deployed twice throughout the duration of the ExoMars rover's initial mission, retrieving four rock cores during each deployment. Incorporated into the tip of the drill bit is Ma\_MISS (Mars Multispectral Imager for Subsurface Studies), a miniature IR spectrometer that will image the borehole as the drill rotates, producing stratigraphic mineralogical maps that will provide context when analysing rock cores (De Sanctis *et al.*, 2017).

Once a core has been acquired it will be photographed using CLUPI (Close-Up Imager), a highly magnified high resolution camera, mounted on the outside of the rover (Josset *et al.*, 2012). This will provide visual context images to accompany the mineralogical information from Ma\_MISS. CLUPI will also be used to photograph the Martian regolith, rocks and outcrops to provide further geological context and to search for potential morphological biomarkers, such as mineral-replaced structures (like those described in §1.2.2), varnishes, visible carbon deposits and biofilms.

### 2.1.2.3 Sample Preparation and Distribution System

The Sample Preparation and Distribution System (SPDS) onboard the ExoMars rover will receive rock cores once they have been acquired by the drill and photographed using CLUPI. These will be crushed into grains with diameters of up to 400  $\mu\text{m}$  (as shown by Figure 2.3), then this crushed material will be deposited in reusable sample containers on the SPDS carousel. As the carousel rotates it will position samples beneath the optical head of each instrument in the analytical drawer.

### 2.1.2.4 Analytical Laboratory Drawer

The ExoMars rover's ALD contains three scientific instruments: MicrOmega, RLS and MOMA (Mars Organic Molecule Analyser). These will each be used in turn to analyse specimens of crushed rock, provided by the SPDS.

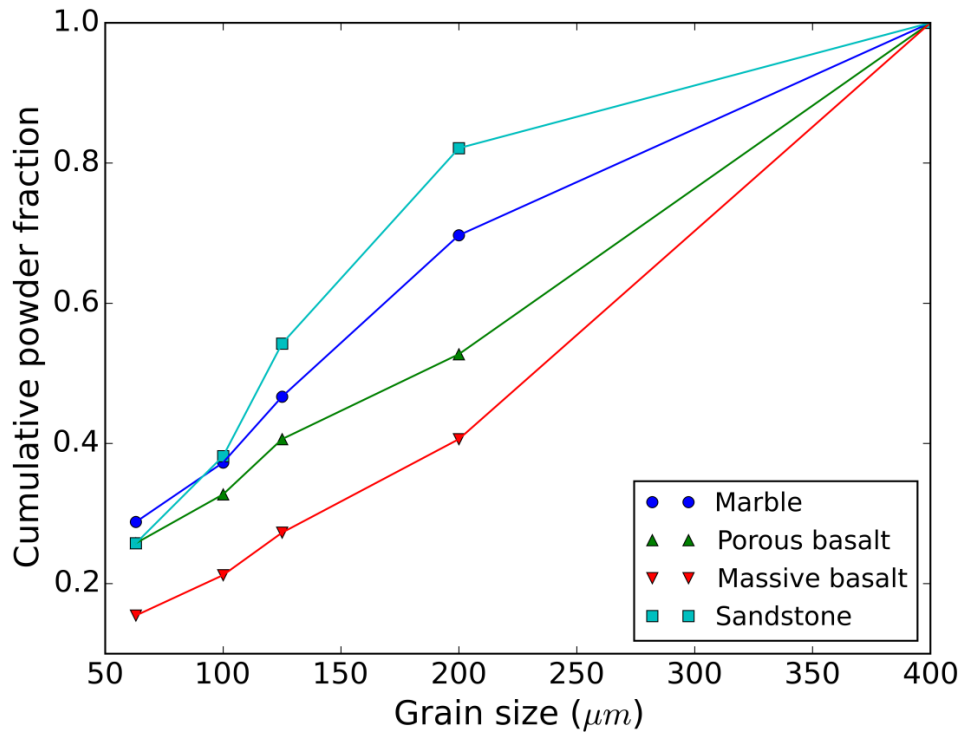


Figure 2.3: The grain size distribution produced by the ExoMars SPDS breadboard for several different materials. Figure reproduced from Schulte et al. (2008).

#### 2.1.2.4.1 MicrOmega

MicrOmega is a combined visible microscope and near-infrared (NIR) imaging spectrometer (Bibring *et al.*, 2017). It will produce grain-scale context images and NIR spectral maps, which will be useful for locating grains worthy of focused study using the other two instruments in the ALD. The visible microscope, designated MicrOmega/VIS, will achieve a maximum spatial resolution of  $4 \mu\text{m}$ , whilst the NIR spectrometer, known as MicrOmega/IR, is capable of a spatial resolution of  $20 \mu\text{m}/\text{pixel}$  in the spectral range  $0.9\text{--}4 \mu\text{m}$  (Leroi *et al.*, 2009). Development of MicrOmega is being led by France, with support from a team in Switzerland.

#### 2.1.2.4.2 RLS

The RLS instrument, a CAD drawing and photograph of which are given in Figure 2.4, will be the first Raman spectrometer to be included on a space mission or deployed on the surface of another planet. Its excitation source will be a continuous wave (CW), 532 nm laser with a footprint size of approximately  $50 \mu\text{m}$ , and it will have a spectral range of  $150 \text{ cm}^{-1}$  to  $3800 \text{ cm}^{-1}$  (dispersed across two diffraction orders), an irradiance of  $0.6 \text{ kW}\cdot\text{cm}^{-2}$  to  $1.0 \text{ kW}\cdot\text{cm}^{-2}$  and a spectral resolution of between  $6 \text{ cm}^{-1}$

and  $8 \text{ cm}^{-1}$  (see §2.4.4 for more detail on the technical specifications of RLS). RLS will perform rapid molecular identification on crushed samples, using images from MicrOmega to identify target grains of interest. The PI of RLS is Fernando Rull Perez of the University of Valladolid and the Centre for Astrobiology in Spain. The development of RLS is led by Spain at the Instituto Nacional de Técnica Aeroespacial (INTA), in cooperation with teams in France, the UK and Germany (Rull *et al.*, 2017).

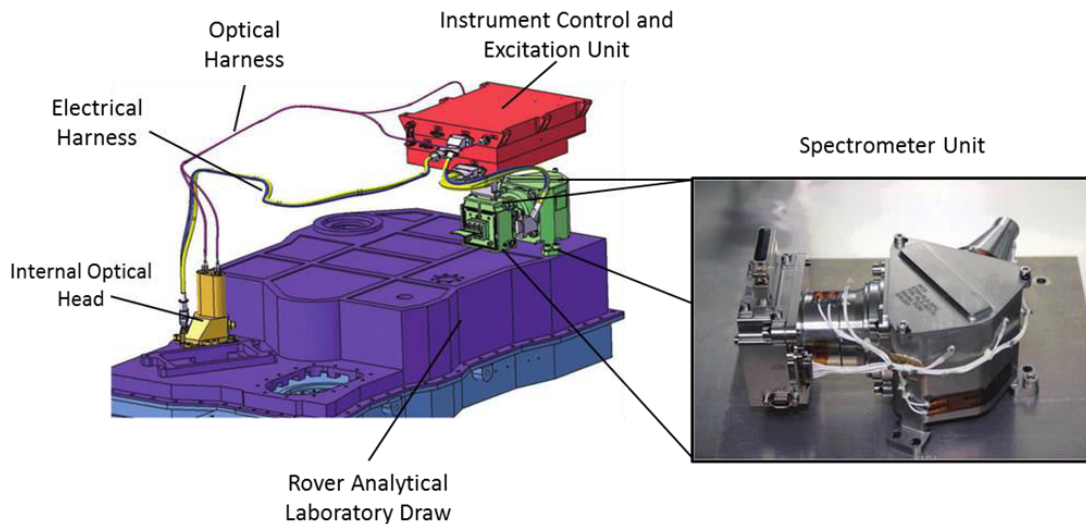


Figure 2.4: CAD diagram of the RLS instrument, showing the instrument control and excitation unit that houses control electronics and the laser, the internal optical head that will introduce laser light to the sample and collect scattered light, and the spectrometer unit that includes the diffraction grating and detector. Image credit: Moral *et al.*, 2016 Inset: A photograph of the spectrometer unit flight model. Image credit: Rull *et al.*, 2017.

### 2.1.2.4.3 MOMA

MOMA will be capable of performing both GC-MS and Laser Desorption-Mass Spectrometry (LD-MS; Goesmann *et al.*, 2017). Being a destructive instrument, MOMA will be the final stage in the analysis of samples in the ALD. GC-MS will be used to analyse volatile compounds in the Martian regolith following thermal vapourisation. This will be carried out in one of the twenty ovens on the SPDS carousel, however these are one-time use only, which means that samples for GC-MS analysis must be carefully selected. Heat resistant or simply less volatile compounds will be analysed using LD-MS, which involves the liberation of ions for mass spectrometric analysis by laser desorption. Combined, these two techniques will give a comprehensive view of the volatile compounds in the Martian regolith.

#### 2.1.2.4.4 Instrument complementarity

The instruments selected for inclusion on the ExoMars rover have been chosen, in part, due to the complementarity of their analytical techniques. This is especially true following several descopes of the mission, after which there is a much greater scientific burden on a smaller number of instruments. MicrOmega works particularly well with the other two instruments in the ALD, as the visible and NIR context maps that it produces will enable the targeting of grains of interest in the crushed material. For example, grains that show evidence of the historical influence of water will be of particular interest, especially those that belonged to sedimentary clasts that might hold clues to the processes occurring on ancient Mars. Furthermore, Raman and IR spectroscopy are extremely complementary. This is because vibrational modes that are Raman active must cause a change in the polarisability of a molecule, whereas IR active modes must cause a dipole change (Smith and Dent, 2005). Although not mutually exclusive, not all modes result in both changes, so analysis by both Raman and IR spectroscopy will more completely elucidate molecular structure.

MOMA is capable of relatively detailed analyses of certain sample types, however as has already been mentioned, the ExoMars SPDS will only carry 20 ovens for GC-MS, which can each only be used once. For this reason it will be necessary to carefully select samples for study using MOMA. RLS is well suited to this task because Raman spectroscopy is rapid and non-destructive, meaning that samples can be passed to MOMA following investigation using RLS. Raman also provides unambiguous molecular identification, which will aid in the identification of samples that should be studied in greater detail.

The research described in this thesis involves laboratory experimentation in preparation for ExoMars and other future planetary missions. Such laboratory work is a valuable and necessary step in the development of space missions, but it is important to consider the impact that the specific environment of a mission's destination will have on the data that it will acquire. Mars exhibits an extreme radiation environment, low average temperatures, a tenuous CO<sub>2</sub> atmosphere and a highly oxidising and biologically inhospitable regolith chemistry. Not only this, but some aspects of a particular mission architecture might also affect the data obtained by an onboard analytical instrument

such as RLS. These include sample preparation such as rock crushing and the resource limitations of the mission.

### 2.2.1 The Martian radiation environment

Unlike the Earth, Mars does not possess a global magnetic field, which means that energetic particles are not deflected into space, but reach the surface of the planet (Hassler *et al.*, 2014). These particles fall into two categories: Galactic Cosmic Rays (GCRs) from extragalactic sources (Simpson, 1983), and Solar Energetic Particles (SEPs) from the Sun (Ryan *et al.*, 2000). Much effort has been spent modelling the Mars surface and subsurface radiation environment to determine the dose received as a function of geographical location and depth (De Angelis *et al.*, 2004). Following the deployment of MSL (Grotzinger *et al.*, 2012), the Curiosity rover's Radiation Assessment Detector (RAD; Hassler *et al.*, 2012) has made detailed measurements of the Martian radiation environment (Hassler *et al.*, 2014; Köhler *et al.*, 2016), enabling the improvement of the validation of these models (Matthiä *et al.*, 2016).

In addition to the sources of ionising radiation described above, the surface of Mars is greatly influenced by UV solar radiation because its tenuous, CO<sub>2</sub> dominated atmosphere is largely transparent at UV wavelengths (Molina-Cuberos *et al.*, 2001). No UV flux measurements have yet been performed on the Martian surface, however like the ionising radiation, it has been extensively modelled (Cockell *et al.*, 2000; Patel *et al.*, 2002).

#### 2.2.1.1 Measurements of Martian radiation

As described above, the MSL-RAD has performed the most reliable, highest resolution measurements of the spectra of energetic particles on the surface of Mars to date (Hassler *et al.*, 2014). The measured average dose rate for GCRs was  $1.84 \pm 0.30$  mSv.day<sup>-1</sup>. During the Curiosity rover's first 300 sols on Mars, a single SEP event was detected by RAD, with a total dose of 50 µSv. On Earth, the majority of GCRs either get deflected by the planet's magnetic field, or interact with gas molecules in the upper atmosphere. However, such interactions do result in showers of secondary particles, which produce an average dose at the Earth's surface of 0.3-0.4 mSv.day<sup>-1</sup> (Cinelli *et al.*, 2017).

As mentioned in §2.2.1, no direct measurements of the UV flux on the surface of Mars have been made, however UV fluxes and fluences were modelled at the surface of Mars by Cockell *et al.* (2000). This work produced a UVA (315-400 nm) fluence of 1126 kJ.m<sup>-2</sup>.day<sup>-1</sup> and a combined UVB and C (200-315 nm) fluence of 361 kJ.m<sup>-2</sup>.day<sup>-1</sup>. The same model actually produced a slightly larger UVA fluence at the Earth's surface, with a value of 1320 kJ.m<sup>-2</sup>.day<sup>-1</sup>, however the more biologically dangerous UVB and C have a combined fluence of only 39 kJ.m<sup>-2</sup>.day<sup>-1</sup>, around ten times less than on Mars.

### 2.2.1.2 Impact on environmentally preserved biomarkers

It has been suggested that the high levels of radiation at the surface and near subsurface of Mars would have a sterilising effect, destroying all non radioresistant organisms, as well as any radioresistant life in a state of cold induced dormancy (Pavlov *et al.*, 2002). Furthermore, there has been some experimentation that demonstrates the radio- and photocatalytic decomposition of a number of biomarkers of astrobiological significance, both in the laboratory (ten Kate *et al.*, 2006; Stalport *et al.*, 2008; Stalport *et al.*, 2009; Shkrob *et al.*, 2010; Poch *et al.*, 2013) and onboard orbital science platforms using solar UV flux (Stalport *et al.*, 2010; Cottin *et al.*, 2012; Noblet *et al.*, 2012), suggesting that these too would be destroyed by radiation on Mars. There is evidence however, that burial under sufficient regolith and rock can help to preserve biomarkers, suggesting that they should be detected by a carefully conceived analytical instrument (Kminek and Bada, 2006).

Only a very small number of these studies have identified daughter compounds following the degradation of organic molecules (Stalport *et al.*, 2009, Stalport *et al.*, 2010). Furthermore, these studies all involved the irradiation of pure molecular samples, which in some cases were combined with a simulant for the Mars regolith, however they did not use natural analogue rock samples. Additionally, none of the references studies involved the use of Raman spectroscopy for the characterisation of samples, either before or after exposure. Finally, the replication of Martian conditions is not comprehensive in each case, with some studies selecting only certain environmental parameters of interest. Given the interaction between parameters such as temperature, atmospheric pressure, atmospheric composition, regolith composition, UV flux and ionising radiation dose, it is important to perform experiments that control all of these

variables before drawing firm conclusions. For these reasons, it will be useful if natural analogue rock samples are exposed to Martian environmental conditions and characterised using Raman spectroscopy, prior to the deployment of the ExoMars rover.

### **2.2.1.3 Impact on Raman spectra**

Little work has been performed so far on investigating the effect that irradiating planetary samples will have on their Raman spectra. Dartnell *et al.* (2007a; 2007b) showed that as biomarkers are decomposed, the intensity of bands in their Raman spectra decreases. However, due to the limitations of flight-instruments, band intensity is not a reliable spectral parameter in planetary Raman spectra. Also it is clear that bands indicative of daughter compounds will be exhibited as they are produced in an irradiated sample, however as stated in §2.2.1.2, only a limited number of studies have successfully identified such compounds.

The author has proposed a programme of research that will involve identifying the products of radio- and photocatalytic decomposition of biomarkers and demonstrating the acquisition of their Raman spectra following irradiation. If this proposal is accepted, this work will be carried out following the submission of this thesis. The effect of irradiation on spectral parameters such as band position and width will also be investigated, expanding upon the work that is presented in Chapter 4.

### **2.2.2 Sample crushing**

As described in §2.1.2.3, rock cores obtained using the ExoMars rover's drill will be crushed before investigation using the analytical instruments within the ALD. Sample crushing can affect the Raman spectrum of a material in a number of possible ways. Crushing can cause an increase in background signal, a broadening of Raman bands, the introduction of new bands to the spectrum, or in the case of certain materials a shift in band positions (Foucher *et al.*, 2013).

Crushing can also affect the minimum detectable limit of low concentration components of a sample. This is because crushing homogenises a sample, mixing those components with the rock matrix. The relatively large laser footprint produced by flight instruments (see §2.4.3) does improve the probability of randomly sampling targets of interest that are at low concentrations. Detection limits for a range of mission targets in a variety of host matrices should be evaluated through a series of analogue studies, prior to the

deployment of any planetary instrument. A programme of research involving such measurements for RLS has been proposed for funding, and will be conducted by the author following the examination of this thesis.

### 2.3 Raman spectroscopy on future missions

A number of international research teams have been recommending the inclusion of Raman spectroscopy on planetary missions for some time, especially Wang *et al.* (1995) who demonstrated the suitability of Raman for the analysis of both lunar and Martian material. With the inclusion of Raman instruments on both the ExoMars rover and NASA's Mars 2020 rover (see §2.3.1 and §2.3.2 below), the community has clearly been convinced of the suitability of Raman spectroscopy for remote robotic planetary exploration, so it seems likely that Raman spectrometers will be included in the payloads of planetary exploration missions for some time. This will facilitate the improvement of the TRL of a number of systems and components and might enable the inclusion of more specialised Raman techniques on future missions.

#### 2.3.1 SuperCam

SuperCam is an instrument currently being developed for NASA's Mars 2020 rover, which will be capable of LIBS, Raman spectroscopy, time-resolved fluorescence, visible and near-infrared spectroscopy and high resolution colour remote micro-imaging, all at remote distances (Maurice *et al.*, 2015; Wiens *et al.*, 2017). Using this combination of techniques, SuperCam will be able to mineralogically, chemically and texturally characterise rocks, investigate stratigraphy and detect organic molecules, biomarkers and volatiles.

#### 2.3.2 SHERLOC

SHERLOC is a deep-ultraviolet (DUV) Raman spectroscopy and fluorescence instrument that has also been included in the Mars 2020 rover's payload (Beegle *et al.*, 2014; Beegle *et al.*, 2015). It will be mounted on an external robotic arm, which will enable the rover to scan SHERLOC across rock surfaces to produce Raman and fluorescence maps. The primary objective of SHERLOC is to establish the potential habitability and aqueous history of a site by mapping the presence of clay minerals, carbonates, sulphates and halides in sedimentary rock surfaces. The spatial information

given by such maps makes it possible to determine the ancient environment that produced these minerals, helping to determine habitability.

### 2.3.3 Future missions

Planetary exploration missions to various destinations across the Solar System are currently being considered by space agencies. There is great interest in new missions to Venus, such as NASA's SAGE (Surface and Atmosphere Geochemical Explorer; Bienstock and Burdick, 2010) and Roscosmos' Venera-D (Vorontsov *et al.*, 2011). The inclusion of a Raman spectrometer in either of these mission's payloads would enable rapid molecular identification, greatly enhancing their scientific output. Furthermore, NASA are developing missions to Jupiter's moon Europa, such as the Europa Clipper (Phillips and Pappalardo, 2014), and Saturn's moon Enceladus, such as the Europa Life Finder (Lunine *et al.*, 2015). Although the payloads of these flyby missions to the icy moons do not include Raman instruments, their success will lead to future surface missions that will benefit from the incorporation of a Raman spectrometer. In addition to the conception of future missions, appropriate instruments are also being developed, such as the Mars Microbeam Raman Spectrometer (MMRS; Wang *et al.*, 2003) and the Compact Integrated Raman Spectrometer (CIRS; Wang *et al.*, 2015).

## 2.4 Raman spectrometers used in this thesis

The Raman spectroscopic data presented in this thesis were acquired using three separate Raman spectrometers: two commercially available, portable Raman systems, the specifications of which are given in §2.4.1 and §2.4.2, and the UK ExoMars RLS breadboard (UKBB) system, whose specifications are given in §2.4.3. The commercial Raman spectrometers were selected for their similarities to the miniaturised hardware that is to be included on the ExoMars rover, which are fully discussed in §2.4.4. These spectrometers also provide a good indication of the potential capabilities of Raman instruments that could be included on other future planetary missions.

### 2.4.1 532 nm benchtop spectrometer

The first spectrometer incorporates a 100 mW, 532 nm, CW, frequency doubled Nd:YAG laser, with a footprint size of around 50  $\mu\text{m}$ , as its excitation source. It can achieve a maximum irradiance at the sample of approximately 1.6  $\text{kW}\cdot\text{cm}^{-2}$ . The

spectrograph provides a maximum resolution of  $10\text{ cm}^{-1}$  and covers a spectral range from  $200\text{ cm}^{-1}$  to  $3400\text{ cm}^{-1}$ .

### 2.4.2 785 nm handheld spectrometer

The second commercial spectrometer uses a 785 nm, CW, NIR laser and can achieve a maximum output power of 120 mW with an irradiance at the sample of approximately  $0.7\text{ kW}\cdot\text{cm}^{-2}$  across a  $75\text{ }\mu\text{m}$  laser spot. The spectrograph covers a spectral range from  $200\text{ cm}^{-1}$  to  $2000\text{ cm}^{-1}$ , with a spectral resolution of  $< 8\text{ cm}^{-1}$ .

### 2.4.3 UK ExoMars RLS breadboard

The UKBB, which is being developed at the University of Leicester as part of preparations for the ExoMars rover mission, uses a 100 mW, 532.3 nm laser with a footprint size of between  $50\text{ }\mu\text{m}$  and  $150\text{ }\mu\text{m}$ . The instrument incorporates a Kaiser Optical HoloSpec spectrograph and a thermoelectrically cooled CCD. In its baseline configuration, the spectral range of the UKBB is  $200\text{ cm}^{-1}$  to  $4000\text{ cm}^{-1}$  and its spectral resolution is around  $3\text{ cm}^{-1}$ .

### 2.4.4 Comparison with RLS specifications

The currently proposed RLS instrument will be equipped with a CW, 532 nm laser that will produce a  $50\text{ }\mu\text{m}$  spot. The RLS spectrograph will have a spectral range from  $150\text{ cm}^{-1}$  to  $3800\text{ cm}^{-1}$ , dispersed across two spectral orders (see §2.5.1 for an explanation of spectral orders). The instrument will achieve an irradiance in the range  $0.6\text{-}1.0\text{ kW}\cdot\text{cm}^{-2}$  and a spectral resolution between  $6\text{ cm}^{-1}$  and  $8\text{ cm}^{-1}$  (Rull and the RLS team, 2014).

The benchtop Raman spectrometer (§2.4.1) and the UKBB (§2.4.3) both use 532 nm lasers, equivalent to the one that RLS will use. The benchtop spectrometer achieves an average spectral resolution within the RLS resolution range, but produces a greater sample irradiance than RLS. However, it is capable of running at five laser power settings equivalent to 20%, 40%, 60%, 80% and 100% power, which enables it to produce flight-representative irradiances. Both the benchtop spectrometer and the UKBB have similar spectral ranges to RLS.

The handheld Raman spectrometer (§2.4.2) is equipped with a 785 nm laser. This is clearly different to RLS, however the data acquired using this system is used to provide

a comparison between Raman spectra obtained using different excitation wavelengths. This is possible because the sample irradiance and spectral resolution achieved by the handheld spectrometer are within the ranges proposed for RLS.

## **2.5 Data analysis methods**

The following subsections describe the general analysis methods that have been used to complete the research presented in this thesis. More specific methodologies are described in Chapters 3 to 6.

### **2.5.1 Extraction of data from a CCD**

As described in §1.3.5, light from a Raman spectrograph must be captured with a detector, which is usually a CCD, although CMOS detectors are also sometimes used. The image acquired by a CCD in a Raman system will look similar to the one in Figure 2.5, with the majority of the light appearing in a number of spectral orders. These are essentially two dimensional histograms, which result from the dispersion of the scattered light by the diffraction grating. The information that they record must be extracted from the CCD image and calibrated in order to produce a recognisable spectrum.

As can be seen in Figure 2.5, the spectral orders are not infinitely thin, but have a vertical thickness across dispersion. This is a result of broadening within the instrument and must be taken account of when extracting a spectrum from a CCD image. Pixel charge must be carefully binned in order to retain as much of the information in the orders as possible, whilst avoiding the inclusion of background signal. Binning simply means summing the charge in multiple pixels, either vertically or horizontally, which if used in the correct situations can improve SNR. This can be performed on-chip (by the CCD itself) or off-chip (as a part of post-processing). In both cases, noise can be reduced as a result of averaging over several pixels, although in the case of on-chip binning noise is further reduced, since read noise is added to fewer pixels (charge is physically added before reaching the readout amplifier). Frame acquisition is also faster with on-chip binning, since there are fewer pixels to clock out after binning. Not all CCDs are capable of on-chip binning, so in some cases binning must be performed off-chip (Gallaway, 2015).

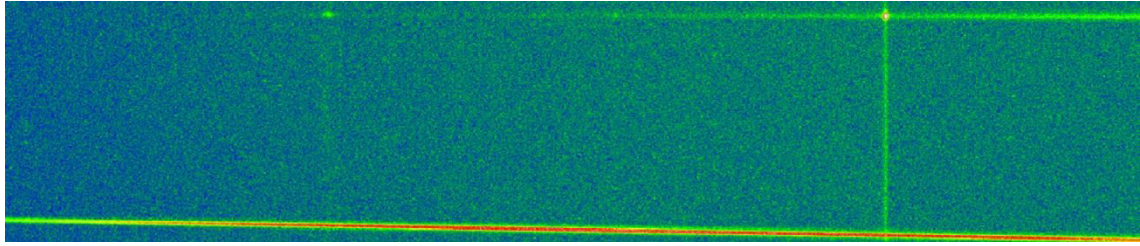


Figure 2.5: A CCD image from the UK ExoMars prototype instrument showing two spectral orders. Wavenumber shift increases from left to right, with the top order dispersing lower wavenumbers. A Raman spectrum of calcite is shown, with three Raman peaks visible as bright spots and the background intensity fading at lower wavenumbers due to the laser line filter. The prototype uses a commercial spectrograph to disperse light from the optical head.

Figure 2.6 shows how light incident on a 2-dimensional CCD array results in an uncalibrated Raman spectrum. Figure 2.6 (a) shows the wavelength dispersed light falling onto the detector, producing a diffraction order containing ambient light, fluorescent emission and several Raman bands, which are labelled in the figure.

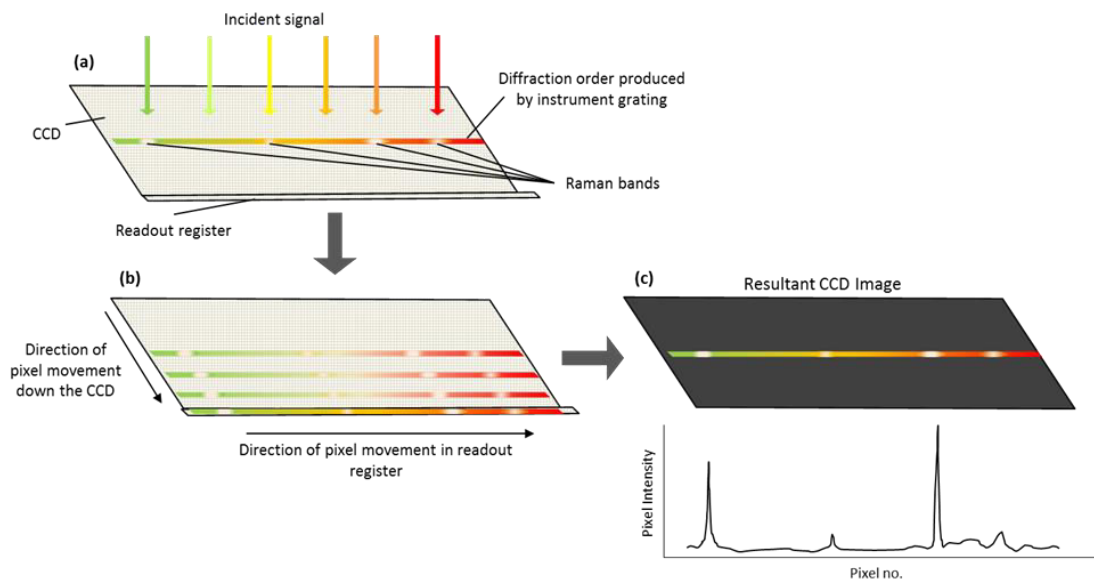


Figure 2.6: (a): Wavelength dispersed light from the spectrometer is incident on the detector, producing one or more spectral orders which include bright spots which are the result of Raman bands. (b): The CCD is read out by moving charge down the device to the readout register. (c): Read-out produces a CCD image, from which a spectrum can be extracted.

Following a period of integration, the signal read out by shifting charge down the device a row at a time into the readout register, as shown in Figure 2.6 (b). Each pixel is then read out to produce a CCD image, as shown in Figure 2.6 (c).

Often, several pixel rows can be shifted into the readout register before being read out, in order to combine pixel signal levels, increasing SNRs. This is known as vertical pixel binning. Then, to extract the Raman spectrum from the CCD image, pixels containing

the signal generated by the diffraction order are summed vertically and the resulting intensity is plotted against horizontal pixel number. An example spectrum can be seen in the figure.

There are numerous CCDs available that could be included in either flight or laboratory instruments, with a range of different device formats, package sizes, pixel sizes and numbers of pixels. A CCD is often selected based on the temperature at which it must operate, although pixel size is also important. The optimum pixel size is determined by the optics geometry, spectral width and nature of the incoming signal. Larger pixel sizes allow more charge to be contained, increasing the maximum signal and therefore dynamic range the detector can achieve. Smaller pixel sizes allow a spectral order to be split across more pixels, which can be beneficial in terms of determining the precise location of the order by centroiding, or detrimental in terms of spreading the signal charge over more pixels and therefore increasing noise. It is desirable for an order to be incident on a minimal number of pixels, however dynamic range may suffer if too few pixels are illuminated due to pixel saturation. A detailed trade-off must be performed to find the optimum balance between the increase in noise associated with a wide diffraction order, and the reduction in dynamic range associated with a narrow one.

### 2.5.2 Wavenumber calibration

The extraction of data from CCD images produces spectra with the intensity of the integrated light against the number of the pixel in which that light fell. Since the scattered light is wavelength dispersed, pixel number relates to wavelength, so in order to make sense of these spectra, a calibration from pixel number to wavelength is necessary. In fact for Raman spectroscopy, because vibrational energy is the quantity being measured, inverse wavelength, or wavenumber, is used instead as it is proportional to energy (Equation 2.1).

$$\bar{\omega} = \frac{1}{\lambda} = \frac{E}{hc} \quad (2.1)$$

Where  $\bar{\omega}$  is wavenumber,  $\lambda$  is wavelength,  $E$  is energy,  $h$  is Planck's constant and  $c$  is the speed of light. A Raman system can be calibrated by acquiring a spectrum of a material with well documented Raman band positions, comparing the pixel number and known wavenumber of bands in the spectrum, fitting a calibration polynomial to these data and applying this polynomial to all other spectra acquired using the system.

Common calibration samples are cyclohexane and polystyrene, however any material may be used, assuming that it has a large number of strong bands covering the entire spectral range of the system. The calibration process should be repeated regularly to account for any mechanical drift, which can result from the expansion or contraction of mechanical components due to changes in temperature. Operating at a different temperature will also affect the wavelength of the laser in an instrument, necessitating recalibration. Components can shift relative to one another due to mechanical shock or vibration, changing the optical path through the instrument chain. Finally, component degradation over the lifetime of an instrument may also affect its calibration.

Given the number of instrument and external factors that can affect the calibration of a Raman spectrometer, RLS and other planetary Raman instruments must be calibrated continuously throughout operation, in order to ensure reliable spectral extraction and interpretation. The sample carousel within the ExoMars rover will include a calibration target, in the form of a disk of polyethylene terephthalate (PET; Rull *et al.*, 2017). PET has numerous strong Raman bands across the entire spectral range of RLS, and will enable spectral calibration at the operating conditions of the instrument, just prior to use. It will also allow calibration of the laser wavelength and power (both of which are dependent on operating temperature), as these will influence the position of Raman peaks.

### **2.5.2.1 Instrument calibration throughout this thesis**

Each of the instruments used to acquire data for this thesis were calibrated at least daily. This was done by first acquiring a spectrum of a polystyrene calibration sample (Figure 2.7). A calibration spectrum has pixel number in abscissa, rather than wavenumber, so a calibration sample must consist of a material with numerous Raman bands of known wavenumber across the entire spectral range of the instrument. This will enable the pixel number and wavenumber of each band to be compared.

The instrument control software was used to complete the calibration process, but this can also be performed manually. Pixel number must be plotted against wavenumber for as many bands as possible in the Raman spectrum, and a calibration polynomial fitted to these datapoints. This curve then allows pixel number to be mapped to wavenumber. As stated above, this process was performed daily for all instruments, however in any situation in which acquired data looked unusual, this could be repeated more frequently

to ensure reliability. The quality of the calibration was evaluated by measuring the RMS error on the polynomial fit, and the calibration was repeated and improved until this value was lower than  $1 \text{ cm}^{-1}$ .

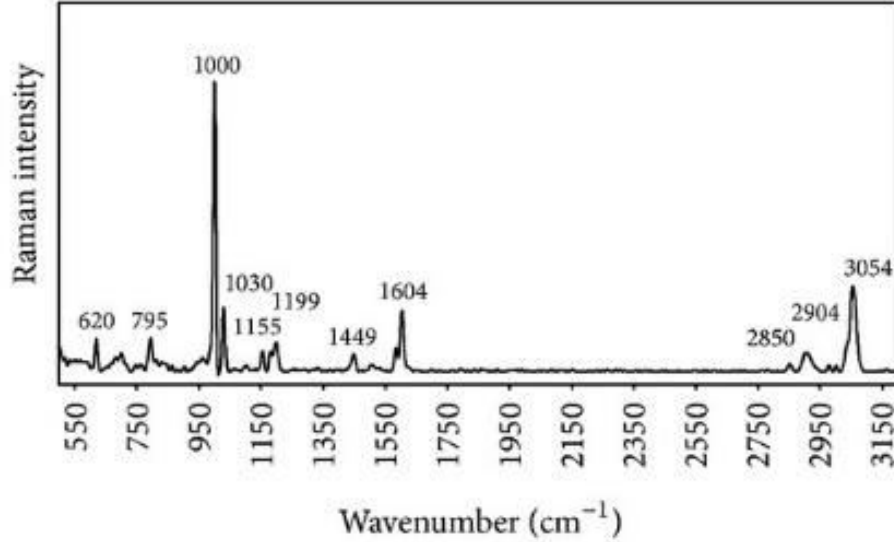


Figure 2.7: Raman spectrum of polystyrene, showing Raman bands across the entire spectral range of most miniaturised Raman spectrometers. Image credit: Serafim *et al.*, 2014.

### 2.5.3 Noise limitations

There are three main sources of noise that affect the quality of spectra obtained. These are shot noise (which increases with the fluorescence and scattering background), dark noise and read noise. Shot noise is the Poissonian noise associated with the randomness inherent in counting photons, so it is equal to the square root of the total number of photons received (Equation 2.2).

$$N_{shot} = \sqrt{(S + B)t} \quad (2.2)$$

Where  $N_{shot}$  is shot noise,  $S$  is signal photon flux,  $B$  is background photon flux and  $t$  is integration time. Dark noise is noise that results from the thermal excitation of electrons within the material of the detector itself. It depends on the number of thermal electrons that are liberated and, like shot noise, is therefore Poissonian (Equation 2.3). It can be reduced by cooling the detector, thereby reducing the number of liberated thermal electrons, however there is no benefit to cooling beyond the point at which dark noise is dominated by other sources of noise.

$$N_{dark} = \sqrt{Dt} \quad (2.3)$$

Where  $N_{dark}$  is dark noise and  $D$  is the rate of liberation of dark noise electrons. Finally, electronics noise is the total noise associated with the sampling and digitisation of the signal. It is entirely dependent on the specific detector system used. Combining these sources of noise gives a total noise calculated using Equation 2.4.

$$N_{tot} = \sqrt{(S + B)t + Dt + N_{electronics}^2} \quad (2.4)$$

Where  $N_{tot}$  is total noise and  $N_{electronics}$  is the noise associated with the sampling of the signal generated in the detector.

#### 2.5.4 **Signal-to-noise ratio**

Signal-to-noise ratio (SNR) is the ratio of the useful signal in a measurement to the noise, which describes all sources of information that are not useful. It is used as a measure of the quality of a measurement, and requirements are often placed on SNR before conclusions are drawn from data. The SNR for a CCD can be calculated using Equation 2.5.

$$\frac{St}{N_{tot}} = \frac{St}{\sqrt{(S + B)t + Dt + N_{electronics}^2}} \quad (2.5)$$

All values of SNR given in this thesis are measured. There are many ways in which SNR can be measured, but in all cases in this thesis the following method is used. Signal is measured as the intensity of a Raman band from base to peak. A spectral region without any bands is selected, in which noise is measured as the root mean square (RMS) deviation of the noise from a function fitted to the background. Finally, SNR is calculated by finding the ratio of these measured values of signal and noise.

In order to distinguish a spectral band from noise it must have a sufficiently high SNR. The appropriate SNR threshold to apply is dependent on the specifics of the analysis being performed, however 10 is a commonly used factor. If the bands in a spectrum do not have sufficiently high SNRs to be positively identified, it might be assumed that increasing integration time will improve SNR, eventually bringing it above the required threshold. In a shot or read noise limited case this would be true, however if the system is instrument noise limited it is not.

### 2.5.5 Background subtraction

Once a spectrum has been successfully extracted and calibrated, bands can be identified and their spectral parameters determined. The positions of the bands can be used to identify the materials in the sample under scrutiny and in some cases, other parameters can yield additional information. It is sometimes desirable to automate this process of band identification and there are a number of ways to achieve this (Yang *et al.*, 2009).

In almost all cases, the background must be reduced or subtracted from the spectrum before bands can be automatically identified. Care must be taken to remove the background, whilst retaining all of the scientific information contained within the spectrum. The simplest way to do this is to select datapoints that are clearly at wavelengths that do not coincide with any bands, fit a polynomial to them, and then subtract this polynomial from the spectrum.

Another method of background subtraction involves taking the Fourier transform of a Raman spectrum, giving a spectrum in the frequency domain that describes the fundamental frequencies that occur in the Raman spectrum. Applying a low-pass filter to this and taking the inverse Fourier transform removes any high frequency or rapidly varying contributions to the spectrum, leaving only the low frequency or slowly varying background. This can then be subtracted from the original spectrum, producing a baselined version (see Figure 2.8 for an example). One of the limitations of this approach is that it can introduce artefacts into the baselined spectrum, in the form of so-called “ringing”, which can be mistaken for spectral features.

Finally, for the measurement of spectral parameters such as band position and width, it is important that the method of background subtraction does not change these parameters, or introduce artefacts. This can be achieved by fitting a polynomial or linear fit to a narrow window around each band, before making spectral measurements.

Figure 2.8 shows an example of what can be achieved with whole spectrum background reduction, however as with all analysis processes, care must be taken to fully understand how this may affect the data and potentially introduce artefacts. At low wavenumbers, three bands in the spectrum of anatase can be seen, with Raman shifts of around 398, 511 and 635  $\text{cm}^{-1}$ , and at higher wavenumbers there appear two bands in the spectrum of carbon, at around 1350 and 1600  $\text{cm}^{-1}$ . There are some features that are not Raman

bands however. In the corrected spectrum, the peak that appears at the lowest Raman shift is in fact an artefact, produced by the background reduction algorithm in response to the sharp rise in intensity at the beginning of the uncorrected spectrum. This is simply the edge of the filter in the Raman instrument, and it is important not to confuse this with a Raman band. There is also a “negative peak” at a high Raman shift that appears in both the uncorrected and corrected spectra. This is likely the result of a hot pixel or cosmic ray that was recording when measuring a dark frame, to be subtracted from the CCD image to correct for ambient light. When the dark frame was subtracted, this feature was produced, however this is not a problem for analysis, assuming that it is not coincident with a Raman band of interest.

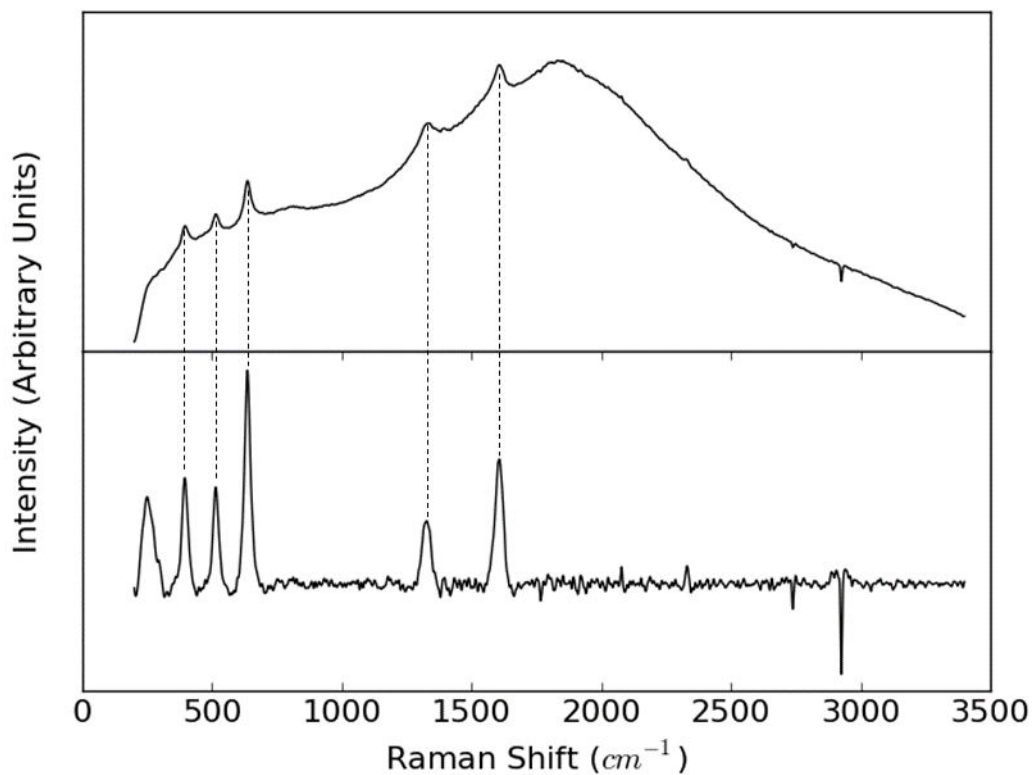


Figure 2.8: Top: Uncorrected Raman spectrum, showing a broad fluorescent background, as well as a number of Raman peaks. Bottom: The same spectrum, following background reduction using the Fourier transform method described in §2.5.5.

### 2.5.6 Band identification

Assuming that the SNR is sufficient to distinguish spectral features from the noise, the next stage in analysis is to determine which features are Raman bands and which are the result of other sources, such as hot pixels and cosmic rays. An ideal Raman band would appear as a delta function with an infinitesimally small width, however optical and electronic broadening within an instrument give Raman bands an expected scale size of

between 30 and around 150  $\text{cm}^{-1}$ . Because they are unrelated to the optical components of the instrument, hot pixels and cosmic rays are much narrower, so can be readily distinguished from bands.

Bands can be identified manually, however if a large number of spectra must be analysed or in the specific case of a space mission, if only the best spectra are to be returned to the user, automated band identification is necessary, as already discussed in §2.5.4. Assuming the spectrum has been baselined, there are a number of methods for automated band identification.

For a baselined spectrum, the simplest methods are to search for any point with an SNR above a certain threshold, any point above a threshold intensity or any point that is a local maximum within  $N$  nearest neighbours. Each of these methods is computationally trivial, however as with most automatic analysis algorithms, the probability of a false positive is quite high.

An alternative approach is to determine the gradient at all points on a spectrum (by differentiation), then peaks can be identified by searching for a sufficiently large gradient, followed by a sufficiently large negative gradient, separated by an appropriate scale size. Similar methods to this include calculating the height to area ratio of suspected bands, fitting a function to suspected bands or measuring their width and applying a threshold to differentiate bands from hot pixels and cosmic rays. Not all of these methods would be effective with particularly noisy data, however each may be useful under specific circumstances.

### 2.5.7 Measurement of band centroids

Once bands have been distinguished from the background and the noise, the final step in analysis before mineral identification can be performed is the measurement of band wavenumber positions. Every band position quoted throughout this thesis is a measured centroid. First, a linear fit to the background in a narrow window around the band is subtracted, as described in §2.5.5 above, as this is least likely to greatly affect band parameters. Then, the centroid of the band is calculated using Equation 2.6.

$$\textit{Centroid} = \frac{\sum_{n=0}^{N-1} f(n)x(n)}{\sum_{n=0}^{N-1} x(n)} \quad (2.6)$$

Where  $n$  in this case is wavenumber,  $x(n)$  is the Raman intensity at a given wavenumber and  $f(n)$  is the Raman intensity at the centre of the window across which the centroid is being calculated.

## Chapter 3

# Avoiding misassignment of Raman bands in planetary spectra

---

As described in Chapter 1, one of the major advantages of Raman spectroscopy is that it can provide unambiguous molecular identification. This is because the Raman shift of a given band depends on the energy of a single molecular vibration, which means that a particular molecule (especially a complex one that exhibits many different vibrations) will give rise to a specific set of bands. This means that a Raman spectrum can be used like a fingerprint to identify a molecule, assuming that the spectral resolution of the instrument and the SNR of the bands are both sufficient.

There is still the possibility of confusion when assigning Raman bands. Some molecular vibrations may be of similar energy, which may result in bands with comparable Raman shifts. If the resolution of the spectrometer used is not sufficient or not enough care is taken, such bands could be confused with one another. Alternatively, certain vibrations may be allowed in multiple similar molecules. They could still be distinguished by the other bands present in the spectra, but if the spectral range available does not include those distinguishing bands, or if their SNR is too low to distinguish them sufficiently from noise, molecules might be misassigned, something that has occurred in the past in the scientific literature (Marshall and Olcott Marshall, 2013). Finally in some cases, background effects can obscure bands or in specific cases mimic them, making misidentification a possibility.

A number of terrestrial analogue samples, with relevance to Mars exploration, have been investigated using the flight-representative and portable Raman spectrometers described in Chapter 2. Each sample provides a case study that highlights the potential for confusion when analysing Raman spectra, but also, more importantly, how such confusion can be avoided, both through careful instrument design and meticulous data analysis.

#### 3.1 Preparation for the ExoMars rover mission

An important stage of preparing for a planetary mission such as ExoMars is the analysis of analogue samples using flight-representative and prototype instruments. This allows the generation of a database of relevant spectra, similar to those that are likely to be acquired by a mission instrument such as RLS, which will be an important tool when analysing mission data. Analogue studies also enable the identification and recommendation of optimum operating modes and analysis methods. Furthermore, such work facilitates the improvement of instrument design for future missions, as the performance of different spectrometers with a range of operational parameters can be assessed.

There is strong interest in automating at least some of the analysis procedures for RLS (Sobron *et al.*, 2008; Rodriguez *et al.*, 2014). This is because the ExoMars rover will be able to transmit only a limited portion of the data it acquires back to Earth. However, the nominal mission plan is to deploy the rover's drill only nine times: twice to perform complete vertical surveys, retrieving five samples during each from incremental depths, and the other seven to retrieve a single subsurface sample at a site of interest. This limited sampling means that the Raman spectra selected for inclusion in the data return must be of the highest quality possible, hence the desire to automatically determine which spectra are most suitable to transmit. A key component of this process would certainly be the automatic identification and assignment of Raman bands that appear in spectra.

An appreciation of the potential for the misassignment of Raman bands, and the specific cases in which this is likely to occur, will be of great importance when establishing whether automatic band assignment is achievable or advisable for RLS. This necessitates the sort of understanding of the capabilities of the instrument that will be engendered by analogue studies, especially considering the expected reduction in

performance when miniaturising scientific instrumentation and developing it for inclusion on a space mission.

### 3.1.1 Reduction in performance for flight

A reduction in the performance of a flight instrument, when compared with state of the art laboratory spectrometers, is an unavoidable consequence of meeting the mass, volume and power budgets described in §1.3.3. This can affect all instrument parameters, but most significantly can result in a reduction in spectral resolution, SNR and in some cases, spectral range. Miniaturised Raman systems also often have larger laser footprints, which means that there is an increased likelihood that multiple materials will be simultaneously sampled during the same spectral acquisition. This can be beneficial, although the reduced operating parameters and increased spot size need to be taken account of when identifying and assigning Raman bands. This is the primary motivation for the work described in this chapter, the rest of which covers four case studies, each relevant to Mars exploration, that highlight a particular source of potential confusion and how it might be avoided.

## 3.2 Partially oxidised carbonaceous mudstone

Two small (approximately 30x15x5 mm) core samples of partially oxidised, Devonian carbonaceous mudstone (Figure 3.1) were studied. These were recovered from an analogue site in Caithness in Northern Scotland, a region whose geology is dominated by Devonian lacustrine sedimentary deposits (Donovan and Foster, 1972). Sedimentary layers can clearly be seen throughout the cores and part of each of them has been oxidised, resulting in a reddening of the rock.



Figure 3.1: A photograph of a carbonaceous mudstone core sample from Caithness, Northern Scotland, used as a Mars analogue. The right sixth of the sample has been oxidised, resulting in the red material that can clearly be identified.

Mudstone is a sedimentary rock, which is produced by the lithification of mud and clay deposits. It must therefore have formed in the presence of water, which means that it is an excellent indicator of the past presence of water within an environment. Mudstone also often traps calcium carbonates, silica and organic material during its formation, making it an ideal matrix for hosting potential geological and biological biomarkers.

### 3.2.1 Relevance to Mars exploration

Mudstone is relatively common in suspected lacustrine environments on Mars (Vaniman *et al.*, 2014), making it a particularly suitable Mars analogue. As discussed in §3.2, mudstone can also include various contaminants that were present during its formation, providing a probe of the ancient Martian environment. The mudstone selected for study here is carbonaceous. The discovery of reduced carbon on Mars would be of great interest and could potentially be significant in the search for signs of life (fully explained in §4.1.4.1), so the analysis of carbonaceous analogues will be useful.

Prior to analysis, it was suspected that these mudstone samples contained iron or iron minerals, because of the reddening of the oxidised region. Given the ubiquity of haematite on Mars, investigation of the oxidation of iron oxide in analogues such as these, specifically the effect of such a reaction on other minerals and potential biomarkers, is important prior to the exploitation of Raman spectroscopic data from Mars.

### 3.2.2 Acquisition of Raman spectra

Raman spectra were acquired from the cores using the 532 nm benchtop instrument described in Chapter 2, calibrated daily as described in §2.5.2.1. This calibration gives confidence that the uncertainty in band position that results from instrument effects will have a maximum of  $\pm 1 \text{ cm}^{-1}$ .

Although it is unlikely that a relatively low powered, optical laser would be sufficiently energetic to cause thermal degradation in the sample, the avoidance of damage was confirmed by acquiring short integration time spectra at numerous locations across the surface of the sample using very low laser power, then illuminating the same site at high power before acquiring comparison spectra at low power again.

Once it was established that no damage was caused by the instrument, both the grey (unoxidised) and red (oxidised) regions were investigated at a large number of spatially separated points, in order to assess the typical spectrum for each region and the level of variation. Spectra were acquired using integration times of between 45 and 60 seconds, with the exact time selected to prevent saturation of the detector. The laser power used was adjusted to match the detector's dynamic range in intensity.

15 spectra were acquired from randomly sampled locations in the grey region, and a further 15 from the red. The positions of the bands in these spectra were determined by measuring band centroids, as described in §2.5.7.

### 3.2.3 Results

The grey, unoxidised regions of the carbonaceous mudstone samples yielded Raman spectra with a single band located at  $1608\text{ cm}^{-1}$  (Figure 3.2A). This is the G band in the Raman spectrum of carbon, usually observed with a Raman shift of between  $1575\text{ cm}^{-1}$  and  $1600\text{ cm}^{-1}$  (Cuesta et al., 1994; Ferrari and Robertson, 2000). This is indicative of the presence of almost perfect crystalline graphite in the mudstone.

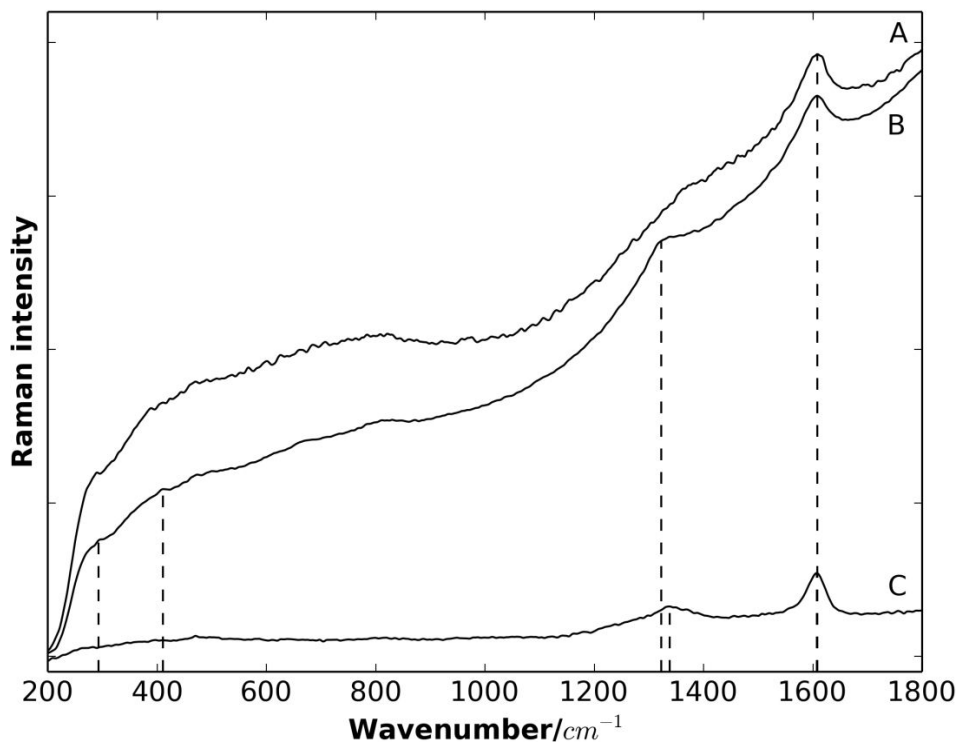


Figure 3.2: Raman spectra acquired from a partially oxidised, Devonian carbonaceous mudstone retrieved from an analogue site in Caithness, Northern Scotland. (A) typical Raman spectrum from the grey, unoxidised regions. (B) typical Raman spectrum from the red, oxidised regions. (C) Raman spectrum of reduced carbon, acquired from a carbonaceous Devonian shale, also from Caithness. Figure reproduced from Harris *et al.*, 2015b.

All spectra acquired from the red, oxidised regions of the cores also exhibited a carbon G band, but in addition, a second band located at  $1323\text{ cm}^{-1}$  also appeared in many of them (Figure 3.2B). A number of bands in the spectrum of carbon occur at similar Raman shifts, so this band could be mistakenly assigned to carbon. However, this Raman shift is too low for  $\text{sp}^3$  carbon (whose main band occurs at  $1332\text{ cm}^{-1}$ ) or the carbon D band (which occurs at around  $1310\text{ cm}^{-1}$  with  $785\text{ nm}$  excitation, and  $1350\text{ cm}^{-1}$  with  $532\text{ nm}$ ; Wang *et al.*, 1990; Matthews *et al.*, 1999). The band does seem to be consistent with the second order band in the spectrum of haematite ( $\alpha\text{-Fe}_2\text{O}_3$ ), which is expected to appear at around  $1330\text{ cm}^{-1}$  (McCarty, 1988). This band is the second order harmonic of the  $660\text{ cm}^{-1}$  band, which itself is not a Raman-active vibrational mode. Two additional, very weak bands can be observed in Figure 3.2B with Raman shifts of  $293\text{ cm}^{-1}$  and  $411\text{ cm}^{-1}$ , which can also be attributed to haematite (de Faria *et al.*, 1997).

The readiness with which haematite and other iron oxide and oxyhydroxide minerals can be confused with reduced carbon in Raman spectra has been previously reported (Marshall *et al.*, 2011; Marshall and Olcott Marshall, 2011; Olcott Marshall *et al.*, 2012). The work presented here demonstrates that despite this potential ambiguity, with careful analysis the spectra of haematite and reduced carbon acquired using flight-representative instruments can be distinguished. By measuring 15 spectra from each region of the sample, the consistency of the position of the band at  $1323\text{ cm}^{-1}$  has been confirmed. Given that the calibration RMS is  $< 1\text{ cm}^{-1}$ , this band can be clearly distinguished from the carbon D band at  $1350\text{ cm}^{-1}$ , giving a positive identification of haematite in the sample.

Great effort must be made to detect the Raman bands in the haematite spectrum that appear in the so-called mineral fingerprint region, located between  $200$  and  $800\text{ cm}^{-1}$  (Marshall and Olcott Marshall, 2011). These bands are not coincident with any of the bands observed in the spectrum of reduced carbon, so would make unambiguous differentiation of haematite and carbon possible. In a lot of cases however, these bands have very low SNRs. In situations in which they cannot be distinguished from the noise, the exact position of the band around  $1320\text{ cm}^{-1}$  must be carefully determined, and the excitation wavelength used must be considered, in order to make this assignment.

### 3.3 Desert varnish

Desert varnishes, alternatively called rock varnishes, are thin, dark-coloured coatings that form on rock surfaces in both hot and cold, arid environments. They are primarily composed of H, O, Al, Si, Mn and Fe (Dorn, 2007).

Two different varieties of desert varnish were investigated in this study, each from a geographically distinct location in the Mojave Desert, USA. Three rock samples coated with a dark black varnish (see Figure 3.3) were retrieved from a stable alluvial fan, descending from the Sylvania Mountains at the northern boundary of Death Valley in California, USA. A further four samples coated with a lighter, brown-coloured varnish were collected from a desert pavement surface in the Cady Valley (Malherbe *et al.*, 2015). By geological observation, it was determined that both sites have been geomorphically stable over geologically significant timescales, making them suitable analogue sites.

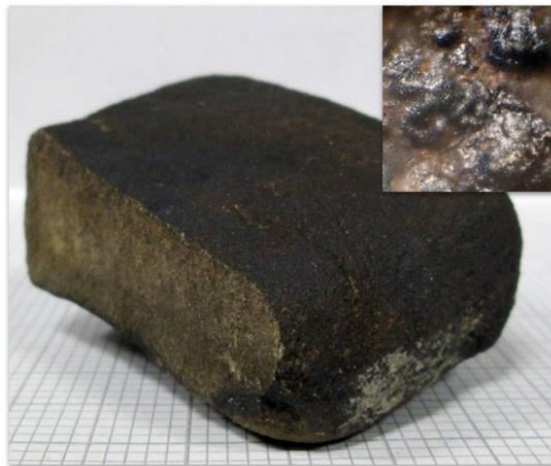


Figure 3.3: A photograph of the dark black varnish that coats the first set of varnish samples studied here. Inset: Microscopic image of the varnish surface, clearly showing botryoidal structures. Image credit: C. Malherbe.

Prior to detailed analysis, it was hypothesised that the darker colour of the varnish on the first set of samples was indicative of an abundance of manganese oxides, whereas the second set of varnish samples must have been rich in iron to produce the lighter, brown colour.

#### 3.3.1 Relevance to Mars exploration

The presence of botryoidal structures (see Figure 3.3) on varnish surfaces, along with the especially high manganese content of many varnishes, led to the hypothesis that

desert varnishes result from epilithic colonisation by manganese-oxidising bacteria, algae and fungi (White, 1924; Laudermilk, 1931). This mechanism for the formation of desert varnishes has subsequently been confirmed by a range of analytical techniques (Krumbein and Jens, 1981; Dorn and Oberlander, 1982; Mancinelli and White, 1996; Perry *et al.*, 2003; Schelble *et al.*, 2005), although several abiotic formation mechanisms are still advocated. This potential association with living organisms means that desert varnishes represent a possible biomarker and they are therefore of great interest during the preparation for planetary exploration and astrobiology missions, such as the ExoMars and Mars 2020 rover missions.

It is suspected that they have been detected on Mars in observations of the Mars Pathfinder landing site (McSween Jr. and Murchie, 1999). Furthermore, varnishes consist largely of clay minerals with iron oxides such as haematite, iron hydroxides like goethite (FeO(OH)) and manganese oxides such as pyrolusite (MnO<sub>2</sub>) (Potter and Rossman, 1979), all of which are abundant on Mars.

#### 3.3.2 Acquisition of Raman spectra

Raman spectra were acquired from all seven desert varnish samples using the 785 nm handheld instrument. It was found that NIR illumination was more suitable than 532 nm for such dark samples, containing high concentrations of iron oxides. Depending on the intensity of the background observed for a given sample, spectra were integrated for between 3 seconds and 30 seconds. The instrument was calibrated daily as described in §2.5.2.1, and all band positions given were obtained by calculating the band centroid, as described in §2.5.7. Most spectra were obtained from the unprepared rock samples due to the practical difficulty of preparing crushed samples, however some small crushed samples were produced and spectra obtained, which proved that the Raman spectra were not altered by the crushing process.

The study of such samples using portable Raman spectrometers is not trivial. The varnish is usually only a few micrometres thick, which results in a small amount of Raman scattering and therefore a very weak signal. Desert varnishes are also primarily composed of clay minerals that are weak Raman scatterers, but which strongly fluoresce and therefore produce an intense background signal. They are also strong absorbers of both the incident laser light and the scattered light, hence their dark appearance, which also contributes to a reduction in signal intensity. These challenges meant that relatively

large numbers of spectra were obtained to achieve confidence in the results, of the order of 20 or 30 spectra per rock sample. This means that in order to be effective and have a good chance of detecting materials such as desert varnishes on Mars, RLS must acquire tens of spectra from each sample.

Given that desert varnishes form such thin layers on rock surfaces, the penetration depth of the laser used for excitation is highly significant. Adar *et al.* (2010) investigated penetration depth in a silicon target, observing that as wavelength is increased, the laser penetrated deeper into the sample. In their experiment, UV lasers only penetrated 5-10 nm, 532 nm light penetrated up to 0.7  $\mu\text{m}$ , 633 nm light up to 3  $\mu\text{m}$  and finally a 785 nm laser penetrated up to a maximum of 12  $\mu\text{m}$ . This means that when using a 785 nm Raman instrument such as the handheld spectrometer used here, it must be considered that some bands in spectra obtained may result from the rock matrix, rather than the varnish itself.

Of course, the ExoMars rover will be investigating crushed rock samples, which means that any desert varnishes that might be present would be mixed with material from their host rock, making it difficult to detect them. However, by studying varnishes in preparation for the ExoMars rover mission, it might still be possible to infer their presence. All samples will be photographed using CLUPI prior to being crushed, and varnishes may be observable in these images. Then, RLS will identify minerals associated with desert varnishes in the crushed material, along with other minerals associated with the host rock matrix. This work will also be of great interest when other future Raman spectrometers are deployed on other planets, such as SuperCam and SHERLOC on NASA's Mars 2020, which will be studying unprepared rock samples.

### 3.3.3 Results

As mentioned in §3.1.1, when investigating mineralogically complex samples such as the desert varnishes discussed here, a single Raman spectrum acquired using a portable spectrometer will often comprise spectral features of multiple mineral phases. This is due to the large laser footprints of such spectrometers, which usually produce laser spots with diameters of around 50  $\mu\text{m}$ . For comparison, the spots produced by Raman microspectrometers usually have diameters of around 2  $\mu\text{m}$ , and different phases in the sample can range in cross-sections from a few micrometres up to 100  $\mu\text{m}$ . It is clear that the expected number of mineral phases sampled is proportional to the laser spot size.

Five spectra are shown in Figure 3.4, representing the full mineralogical range of the desert varnish samples. Spectra of rutile, anatase, haematite and goethite are also provided for comparison. Inspection of the varnish spectra shows that at least some of them are superpositions of multiple mineral spectra.

At first inspection, spectrum A appears to be a perfect spectrum of rutile, with bands at  $464\text{ cm}^{-1}$  and  $611\text{ cm}^{-1}$ , compared with those at  $451\text{ cm}^{-1}$  and  $612\text{ cm}^{-1}$  in the spectrum of pure rutile, also seen in Figure 3.4. The band at  $464\text{ cm}^{-1}$  does have a slightly higher Raman shift than expected, but upon closer inspection, a weak shoulder is observed to the left of the band. It is proposed that this band and shoulder are a superposition of the rutile band, which is in fact the shoulder, and the quartz ( $\text{SiO}_2$ ) band at  $464\text{ cm}^{-1}$  (Hemley, 1987; Gillet *et al.*, 1990).

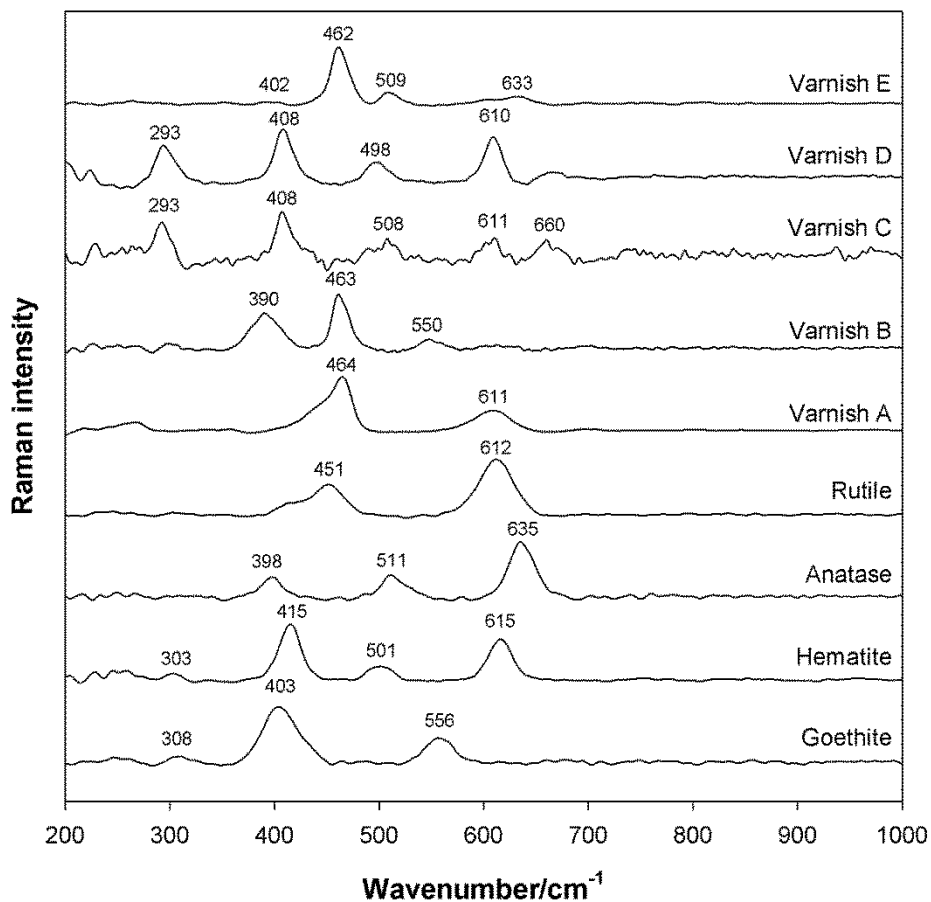


Figure 3.4: Representative Raman spectra from samples of desert varnish, labelled Varnish A-E, with spectra of rutile, anatase, haematite and goethite included for comparison. All spectra were acquired using a 785 nm, handheld Raman spectrometer and have been baseline corrected by Fourier transformation. Figure reproduced from Harris *et al.*, 2015b.

Spectrum B appears to contain a mixture of quartz, identified by the  $464\text{ cm}^{-1}$  band, and goethite ( $\alpha\text{-FeO(OH)}$ ), an iron hydroxide mineral that is fairly common on Mars

(Klingelhoefer *et al.*, 2005). The bands at  $390\text{ cm}^{-1}$  and  $550\text{ cm}^{-1}$  are attributed to goethite, based on the appearance of similar bands in the reference spectrum.

The superposition of multiple Raman bands in a single spectrum can lead to complex relative intensity profiles, which introduces the potential for the misassignment of bands. In spectrum C, the bands with Raman shifts of  $293\text{ cm}^{-1}$ ,  $408\text{ cm}^{-1}$ ,  $508\text{ cm}^{-1}$  and  $611\text{ cm}^{-1}$  are attributed to haematite, however an additional band is also visible at  $660\text{ cm}^{-1}$ , along with several other much weaker bands. These are possibly indicative of the presence of either magnetite (iron(II,III) oxide;  $\text{Fe}_3\text{O}_4$ ) or maghemite ( $\text{Fe}_2\text{O}_3$ ), which have bands at  $670\text{ cm}^{-1}$  and  $665\text{ cm}^{-1}$  respectively (Hanesch, 2009). The band in spectrum C at  $611\text{ cm}^{-1}$  is slightly lower than this however, and the band at  $508\text{ cm}^{-1}$  is also redshifted relative to the band at  $501\text{ cm}^{-1}$  in the haematite reference spectrum, and that at  $498\text{ cm}^{-1}$  in spectrum D, which itself appears to be a perfect haematite spectrum. This is due to yet another band superposition, this time an extremely weak detection of the band, at around  $503\text{ cm}^{-1}$ , in the spectrum of the feldspar plagioclase (Wang *et al.*, 1995), one of the primary constituents of the host rock.

The analysis of spectrum C demonstrates that a Raman spectrum can be significantly modified by the simultaneous detection of two or more signals in close proximity. The shape of the background can also dramatically alter the relative intensities of bands, if its intensity varies with wavenumber. Insufficient spectral resolution could result in the misassignment of the bands in a spectrum. As seen in Figure 3.4, the distinction between anatase and haematite can be challenging, particularly because the strongest band in the spectrum of anatase, with a Raman shift of  $151\text{ cm}^{-1}$ , is inaccessible using portable spectrometers and even some laboratory instruments, given their limited spectral range at low wavenumbers. The three main bands of anatase and haematite are indeed centred about similar positions ( $398\text{ cm}^{-1}$ ,  $511\text{ cm}^{-1}$  and  $635\text{ cm}^{-1}$  for anatase and  $415\text{ cm}^{-1}$ ,  $501\text{ cm}^{-1}$  and  $615\text{ cm}^{-1}$  for haematite). It is therefore difficult to distinguish between them if the spectral resolution of the instrument used is worse than around  $10\text{ cm}^{-1}$ . Figure 3.5 shows a simulated spectrum that includes all of these bands and shows how a poor spectral resolution can prevent their differentiation.

Spectrum E belongs to part of the desert varnish where quartz is detected together with either haematite, anatase or both. The band positions are closer to those of anatase, however they are offset from the expected positions sufficiently to suggest that they are

superpositions of the bands from both spectra. They are also very broad, supporting the conclusion that both anatase and haematite are present, although their low intensity makes measurement of the band widths difficult.

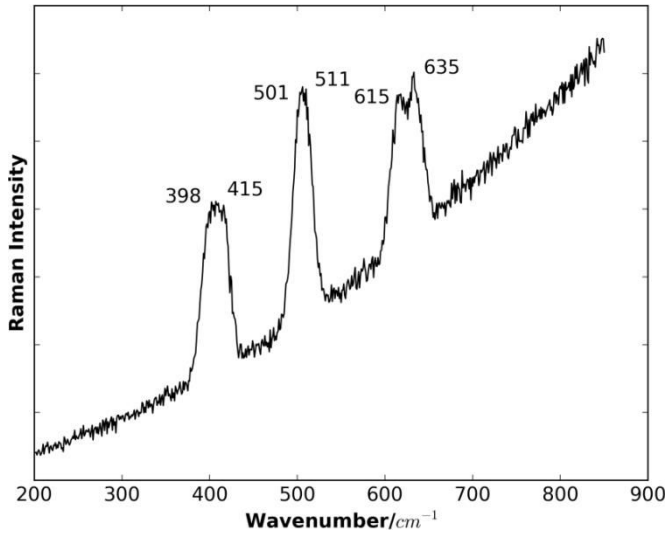


Figure 3.5: A simulated Raman spectrum containing bands at 398, 511 and 635  $\text{cm}^{-1}$  from the spectrum of anatase, and 415, 501 and 615  $\text{cm}^{-1}$  from the spectrum of haematite. A simulated fluorescence background and Poissonian shot noise have also been incorporated. Due to low spectral resolution, which was modelled by giving all bands a FWHM of 20  $\text{cm}^{-1}$ , the spectra of the two minerals cannot be resolved. Only the bands at 615/635  $\text{cm}^{-1}$  appear as a doublet.

### 3.4 Hydrated calcium sulphates

Calcium sulphate (Figure 3.6) at three different levels of hydration were studied. Pure, powdered samples of gypsum, bassanite and anhydrite were obtained and their composition was verified using additional analytical techniques, such as powder X-ray diffraction (XRD). Gypsum molecules incorporate two water molecules each (chemical formula  $\text{CaSO}_4 \cdot 2\text{H}_2\text{O}$ ). Bassanite is a hemihydrate, containing one water molecule for every two calcium sulphate molecules (chemical formula  $2\text{CaSO}_4 \cdot \text{H}_2\text{O}$ ). The last calcium sulphate studied was anhydrite, also known as anhydrous calcium sulphate since its structure does not include any water molecules (chemical formula  $\text{CaSO}_4$ ).

#### 3.4.1 Relevance to Mars exploration

Calcium carbonate has already been detected during previous missions to Mars (Langevin *et al.*, 2005; Boynton *et al.*, 2009; Wray *et al.*, 2010). Its detection on Mars is of great interest, as its level of hydration can describe the environmental conditions in which it formed (Wang *et al.*, 2006b). Gypsum in particular also makes an excellent host for extremophilic, microbial life and therefore is a target of considerable interest for astrobiology missions such as the ExoMars rover (Parnell *et al.*, 2004).



Figure 3.6: Left: Gypsum. Image credit: James Smith, Brigham Young University. Middle: Bassanite. Image credit: Lou Perloff / Photo Atlas of Minerals. Right: Anhydrite. Image credit: Michael P. Klimetz.

### 3.4.2 Acquisition of Raman spectra

Each powder sample was compressed in a sample container, approximately 2 cm in diameter, representative of the ExoMars rover's SPDS which will deliver samples to the RLS instrument. Raman spectra were acquired from several randomly sampled, spatially separated positions on the surface of each compressed sample. Great care was taken to ensure that samples were not excessively heated and therefore thermally altered by the laser during data acquisition.

### 3.4.3 Results

The spectrum shown in Figure 3.7 demonstrates the typical data obtained from the gypsum sample using the 532 nm benchtop spectrometer. The key bands for identification of gypsum are all evident, at  $1008\text{ cm}^{-1}$  ( $\nu_1$ ),  $416\text{ cm}^{-1}$  and  $495\text{ cm}^{-1}$  ( $\nu_2$ ),  $1118\text{ cm}^{-1}$ ,  $1136\text{ cm}^{-1}$  and  $1143\text{ cm}^{-1}$  ( $\nu_3$ ) and  $618\text{ cm}^{-1}$ ,  $620\text{ cm}^{-1}$  and  $672\text{ cm}^{-1}$  ( $\nu_4$ ) (Berenblut *et al.*, 1973). These bands are superposed on an intense background that has a peak intensity at around  $2000\text{ cm}^{-1}$ .

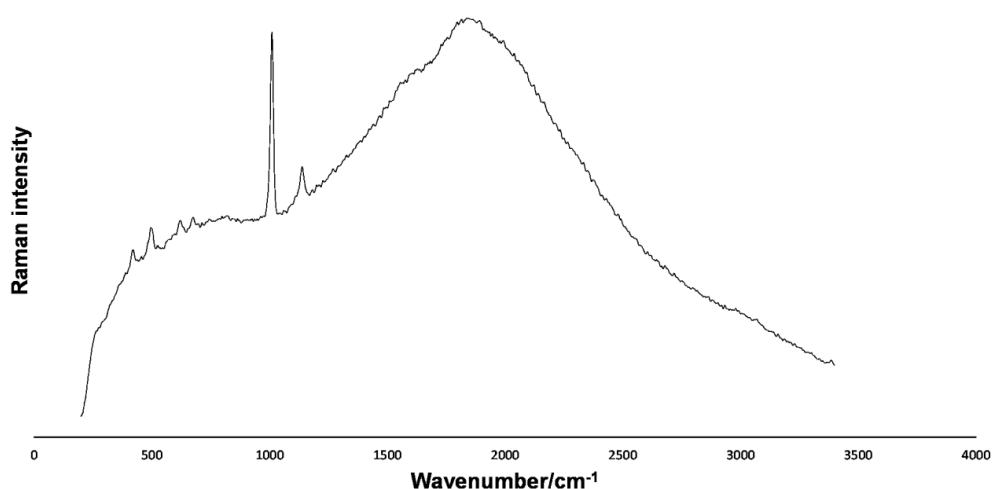


Figure 3.7: Uncorrected spectrum of gypsum, acquired using a 532 nm benchtop Raman spectrometer. Figure reproduced from Harris *et al.*, 2015b.

Variation of up to around  $3\text{ cm}^{-1}$  is discernible in band position between samples, allowing differentiation between the different hydrated forms of calcium sulphate. The upper limit of the spectrometer's spectral range is just sufficient to enable observation of one of the water stretch modes, at around  $3394\text{ cm}^{-1}$  (Auer and Skinner, 2008), however it is not sufficient to detect the high frequency gypsum band at  $3490\text{ cm}^{-1}$ , or those of bassanite at  $3554\text{ cm}^{-1}$  and  $3616\text{ cm}^{-1}$  (Knittle *et al.*, 2001).

### 3.5 Bacterially colonised evaporite

A sample of bacterially colonised, hypersaline evaporite (Figure 3.8) was retrieved from the bottom of a salt evaporation pond, also known as a saltern, near to the port town of Eilat in southern Israel (Culka *et al.*, 2014b). Stratification of the crystalline material can clearly be seen in the photograph of the sample shown in Figure 3.8. These differently coloured layers are the result of colonisation by different species of cyanobacteria and purple sulphur bacteria, a class of anaerobic, photosynthetic bacteria that use hydrogen sulphide, rather than water, as a reducing agent in photosynthesis.



Figure 3.8: Photograph of a hypersaline evaporite analogue sample, retrieved from the bottom of a saltern near the town of Eilat, southern Israel. The coloured strata indicate colonisation by cyanobacteria and purple sulphur bacteria. Image credit: J. Jehlička and A. Oren.

It is well documented in the literature that this colouration of the strata is the direct result of the presence of carotenoids and other molecular pigments (e.g. Jehlička and Oren, 2013a). The red pigment observed is usually bacterioruberin, whereas purple is

likely to be bacteriorhodopsin, a polyene chain-based protein (Oesterhelt, 1998). Orange and green regions in other samples have been found to contain echinenone and myxoxanthophyll (Jehlička and Oren, 2013a; Culka *et al.*, 2014a).

#### 3.5.1 Relevance to Mars exploration

Evaporitic minerals such as these were first discovered on Mars by the MER rovers (Wang *et al.*, 2006b). Since then, they have become a key target for Mars exploration missions, particularly those with an astrobiological focus, due to their potential for colonisation by halophilic microorganisms. As such, the study of terrestrial hypersaline analogues has also become greatly important in preparation for the next generation of missions to Mars.

Colonies of bacteria enclosed within fluid inclusions in halite crystals, and the molecular pigments that they synthesise, have been investigated in great detail (Jehlička and Oren, 2013a; Culka *et al.*, 2014a). This has improved our understanding of the survivability and detectability of biomarkers such as these under current Martian conditions (Jehlička and Oren, 2013b). However, despite the relatively high Raman scattering cross section of pigment molecules, and the signal enhancement that can be achieved using carefully selected excitation wavelength, unambiguous identification of a specific carotenoid can prove difficult due to the complexity of the molecule (de Oliveira *et al.*, 2010).

#### 3.5.2 Acquisition of Raman spectra

Numerous differently coloured regions could easily be identified by observation within the evaporite (as seen in Figure 3.8). Small pieces of each coloured section were broken off from the main sample to isolate them, resulting in red, purple, pink (a mixture of red and purple), orange, green and black samples. The evaporite was quite brittle, so these samples were easily crushed to produce grains with diameters of between 100 and 200  $\mu\text{m}$ , as measured under a microscope, to match the grain size distribution planned for the ExoMars SPDS.

Raman spectra were acquired from each using the UK ExoMars RLS breadboard system. Each coloured sample was randomly sampled with integration times of between 8 seconds and 40 seconds, depending on the strength of the Raman response and the intensity of the background signal. Due to the resonance Raman effect, the 532 nm light

from the breadboard system produced a strong Raman response, so carotenoid spectra were extremely clear in almost every spectrum obtained. Around 10 spectra were acquired from each sample, in order to gain statistical confidence in the precise position of each band, but for simple identification, far less would have been required.

### 3.5.3 Results

Figure 3.9 provides a comparison of the spectra acquired from the six, visually identified, coloured layers within the evaporite sample. All three primary carotenoid Raman bands can clearly be seen in each spectrum, generally designated  $\nu_1$ ,  $\nu_2$  and  $\nu_3$ . In the spectra from the red, pink and purple layers, labelled A, E and F respectively in Figure 3.9, these bands have Raman shifts of  $1510\text{ cm}^{-1}$  ( $\nu_1$ ),  $1154\text{ cm}^{-1}$  ( $\nu_2$ ) and  $1012\text{ cm}^{-1}$  ( $\nu_3$ ). In the green and orange spectra, C and D on Figure 3.9,  $\nu_1$  is shifted to  $1516\text{ cm}^{-1}$  and  $1515\text{ cm}^{-1}$  respectively, whilst  $\nu_2$  is shifted to  $1157\text{ cm}^{-1}$  in both cases and the position of  $\nu_3$  remains unchanged. Finally, the spectrum of the black pigment, labelled B on Figure 3.9, has band positions of  $1509\text{ cm}^{-1}$  ( $\nu_1$ ),  $1152\text{ cm}^{-1}$  ( $\nu_2$ ), and  $1512\text{ cm}^{-1}$  ( $\nu_3$ ), but also shows evidence of a shoulder to the right of the  $\nu_1$  band.

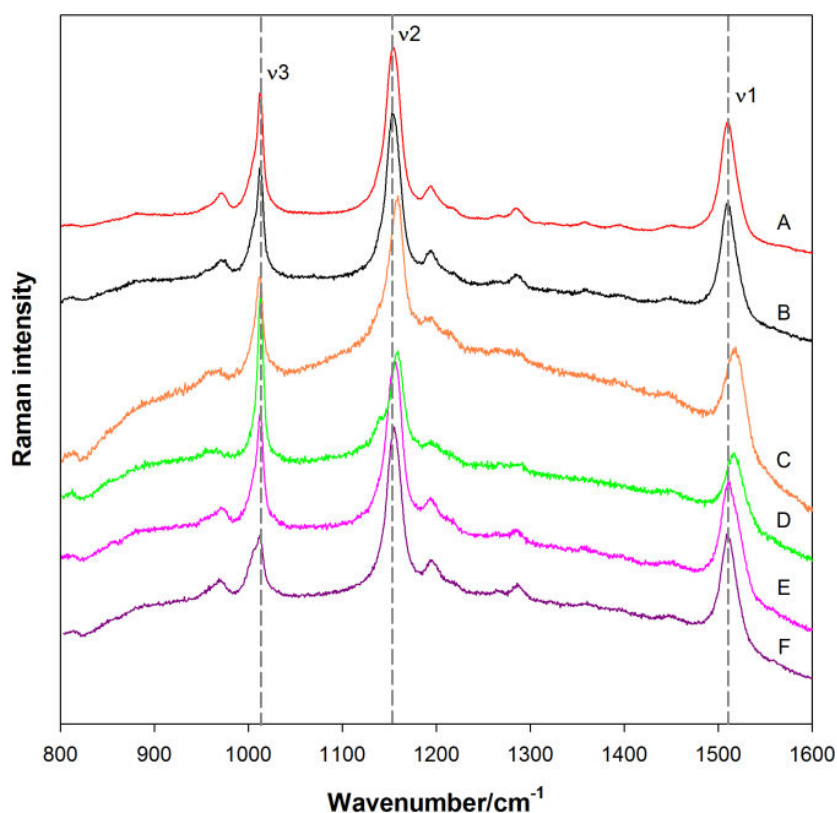


Figure 3.9: Colour-coded Raman spectra from six, differently coloured pigments found in the hypersaline evaporite sample from Eilat, Israel. In each spectrum, the three primary carotenoid bands are apparent, along with several other, weaker bands. Figure reproduced from Harris et al., 2015b.

### 3.6 Discussion

In each case presented here, there is the distinct possibility that Raman bands could be misassigned as part of the analysis of these analogue samples, due to confusion that could arise, largely as a result of the larger spot size, lower spectral resolution and lower sensitivity of portable and flight-representative spectrometers used. Although unambiguous molecular identification should be possible given the positions of bands in a spectrum, the limitations of such instruments can result in signatures with multiple possible interpretations. One cause of this is the large laser spots (50  $\mu\text{m}$  compared with 2  $\mu\text{m}$  for a lab instrument) that portable instruments tend to produce (due to their small size, necessitating a reduction in optical capabilities). Illuminating a larger region of a specimen will increase the probability that more than one mineral is sampled, potentially obscuring or deforming bands by the superposition of multiple spectra. The poorer spectral resolution of flight-like spectrometers can add to this problem, making it difficult to resolve Raman bands that are spectrally near to each other, once again either obscuring or deforming bands due to superposition effects. Lastly, reduced sensitivity at the low wavenumber end of the spectrum, where broad filtering (as explained in §1.3.5.3), or incomplete filtering and leakage of the laser line, will cause the lowest observable limit to be higher. This could potentially preclude diagnostic bands that could assist with band assignment, such as the  $E_g(1)$  band in the spectrum of anatase, with a Raman shift of 151  $\text{cm}^{-1}$ .

#### 3.6.1 Partially oxidised carbonaceous mudstone

If all bands in the spectrum of haematite are visible, with good SNRs, it should be immediately and unambiguously identifiable. If the background is particularly high however, as it can be when using certain flight model optical configurations, some bands in haematite's Raman spectrum can be obscured. This is the case for the spectrum shown in Figure 3.2B, in which the bands  $A_{1g}(1)$  (225  $\text{cm}^{-1}$ ),  $A_{1g}(2)$  (498  $\text{cm}^{-1}$ ),  $E_1(1)$  (247  $\text{cm}^{-1}$ ) and  $E_1(5)$  (613  $\text{cm}^{-1}$ ) are missing and the bands  $E_1(2)$  (293  $\text{cm}^{-1}$ )/ $E_1(3)$  (299  $\text{cm}^{-1}$ ) and  $E_1(4)$  (412  $\text{cm}^{-1}$ ) either have extremely low SNRs or are also absent, making mineral assignment difficult. However, with statistically robust measurement of the Raman shift of the band at around 1320  $\text{cm}^{-1}$ , combined with knowledge of the excitation wavelength dependent dispersion of the D band in the spectrum of reduced carbon, and at least some evidence of the low frequency haematite bands, this spectrum

can be attributed to the presence of haematite (Marshall *et al.*, 2011; Marshall and Olcott Marshall, 2011; Olcott Marshall *et al.*, 2012). It is important that all of these factors are considered when analysing spectra from upcoming planetary missions.

It is important to understand the limitations of a Raman system if it is to be used to gain quantitative information about a sample, such as in the quantitative analysis of reduced carbon spectra to elucidate its thermal history. As discussed in §3.1, a rover such as ExoMars will be capable of transmitting only a limited selection of the data that it acquires, so some analysis must be performed prior to transmission. The processing capabilities of a flight instrument on board a rover are not sufficient to reliably measure band intensities and calculate relative intensity ratios, but it may be possible to differentiate separate carbon populations by carefully measuring the width and Raman shift of the G band in the spectrum of reduced carbon. This extremely valuable method of analysing reduced carbon spectra acquired in situ is discussed in greater depth in Chapters 4 and 5.

Since ExoMars will analyse crushed rock samples, spatial information will be lost, such as that in the mudstone sample. It would not be possible for RLS to capture the change from one material to the other across the sample. However, all samples will also be photographed by CLUPI, so such spatial information will be observed, and it may be possible to match this with the spectra obtained. Another possible limitation could be the number of spectra that are acquired of each sample. Given that haematite is such a weak Raman scatterer, many of the spectra obtained here did not include any Raman bands. Given that ExoMars samples will be crushed and mixed, this problem will be exacerbated, as all phases of the rock sample will be evenly distributed. This could mean that a very large number of spectra need be acquired in order to identify certain materials. Finally, when working in a laboratory it is useful to analyse some spectra, before returning to the sample to acquire more based on the preliminary data. It is unclear whether this will be possible on the ExoMars rover mission, however this could significantly impact the success of the spectral analysis.

### **3.6.2 Desert varnish**

High concentrations of iron oxides in an environment contribute significantly to the preservation of biomarkers and therefore the creation of protective geological niches, such as desert varnishes. This makes the detection and differentiation of iron oxides a

high priority for missions to other planets, especially astrobiology missions. Investigation of the desert varnish samples selected for this study, demonstrated another example of potential ambiguity when assigning bands in the Raman spectrum of haematite. It is possible to confuse bands in the spectra of both stable allotropes of titanium oxide, anatase and rutile, with those in the haematite spectrum, due to several bands occurring at similar spectral positions.

Usually, the most telling diagnostic band in the anatase spectrum is the low frequency band at  $151\text{ cm}^{-1}$ . Unfortunately, wavenumbers this low are often inaccessible using portable or miniaturised spectrometers, which usually have a lower wavenumber limit of around  $200\text{ cm}^{-1}$  (due to filtering; see §1.3.5.3). For this reason, a spectrometer with a spectral resolution of at least  $10\text{ cm}^{-1}$  is required, to ensure that the other anatase bands can be distinguished from their neighbouring haematite bands. A poorer resolution than this would lead to the degeneration of the bands in the spectra of anatase and haematite, making it difficult to differentiate them. Even if the resolution of the spectrometer used is sufficient, if significant broadening is caused as a result of its optical configuration, as is the case with some flight instruments, it may still not be possible to completely resolve the bands and therefore great care must be taken when interpreting the data.

Another challenge associated with analysing spectra acquired from complex mineralogical samples such as the desert varnish is high fluorescence background. For samples with very high fluorescence, it is possible that only the strongest band in the haematite spectrum will be observable, with a Raman shift of  $610\text{ cm}^{-1}$ . This band is also present in the spectrum of rutile however, so the presence of haematite can only be confirmed if the other bands in its spectrum, at  $293$ ,  $408$  and  $498\text{ cm}^{-1}$ , can be identified, or if it can be determined that the other band in the spectrum of rutile, with a shift of  $451\text{ cm}^{-1}$ , is not present.

### **3.6.3 Hydrated calcium sulphates**

In order to differentiate between the spectra of gypsum, bassanite and anhydrite, a spectral range from  $200$  to  $3600\text{ cm}^{-1}$  is necessary. A resolution of less than  $2\text{-}3\text{ cm}^{-1}$  is also required, so that the slight shifts in the position of the  $\nu_1$  band that result from varying the level of hydration can be observed. This is particularly important when investigating samples that contain multiple components, such as gypsum and bassanite, where the bands appear as a doublet, or high intensity band with a weaker shoulder.

### 3.6.4 Bacterially colonised evaporite

In the Raman spectrum of the carotenoid, the positions of the bands,  $\nu_1$  and  $\nu_2$ , depend on the length of the conjugated chain (see Figure 3.10 for an example), or in other words the number of carbon-carbon double bonds in the primary carbon chain. The longer the conjugate chain, the lower the Raman shift at which  $\nu_1$  and  $\nu_2$  will appear, with  $\nu_1$  experiencing a more dramatic shift (Marshall and Olcott Marshall, 2010). Ideally, calibration of this shift would allow different carotenoids to be identified based on their Raman spectra. Considering the spectra presented in Figure 3.9, the  $\nu_1$  shift is measureable, even with the limitations of the flight-representative spectrometer used. It could be inferred that the carotenoids responsible for the red, pink and purple colouration are based on longer conjugate chains than the green and orange pigments.

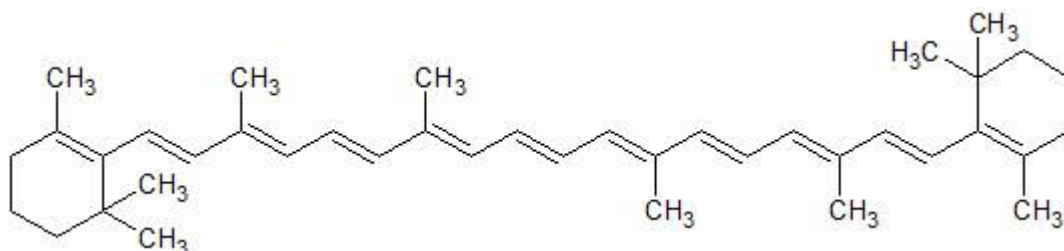


Figure 3.10: A molecular diagram of  $\beta$ -carotene, a carotenoid with a 19-bond conjugated chain.

There are however other situations that would cause electron delocalisation within carotenoid molecules, causing unrelated shifts in the bands in the carotenoid spectrum. The positions of  $\nu_1$  and  $\nu_2$  can vary according to the host matrix. In other words, variation will be observed between the spectra of a pure carotenoid sample, and that of a carotenoid in an inorganic matrix, such as a geological substrate or that same carotenoid in living tissue. Furthermore, inter-carotenoid interactions can significantly affect their molecular properties and therefore their spectra (de Oliveira *et al.*, 2010). Carotenoid bonding within the biomass can cause the delocalisation of electrons that can cause the  $\nu_1$  band position to shift. This problem is exacerbated when carotenoids are in solution, as they are extremely hydrophobic and therefore tend to crystallise in solution, increasing inter-carotenoid interaction (Jehlička and Oren, 2013a). Finally, small shifts in band positions can occur following molecular conformation, isomerism and substitution of the terminal group in the molecule, however these shifts are too small to observe with most instruments.

As a result of the challenges in analysing carotenoid spectra, unambiguous identification of particular carotenoids with the RLS instrument will likely not be possible. Large differences in chain length could be detected by large shifts in band position, so long as the instrument used is capable of a spectral resolution of at least  $3\text{ cm}^{-1}$ . However, carotenoids with similar structures are certainly not as easy to differentiate (Jehlička and Oren, 2013a). It will therefore be necessary to utilise other analytical techniques if the identity of a particular pigment is required. Particularly useful techniques for pigment identification are chromatography (Jehlička *et al.*, 2013) and optical imaging (Jehlička *et al.*, 2014). Techniques such as these do require large amounts of test material to be isolated from their natural environment, which will not be achievable by a remote mission, but will require sample return or astronaut deployment for laboratory analysis. However, Raman spectroscopy still provides a rapid, non-destructive method of detecting carotenoids at extremely low concentrations in a range of host matrices, making it a powerful tool for remote planetary astrobiology.

### 3.6.5 Recommendations

The volume and mass budgets of space missions are extremely restrictive, however a number of recommendations regarding the minimum advisable specification of a Raman system can be made based on this work. A spectral resolution of at least  $3\text{ cm}^{-1}$  is required to ensure that key diagnostic bands from the demanding samples presented in this chapter are all discernible and correctly assigned. This resolution must be maintained over the entire spectral range, which should cover Raman shifts from  $100\text{ cm}^{-1}$  to  $4000\text{ cm}^{-1}$ , enabling unambiguous mineral identification using the fingerprint region at low wavenumbers, and observation of the stretch modes of water at high wavenumbers.

As has already been discussed, the ExoMars rover will be crushing samples obtained by the drill prior to analysis by the instruments in the ALD. This is necessary preparation for some instruments, however it is unfortunate for RLS, as such sample preparation is not required for Raman spectroscopy, but it will result in the loss of spatial information. This is significant for many of the samples investigated in this chapter, including the partially oxidised carbonaceous mudstone and the desert varnish samples. It is recommended that future planetary Raman instruments are able to study unprepared samples, ideally in addition to also studying crushed samples to provide maximum

information. The SHERLOC Raman instrument for example, due for inclusion on the arm of NASA's Mars 2020 rover, will be used to scan across the surface of rocky outcrops, and so will be able to provide two dimensional maps for Raman information.

Some materials readily produce strong Raman spectra, however others are weak Raman scatterers. As has been seen in this chapter with the haematite in the mudstone, and with some of the minerals observed in desert varnishes, certain materials require more spectra in order to make a positive identification. It is currently unclear how many spectra will be obtained from a given sample by the RLS instrument, however it is recommended that this is at least 20, although as many as possible should be acquired. This will enable the detection of weak Raman scatterers in relatively low concentrations. It is also important that detection limits are comprehensively modelled, so that it is understood what a negative detection means for possible low concentrations of materials that could still be present but unseen. Finally, if possible it is recommended that there be opportunity built into the mission for spectra to be analysed, before acquiring further spectra of the same sample if initial results prove interesting.

### **3.7 Future work**

This is by no means a comprehensive list of all possible sources of confusion or ambiguity when analysing geological Raman spectra. Prior to the deployment of the first Raman spectrometer on Mars, or any other planetary body, it will be important to construct a more complete database of situations similar to those presented here. To this end, future work will focus on expanding the work in this chapter to cover more minerals of interest for Mars and planetary exploration, refining the recommendations given in §3.6.5.

Given the interest in hydrated minerals and the subtle differences between the calcium sulphate spectra discussed in §3.4, one example of a set of minerals worth investigating in further detail is the magnesium sulphate minerals. Like their calcium-containing counterparts, magnesium sulphates exist in a range of different hydration levels and are known to be relatively abundant on Mars.

### **3.8 Summary**

Raman spectra have successfully been acquired from a range of Mars analogues, using portable, and in some cases, flight-like Raman spectrometers. Representative rock

matrices, metal mineral inclusions, hydrated minerals and biomarkers have all been investigated. In each case, there is the significant potential of misassignment of spectral bands, given the reduced capabilities of portable Raman instruments, if sufficient care is not taken over the analysis.

The study presented in this chapter shows that it is possible to misassign haematite as reduced carbon, especially when neither the low frequency bands, nor the carbon D band, appear in the spectrum of a sample containing both minerals. In this case, great care must be taken in the measurement of the Raman shift of the second order haematite band, in order to demonstrate that it does not belong to the spectrum of reduced carbon.

Similar care must be taken when studying samples containing both haematite and anatase. The spectra of both minerals contain three, similarly positioned bands that can only be distinguished if the spectral resolution of the spectrometer used is sufficient, although corroboratory bands can be detected if its spectral range extends to low enough wavenumbers. Ideally, an instrument with a lower spectral limit of around  $100\text{ cm}^{-1}$  should be used so that the  $151\text{ cm}^{-1}$  band can be detected, however if this is not possible, precise measurement of the other bands should be sufficient.

It has additionally been demonstrated that calcium sulphates of varying levels of hydration can be distinguished by their Raman spectra, as long as the Raman system used has a spectral resolution of only a few wavenumbers, and a spectral range from  $200\text{ cm}^{-1}$  to at least  $3600\text{ cm}^{-1}$ . This ensures that all bands in the spectra of gypsum, bassanite and anhydrite will be detected and that shifts caused by varying the hydration level can be reliably verified.

Finally, due to the large number of variables that can affect the Raman spectra of carotenoids, it is not possible to use a carotenoid spectrum to identify the exact carotenoid that it belongs to. In carefully controlled circumstances, it is however possible to differentiate between carotenoids with conjugate carbon chains of significantly different lengths, by observing the band shifts that this causes.

Future work will involve investigating more potential sources of confusion when analysing planetary Raman spectra. A database of such examples and how to avoid misassignment of bands must be produced prior to the deployment of the first Raman spectrometer on Mars, or any other planetary body.

## Chapter 4

# Differentiation of distinct populations of reduced carbon

---

In the search for signs of life on Mars, molecules or minerals must be identified that act as biomarkers, either indicating the presence of extant living organisms, or recording the influence of long extinct, ancient life. Such biomarkers must be robust, persisting in the Martian environment for sufficient time to be detectable by the scientific instruments employed by astrobiological missions. Reduced carbon may be a suitable biomarker if its biogenicity can be determined, however its large number of abiotic sources makes such analysis difficult. Nevertheless, the detection of reduced carbon on Mars, or on any other planetary body, is a vital step in the search for signs of life, as its presence is a good indicator of a viable habitat. This chapter aims to determine whether Raman spectroscopy is an appropriate analytical technique for the analysis of reduced carbon, and what conclusions can be drawn from its presence.

### 4.1 Forms of carbon

In terms of molecular bonding, carbon is the most versatile known element. Carbon atoms can be tetra-, di- or monovalent, which means that they can bond with up to four other atoms, forming single, double or triple bonds. Carbon is also self-linking, which means that carbon atoms readily bond with other carbon atoms and can form much longer chains and larger structures than other elements (Walsh, 1947; Benfey, 1958).

These properties enable carbon atoms to form the basis of a wide range of different molecules and therefore molecular materials.

#### 4.1.1 Diamond

Diamond is a crystalline material, whose molecular structure consists of tetrahedrally arranged carbon atoms (Figure 4.1). It is the hardest known naturally occurring mineral on both the Mohs and Vickers hardness scales. The bonding orbitals in diamond are  $sp^3$  hybridised, which means that the 2s and 2p valence orbitals associated with each carbon atom have been mixed, producing four covalent bonds of equal strength and bond angle. Diamond is formed at extremely high pressures (a minimum of  $5 \times 10^9$  Pa) and temperatures (a minimum of 1500 K), which are achieved on Earth by burial at depths of at least 140 km. The Raman spectrum of  $sp^3$ , or diamond-like carbon (Figure 4.1) includes a single strong first order band at  $1332 \text{ cm}^{-1}$  (Prawer and Nemanich, 2004).

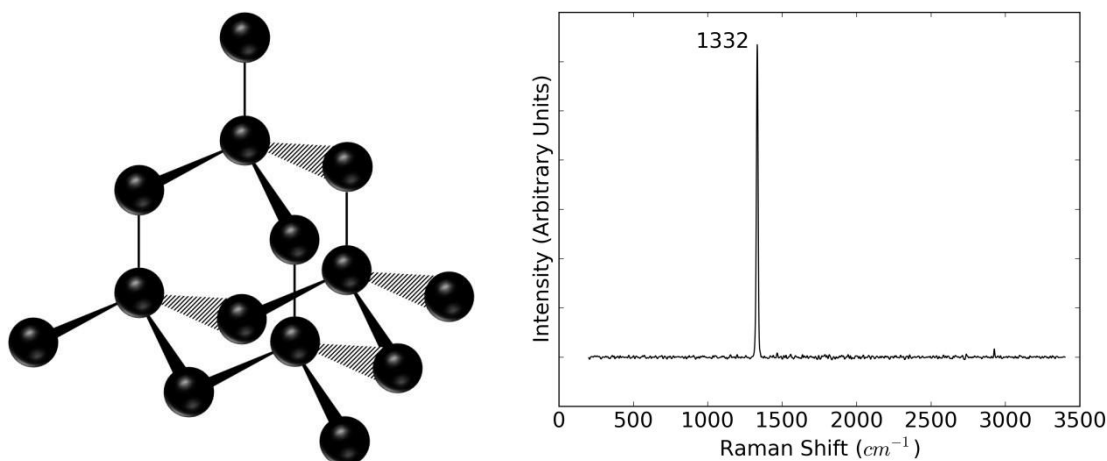


Figure 4.1: Left: Tetrahedral molecular structure of diamond, where each black sphere represents a carbon atom. Right: Raman spectrum of diamond.

#### 4.1.2 Graphite

Graphite is the most stable form of carbon, made up of stacked layers of  $sp^2$  hybridised carbon atoms (Figure 4.2), a single layer of which is known as graphene. Each carbon atom forms covalent bonds with three other carbon atoms in a planar configuration, using free electrons from the 2s orbital and two of the 2p orbitals in its valence shell. The remaining free electrons are delocalised, allowing them to move freely in any direction parallel to the planes of carbon atoms, giving graphite its electrical conductivity properties. Individual graphene layers are bonded together to form graphite by the van der Waals force.

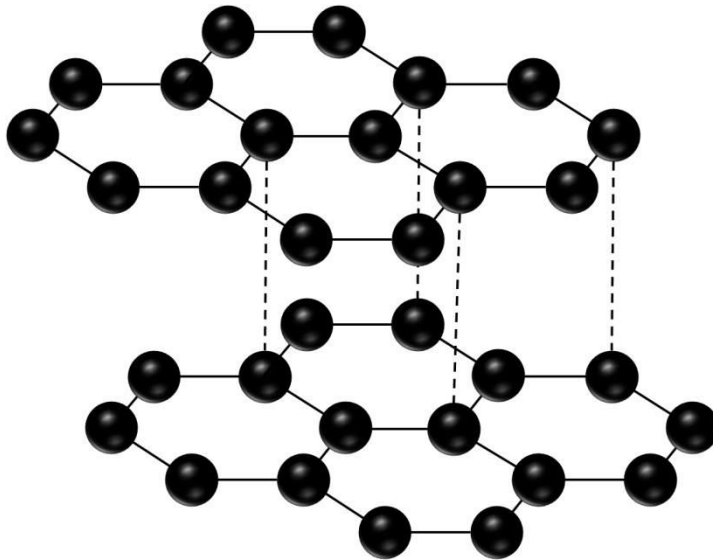


Figure 4.2: Planar molecular structure of graphite, where each black sphere represents a carbon atom, solid lines represent covalent bonds and dashed lines represent van der Waals bonding.

The Raman spectrum of perfect crystalline graphite has a single band with a Raman shift in the range  $1575\text{-}1600\text{ cm}^{-1}$ , which has been designated in the literature as the carbon G band (Cuesta *et al.*, 1994; Ferrari and Robertson, 2000). The G band results from the in-plane stretching of C-C bonds in the graphite lattice (Figure 4.3) (Ferrari and Robertson, 2000). A perfect graphite crystal is assumed to be infinitely large, but whilst real samples must have a finite crystal size, an ideal graphite spectrum (Figure 4.3) may be obtained from crystals which are sufficiently large.

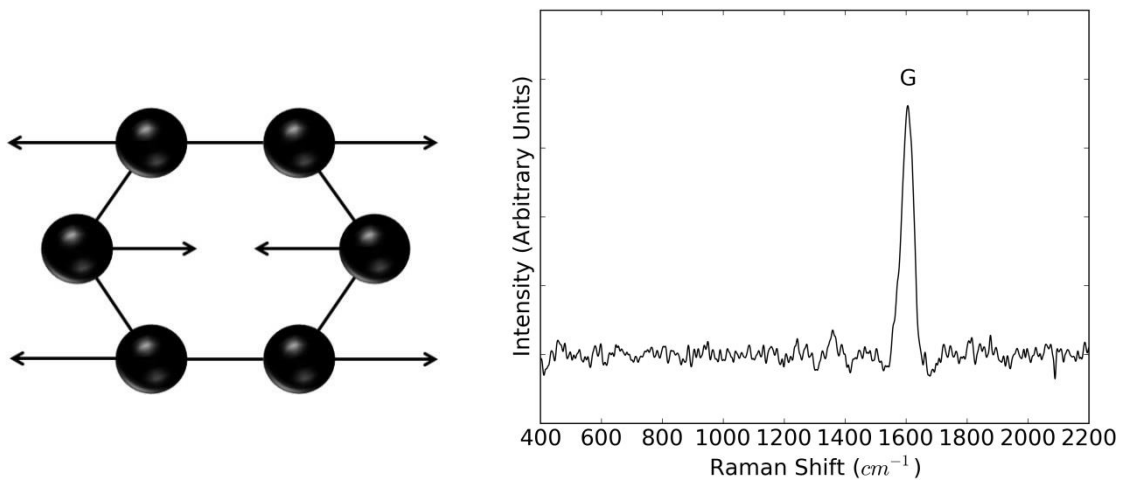


Figure 4.3: Left: Schematic of C-C stretching in a graphite ring. Right: Raman spectrum of graphite exhibiting the carbon G band.

### 4.1.3 Amorphous carbon

Amorphous carbon (Figure 4.4) describes all carbonaceous material (CM) that contains a mixture of  $sp^2$  and  $sp^3$  hybridised orbitals. The bonds between the carbon atoms in specimens of amorphous carbon are of irregular lengths and there are a significant

number of dangling bonds, which result in intra-molecular voids and also irregular bond angles. Amorphous carbon has a number of natural forms and sources, but generally results from the decomposition or oxidation of organic compounds (Thrower, 1996).

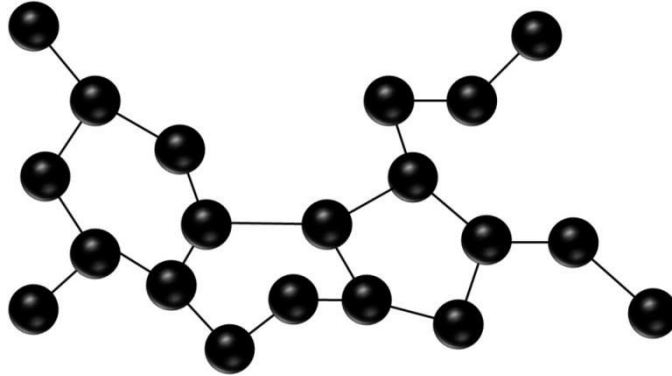


Figure 4.4: An example of the irregular molecular structure of amorphous carbon.

#### 4.1.4 Reduced carbon

Reduced carbon is CM composed of nanocrystalline,  $sp^2$  hybridised, or unsaturated carbon. It is also known as nanocrystalline graphite, as it is composed of small graphite crystals with varying diameters (Figure 4.5). It is a macromolecular form of carbon that results from the geothermal processing of residual hydrocarbons from both abiotic and biotic sources, otherwise known as organic debris. Such debris must be buried, placing it at extremely high temperatures and pressures, causing graphitisation of hydrocarbons. This involves the removal of functional groups to first produce amorphous carbon, then hydrogen atoms to produce larger and more complex aromatic structures, increasing the level of order of the CM, with perfect crystalline graphite as the eventual end-point (Buseck and Huang, 1985). CM from any point in the metamorphosis from amorphous carbon to graphite is described as reduced carbon, so the term covers carbon with widely varying levels of thermal maturity and therefore order.

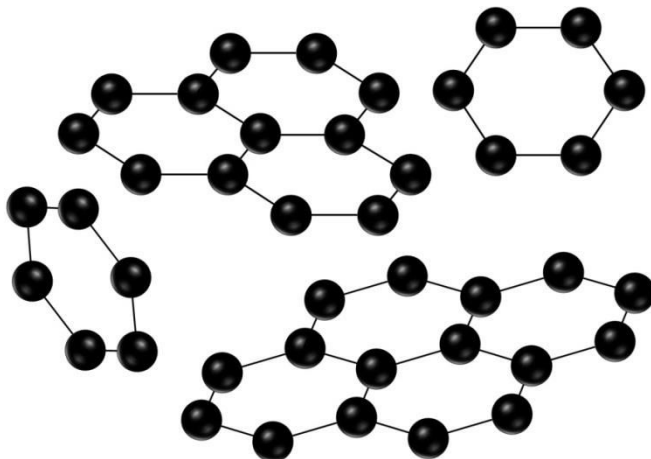


Figure 4.5: An example of the molecular structure of reduced carbon, or nanocrystalline graphite.

**4.1.4.1**            **Relevance to the search for life**

Living organisms synthesise a multitude of organic compounds that are vital to life processes and in the case of extremophiles, to survive harsh environmental conditions, such as extremes of salinity, UV exposure, temperature, pressure, acidity or dehydration. These organic molecules could be buried and geothermally processed as described in §4.1.4, producing reduced carbon. Reduced carbon might therefore be a remnant of life, although given the geological time required for the metamorphosis of organic debris, those organisms from which it originated could be long extinct.

Reduced carbon does have a number of abiotic sources. It has been detected in a number of confirmed meteorites (Sephton, 2002) and many have theorised that significant quantities could be delivered to planetary surfaces by meteoritic impact (Chyba and Sagan, 1992). Large quantities of reduced carbon are also produced by magmatic action and incorporated into rocks associated with volcanic activity, such as igneous basalts (Steele *et al.*, 2012).

It is not possible to determine the biogenicity of reduced carbon using Raman spectroscopy alone (Pasteris and Wopenka, 2002; Pasteris and Wopenka, 2003; Marshall *et al.*, 2010). Nevertheless, the detection of reduced carbon on Mars, even that with an abiotic source, would be an extremely significant result. Abiotic reduced carbon would still provide microbial life with a source of elemental carbon for use in biochemical synthesis, so could therefore indicate potential habitats where life might be able to thrive. Such habitats could then be investigated further using additional analytical techniques, which are more time-consuming than Raman spectroscopy and in some cases destructive, but that may be capable of determining biogenicity. For example, isotope-ratio mass spectrometry can be used to measure the isotope ratios of carbon and oxygen in aragonite, elucidating its biogenicity (Grossman and Ku, 1986).

**4.1.4.2**            **Raman spectrum**

The Raman spectrum of reduced carbon presents two particularly strong primary bands, the first of which is the carbon G band, described in §4.1.2 and shown in Figure 4.3, with a Raman shift of between 1575 cm<sup>-1</sup> and 1600 cm<sup>-1</sup>.

The second band in the Raman spectrum of reduced carbon is designated the carbon D band. It results from the breathing mode of six-fold aromatic rings of sp<sup>2</sup> carbon atoms

(Figure 4.6), which means that it does not occur in the spectrum of perfect crystalline graphite. It is associated with the level of disorder in reduced carbon, since as disorder increases, reduced carbon looks less like perfect graphite, contains more distinct aromatic rings and so D band intensity increases (Cuesta *et al.*, 1994). The D band is excitation wavelength dispersive, its spectral position shifting to lower wavenumbers as excitation wavelength is increased. The band appears at Raman shifts of between  $1310\text{ cm}^{-1}$  and  $1410\text{ cm}^{-1}$  in response to respective excitation wavelengths in the range 782 nm down to 351 nm (Wang *et al.*, 1990; Matthews *et al.*, 1999). In response to 532 nm excitation, the carbon D band has a Raman shift of  $1350\text{ cm}^{-1}$  (Figure 4.6).

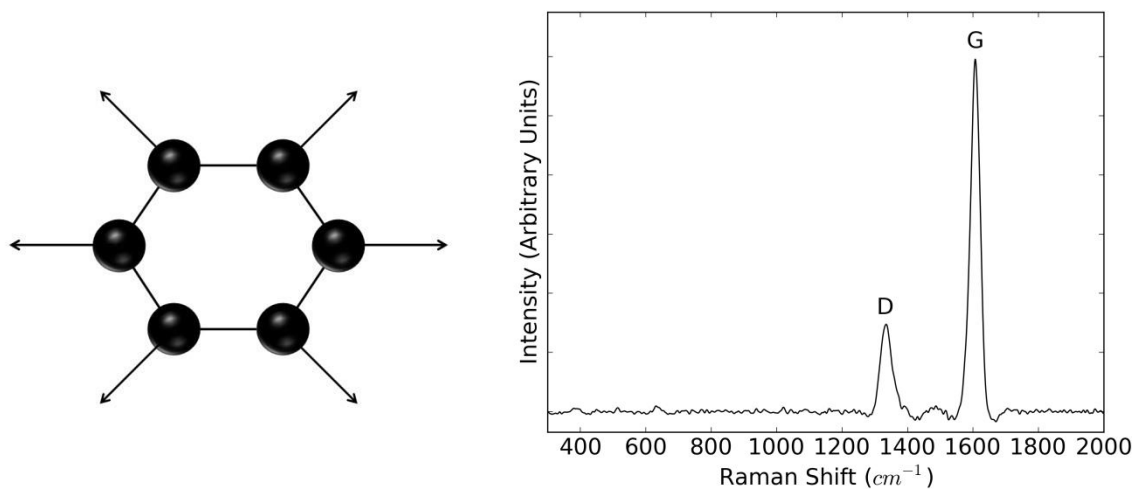


Figure 4.6: Left: Schematic of the breathing mode of aromatic carbon. Right: Raman spectrum of reduced carbon exhibiting the carbon D and G band.

## 4.2

### Modelling the uncertainty in spectral measurements

In order to quantitatively analyse Raman spectra of reduced carbon, measurements of spectral parameters such as the positions and widths of Raman bands can be made (see §4.3.3 for an example of this). Such parameters are susceptible to uncertainty induced by noise, as well as by analysis techniques such as background subtraction. In order to determine the magnitude of the measurement uncertainty caused by noise and therefore the minimum SNR is required for quantitative analysis, the background signal and noise in a Raman spectrum have been modelled.

The fluorescence background was modelled by fitting a polynomial to the background signal of an experimentally acquired spectrum. The model allowed each coefficient of the polynomial to vary randomly, according to a Gaussian probability distribution centred at its fitted value, in order to generate random background profiles (an example

profile appears in Figure 4.7). A single Gaussian, with a mean of  $1600\text{ cm}^{-1}$  and a FWHM of  $50\text{ cm}^{-1}$ , was superimposed onto this background to model a Raman band. Noise was added to the spectrum by replacing each intensity with a new value drawn from a Gaussian distribution, centred at  $n$  and with a value of  $\sigma$  equal to  $\sqrt{n}$ , where  $n$  is the initial intensity value.

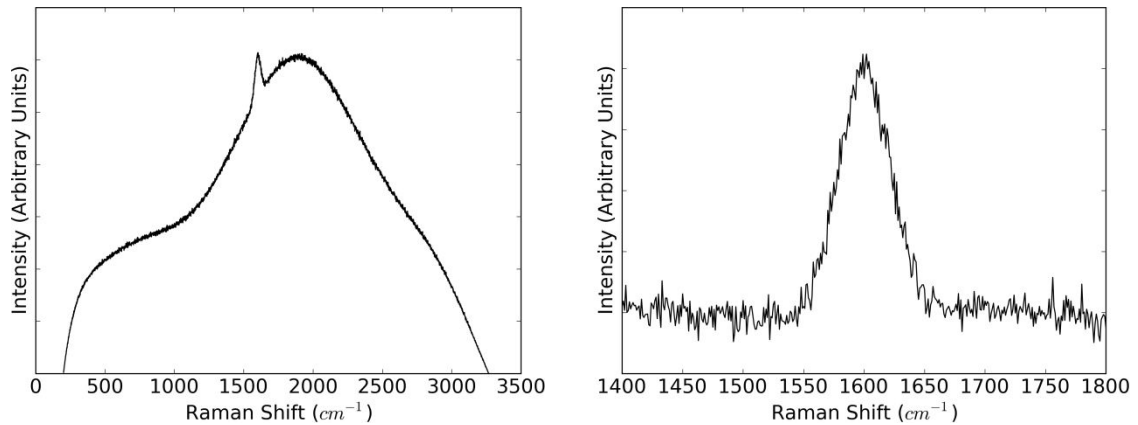


Figure 4.7: Left: A model Raman spectrum with a fluorescence background, a band at  $1600\text{ cm}^{-1}$ . Right: A close-up of the band, following the subtraction of a quadratic fit to the background.

Background subtraction was performed on model spectra by fitting a polynomial to the background in a narrow window around the band, producing reduced spectra (e.g. Figure 4.7). Band position and width were measured in simulated spectra and the standard deviation from the mean of each set of measurements was calculated to determine the measurement uncertainties. This was repeated for spectra generated with a range of band intensities, and therefore SNRs, in order to determine measurement uncertainty as a function of SNR (Figure 4.8).

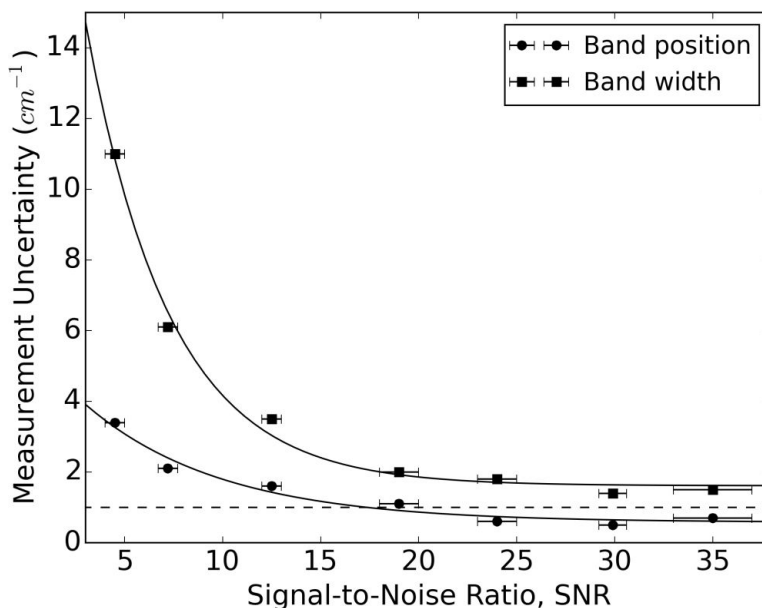


Figure 4.8: Uncertainty on measurements of band position and width, as functions of signal-to-noise ratio. The horizontal dashed line indicates a measurement uncertainty of  $1\text{ cm}^{-1}$ .

Figure 4.8 shows that as SNR increases, measurement uncertainty decreases following the curve fit to the data. Uncertainty in band position measurement falls below  $1 \text{ cm}^{-1}$  for SNRs of greater than 17.4, therefore ideally, Raman spectra should have a minimum SNR of at least this if spectral parameters such as band position are to be determined. Figure 4.8 also shows that whilst measurement uncertainty continues to improve with SNR, the rate at which this occurs slows, so a greater SNR may not be necessary.

### 4.3 Nakhla meteorite analogue

The following subsection describes an investigation of a terrestrial Mars analogue rock sample, selected for study due to the hypothesis that it contained multiple populations of reduced carbon originating from distinct sources. The first aim of this work was to determine if it is possible to detect very low concentrations of reduced carbon in natural rock samples, using a portable, flight-representative Raman spectrometer. The second goal was to establish whether different reduced carbon populations within the same sample could be differentiated based solely on their Raman spectrum.

#### 4.3.1 Rock sample

A sample of rock (Figure 4.9) was obtained from a field site in Helen's Bay, County Down, Northern Ireland (Irish Grid Reference J459831) as an analogue of the Nakhlite class of Martian meteorites (Treiman, 2005). The sample was retrieved from a region of exposed basaltic lava (Sharpe, 1970; Craig, 1984), cross-cut with millimetre sized carbon-rich, quartz veinlets. Small portions of the rock were crushed, producing grains with a range of scale sizes from  $250 \mu\text{m}$  to  $300 \mu\text{m}$ , representative of the crushed samples that will be produced by the ExoMars rover SPDS (Schulte *et al.*, 2008).



Figure 4.9: Photograph of a terrestrial rock obtained from a field site in Helen's Bay, County Down, Northern Ireland, selected as an analogue of the Nakhlite class of Martian meteorites. The lighter coloured regions on the top surface are carbon-rich, quartz veinlets that cross-cut the rock.

### 4.3.2 Acquisition of Raman spectra

The 532 nm benchtop Raman spectrometer, described in Chapter 2, was used to study the analogue sample from Helen's Bay. Three separate targets of interest were identified, following a visual inspection of the unprepared rock specimen. These were the carbon-rich quartz veinlets, one of the light grey rock surfaces and another black surface. Each of these target areas were randomly sampled with the Raman instrument on the surface of the unprepared rock sample to produce approximately twenty Raman spectra, integrating for between 20 seconds and 60 seconds, ensuring that the full dynamic range of the detector was used in order to maximise SNR. Further to this, a crushed sample of the rock was prepared following a procedure analogous to the ExoMars SPDS. All of the spectra presented here originate from the solid rock sample, however this analysis made it possible to identify the same spectra amongst those obtained from the crushed sample. This demonstrated that it will be possible to achieve similar results on Mars, when the RLS instrument obtains Raman spectra from samples crushed by the ExoMars SPDS.

Calcite and haematite were both detected in the Helen's Bay analogue. Calcite was clearly indicated by bands at  $287\text{ cm}^{-1}$ ,  $716\text{ cm}^{-1}$  and  $1088\text{ cm}^{-1}$  (Figure 4.10c) (Jorge Villar and Edwards, 2006), enabling its differentiation from aragonite and vaterite, the other polymorphs of calcium carbonate ( $\text{CaCO}_3$ ) (Kontoyannis and Vagenas, 2000). The Raman spectrum of aragonite includes strong bands at  $701\text{ cm}^{-1}$  and  $1084\text{ cm}^{-1}$ , and the spectrum of vaterite exhibits a doublet at  $740\text{ cm}^{-1}$  and  $751\text{ cm}^{-1}$  and a triplet at  $1075\text{ cm}^{-1}$ ,  $1081\text{ cm}^{-1}$  and  $1090\text{ cm}^{-1}$  (Gauldie *et al.*, 1997). The presence of haematite was not as clearly marked, as the only band that was easily discernible was that at  $1324\text{ cm}^{-1}$  (Figure 4.10d). Haematite is a relatively weak Raman scatterer, so the other bands expected to be present in its spectrum are likely swamped by background fluorescence and other inelastic scattering effects other than Raman. However, as discussed in Chapter 3, the second order band is sufficiently indicative of its presence.

### 4.3.3 Reduced carbon analysis

Figure 4.10a shows a Raman spectrum of reduced carbon, with the carbon D band at  $1336\text{ cm}^{-1}$  and G band at  $1607\text{ cm}^{-1}$ . Figure 4.11 shows a comparison of the G band in spectra from the quartz veinlets, the bulk rock and from a control sample of similar basalt from Dounan's Point, Scotland, that does not contain reduced carbon. This shows

qualitatively that band morphology varies, motivating a statistical, quantitative comparison. In order to make precise measurements on the G band, it was first necessary to subtract the background from the spectrum. Some methods of background subtraction or reduction were discussed in Chapter 2, however in this case it was not necessary to reduce the background across the entire spectral range, but just in the region around the G band. It was assumed that over such a small wavenumber range the background is approximately linear, so a linear fit was made to points either side of the band and this fit was subtracted.

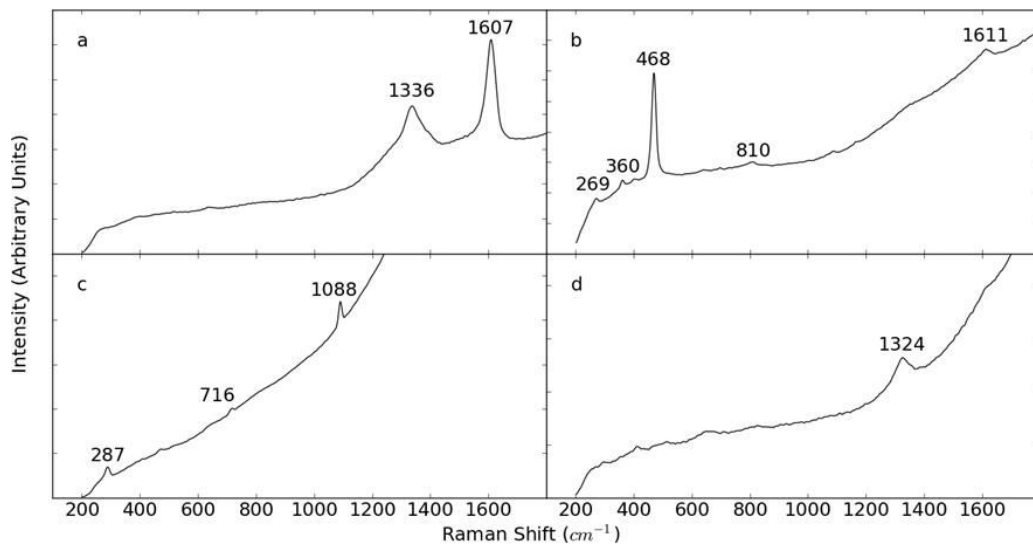


Figure 4.10: Unmodified Raman spectra from the Helen's Bay analogue sample. (a) Reduced carbon. (b) The strong band at  $468\text{ cm}^{-1}$  and the weaker ones at  $269\text{ cm}^{-1}$ ,  $360\text{ cm}^{-1}$  and  $810\text{ cm}^{-1}$  indicate the presence of quartz, whilst the band at  $1611\text{ cm}^{-1}$  is the carbon G band. (c) Calcite. (d) Haematite. Figure reproduced from Parnell *et al.*, 2014.

With the background modelled and subtracted, the centroid position of the G band in each spectrum could be calculated and its FWHM measured. These variables were plotted against each other on a cross-plot, which provides simple principle components analysis (Figure 4.12). Datapoints representing reduced carbon spectra from the quartz veinlets, and those acquired from elsewhere on the rock surface, clearly resolve into two distinct populations, with a statistically significant separation between the population means. This suggests that these carbon populations originate from separate sources and have experienced different thermal histories, making this differentiation possible.

The red triangles seen in Figure 4.12 originate from a paper by Steele *et al.* (2012), and represent Raman spectra obtained from carbonaceous Martian meteorites. They are provided for reference, although it is not possible to know precisely how this analysis was performed, so these datapoints and the ones obtained from the Helen's Bay sample

may not be comparable. Atmospheric entry may also have significantly modified the carbon in the meteorites, making the data less useful for assessment of the appropriateness of the Helen's Bay sample as an analogue. Nevertheless, the random distribution of these points shows that Martian meteorites contain carbon with a range of different thermal histories, and also possibly suggests that more analogues rich in reduced carbon should be sought, in order to prepare for deployment of RLS more comprehensively.

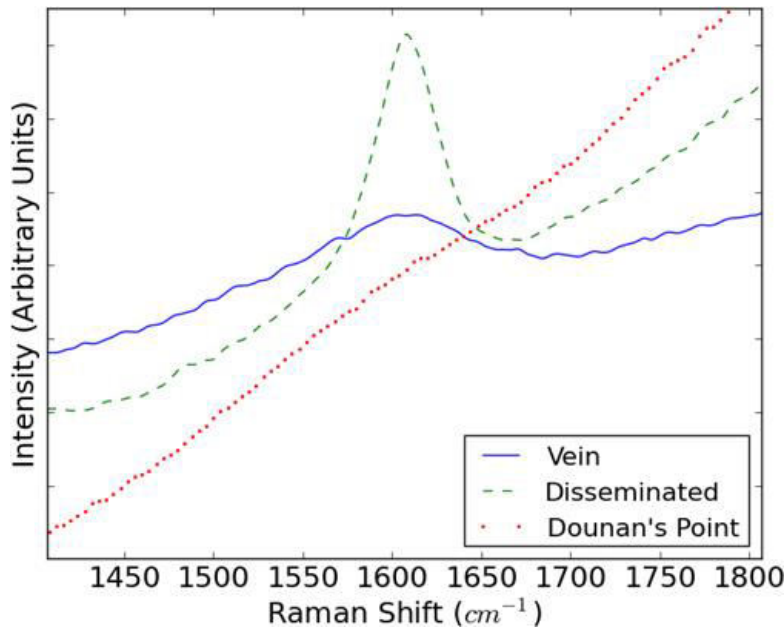


Figure 4.11: Close-up view of the carbon G band in three different Raman spectra. The solid and dashed lines represent two distinct carbon populations in the Helen's Bay analogue sample, found respectively in the quartz veinlets and homogeneously disseminated throughout the rock. The dotted line is typical of the spectra from a similar basalt from Dounan's Point, Scotland, that does not contain reduced carbon. Figure reproduced from Parnell *et al.*, 2014.

Reduced carbon was readily detected using a portable, flight-representative Raman spectrometer, targeting both the unprepared surface of the Helen's Bay analogue and the crushed samples from the same rock. The separation of two reduced carbon populations that is seen in Figure 4.12 is an important result, since it presents the possibility of distinguishing distinct sources of carbon within a single sample. Given the multiple possible sources of reduced carbon that were described in §4.1.4.1, this could be an extremely powerful technique in the analysis of Raman spectroscopic data returned from Mars by RLS or another future Raman instrument.

The successful detection and identification of haematite in yet another Mars analogue sample is also significant, given the mineral's abundance on Mars, and its possible role in the formation of primordial life (Christensen *et al.*, 2001; Arora *et al.*, 2007). According to such a model, iron oxide precursors act as a template for molecular evolution, which is likely a key step in the development of the simplest, single-celled living organisms. As in Chapter 3, care must be taken to successfully identify the

second order haematite band with a Raman shift of around  $1335\text{ cm}^{-1}$ , rather than confusing it with the D band in the spectrum of reduced carbon.

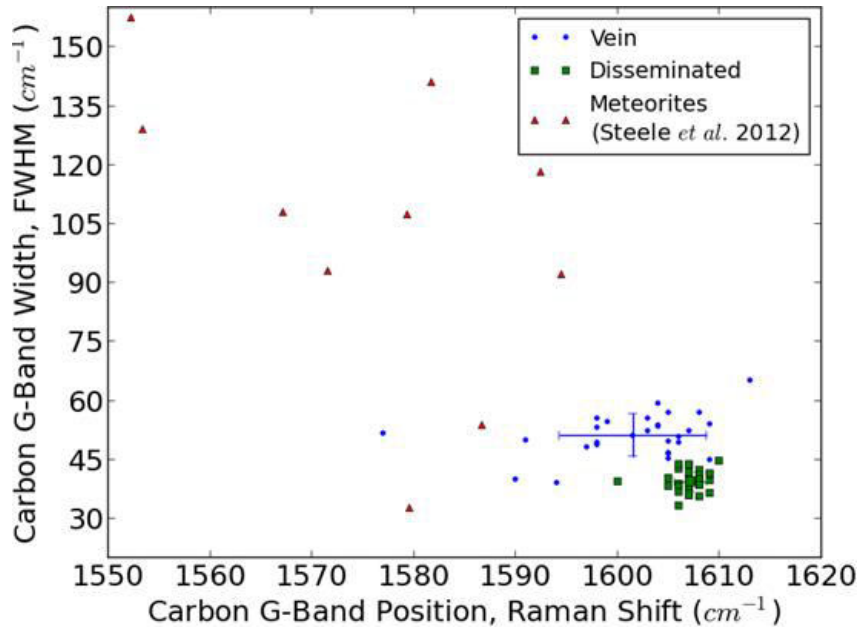


Figure 4.12: Cross-plot showing the centroid position and FWHM of the carbon G band in several Raman spectra acquired from the Helen's Bay analogue. There is clear separation between two carbon populations, one found in the quartz veinlets and the other homogeneously disseminated throughout the rock. The datapoints with error bars represent the mean of each population (note that the error bar for disseminated carbon is very small and obscured by the surrounding datapoints). Points marked by red triangles are representative of data from the Martian meteorites measured by Steele *et al.* (2012) for comparison. Figure reproduced from Parnell *et al.*, 2014.

#### 4.4 Carbon-rich shale samples

The following subsection follows on from the study presented in §4.3, extending the work to the analysis of many similar carbon-rich samples. Given that the previous investigation established that different populations of reduced carbon could be differentiated using Raman spectroscopy alone, the research presented in this subsection was to determine whether Raman spectroscopy could be applied to separate samples that had been identified by other means as having different thermal histories. A secondary goal was to compare the visual assessment of thermal history with information obtained from the Raman spectra acquired.

##### 4.4.1 Rock samples

A total of 21 shale samples were retrieved from a field site near Caithness, Northern Scotland, which is part of the Orcadian Basin. The Basin is a carbon-rich sedimentary basin of Devonian age, which covers a large region of Northern Scotland, the entire of

the Orkney Islands and part of the Shetland Islands, as well as stretching out into the North Sea (Figure 4.13). It contains a non-marine, mixed fluvial-lacustrine succession, in which the lacustrine rocks are rich in organic carbon that has been deposited by algae (Donovan, 1975; Trewin, 1986).

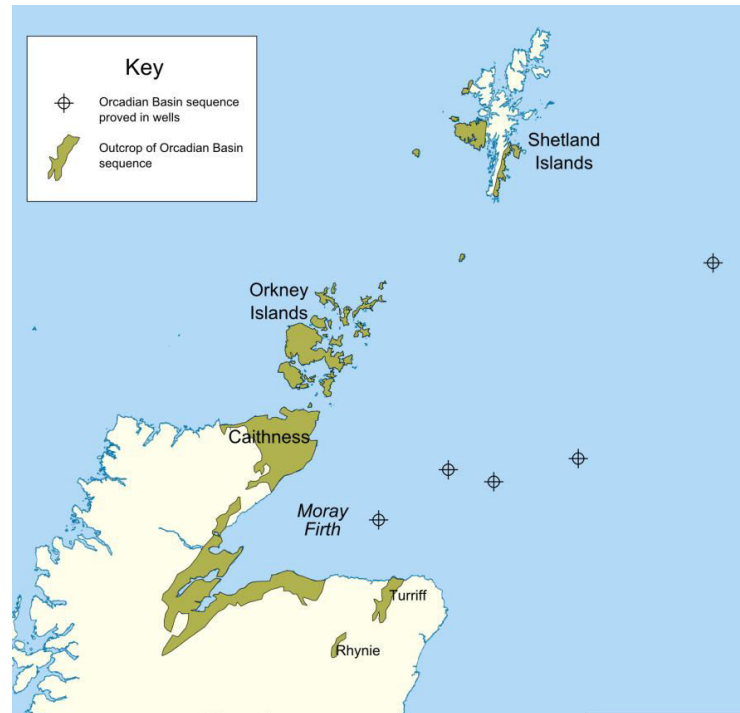


Figure 4.13: Map of Northern Scotland showing the location of the Orcadian Basin, which is marked in green. The target marks in the North Sea are sites that have been drilled and confirmed as part of the Basin. Image credit: M.G. Norton.

The thermal maturity of rocks varies throughout the basin. Thermal maturity is a qualitative measure of the geothermal processing that rock has undergone, with a specimen considered more thermally mature if it has been exposed to greater temperatures and pressures. As a result, rocks of different thermal maturity have also released different quantities of hydrocarbons into their surroundings (Hillier and Marshall, 1992). Most notably, there is a discontinuity in thermal maturity across a major lineament called Brough Fault, where rocks on the Fault's western side are less thermally mature than those to its east.

Figure 4.14 shows a close-up view of the region of the Basin from which the analogue samples for this study were retrieved. The figure also shows how samples in three categories of thermal maturity, designated low, moderate and high, according to Hillier and Marshall (1992), were recovered from different geographical locations. Six samples within each category of thermal maturity were obtained, as well as a further three

samples of red shale. Red shale is shale that has been uplifted following thermal alteration and oxidised, causing the precipitation of iron oxide and therefore a reddening in colour, producing rock similar to the partially oxidised mudstone studied in §3.2. Red shale also has extremely low total organic carbon concentrations.

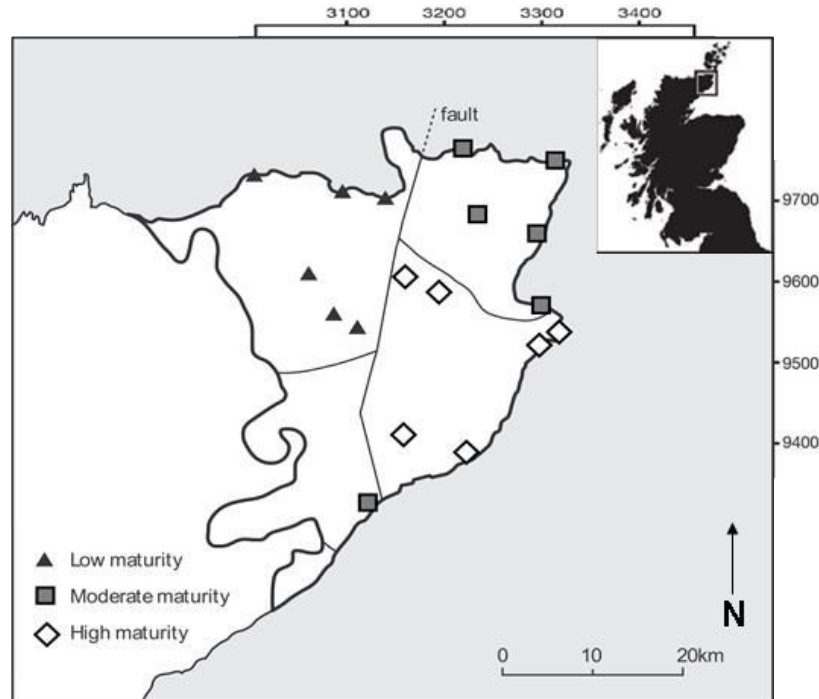


Figure 4.14: Map of the Caithness region of the Orcadian Basin, showing sites from where samples were retrieved and the level of thermal maturity at each site. Figure reproduced from Hutchinson *et al.*, 2014a.

The total organic carbon concentration and extractable carbon fraction of each of the shale samples was independently assessed using an elemental analyser produced by LECO Corporation (St. Joseph, MI, USA) and thin layer chromatography. This information, which is summarised in Table 4.1, can be used to corroborate the initial thermal maturity designations, which were based on sampling site alone. A small specimen of each sample was crushed and labelled ORCRAM1-ORCRAM21, so that a blind study could be conducted. This was important in order to demonstrate the capability of a portable Raman spectrometer in distinguishing between different levels of thermal maturity.

#### 4.4.2 Acquisition of Raman spectra

Powdered samples were placed in cylindrical holders, compacted and flattened using a blade. This method is mechanically equivalent to the way in which the ExoMars SPDS will prepare samples for analysis (Schulte *et al.*, 2008). These flattened surfaces were randomly sampled with the 532 nm, benchtop Raman spectrometer described in §2.3.1.

Tens of spectra were acquired from each sample in order to reduced measurement uncertainties and integration times were selected to make maximum use of the dynamic range of the detector. It is not yet clear how many spectra will be obtained by RLS for a given sample, although a similar number seems achievable and will certainly be required in order to achieve comparable results to these on Mars. Care was taken to ensure that samples were not thermally altered by the laser. In most cases, the best SNR was achieved by slightly defocusing the spectrometer, placing its focal plane above the sample surface. This effect is due to the increase in the size of the illumination and collection cones, increasing the probability of illuminating carbon-rich grains within the powdered material.

#### 4.4.3 Results

Figure 4.15 shows an example Raman spectrum from one of the ORCRAM samples, clearly exhibiting the carbon D and G bands obtained from reduced carbon. Both bands were evident in spectra acquired from all 21 ORCRAM samples, with SNRs of at least 10, clearly indicating the presence of reduced carbon in every sample. Given the information in Table 4.1, this means that reduced carbon was successfully detected down to a minimum total organic carbon concentration of 0.08 %. Also shown is a close-up comparison of the carbon G band in spectra from two of the samples. It is very clear that the mean position of the G band varies from sample to sample and that its width is highly variable, motivating a more careful, statistically robust analysis of these variables across the whole sample set.

The photon counts obtained from ORCRAM17 were extremely low, resulting in a large uncertainty associated with the parameters derived from those spectra. For this reason, ORCRAM17 was not included in the analysis that follows in §4.4.4. Likewise, ORCRAM18 was also not included, due to an extremely high variance in band position between the spectra acquired from different positions on the sample, given that this level of variation was not observed in the other samples. This unusual variation is likely because ORCRAM18 was retrieved from a field site that included multiple sources of carbon with different thermal maturities. These have contaminated the crushed sample, which makes ORCRAM18 an unsuitable sample for this study.

#### 4.4 Carbon-rich shale samples

Table 4.1: Details of the 21 shale samples analysed in this study, including an assessment of thermal maturity based on sampling site, total organic carbon concentration (TOC) and the fraction of this that could be successfully extracted. Table reproduced from Hutchinson *et al.*, 2014a.

Sample ID	Total organic carbon concentration (%)	Extractable carbon fraction (extract/TOC)	Maturity	Comment
ORCRAM1	0.89	0.363	Low	
ORCRAM2	0.16	0.056	Moderate	
ORCRAM3	3.42	0.018	Moderate	Very high TOC
ORCRAM4	0.4	0.015	High	
ORCRAM5	0.52	0.681	Low	
ORCRAM6	0.36	0.333	Low	
ORCRAM7	0.88	0.139	Low	
ORCRAM8	0.53	0.145	Low	
ORCRAM9	0.64	0.264	Low	
ORCRAM10	0.22	0.018	High	
ORCRAM11	0.46	0.004	High	
ORCRAM12	0.33	0.051	High	
ORCRAM13	0.51	0.106	High	
ORCRAM14	0.41	0.020	High	
ORCRAM15	0.95	0.111	Moderate	
ORCRAM16	0.18	0.044	Moderate	(Extract/TOC) high
ORCRAM17	0.8	0.036	Moderate	Low counts in G band
ORCRAM18	0.36	0.036	Moderate	High sample variance
ORCRAM19	0.1	0.100		Red shale
ORCRAM20	0.08	0.025		Red shale
ORCRAM21	0.08	0.050		Red shale

In the spectra from the remaining samples, the G band was significantly more intense than the D band, suggesting that the entire sample set was of relatively high thermal

maturity and therefore almost entirely graphitic. As discussed in §1.3.2.3 however, given the number of variables that affect band intensity and the limitations of miniaturised spectrometers, the measurement of relative intensities here is not considered to be reliable. Instead, the aim of this particular research project was to determine whether other spectral parameters, such as band position and width, also correlated with the thermal maturity of the samples. If such parameters were found, it would then be possible to use these as a proxy for thermal maturity when analysing data returned by future space missions.

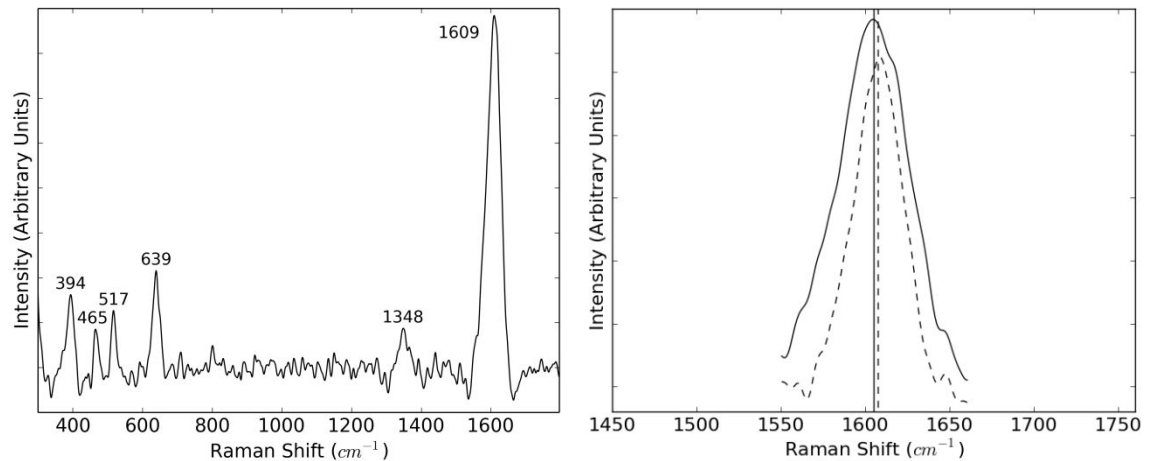


Figure 4.15: Left: Raman spectrum acquired from the shale sample designated ORCRAM11. This spectrum was produced by acquiring 60 spectra at the same location on the sample, reducing their background using Fourier transformation, selecting the 33 spectra with the highest SNR and co-adding these frames. The carbon *D* and *G* bands are both visible, at 1348  $\text{cm}^{-1}$  and 1609  $\text{cm}^{-1}$  respectively. The low frequency bands are indicative of the presence of anatase and quartz in the sample. Right: Close-up of the carbon *G* band in spectra acquired from ORCRAM9 (solid line) and ORCRAM13 (dashed line). The vertical lines represent the centroid positions of the two bands. Figure reproduced from Hutchinson *et al.*, 2014a.

#### 4.4.4 Raman analysis of thermal maturity

The data presented in §4.4.3 demonstrates the ability to detect reduced carbon in powdered rock samples down to concentrations as low as 0.08 %, or 800 ppm. This limit was the lowest concentration measured in this study, however through multi-position sampling and using sufficiently long integration times it is expected that concentrations of reduced carbon as low as 0.008 %, or 80 ppm, could be successfully detected, as suggested by other similar studies (e.g. Wang *et al.*, 2001).

It was suggested by Pasteris and Wopenka (1991) that, like the ratio of *D* and *G* band intensities, the spectral position and width of the carbon *G* band are also dependent on the thermal maturity of a sample of reduced carbon. In order to determine whether this

would hold true for the shale samples under scrutiny utilising a miniaturised Raman spectrometer, the centroid position and FWHM of the G band was measured in each spectrum in the same way as described in §4.3.4. A cross-plot of these variables appears in Figure 4.16.

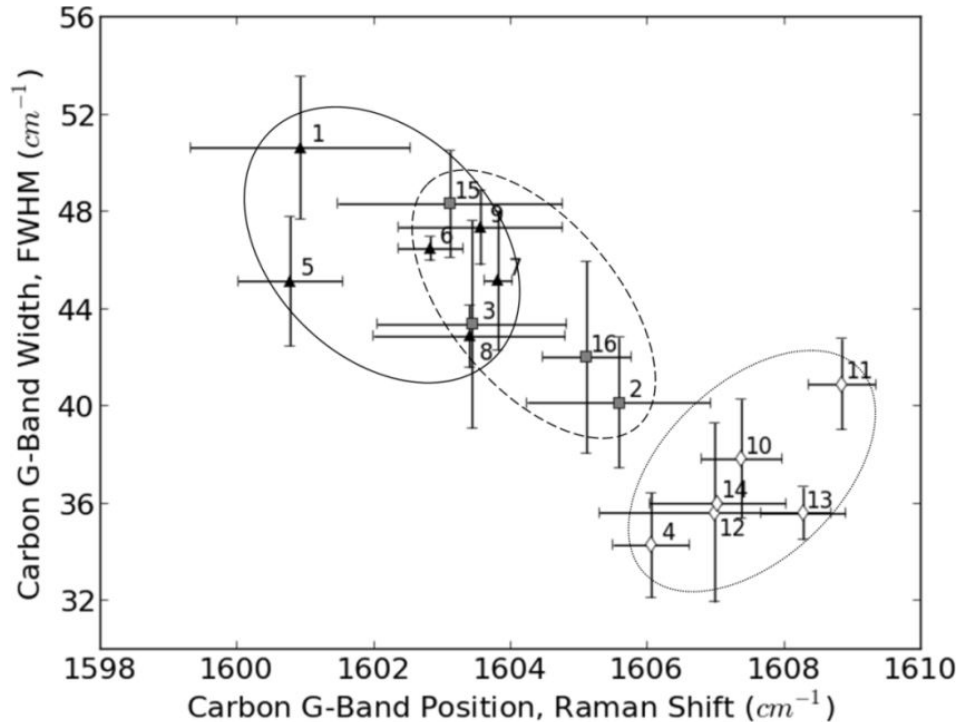


Figure 4.16: A cross-plot of the FWHM of the carbon G band against its centroid position, illustrating clearly separated regions for samples with low (black triangles), moderate (grey squares) and high (white diamonds) levels of thermal maturity, according to the geographical site from which they were retrieved. Figure reproduced from Hutchinson *et al.*, 2014a.

The position and FWHM of the G band in each spectrum, depicted by the cross-plot in Figure 4.16, clearly separate the samples with different levels of thermal maturity. Datapoints representative of samples from each maturity level are clustered together on the cross-plot. This is particularly true of the high thermal maturity samples, ORCRAM4 and ORCRAM10-14, whose spectra have much narrower G bands at much higher Raman shifts, placing them in the bottom right-hand corner of the cross-plot shown in Figure 4.16. The plot also shows that the uncertainties associated with measurements of band width and position are comparable to those calculated in §4.2 by modelling background signal and noise in a Raman spectrum. This shows that the error bars shown in Figure 4.16 are dominated by measurement effects, suggesting that the separation and clustering of datapoints shown on the plot is a genuine sample effect.

There is some overlap between the regions occupied by low and moderate maturity datapoints. However, given that this categorisation was made entirely based on the

geographical location from which the samples were sourced, this was expected. This means that the experiment was a successful demonstration of the use of this analytical technique for distinguishing between populations of reduced carbon with different levels of thermal maturity.

In order to confirm the Raman spectroscopic analysis of these shale samples, extractable carbon fraction data were acquired for each of the samples studied. Such analysis is challenging to accomplish on a space mission, so techniques such as Raman spectroscopy must be relied upon to provide similar information. However, in this case other techniques must be used to verify the thermal maturity categorisation and confirm that Raman spectroscopy will be an appropriate tool for this purpose on planetary missions, proving the process is valid. Consideration of the information provided in Table 4.1, reveals that samples with a high level of thermal maturity have extractable carbon fractions of between 0.004 and 0.106, whereas low thermal maturity samples fall within the range from 0.139 to 0.681. Thus the earlier classification based on sampling site is confirmed. Extractable carbon fraction is plotted against the position of the G band in Figure 4.17, once again demonstrating a clustering of datapoints that makes it possible to distinguish between sources of reduced carbon based on their level of thermal maturity.

The indefinite boundary between the regions occupied by samples of low and moderate thermal maturity in Figure 4.16 still requires consideration. ORCRAM7 and ORCRAM8, both classified as low thermal maturity, appear in the region of overlap. Looking at Table 4.1, the extractable carbon fractions of these samples were measured to be 0.139 and 0.145 respectively. These values are at the lower end of the range for low thermal maturity samples, suggesting that they are the most thermally mature of this group, indicating why they appear close to the moderate thermal maturity samples on the cross-plot.

Of course, this work is in preparation for the deployment of the ExoMars rover and the RLS instrument. It is therefore important that it will be possible to recreate this analysis on Raman spectra acquired by RLS on Mars. Assuming a sufficient number of Raman spectra are acquired from each sample, it will certainly be possible to detect reduced carbon, and measure its spectral parameters. It will then be possible to qualitatively compare the thermal maturity of reduced carbon detected in separate samples, however

this will require some fortuitous sampling, because there is no guarantee that reduced carbon will be present in every sample obtained by the ExoMars drill.

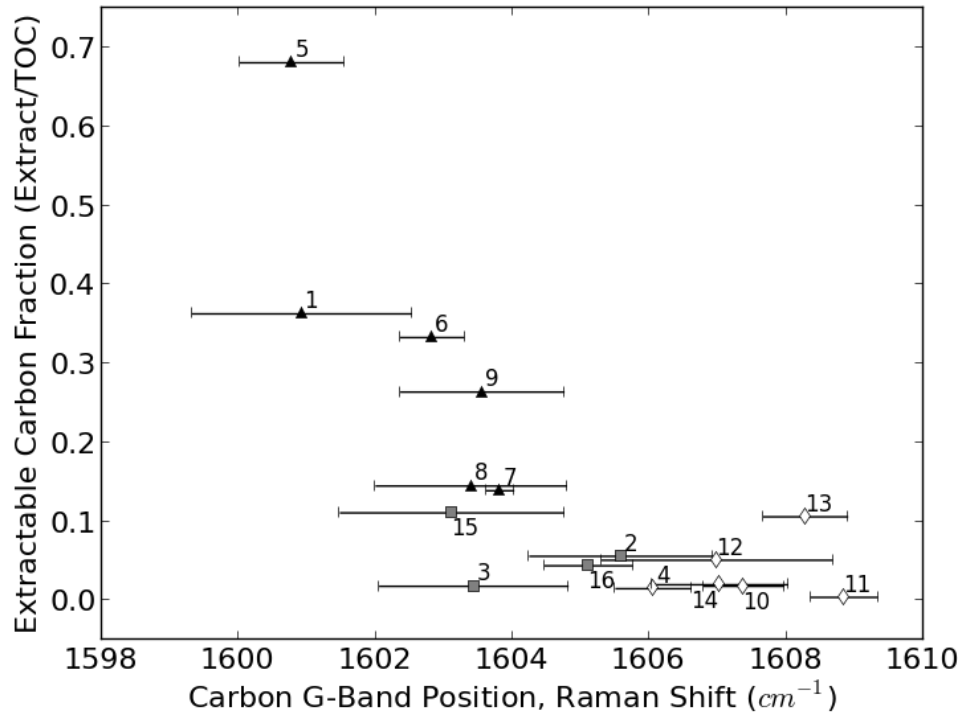


Figure 4.17: Plot of extractable carbon fraction against carbon *G* band position. A general correlation is observed and samples with different levels of thermal maturity are separated into distinct clusters. Low thermal maturity samples are represented by black triangles, moderate by grey squares and low by white diamonds.

#### 4.5 Summary

Quartz, anatase, calcite, haematite and reduced carbon have all been successfully detected by Raman spectroscopy in a basaltic analogue of the Nakhilite class of Martian meteorites. This was accomplished using a 532 nm benchtop Raman spectrometer, functionally representative of the ExoMars RLS instrument. Reduced carbon was identified by the appearance of the carbon D and G bands in spectra acquired from some surfaces of the unprepared rock sample, as well as from a series of quartz veinlets cross-cutting the rock. The organic carbon content of the sample was measured to be 0.15-0.20 wt. %. Furthermore, it has been demonstrated that measurement of the exact position and width of the G band enables the differentiation of the carbon spectra obtained from the different locations, potentially providing a means of distinguishing between distinct populations of reduced carbon. It was concluded that this was due to differences in the thermal maturity of these carbon populations.

A further study was conducted on 21 samples of carbon-rich, Devonian shale, using the same Raman spectrometer. These samples were acquired from separate geographical regions known to have undergone different levels of geothermal processing, therefore the samples were categorised as low, moderate and high thermal maturity, entirely based upon the site from which they were sourced. Reduced carbon was detected in all 21 samples, identified by the appearance of the carbon D and G bands in the Raman spectra obtained from every sample. As with the study of the Helen's bay analogue, the width and position of the G band were measured in each spectrum and plotted on a cross-plot. Datapoints on the cross-plot clustered in this parameter space according to their thermal maturity. This was confirmed by measuring the total organic carbon concentration and extractable carbon fraction of each sample.

It will be possible to perform this analysis on Raman spectra acquired by the RLS instrument in order to detect reduced carbon, infer its thermal maturity and compare this qualitatively between samples obtained in different locations. As discussed in §4.4.2, the success of such investigation on Mars will depend on the number of spectra acquired from each sample, as reduced carbon was not observed in every single spectrum produced by the experiments detailed in this chapter. It is recommended that RLS be used to acquire at least 20 spectra per sample, however even more would be beneficial. It is also recommended that the mission be operated to enable quick analyses to be made, before acquiring more spectra informed by the results of the first set of analysis. This would allow particular grains to be retargeted, or additional spectra to be sought on which to make repeat measurements. The success of the study of reduced carbon on Mars by RLS will also depend on how many samples or investigated which contain reduced carbon, as discussed in §4.4.4. In order to maximise this, the drill should be operated as many times as possible, as it is unlikely that reduced carbon will be detected in advance by any of the other instruments, such as PanCam or WISDOM.

Nevertheless, it has been demonstrated that reduced carbon can be successfully detected using a miniaturised Raman spectrometer, similar to the RLS instrument, which will be deployed on Mars as part of the payload of the ExoMars rover. Furthermore, it has been determined that the position and width of the carbon G band are indicative of a sample's thermal maturity. This means that these spectral parameters can be used to distinguish between multiple populations of reduced carbon, even within the same physical sample.

This will be an extremely useful technique in the analysis of reduced carbon Raman spectra returned from future planetary missions.

## Chapter 5

# Comparison of 532 nm and 785 nm excitation for Raman spectroscopy of reduced carbon

---

Chapter 4 presented reduced carbon as a target of great interest for detection by surface planetary exploration missions, particularly those exploring the surface of Mars. If detected on the surface of another planet, reduced carbon may be a remnant of ancient living organisms (Pasteris and Wopenka, 2003), although it also has a number of abiotic sources, such as magmatic activity (Steele *et al.*, 2012) and meteoritic impact (Chyba and Sagan, 1992; Sephton, 2002). Even if abiotic reduced carbon is detected, it would provide an environmental source of elemental carbon for use in biochemical synthesis by microbial life (e.g. Johnston and Vestal, 1991). It would therefore highlight suitable habitats that could potentially harbour life and so should be investigated further with the full range of analytical instrumentation available to a particular mission.

The research presented in this chapter is focused on determining the optimum configuration and operating modes of portable Raman spectrometers for readily detecting and characterising reduced carbon. A set of specimens of Archean carbonaceous chert were studied using two different flight-representative, portable Raman systems, one utilising 532 nm excitation and the other equipped with a 785 nm illumination source. The responses of these instruments were compared in order to recommend the most appropriate excitation wavelength for carbon analysis.

**5.1**                    **Analogue samples**

Archean chert provides an extensive source of potential carbonaceous Mars analogues. Twelve samples of Archean chert, obtained from the East Pilbara Terrane in Western Australia, were studied as part of this work as they provide an excellent source of ancient reduced carbon. The rock specimens selected represent the geological diversity of the Terrane, sampling the full range of ages and mineralogies that it exhibits.

**5.1.1**                **Archean chert**

Chert is an extremely hard, silica-rich sedimentary rock, which is found as a replacement mineral within other sedimentary rocks, such as dolomite, sandstone and limestone. It forms as a result of the diagenetic alteration of these rocks, the same process that transforms organic debris into reduced carbon as described in §4.1.4. This means that cherts often contain significant concentrations of reduced carbon that can be used to evaluate the extent of the geothermal processing that they have experienced.

As a consequence of the long timescales involved in diagenesis, cherts tend to be relatively old. Many significant chert beds originated in the Cretaceous period (145-66 mya; million years ago), although a few examples of cherts considerably older than this also exist. In fact, some of the oldest rocks on Earth are cherts, with origins as far back as the Archean eon (4000-2500 mya), motivating great interest in their study as probes of ancient geology.

**5.1.2**                **Geological setting**

The Archean cherts studied here were part of the Pilbara Craton, Western Australia, and as such are members of the Pilbara Supergroup (e.g. Van Kranendonk, 2006), a stratigraphic supergroup that includes a wide range of chert and non-chert units. The Pilbara Craton is one of only two known unspoilt Archean chert crusts on Earth, the other being Kaapvaal Craton, South Africa, leading many to suggest that the two locations were once contiguous, prior to tectonic activity (Nelson *et al.*, 1999).

The East Pilbara Terrane, which includes rock aged between 3.53 Ga and 3.17 Ga (gigaannum; 1 Ga = 10<sup>9</sup> years), in the northeast of the Pilbara Craton, includes both the 3.525 Ga-3.427 Ma Warrawoona Group and the much younger Kelly Group (Van Kranendonk *et al.*, 2007). The majority of the Warrawoona Group is the result of

volcanic deposition, however the ca. 3.49 Ga chert-barite Dresser Formation, found in the lower region of the Group, shows evidence of subaerial deposition (Van Kranendonk and Pirajno, 2004; Van Kranendonk *et al.*, 2007; Van Kranendonk *et al.*, 2008). The Apex Basalt, part of the upper Warrawoona Group, contains a layer of stratiform chert that is pierced by syndimentary hydrothermal fracture-fill veins, which are approximately 3.46 Ga old and are informally referred to as the Apex chert (Brasier *et al.*, 2011). Overlying the Warrawoona Group is the distinct Kelly Group, which is separated from the former by a buried erosional surface. The most ancient unit in the Kelly Group is the ca. 3.43 Ga Strelley Pool Chert (Van Kranendonk, 2006; Van Kranendonk *et al.*, 2007).

In the study presented in this chapter, twelve chert samples from the East Pilbara Terrane were studied. Four of these (which will now be referred to as DFM1-DFM4) were from the Dresser Formation, a further five (labelled as AC1-AC5) were from the Apex chert (Marshall *et al.*, 2011; Olcott Marshall *et al.*, 2012; Olcott Marshall *et al.*, 2014) and the remaining three (referred to as SPC1-SPC3) were part of the Strelley Pool chert (e.g., Allwood *et al.*, 2006).

### **5.1.3 Relevance to Mars exploration**

The relevance, in terms of Mars exploration, of studying rock samples rich in reduced carbon has been explored in great detail in §4.1.4.1. Furthermore, as described in §5.1.1, cherts are excellent candidates for such study, since the diagenetic processes responsible for the conversion of sedimentary rock into chert are also responsible for the formation of reduced carbon. The prevalence of sedimentary rock on Mars is well documented (Grotzinger *et al.*, 2011), which also means that there is sufficient progenitor material on the planet for these processes to occur, making cherts a good representation of Martian rock. Finally, between 70% and 90% of the exposed Martian crust was in place approximately 4 Gya (gigayears ago; Taylor and McLennan, 1985), so terrestrial Archean rock samples are of the correct age to make appropriate Mars analogues.

## **5.2 Raman spectroscopic study**

In order to evaluate the effects of excitation wavelength selection when studying reduced carbon, Raman spectra were acquired from the twelve chert samples using both the benchtop 532 nm and the handheld 785 nm Raman spectrometers, which are

described in §2.3. The goal was to comprehensively investigate the unprepared surfaces of the rocks, identifying any inorganic minerals that may be present, whilst also obtaining sufficient reduced carbon spectra with which to perform a statistically robust analysis. This approach facilitated the assessment of the thermal maturity of the samples, and also enabled recommendations to be made regarding the optimum excitation wavelength and operating modes for reduced carbon analysis.

### 5.2.1 Acquisition of Raman spectra

The twelve chert specimens were first visually examined in order to identify distinct regions of interest on their surfaces, in terms of chromatic, textural, structural and morphological differences. In order to fully characterise the samples, it is necessary to investigate sufficient regions to fully cover the range of all surface variations. Each separate region was interrogated using Raman spectroscopy, recording at least ten spectra from each region, using both spectrometers mentioned in §5.2. This revealed the characteristic spectra from each region, making it possible to identify each mineralogical component and determine the mean of measured spectral parameters. Integration time and laser power were selected to make maximum use of the dynamic range of the detectors in both spectrometers, whilst taking care to avoid thermal alteration of the samples.

For the study described in this chapter, Raman spectra were obtained from the solid rock samples, rather than crushed samples as will be investigated by the ExoMars rover and the RLS instrument. It is extremely difficult to crush hard rock such as chert, so this may not have been possible given the time and resources available. However, the goal of this study was to investigate whether it would be possible to observe differences in the reduced carbon spectra from multiple samples. Numerous studies were performed to ensure that Raman spectra are unaffected by the crushing process, including those presented in Chapters 3 and 4. It was observed that crushing a rock sample causes only a small increase in the intensity of the background signal, but does not alter spectral parameters. Additionally, it was demonstrated in Chapter 4 that reduced carbon is readily detected in crushed samples, so for the purpose of this study solid rock samples were appropriate.

### 5.2.2 Spectroscopic results

Many Raman spectra from each of the chert specimens include a particularly strong, narrow band, with a mean position of  $466 \pm 2 \text{ cm}^{-1}$  (see Figure 5.1, a Raman spectrum obtained from AC1). This is attributed to the symmetric stretch mode of Si-O-Si, which according to Kingma and Hemley (1994) usually has a Raman shift of  $465 \text{ cm}^{-1}$ . The appearance of this band is indicative of the presence of crystalline silica (silicon dioxide;  $\text{SiO}_2$ ). However, the weaker corroborative bands that are observed between  $200 \text{ cm}^{-1}$  and  $400 \text{ cm}^{-1}$  are obscured by the Rayleigh filtering and the high background intensity. This silica abundance is expected of cherts, given that it is their primary constituent.

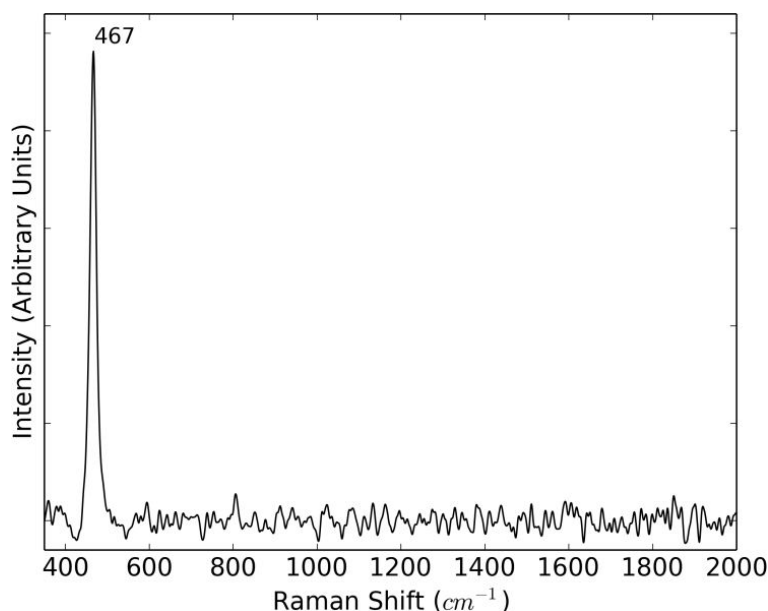


Figure 5.1: A Raman spectrum attributed to silica, obtained from sample AC1 with 532 nm excitation and an integration time of 50 seconds. The background continuum has been reduced using a Fourier transform reduction method. Figure reproduced from Harris *et al.*, 2015b.

One of the regions of interest identified on the surface of sample AC1 was a small, green-coloured area. Spectra acquired from this region (see Figure 5.2, which shows a Raman spectrum obtained from the green region of AC1) exhibit bands with Raman shifts of  $1005 \text{ cm}^{-1}$ ,  $1157 \text{ cm}^{-1}$  and  $1519 \text{ cm}^{-1}$ , which all appear in the typical spectra of carotenoids (de Oliveira *et al.*, 2010). The bright green colour of this area suggests that this is a modern microbial colonisation, rather than a molecular remnant of ancient life, since extinct pigment molecules degrade resulting in a reduction in colour intensity. Whilst this concentration of active biomarkers is not representative of any foreseen Martian field site, the comparison of excitation wavelengths in determining the presence of biomolecules is of great interest. This comparison is presented in §5.3.

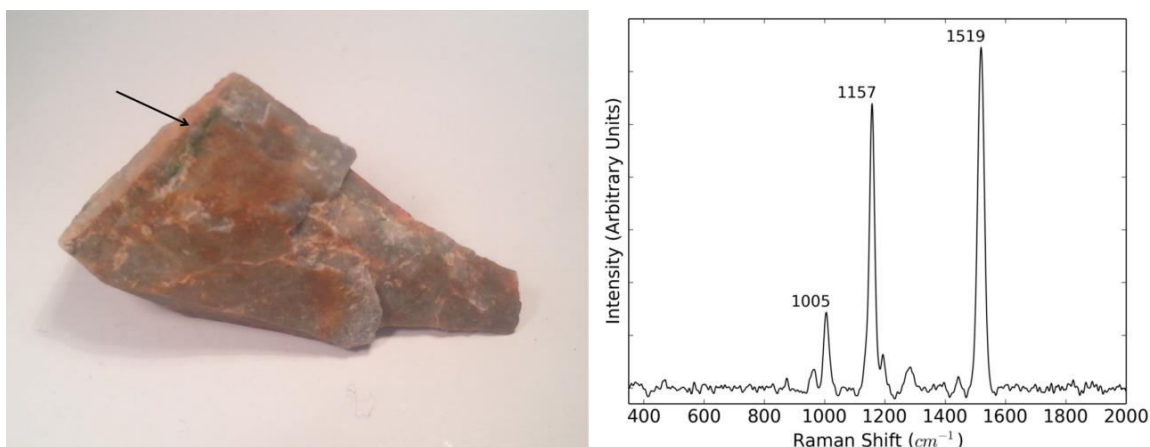


Figure 5.2: Left: Photograph of sample AC1, with the green-coloured region of interest indicated with an arrow. Right: Raman spectrum acquired from the green area, obtained using 532 nm excitation over a 30 second integration. The bands with Raman shifts of 1005  $\text{cm}^{-1}$ , 1157  $\text{cm}^{-1}$  and 1519  $\text{cm}^{-1}$  suggest the presence of a carotenoid. The background has been reduced using a Fourier transform reduction method. Figure reproduced from Harris *et al.*, 2015b.

Haematite was detected in several of the chert specimens, most notably SPC3. It was identified by bands in the Raman spectrum of haematite at 294  $\text{cm}^{-1}$ , 409  $\text{cm}^{-1}$ , 496  $\text{cm}^{-1}$  and 611  $\text{cm}^{-1}$  (see Figure 5.3, which shows a Raman spectrum obtained from SPC3). A relatively strong, broad band is also observed at around 1320  $\text{cm}^{-1}$ , which is identified as the second order, harmonic overtone of a first order band at around 660  $\text{cm}^{-1}$ . This band results from an odd symmetry, IR-active phonon mode that is normally forbidden. However, it is allowed to become active as crystallite size is reduced and lattice defects are introduced (Shim and Duffy, 2002). The band at 660  $\text{cm}^{-1}$  is often too weak to be observed in spectra, particularly those acquired in situ or from unprepared rock samples, but its overtone is much more intense and often observed, as is the case here.

### 5.2.3 Reduced carbon analysis

As expected for cherts (see §5.1.1), as well as the ubiquitous silica matrix, modern bacterial colonisation and inorganic compounds, some Raman spectra obtained from specific areas on the surfaces of the samples exhibited the carbon D and G bands (see Figure 5.4, a Raman spectrum obtained from DFM1). The presence of both bands indicates the presence of reduced carbon in those samples, rather than perfect graphite, whose spectrum is discussed in §4.1.2, or unprocessed organic material, which could have a wide range of spectra, depending on the exact molecules present in the sample.

Figure 5.3: Raman spectrum of haematite from sample SPC3, acquired using a 785 nm instrument and an integration time of 60 seconds. The continuous background has been reduced by a Fourier transform subtraction method. Figure reproduced from Harris *et al.*, 2015b.

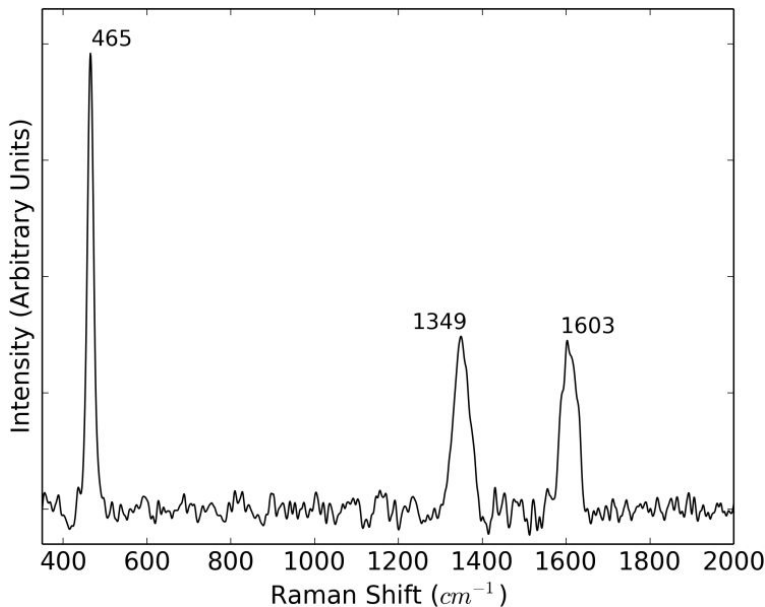
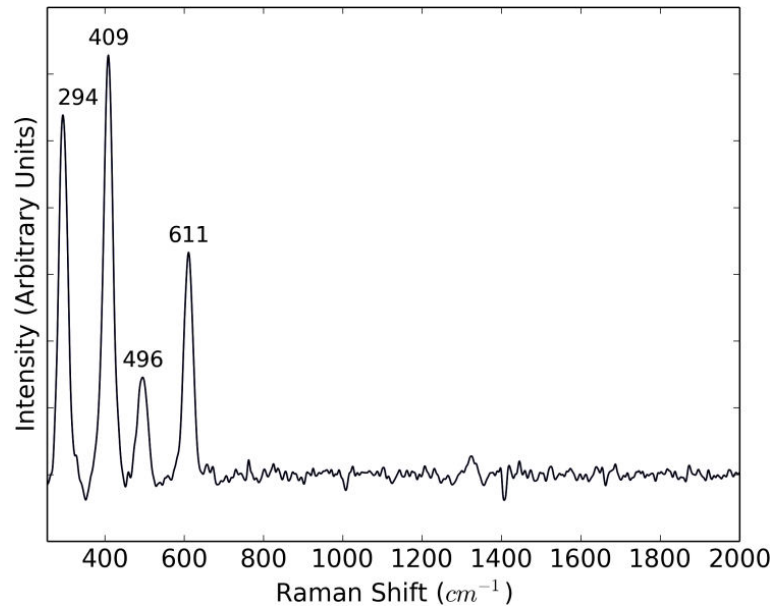


Figure 5.4: Raman spectrum of reduced carbon, acquired from sample DFM1 using 532 nm excitation, integrating for 60 seconds. The bands at 1349  $\text{cm}^{-1}$  and 1603  $\text{cm}^{-1}$  are the carbon D and G bands respectively, whereas the band at 465  $\text{cm}^{-1}$  is produced by the silica rock matrix. Figure reproduced from Harris *et al.*, 2015b.

It was demonstrated in Chapter 4 that distinct populations of reduced carbon can be distinguished according to their different thermal histories and therefore maturity, by comparison of the spectral position and width of the carbon G band. The same analysis was performed on spectra from the chert samples in order to further validate the technique and to provide a complete analysis of the cherts. This analysis also enables the comparison of the reduced carbon found in the chert samples with that in samples previously studied, in order to determine which samples are more thermally mature.

It was necessary to measure the position and FWHM of the G band and plot these parameters against one another (see Figure 5.5, a cross-plot of G band FWHM against position). As discussed in Chapter 4, it is necessary to remove or reduce the spectral

background prior to these measurements. As an initial check, the position and width of the carbon G band were measured with and without Fourier background reduction. In uncorrected spectra, a systematic offset of a few wavenumbers (to higher frequencies) was noticed and an increase in the uncertainty in both the position and width of the band for a given chert sample was observed. Both instruments were calibrated prior to each measurements following the calibration protocol described in §2.5.2, and calibration accuracy was measured to be less than  $1 \text{ cm}^{-1}$ . Since the avoidance of band distortion was of high priority, a linear fit to the background surrounding the G band was subtracted in order to ensure that any spectral alteration was consistent. The Fourier background reduction method was only used for the elucidation of bands where they may not have been immediately visible.

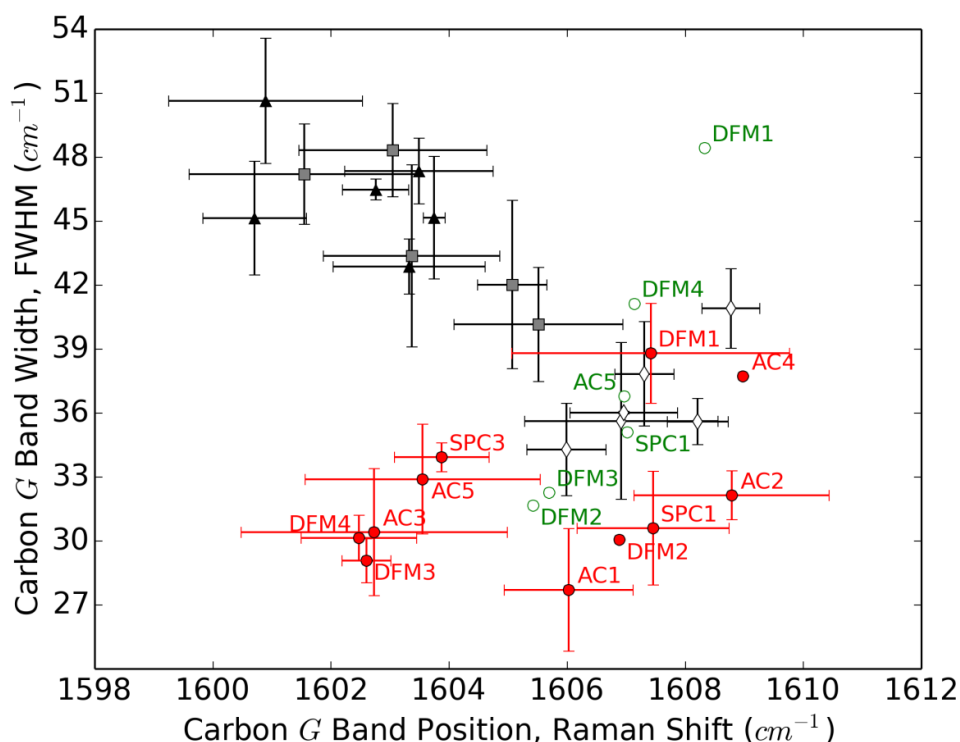


Figure 5.5: A cross-plot showing the carbon G band width versus its position. Green, open circles represent spectra acquired using 532 nm excitation, and red filled circles represent those obtained with a 785 nm source. Datapoints represented by diamonds, squares and triangles are replicated from Figure 4.8, which shows the same information for the shale samples studied in Chapter 4. The error bars represent standard deviations of multiple measurements from many spectra. Figure reproduced from Harris *et al.*, 2015b.

In general, the carbon G band in spectra from the chert samples is narrower and appears at higher Raman shifts than the equivalent band in spectra from the shale samples studied in Chapter 4. According to the analysis in Chapter 4, this suggests that the cherts are of high thermal maturity and indeed, the chert datapoints in Figure 5.5 are

coincidental with those representing the shale samples with the highest levels of thermal maturity. This is the expected result, as the cherts are much older and by definition, have undergone more intense thermal processing than the shales.

### 5.3 Comparison of 532 nm and 785 nm Raman spectroscopy

A Raman spectrum of the carotenoid on the surface of sample AC1 was obtained using the benchtop 532 nm spectrometer, but could not be acquired with the handheld 785 nm instrument. This is most likely the result of the resonance enhancement of the carotenoid spectrum that occurs following excitation with 532 nm radiation (Marshall *et al.*, 2007; Vitek *et al.*, 2009a). The use of 532 nm excitation by the RLS instrument will be greatly advantageous if carotenoids or other biological pigments are present in any samples that it studies, because this resonance effect will enable the detection of particularly low concentrations of such molecules, all considered to be unambiguous biomarkers.

Haematite could only easily be detected with the 785 nm spectrometer. It is thought that this is because 532 nm photons are readily absorbed by haematite, which is dark and often red in colour.

The dispersion of the carbon D band was observed between spectra obtained using 532 nm and 785 nm excitation in each chert specimen for which it was possible to obtain spectra using both instruments, with a mean difference in the Raman shift of the D band of  $38 \pm 4 \text{ cm}^{-1}$ . This dispersion is clearly seen in Figure 5.6, which shows a comparison of the carbon D and G bands in spectra acquired from sample DFM1 with each of the spectrometers.

Reduced carbon was much more readily detected using the 785 nm spectrometer, compared with the 532 nm instrument. In fact, reduced carbon was successfully detected in every chert sample with 785 nm excitation, however as shown in Table 5.1, spectra from approximately only half of the samples exhibited reduced carbon spectra in response to 532 nm illumination. Figure 5.6 not only demonstrates the dispersive nature of the carbon D band, but shows how, in examples where reduced carbon spectra could be acquired with both excitations wavelengths, the intensity of the fluorescent background is greatly increased in response to 532 nm light. Moreover, the SNR of both of the bands in the reduced carbon spectrum are improved in the 785 nm spectrum (see

Table 5.1). The level of noise in each spectrum was defined as the root mean square of the deviation from a polynomial fit to the region between  $600\text{ cm}^{-1}$  and  $1200\text{ cm}^{-1}$ . For those samples in which reduced carbon was not detected using 532 nm excitation, SNR was poorer in the 785 nm spectra, suggesting that low SNR is the reason for the lower detection rate with the 532 nm spectrometer.

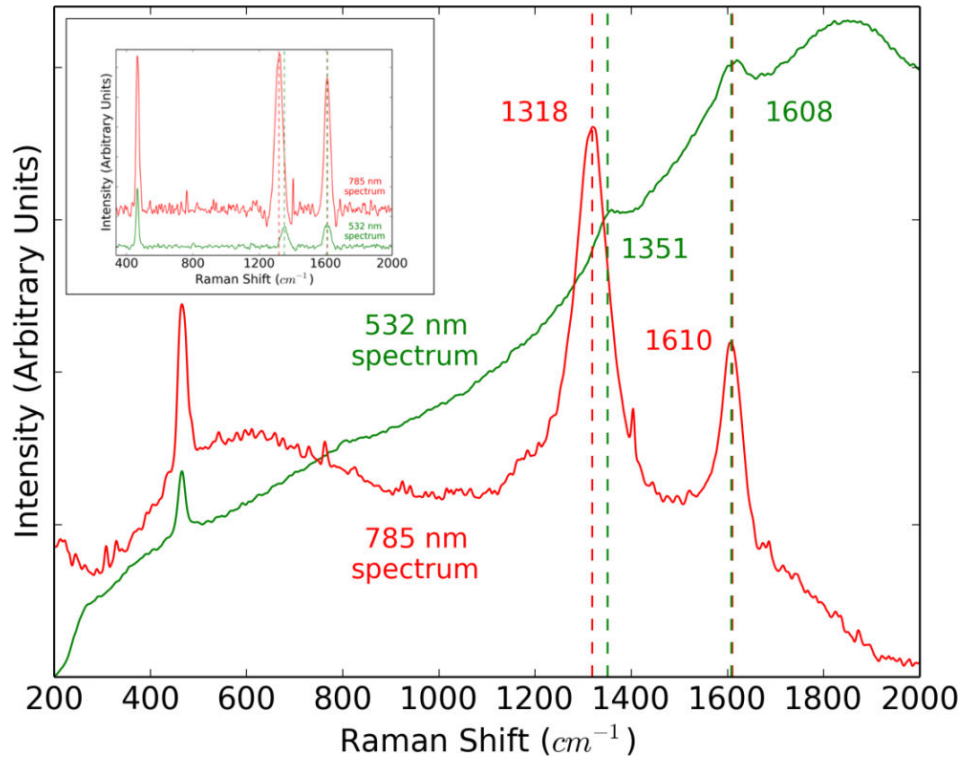


Figure 5.6: Raman spectra from the sample DFM1. The green spectrum was acquired using 532 nm excitation, and the spectrum in red with 785 nm. The spectra were integrated for 60 s. Inset: Same spectra after Fourier transform background reduction, showing that the variation in band intensity is the result of the difference in excitation wavelength, rather than an effect of the background continuum. Figure reproduced from Harris *et al.*, 2015b.

### 5.3.1 Recommendations

The data presented in §5.3 confirm that it is possible to detect reduced carbon in natural rock samples such as Archean cherts, using portable, flight-representative Raman spectrometers with no sample preparation. They also show that a significant SNR improvement and background reduction is achieved with a 785 nm excitation source, compared with 532 nm illumination. Furthermore, reduced carbon was detected in every specimen studied using the 785 nm spectrometer. However, reduced carbon was not detected in around half of these samples when using the 532 nm system. In conclusion, if one of the primary scientific objectives of a new instrument proposal is the detection and characterisation of reduced carbon in natural rock samples, 785 nm excitation or

similar should be considered. For example an astrobiology mission with a science goal of identifying potential microbial habitats, or of identifying specific signs of past life.

Table 5.1: Indication of the chert samples in which reduced carbon was detected by Raman spectroscopy with 532 nm and 785 nm excitation, and the maximum SNR of the carbon D and G bands.

	532 nm			785 nm		
	Detected	Optimum D band SNR	Optimum G band SNR	Detected	Optimum D band SNR	Optimum G band SNR
<b>DFM1</b>	✓	17	18	✓	68	60
<b>DFM2</b>	✓	13	9	✓	15	10
<b>DFM3</b>	✓	4	6	✓	65	84
<b>DFM4</b>	✓	45	32	✓	59	51
<b>AC1</b>				✓	21	12
<b>AC2</b>				✓	25	17
<b>AC3</b>				✓	27	24
<b>AC4</b>				✓	23	13
<b>AC5</b>	✓	13	16	✓	30	28
<b>SPC1</b>				✓	19	18
<b>SPC2</b>	✓	8	8	✓	59	60
<b>SPC3</b>				✓	5	3

There are limitations associated with the use of a 785 nm source for Raman spectroscopy that must also be taken into account. According to the relationship between Raman intensity and excitation wavelength discussed in §1.3.5.1, band intensity will be reduced when using a 785 nm spectrometer relative to other wavelengths, thus reducing SNR and potentially preventing the detection of weak bands. Additionally, space and planetary missions tend to have multiple scientific objectives, which means that reduced carbon is unlikely to be the only important target of interest for a mission Raman spectrometer. Consequently, a trade-off must be performed during the design of such an instrument, considering the excitation wavelength most appropriate for all targets and science goals.

Recalling the scientific objectives of the ExoMars mission and rover given in §2.1, of direct relevance to the detection and characterisation of reduced carbon is the evaluation

of the habitability of the Martian subsurface. The results of the study presented here suggest that the ExoMars RLS instrument, equipped with a 532 nm excitation source, may not be capable of consistently acquiring spectra with sufficiently high SNRs to enable the identification of reduced carbon. However, RLS will be able to take advantage of the resonance enhancement of the Raman spectra of biomolecular pigments (such as carotenoids), which occurs as a result of the use of 532 nm excitation, as discussed in §5.3. This is made apparent by inspection of spectra obtained from the sample AC1, where carotenoids were readily detected on the surface of the sample using the 532 nm instrument (Figure 5.2). This aligns RLS with one of the other science goals of the ExoMars mission: the search for signs of either extant or extinct life on Mars.

An instrument equipped with a 785 nm excitation source would have opposing strengths compared with those of RLS. The use of 785 nm excitation would facilitate the detection and characterisation of reduced carbon, fulfilling the ExoMars objective regarding the determination of subsurface habitability. However, a 785 nm instrument would not cause resonance in pigment molecules and therefore it is unlikely that they would be detected. As a result, an instrument using 785 nm excitation would not be as successful in the search for signs of life, given that reduced carbon is not an unambiguous biomarker, as discussed in §4.1.4.1. This is the basis of the trade-off that must be performed when selecting excitation wavelength for a Raman instrument on a planetary mission. In the case of ExoMars and RLS, 532 nm excitation was selected at a time when the detection of molecular pigments on Mars seemed likely. Following improvements in the modelling of the Martian radiation environment (§2.2.1) and studies of the radio- and photodecomposition of such pigments (§2.2.1.3), their presence on Mars seems more improbable. It is possible that these molecules could persist in the Martian subsurface, thanks to the shielding afforded by the Martian regolith, so it is still conceivable that they could be detected by RLS in samples retrieved using the ExoMars rover's drill. Reduced carbon on the other hand is expected to be found in abundance on Mars, so according to this particular trade-off, a 785 nm instrument would be preferable.

If both reduced carbon and carotenoids were targets of a particular mission, excitation wavelength would be selected based upon the mission priorities. Alternatively, this challenge could be overcome by incorporating multiple Raman instruments in a

payload, several excitation wavelengths in the same instrument or by using a tunable laser as an excitation source. However, there are currently no tunable lasers with sufficiently high TRL for inclusion on a space mission. These solutions would also significantly increase the mass and volume of a Raman instrument, which may not be possible given the mass and volume budgets of the mission.

### 5.3.2 UV Raman study of reduced carbon

Looking beyond the ExoMars mission to the deployment of the SHERLOC instrument onboard NASA's Mars 2020 mission, it is important to consider the use of UV excitation and the resulting instrument performance, in the context of the detection and characterisation of reduced carbon. As stated in §1.3.5.1, utilising a UV excitation source provides a number of advantages over the use of longer wavelength lasers. Due to the enhanced Raman signal that results from excitation by higher energy photons, an instrument may achieve higher SNR values for reduced carbon bands, compared with those given in Table 5.1. Of course, there would be other changes to the reduced carbon spectrum as a result of UV excitation. The dispersive carbon D band would shift to higher wavenumbers, as explained in §4.1.4.2. It has also been observed that D band intensity decreases with decreasing excitation wavelength (Matthews *et al.*, 1999), however since the focus of the analysis presented here has been the G band, this change would not be detrimental.

It is possible that the increased energy density at the sample that would result from the use of a UV source could induce thermal degradation. Great care would be required when studying carbonaceous material using UV Raman, as the incident laser light would have the potential to affect the apparent thermal maturity of the sample. The increased excitation energy may break molecular bonds within the material, which would increase the level of disorder in a sample of reduced carbon, shifting the carbon G band to lower wavenumbers and making the sample appear to be of lower thermal maturity.

## 5.4 Summary

Twelve samples of Archean chert were studied using two flight-representative, portable Raman spectrometers, one equipped with a 532 nm excitation source, and the other using a 785 nm source. A comprehensive analysis of the chert specimens was

performed, identifying regions and targets of interest on the unprepared rock surfaces before sampling each of these with each of the Raman systems. According to the Raman spectra acquired, the cherts are all primarily composed of silica and contain varying levels of haematite and reduced carbon. A modern microbial colonisation was also observed on the surface of one of the samples, from which a carotenoid spectrum was acquired.

A comparison of the two excitation wavelengths was made, specifically with regards to the detection and characterisation of reduced carbon. In every chert sample studied, reduced carbon was successfully detected using 785 nm excitation, however it was only detected in approximately half of the samples with 532 nm illumination. An improvement in SNR and a reduction in background was observed in the 785 nm spectra compared to the 532 nm spectra, although there was no appreciable variation between the band widths and positions measured in spectra acquired using the two wavelengths. For these reasons, it is recommended that 785 nm is strongly considered as the excitation wavelength of future space Raman instruments, if the detection and characterisation of reduced carbon is a particularly high priority for the mission, as a marker of either microbial habitats or extinct life.

# Chapter 6

## Summary, conclusions and future work

---

The research presented has involved the Raman spectroscopic study of several sets of Mars analogue samples using the UK ExoMars RLS breadboard system, and two flight-representative, portable Raman spectrometers, one equipped with a 532 nm excitation source and the other using 785 nm. The work has primarily focused on the detection and characterisation of reduced carbon, but studies have also been conducted that further the understanding of the spectral response of typical rock matrices, other target minerals and biomarkers.

### 6.1 Differentiation of reduced carbon populations

§4.3 presents the study of a basaltic Mars analogue sample from Helen's Bay, Northern Ireland, using a benchtop 532 nm Raman spectrometer. Reduced carbon was detected in quartz veinlets that cross-cut the rock and almost ubiquitously throughout the sample. Reduced carbon was identified by the presence of the carbon D and G bands in its spectrum, with Raman shifts of around  $1350\text{ cm}^{-1}$  and  $1600\text{ cm}^{-1}$  respectively. As highlighted in Chapter 3, care must be taken not to confuse the D band with the second order band in the Raman spectrum of haematite, which has a Raman shift of around  $1320\text{ cm}^{-1}$ . It is well documented in the literature that measurement of the relative intensity of the two carbon bands can elucidate the level of order in a carbon specimen. However, given the number of experimental variables that can affect Raman band intensity, and the limitations of miniaturised instrumentation, the use of band intensities for quantitative analysis is not recommended for space missions.

It was demonstrated that the level of order in a specimen of carbon also correlates with the width and Raman shift of the carbon G band. By comparison of these parameters the level of order in different carbon specimens can be compared, which enables the differentiation of distinct populations of carbon with different thermal histories, and therefore different levels of thermal maturity. This analysis was performed for the Helen's Bay basalt identifying two separate carbon populations: the carbon deposits within the quartz veinlets and carbon that was disseminated throughout the rock.

§4.4 reported a similar, but expanded study of 21 carbonaceous shale samples from Caithness, Northern Scotland. These shales represented the diverse thermal history of the region and were divided into groups of low, intermediate and high thermal maturity samples. Initially these categories were identified entirely by the geographical source of the samples, however this categorisation was later corroborated by measurement of the extractable carbon fractions of the shales. Once again, the width and Raman shift of the carbon G band were measured in Raman spectra from each of the samples, which made it possible to identify which category each belonged to. This was especially clear in the high thermal maturity specimens. As a result of this study, it was concluded that Raman spectroscopy could be used to qualitatively compare the thermal maturity of carbonaceous samples and as such, differentiate carbon populations according to their distinct thermal histories. This will be an extremely powerful technique for planetary exploration when the first Raman instruments are deployed on Mars and elsewhere in the Solar System.

In Chapter 5, a set of 12 carbonaceous Archean cherts was studied, using both the benchtop 532 nm Raman spectrometer, and also a handheld 785 nm system. A similar study to those described in §6.1 was performed, which showed that reduced carbon could be successfully detected in all of the samples and that their thermal maturity appeared to be similar to the most mature shale samples. It was observed that reduced carbon was much more readily detected using the 785 nm spectrometer. Given the similar operating parameters of the two instruments, it was concluded that this difference was due to the excitation wavelength used. Although reduced carbon was successfully detected in all samples using 785 nm excitation, it was only seen in around half of them using 532 nm light. Furthermore, the spectra acquired using the 785 nm

spectrometer exhibited enhanced signal-to-noise ratios and reduced background signals. Whilst this could be specific to the cherts studied, which means this work should be repeated with other rock types, they were selected as suitable Mars analogues. As such, it is recommended that if reduced carbon is a primary target of a mission for which a Raman instrument is proposed, 785 nm excitation might be the most appropriate to choose.

Additional instrument recommendations were given in Chapter 3, following the presentation of a number of case studies which demonstrate significant potential for the misassignment of bands. Although Raman spectroscopy is an unambiguous technique, the limitations of miniaturised or portable spectrometers can introduce a risk of confusing bands. This can be avoided if the effect of reducing spectral resolution or range is well understood. As a result of the studies presented in Chapter 3, it was recommended that Raman spectrometers included on planetary missions should have a spectral range covering Raman shifts from  $100\text{ cm}^{-1}$  to at least  $4000\text{ cm}^{-1}$  to ensure that all diagnostic bands can be observed. It was also suggested that such an instrument should have a spectral resolution of at least  $3\text{ cm}^{-1}$  to ensure that precise spectral positions for bands can be determined.

It has been discussed many times throughout this thesis that rock samples obtained by the ExoMars rover will be crushed prior to analysis. This means that the RLS instrument will be unable to glean spatial information about the samples under study. It has been shown several times in the work presented here, as well as in the literature, that spatial information can be highly valuable, so it is recommended that future planetary Raman instruments should be designed to interrogate unprepared rock samples. SHERLOC onboard NASA's Mars 2020 rover will do so on rocky outcrops on the rover's exterior, however a future instrument could be designed to produce Raman maps of the surface of rock cores provided by a drill like the ExoMars rover's. This would provide unprecedented geological stratigraphic information, as well as giving the best chance of detecting signs of life.

Finally, in order to maximise the chances of successfully detecting weak Raman scatterers, sufficient spectra must be acquired. In order to completely recreate the reduced carbon study presented in Chapter 5, at least 10 samples of reduced carbon must be obtained. The ExoMars rover will deploy its drill a limited number of times, so

this will not be possible. For future missions, it is recommended that more samples are obtained to achieve this. At least 20 spectra should be obtained from each sample in order to comprehensively determine their constituents, and missions should be planned to allow additional spectra to be acquired from the same sample following a quick analysis, in order to make repeat measurements and to target specific locations on samples.

### 6.3 Complementary instruments

As discussed several times throughout this thesis, a Raman spectrometer can shoulder a great deal of the analytical burden of a planetary mission, however a wealth of information can be gained by included complementary instruments in the mission payload.

Raman spectroscopy provides unambiguous molecular analysis, however sometimes it can be difficult to assign Raman bands, given the large number of possibilities and the extensive data available in the literature. This process can be assisted with information on the elemental composition of a sample, which can be provided by laser induced breakdown spectroscopy, or X-ray fluorescence, both of which would be good techniques to use alongside Raman spectroscopy on a planetary mission.

Raman is also rapid and non-destructive, which does mean that it only interrogates the surface of a sample, whether that be a solid rock sample or the top layer of a crushed sample. For this reason, techniques that provide comprehensive chemical analysis can work well in conjunction with Raman spectroscopy. Analysis of Raman spectra can quickly identify the samples that are worth using more intensive techniques on, such as gas chromatography-mass spectrometry, which can provide extremely in depth information about a sample. LIBS, XRF and GC-MS are all highly complementary with Raman spectroscopy.

Finally, microscopic context imaging improves the effectiveness of Raman spectroscopy. A high resolution context image of a sample, at microscopic magnification, would enable Raman spectra to be obtained of specific features on that sample, which would greatly improve the quality of the Raman analysis.

**6.4**                      **Suggestions for future work**

Much preparatory work is still to be completed prior to the deployment of the ExoMars rover and the RLS instrument on Mars. Chapter 3 warns of a number of situations in which the misassignment of Raman bands is possible, however it is by no means an exhaustive list. Effort should be made to continue this research, identifying potential sources of confusion and determining the minimum instrument specification required to ensure that the interpretation of Raman spectra remains unambiguous.

There are clearly a large number of minerals that are worthy of study, however there are a select few that have already gained significant interest in the literature. Chapter 3 explains how calcium sulphates are of interest on planetary exploration missions, as they can exist at several levels of hydration and therefore record information about the water environment at the time of their formation, as well as providing a molecular source of water for exploitation by living organisms. Calcium sulphates are not the only hydrated minerals that have already been detected on Mars however. Phyllosilicates and other hydrated sulphates, for example those of magnesium, have also been detected, so should be considered for future studies to ensure that they can be detected and correctly distinguished.

Also worth investigation are polymorphic crystalline materials, such as calcium carbonate, which can exist as calcite, aragonite and vaterite, depending on its crystal structure. Their abundances are extremely sensitive to the geochemical conditions at the time of their formation, therefore their detection is of great interest to planetary scientists. Finally, although the chances of their detection are quite low, more research is required into the detection and characterisation of biological molecules, such as scytonemin and various organic acids, using flight-representative Raman spectrometers.

The detection of such molecules is not considered likely, because of degradation due to the Martian radiation environment. This leads to another line of inquiry for future research however, involving the investigation of the degradation pathways of these biomarkers. If a degradation product of one of these biomarkers is found to be stable or semi-stable in the Martian environment and it has no abiotic source, it could provide an ideal target for Mars missions. In this case, relevant analogue studies would also need to be conducted to ensure that this new biomarker could be detected using the current generation of flight hardware.

**6.5 Concluding remarks**

To summarise, significant progress has been made in preparing for the arrival of the RLS instrument on the surface of Mars. The limitations of the instrument are now better understood and strategies have been developed for negating them. Techniques have also been developed for the analysis of the data that will be returned by RLS and the ExoMars rover. More work is still necessary, however some of the areas in which this will have the greatest impact have been identified and discussed in §2.2.1 and §2.2.2. Furthermore, this research has also made it possible to make recommendations for the design of future instruments that should ensure that Raman instruments are considered for inclusion in the science payloads of future planetary missions.

# Glossary

<b>Abiotic</b>	A non-living process or element of the environment that affects the conditions in that environment.
<b>Aeolian</b>	An aeolian process is driven by the wind.
<b>Alluvial</b>	An alluvial plain is created through long periods of repeated flood deposition.
<b>Carbonaceous</b>	Related to or containing carbon.
<b>Devonian</b>	A period of geological history, which covers from around 419.2 to 358.9 million years ago.
<b>Epithermal</b>	Describes neutrons whose kinetic energy exceeds thermal motion.
<b>Fluvial</b>	A fluvial process is driven by flowing water (i.e. rivers or streams).
<b>Hygroscopic</b>	A hygroscopic material is one that has a predilection for absorbing and retaining water from its surrounding environment.

<b>In situ</b>	Having occurred directly at the location in question.
<b>Lacustrine</b>	Any feature or process relating to a lake.
<b>Lithification</b>	Process by which sedimentary deposits are compressed, expelling fluids and gradually forming solid rock.
<b>Morphology</b>	The shape, structure or form of an object.
<b>Nadir</b>	The downward pointing direction. It is opposite to the zenith.
<b>Occultation</b>	The blocking from view of one object by another.
<b>Organic molecule</b>	Molecules based upon chains or rings of carbon atoms.
<b>Soft landing</b>	A controlled spacecraft landing in which the craft suffers no damage.
<b>Superoxide</b>	A compound based around the so-called superoxide anion, $O_2^-$ .
<b>Topography</b>	The study of the shape and features of the surface of a planetary body.

# References

- Acuña, M.H., Connerney, J.E.P., Lin, R.P., Mitchell, D., Carlson, C.W., McFadden, J., Anderson, K.A., Rème, H., Mazelle, C., Vignes, D., Wasilewski, P. and Cloutier, P. (1999) Global distribution of crustal magnetization discovered by the Mars Global Surveyor MAG/ER experiment. *Science* 284:790-793.
- Adar, F., Lee, E., Mamedov, S. and Whitley, A. (2010) Experimental evaluation of the depth resolution of a Raman microscope. *Microsc. Microanal.* 16:361.
- Albee, A.L., Arvidson, R.E., Palluconi, F. and Thorpe, T. (2001) Overview of the Mars global surveyor mission. *J. Geophys. Res.* 106:23291-23316.
- Amils, R., González-Toril, E., Fernández-Remolar, D., Gómez, F., Aguilera, Á., Rodríguez, N., Malki, M., García-Moyano, A., Fairén, A.G., de la Fuente, V. and Sanz, J.L. (2007) Extreme environments as Mars terrestrial analogs: the Rio Tinto case. *Planet. Space Sci.*, 55(3), 370-381.
- Arora, A.K., Tomar, V., Aarti, N., Venkateswararao, K.T. and Kamaluddin (2007) Haematite-water system on Mars and its possible role in chemical evolution. *Int. J. Astrobiol.* 6:267-271.
- Auer, B.M. and Skinner, J.L. (2008) IR and Raman spectra of liquid water: Theory and interpretation. *J. Chem. Phys.* 128, doi:10.1063/1.2925258.
- Barlow, N.G. (2008) *Mars: An introduction to its interior, surface, and atmosphere*, Cambridge University Press, Cambridge, UK.
- Beegle, L.W., Bhartia, R., DeFlores, L.P., Darrach, M., Kidd, R.D., Abbey, W., Asher, S.A., Burton, A., Clegg, S.M., Conrad, P.G., Edgett, K.S., Ehlmann, B.L., Langenhorst, F., Fries, M., Hug, W., Nealson, K.H., Popp, J., Sobron, P., Steele, A., Wiens, R.C. and Williford, K.H. (2014) SHERLOC: Scanning Habitable Environments with Raman &

Luminescence for Organics & Chemicals, an investigation for 2020 [abstract 2835]. Presented at the 45<sup>th</sup> Lunar and Planetary Science Conference, 17-21 March 2014, The Woodlands, TX, USA.

Beegle, L.W., Bhartia, R., White, M., DeFlores, L.P., Abbey, W., Wu, Y.-H., Cameron, B., Moore, J., Fries, M., Burton, A., Edgett, K.S., Ravine, M.A., Hug, W., Reid, R., Nelson, T., Clegg, S.M., Wiens, R.C., Asher, S.A. and Sobron, P.S. (2015) SHERLOC: Scanning Habitable Environments with Raman & Luminescence for Organics & Chemicals. Presented at the *IEEE Aerospace Conference 2015*, 7-14 March 2015, Big Sky, MT, USA.

Benfey, O.T. (1958) August Kekulé and the birth of the structural theory of organic chemistry in 1858. *J. Chem. Educ.* 35:21-23.

Benner, S.A., Devine, K.G., Matveeva, L.N. and Powell, D.H. (2000) The missing organic molecules on Mars. *Proc. Natl. Acad. Sci. U.S.A.* 97:2425-2430.

Berenblut, B.J., Dawson, P. and Wilkinson, G.R. (1973) A comparison of the Raman spectra of anhydrite (CaSO<sub>4</sub>) and gypsum (CaSO<sub>4</sub>·2H<sub>2</sub>O). *Spectrochim. Acta A* 29:29-36.

Bibring, J.-P., Langevin, Y., Mustard, J.F., Poulet, F., Arvidson, R., Gendrin, A., Gondet, B., Mangold, N., Pinet, P., Forget, F. and the OMEGA team (2006) Global mineralogical and aqueous Mars history derived from OMEGA/Mars Express data. *Science* 312:400-404.

Bibring, J.-P. (2011) Mars Reconnaissance Orbiter. In the *Encyclopedia of Astrobiology*, edited by M. Gargaud, R. Amils, J.C. Quintanilla, H.J. Cleaves II, W.M. Irvine, D.L. Pinti and M. Viso, Springer Verlag GmbH, Heidelberg, Germany, pp 984-985.

Bibring, J.-P., Hamm, V., Pilorget, C. and Vago, J.L. (2017) The MicrOmega Investigation Onboard ExoMars. *Astrobiology*, 17:621-626.

Bienstock, B. and Burdick, G. (2010) IPPW-7 The SAGE New Frontiers Mission to Venus. Available online at <https://solarsystem.nasa.gov/docs/pr450.pdf>

- Binder, A.B., Arvidson, R.E., Guinness, E.A., Jones, K.L., Morris, E.C., Mutch, T.A., Pieri, D.C. and Sagan, C. (1977) The geology of the Viking Lander 1 site. *J. Geophys. Res.* 82:4439-4451.
- Boynton, W.V., Feldman, W.C., Squyres, S.W., Prettyman, T.H., Brückner, J., Evans, L.G., Reedy, R.C., Starr, R., Arnold, J.R., Drake, D.M., Englert, P.A.J., Metzger, A.E., Mitrofanov, I., Trombka, J.I., d'Uston, C., Wänke, H., Gasnault, O., Hamara, D.K., Janes, D.M., Marcialis, R.L., Maurice, S., Mikheeva, I., Taylor, G.J., Tokar, R. and Shinohara, C. (2002) Distribution of hydrogen in the near surface of Mars: Evidence for subsurface ice deposits. *Science* 297:81-85.
- Boynton, W.V., Ming, D.W., Kounaves, S.P., Young, S.M.M., Arvidson, R.E., Hecht, M.H., Hoffman, J., Niles, P.B., Hamara, D.K., Quinn, R.C., Smith, P.H., Sutter, B., Catling, D.C. and Morris, R.V. (2009) Evidence for calcium carbonate at the Mars Phoenix landing site. *Science* 325:61-64.
- Brasier, M.D., Green, O.R., Lindsay, J.F., McLoughlin, N., Stoakes, C.A., Brasier, A.T. and Wacey, D. (2011) *Geology and Putative Microfossil Assemblage of the c. 3460 Ma 'Apex Chert', Chinaman Creek, Western Australia: A Field and Petrographic Guide*, Geological Survey of Western Australia, Perth, Australia.
- Brown, F.S., Adelson, H.E., Chapman, M.C., Clausen, O.W., Cole, A.J., Cragin, J.T., Day, R.J., Debenham, C.H., Fortney, R.E., Gilje, R.I., Harvey, D.W., Kropp, J.L., Loer, S.J., Logan Jr., J.L., Potter, W.D. and Rosiak, G.T. (1978) The biology instrument for the Viking Mars mission. *Rev. Sci. Instrum.* 49:139-182.
- Buseck, P.R. and Huang, B. (1985) Conversion of carbonaceous material to graphite during metamorphism. *Geochim. Cosmochim. Acta* 49:2003–2016.
- Cabane, M., Coll, P., Szopa, C., Israel, G., Raulin, F., Sternberg, R., Mahafy, P., Person, A., Rodier, C., Navarro-González, R., Niemann, H., Harpold, D. and Brinckerhoff, W. (2004) Did life exist on Mars? Search for organic and inorganic signatures, one of the goals for “SAM” (sample analysis at Mars). *Adv. Space Res.* 33:2240-2245.
- Cadogan, D., Sandy, C. and Grahne, M. (2002) Development and evaluation of the Mars Pathfinder inflatable airbag landing system. *Acta Astronaut.* 50:633-640.

- Campion, A. and Kambhampati, P. (1998) Surface-enhanced Raman scattering. *Chem. Soc. Rev.* 27:241-250.
- Carr, M.H. (1999) Retention of an atmosphere on early Mars. *J. Geophys. Res.* 104:21897-21909.
- Castro, K., Pérez-Alonso, M., Rodríguez-Laso, M.D. and Madariaga, J.M. (2004) Raman fibre optic approach to artwork dating. *Spectrochim. Acta A* 60:2919-2924.
- Catling, D.C., Claire, M.W., Zahnle, K.J., Quinn, R.C., Clark, B.C., Hecht, M.H. and Kounaves, S. (2010) Atmospheric origins of perchlorate on Mars and in the Atacama. *J. Geophys. Res.-Planet.* 115, doi:10.1029/2009JE003425.
- Cavicchioli, R., Siddiqui, K.S., Andrews, D. and Sowers, K.R. (2002) Low-temperature extremophiles and their applications. *Curr. Opin. Biotech.* 13:253-261.
- Chapman, C.R., Pollack, J.B. and Sagan, C. (1969) An analysis of the Mariner-4 cratering statistics. *Astron. J.* 74:1039-1051.
- Chicarro, A., Martin, P. and Trautner, R. (2004) The Mars Express mission: an overview. *Eur. Space Agency Spec. Publ.* 1240:3-13.
- Christensen, P.R., Morris, R.V., Lane, M.D., Bandfield, J.L. and Malin, M.C. (2001) Global mapping of Martian hematite mineral deposits: remnants of water-driven processes on early Mars. *J. Geophys. Res.* 106:23873-23885.
- Chyba, C. and Sagan, C. (1992) Endogenous production, exogenous delivery and impact-shock synthesis of organic molecules: an inventory for the origins of life. *Nature* 355:125-132.
- Ciarletti, V., Corbel, C., Plettmeier, D., Cais, P., Clifford, S.M. and Hamran, S.E. (2011) WISDOM GPR designed for shallow and high-resolution sounding of the Martian subsurface. *Proceedings of the IEEE* 99:824-836.
- Cinelli, G., Gruber, V., De Felice, L., Bossew, P., Hernández-Ceballos, M.A., Tollefsen, T., Mundigl, S. and De Cort, M. (2017) European annual cosmic-ray dose map and estimation of population exposure. In *EGU General Assembly Conference Abstracts* 19:13343.

- Clark, B.C. (1978) Implications of abundant hygroscopic minerals in the Martian regolith. *Icarus* 34:645-665.
- Coates, A.J., Jaumann, R., Schmitz, N., Leff, C.E., Josset, J.L., Griffiths, A.D., Paar, G., Hancock, B.K., Barnes, D.P., Tyler, L. and Gunn, M. (2015) PanCam on the ExoMars 2018 Rover: A Stereo, Multispectral and High-Resolution Camera System to Investigate the Surface of Mars [abstract 1812]. Presented at the *46th Lunar and Planetary Science Conference*, 16-20 March 2015, The Woodlands, TX, USA.
- Cockell, C.S., Catling, D.C., Davis, W.L., Snook, K., Kepner, R.L., Lee, P. and McKay, C.P. (2000) The ultraviolet environment of Mars: biological implications past, present, and future. *Icarus* 146:343-359.
- Cockell, C.S., Rettberg, P., Rabbow, E. and Olsson-Francis, K. (2011) Exposure of phototrophs to 548 days in low Earth orbit: microbial selection pressures in outer space and on early earth. *ISME J.* 5:1671-1682.
- Cottin, H., Guan, Y.Y., Noblet, A., Poch, O., Saiagh, K., Cloix, M., Macari, F., Jérôme, M., Coll, P., Raulin, F., Stalport, F., Szopa, C., Bertrand, M., Chabin, A., Westall, F., Chaput, D., Demets, R. and Brack, A. (2012) The PROCESS experiment: an astrochemistry laboratory for solid and gaseous organic samples in low-Earth orbit. *Astrobiology* 12:412-425.
- Craddock, R.A. and Howard, A.D. (2002) The case for rainfall on a warm, wet early Mars. *J. Geophys. Res.-Planet.* 107, doi:10.1029/2001JE0011505.
- Craig, L.E. (1984) Stratigraphy in an accretionary prism: the Ordovician rocks in North Down, Ireland. *T. Roy. Soc. Edin.-Earth* 74:183-191.
- Crisp, J.A., Adler, M., Matijevic, J.R., Squyres, S.W., Arvidson, R.E. and Kass, D.M. (2003) Mars exploration rover mission. *J. Geophys. Res.-Planet.* 108, doi:10.1029/2002JE002038.
- Cuesta, A., Dhamelin-court, P., Laureyns, J., Martinez-Alonso, A. and Tascón, J.D. (1994) Raman microprobe studies on carbon materials. *Carbon* 32:1523-1532.
- Culka, A., Osterrothová, K., Jehlička, J., Hutchinson, I.B., Ingley, R., McHugh, M., Oren, A. and Edwards, H.G.M. (2014a) Detection of Pigments of Halophilic Endoliths

from Gypsum: Portable Raman Instrument and ESA's Prototype Analysis [abstract 5067]. Presented at the 11<sup>th</sup> International GeoRaman Conference, 15-19 June 2014, St. Louis, MO, USA.

Culka, A., Osterrothová, K., Hutchinson, I.B., Ingley, R., McHugh, M., Oren, A., Edwards, H.G.M. and Jehlička, J. (2014b) Detection of pigments of halophilic endoliths from gypsum: Raman portable instrument and European Space Agency's prototype analysis. *Phil. Trans. R. Soc. A* 372, doi:10.1098/rsta.2014.0203.

Dartnell, L.R., Desorgher, L., Ward, J.M. and Coates, A.J. (2007a) Modelling the surface and subsurface martian radiation environment: implications for astrobiology. *Geophys. Res. Lett.* 34, doi:10.1029/2006GL027494.

Dartnell, L.R., Desorgher, L., Ward, J.M. and Coates, A.J. (2007b) Martian sub surface ionising radiation: biosignatures and geology. *Biogeosci. Discuss.* 4:455-492.

Davila, A.F., Willson, D., Coates, J.D. and McKay, C.P. (2013) Perchlorate on Mars: a chemical hazard and a resource for humans. *Int. J. Astrobiol.* 12:321-325.

De Angelis, G., Cloudsley, M.S., Singleterry, R.C. and Wilson, J.W. (2004) A new Mars radiation environment model with visualization. *Adv. Space Res.* 34:1328-1332.

de Faria, D.L.A., Venâncio Silva, S. and de Oliveira, M.T. (1997) Raman microspectroscopy of some iron oxides and oxyhydroxides. *J. Raman Spectrosc.* 28:873-878.

de Oliveira, V.E., Castro, H.V., Edwards, H.G.M. and de Oliveira, L.F.C. (2010) Carotenes and carotenoids in natural biological samples: a Raman spectroscopic analysis. *J. Raman Spectrosc.* 41:642-650.

De Sanctis, M.C., Altieri, F., Ammannito, E., Biondi, D., De Angelis, S., Meini, M., Mondello, G., Novi, S., Paolinetti, R., Soldani, M. and Mugnuolo, R. (2017) Ma\_MISS on ExoMars: mineralogical characterization of the martian subsurface. *Astrobiology*, 17:612-620.

Des Marais, D.J., Nuth III, J.A., Allamandola, L.J., Boss, A.P., Farmer, J.D., Hoehler, T.M., Jakosky, B.M., Meadows, V.S., Pohorille, A., Runnegar, B. and Spormann, A.M. (2008) The NASA astrobiology roadmap. *Astrobiology*, 8:715-730.

- Díaz, E., Moral, A.G., Canora, C.P., Ramos, G., Barcos, O., Prieto, J.A.R., Hutchinson, I.B., Ingley, R., Colombo, M., Canchal, R., Dávila, B., Manfredi, J.A.R., Jiménez, A., Gallego, P., Pla, J., Margoillés, R., Rull, F., Sansano, A., López, G., Catalá, A. and Tato, C. (2011) ExoMars Raman laser spectrometer breadboard overview. In *Proc. SPIE 8152, Instruments, Methods, and Missions for Astrobiology XIV*, doi:10.1117/12.896182.
- Direito, S.O.L., Ehrenfreund, P., Marees, A., Staats, M., Foing, B. and Röling, W.F.M. (2011) A wide variety of putative extremophiles and large beta-diversity at the Mars Desert Research Station (Utah). *Int. J. Astrobiol.* 10:191-207.
- Donovan, R.N. (1975) Devonian lacustrine limestones at the margin of the Orcadian Basin, Scotland. *J. Geol. Soc. London* 131:489–510.
- Donovan, R.N. and Foster, R.J. (1972) Subaqueous shrinkage cracks from the Caithness Flagstone series (Middle Devonian) of northeast Scotland. *J. Sediment. Res.* 42:309-317.
- Dorn, R.I. and Oberlander, T.M. (1981) Microbial origin of desert varnish. *Science* 213:1245-1247.
- Dorn, R.I. and Oberlander, T.M. (1982) Rock varnish. *Prog. Phys. Geog.* 6:317-367.
- Dorn, R.I. (2007) Rock varnish. In *Geochemical sediments and landscapes*, edited by D.J. Nash and S.J. McLaren, Blackwell Publishing, Oxford, UK, pp 246-297.
- Edwards, H.G.M., Jorge Villar, S.E., Jehlička, J. and Munshi, T. (2005a) FT-Raman spectroscopic study of calcium-rich and magnesium-rich carbonate minerals. *Spectrochim. Acta A* 61:2273-2280.
- Edwards, H.G.M., Moody, C.D., Jorge Villar, S.E. and Wynn-Williams, D.D. (2005b) Raman spectroscopic detection of key biomarkers of cyanobacteria and lichen symbiosis in extreme Antarctic habitats: evaluation for Mars Lander missions. *Icarus* 174:560-571.
- Edwards, H.G.M., Jorge Villar, S.E., Parnell, J., Cockell, C.S. and Lee, P. (2005c) Raman spectroscopic analysis of cyanobacterial gypsum halotrophs and relevance for sulfate deposits on Mars. *Analyst* 130:917-923.

- Edwards, H.G.M., Hutchinson, I.B. and Ingley, R. (2012) Raman spectroscopy and the search for life signatures in the ExoMars Mission. *Int. J. Astrobiol.* 11:269-278.
- Edwards, H.G.M., Hutchinson, I.B., Ingley, R. and Jehlička, J. (2014) Biomarkers and their Raman spectroscopic signatures: a spectral challenge for analytical astrobiology. *Phil. Trans. R. Soc. A* 372, doi:10.1098/rsta.2014.0193.
- Edwards, Jr., C.D., Arnold, B., DePaula, R., Kazz, G., Lee, C. and Noreen, G. (2006) Relay communications strategies for Mars exploration through 2020. *Acta Astronaut.* 59:310-318.
- Edwards, Jr., C.D., Bruvold, K.N., Erickson, J.K., Gladden, R.E., Guinn, J.R., Ilott, P.A., Jai, B., Johnston, M.D., Kornfield, R.P., Martin-Mur, T.J., McSmith, G.W., Thomas, R.C. and Varghese, P. (2010) Telecommunications relay support of the Mars Phoenix Lander mission. Presented at the *IEEE Aerospace Conference 2010*, 6-13 March 2010, Big Sky, MT, USA.
- Ehlmann, B.L., Mustard, J.F., Fassett, C.I., Schon, S.C., Head III, J.W., Des Marais, D.J., Grant, J.A. and Murchie, S.L. (2008) Clay minerals in delta deposits and organic preservation potential on Mars. *Nature Geosci.* 1:355-358.
- Eliasson, C., Macleod, N.A. and Matousek, P. (2007) Noninvasive detection of concealed liquid explosives using Raman spectroscopy. *Anal. Chem.* 79:8185-8189.
- Esposito, F., Debei, S., Bettanini, C., Molfese, C., Arruego Rodriguez, I., Colombatti, G., Harri, A.M., Montmessin, F., Wilson, C., Aboudan, A. and Abbaki, S. (2014) The DREAMS Experiment of the ExoMars 2016 Mission for the study of Martian environment during the dust storm Season. In *Eighth International Conference on Mars*, 1791:1246.
- Farmer, J.D. and Des Marais, D.J. (1999) Exploring for a record of ancient Martian life. *J. Geophys. Res.-Planet.* 104:26977-26995.
- Fassett, C.I. and Head, J.W. (2005) Fluvial sedimentary deposits on Mars: Ancient deltas in a crater lake in the Nili Fossae region. *Geophys. Res. Lett.* 32, doi:10.1029/2005GL023456.

- Ferrari, A.C. and Robertson, J. (2000) Interpretation of Raman spectra of disordered and amorphous carbon. *Phys. Rev. B* 61:14095-14107.
- Ferrari, A.C. and Robertson, J. (2001) Resonant Raman spectroscopy of disordered, amorphous, and diamondlike carbon. *Phys. Rev. B* 64, doi:10.1103/PhysRevB.64.075414.
- Fernández-Remolar, D.C., Gómez-Elvira, J., Gómez, F., Sebastian, E., Martín, J., Manfredi, J.A., Torres, J., González Kesler, C. and Amils, R. (2004) The Tinto River, an extreme acidic environment under control of iron, as an analog of the Terra Meridiani hematite site of Mars. *Planet. Space Sci.*, 52:239-248.
- Fernández-Remolar, D.C., Morris, R.V., Gruener, J.E., Amils, R. and Knoll, A.H. (2005) The Río Tinto Basin, Spain: mineralogy, sedimentary geobiology, and implications for interpretation of outcrop rocks at Meridiani Planum, Mars. *Earth Planet. Sci. Lett.*, 240:149-167.
- Ferri, F., Forget, F., Lewis, S.R. and Karatekin, Ö. (2012) ExoMars Atmospheric Mars Entry and Landing Investigations and Analysis (AMELIA). Presented at the *European Geosciences Union General Assembly 2012*, 22-27 April 2012, Vienna, Austria.
- Fjeldbo, G., Fjeldbo, W.C. and Eshleman, V.R. (1966) Models for the atmosphere of Mars based on the Mariner 4 occultation experiment. *J. Geophys. Res.* 71:2307-2316.
- Folkner, W.M., Yoder, C.F., Yuan, D.N., Standish, E.M. and Preston, R.A. (1997) Interior structure and seasonal mass redistribution of Mars from radio tracking of Mars Pathfinder. *Science* 278:1749-1752.
- Foucher, F., Lopez-Reyes, G., Bost, N., Rull-Perez, F., Rößmann, P. and Westall, F. (2013) Effect of grain size distribution on Raman analyses and the consequences for in situ planetary missions. *J. Raman Spectrosc.* 44:916-925.
- Gallaway, M. (2015) *An Introduction to Observational Astrophysics*, Springer International Publishing AG, Cham, Switzerland.
- Gauldie, R.W., Sharma, S.K. and Volk, E. (1997) Micro-Raman spectral study of vaterite and aragonite otoliths of the coho salmon, *Oncorhynchus kisutch*. *Comp. Biochem. Phys. A* 118:753-757.

Gillet, P.H., Le Cleac'h, A. and Madon, M. (1990) High temperature Raman spectroscopy of SiO<sub>2</sub> and GeO<sub>2</sub> polymorphs: anharmonicity, thermodynamic properties and phase relations among the SiO<sub>2</sub> polymorphs at high temperatures. *J. Geophys. Res.* 95:635-21.

Goesmann, F., Brinckerhoff, W.B., Raulin, F., Goetz, W., Danell, R.M., Getty, S.A., Siljeström, S., Mißbach, H., Steininger, H., Arevalo Jr, R.D. and Buch, A. (2017) The Mars Organic Molecule Analyzer (MOMA) instrument: characterization of organic material in martian sediments. *Astrobiology* 17:655-685.

Golombek, M.P., Cook, R.A., Economou, T., Folkner, W.M., Haldemann, A.F.C., Kallemeyn, P.H., Knudsen, J.M., Manning, R.M., Moore, H.J., Parker, T.J., Rieder, R., Schofield, J.T., Smith, P.H. and Vaughan, R.M. (1997) Overview of the Mars Pathfinder mission and assessment of landing site predictions. *Science* 278:1743-1748.

Golombek, M., Grant, J., Kipp, D., Vasavada, A., Kirk, R., Ferguson, R., Bellutta, P., Calef, F., Larsen, K., Katayama, Y., Huertas, A., Beyer, R., Chen, A., Parker, T., Pollard, B., Lee, S., Sun, Y., Hoover, R., Sladek, H., Grotzinger, J.P., Welch, R., Noe Dobrea, E., Michalski, J. and Watkins, M. (2012) Selection of the Mars Science Laboratory landing site. *Space Sci. Rev.* 170:641-737.

Greeley, R., Lancaster, N., Lee, S. and Thomas, P. (1992) Martian aeolian processes, sediments, and features. In *Mars*, edited by H.H. Kieffer, B.M. Jakosky, C.W. Snyder and M.S. Matthews, The University of Arizona Press, Tucson, AZ, USA, pp 730-766.

Grossman, E.L. and Ku, T.L. (1986) Oxygen and carbon isotope fractionation in biogenic aragonite: temperature effects. *Chem. Geol. (Isot. Geosci. Sect.)* 59:59-74.

Grotzinger, J.P., Beaty, D., Dromart, G., Gupta, S., Harris, M., Hurowitz, J., Kocurek, G., McLennan, S., Milliken, R., Ori, G.G. and Sumner, D. (2011) Mars sedimentary geology: key concepts and outstanding questions. *Astrobiology* 11:77-87.

Grotzinger, J.P., Crisp, J., Vasavada, A.R., Anderson, R.C., Baker, C.J., Barry, R., Blake, D.F., Conrad, P., Edgett, K.S., Ferdowski, B., Gellert, R., Gilbert, J.B., Golombek, M., Gómez-Elvira, J., Hassler, D.M., Jandura, L., Litvak, M., Mahaffy, P., Maki, J., Meyer, M., Malin, M.C., Mitrofanov, I., Simmonds, J.J., Vaniman, D., Welch,

R.V. and Wiens, R.C. (2012) Mars Science Laboratory mission and science investigation. *Space Sci. Rev.* 170:5-56.

Grotzinger, J.P., Sumner, D.Y., Kah, L.C., Stack, K., Gupta, S., Edgar, L., Rubin, D., Lewis, K., Schieber, J., Mangold, N., Milliken, R., Conrad, P.G., Des Marais, D., Farmer, J.D., Sieback, K., Calef III, F., Malin, M., Blake, D., Gellert, R., Mahaffy, P., Wiens, R.C., Maurice, S., Grant, J.A., Wilson, S., Anderson, R.C., Beegle, L., Arvidson, R., Hallet, B., Sletten, R.S., Rice, M., Bell III, J., Griffes, J., Ehlmann, B.L., Anderson, R.B., Bristow, T.F., Dietrich, W.E., Dromart, G., Eigenbrode, J., Fraeman, A., Hardgrove, C., Herkenhoff, K., Jandura, L., Kocurek, G., Lee, S., Leshin, L.A., Leveille, R., Limonadi, D., Maki, J., McCloskey, S., Meyer, M., Minitti, M., Newsom, H., Oehler, D., Okon, A., Palucis, M., Parker, T., Rowland, R., Schmidt, M., Squyres, S., Steele, A., Stolper, E., Summons, R., Treiman, A., Williams, R., Yingst, A. and the MSL Science Team (2014) A habitable fluvio-lacustrine environment at Yellowknife Bay, Gale Crater, Mars. *Science* 343, doi:10.1126/science.1242777.

Grotzinger, J.P. (2014) Habitability, taphonomy, and the search for organic carbon on Mars. *Science* 343:386-387.

Hammes, F. and Verstraete, W. (2002) Key roles of pH and calcium metabolism in microbial carbonate precipitation. *Rev. Environ. Sci. Biotechnol.* 1:3-7.

Hanesch, M. (2009) Raman spectroscopy of iron oxides and (oxy) hydroxides at low laser power and possible applications in environmental magnetic studies. *Geophys. J. Int.* 177:941-948.

Harris, D.C. and Bertolucci, M.D. (1978) *Symmetry and Spectroscopy: An Introduction to Vibrational and Electronic Spectroscopy*. Courier Dover Publications, Mineola, NY, USA.

Harris, J.K., Cousins, C.R., Gunn, M., Grindrod, P.M., Barnes, D., Crawford, I.A., Cross, R.E. and Coates, A.J. (2015) Remote detection of past habitability at Mars-analogue hydrothermal alteration terrains using an ExoMars Panoramic Camera emulator. *Icarus* 252:284-300.

Harris, L.V., Hutchinson, I.B., Ingley, R., Marshall, C.P., Olcott Marshall, A. and Edwards, H.G.M. (2015a) Selection of portable spectrometers for planetary exploration:

a comparison of 532 nm and 785 nm Raman spectroscopy of reduced carbon in Archean cherts. *Astrobiology* 15:420-429.

Harris, L.V., McHugh, M., Hutchinson, I.B., Ingley, R., Malherbe, C., Parnell, J., Olcott Marshall, A. and Edwards, H.G.M. (2015b) Avoiding misidentification of bands in planetary Raman spectra. *J. Raman Spectrosc.* 46:863-872.

Hassler, D.M., Zeitlin, C., Wimmer-Schweingruber, R.F., Böttcher, S., Martin, C., Andrews, J., Böhm, D.E., Bullock, M.A., Burmeister, S., Ehresmann, B., Epperly, M., Grinspoon, D., Köhler, J., Kortmann, O., Neal, K., Peterson, J., Posner, A., Rafkin, S., Seimetz, L., Smith, K.D., Tyler, Y., Weigle, G., Reitz, G. and Cucinotta, F.A. (2012) The radiation assessment detector (RAD) investigation. *Space Sci. Rev.* 170:503-558.

Hassler, D.M., Zeitlin, C., Wimmer-Schweingruber, R.F., Ehresmann, B., Rafkin, S., Eigenbrode, J.L., Brinza, D.E., Weigle, G., Böttcher, S., Böhm, E., Burmeister, S., Guo, J., Köhler, J., Martin, C., Reitz, G., Cucinotta, F.A., Kim, M.-H., Grinspoon, D., Bullock, M.A., Posner, A., Gómez-Elvira, J., Vasavada, A., Grotzinger, J.P. and the MSL Science Team (2014) Mars' surface radiation environment measured with the Mars Science Laboratory's Curiosity rover. *Science* 343, doi:10.1126/science.1244797.

Head III, J.W., Hiesinger, H., Ivanov, M.A., Kreslavsky, M.A., Pratt, S. and Thomson, B.J. (1999) Possible ancient oceans on Mars: evidence from Mars Orbiter Laser Altimeter data. *Science* 286:2134-2137.

Hecht, M.H., Kounaves, S.P., Quinn, R.C., West, S.J., Young, S.M.M., Ming, D.W., Catling, D.C., Clark, B.C., Boynton, W.V., Hoffman, J., DeFlores, L.P., Gospodinova, K., Kapit, J. and Smith, P.H. (2009) Detection of perchlorate and the soluble chemistry of martian soil at the Phoenix lander site. *Science* 325:64-67.

Hemley, R.J. (1987) Pressure dependence of Raman spectra of SiO<sub>2</sub> polymorphs:  $\alpha$ -quartz, coesite, and stishovite. In *High-Pressure Research in Mineral Physics*, edited by M.H. Manghnani and Y. Syono, Terra Scientific Publishing Company, Tokyo, Japan, pp 347-359.

Henson, M.J. and Zhang, L. (2006) Drug characterization in low dosage pharmaceutical tablets using Raman microscopic mapping. *Appl. Spectrosc.* 60:1247-1255.

- Hillier, D., Marshall, J.E.A. (1992) Organic maturation, thermal history and hydro-carbon generation in the Orcadian Basin, Scotland. *J. Geol. Soc. London* 149:491-502.
- Horneck, G. (2000) The microbial world and the case for Mars. *Planet. Space Sci.* 48:1053-1063.
- Houtkooper, J.M. and Schulze-Makuch, D. (2007) A possible biogenic origin for hydrogen peroxide on Mars: the Viking results reinterpreted. *Int. J. Astrobiol.* 6:147-152.
- Howe, S.D., O'Brien, R.C., Ambrosi, R.M., Gross, B., Katalenich, J., Sailer, L., Webb, J., McKay, M., Bridges, J.C. and Bannister, N.P. (2011) The Mars Hopper: an impulse-driven, long-range, long-lived mobile platform utilizing in situ Martian resources. *Proc. Inst. Mech. Eng. G J. Aerosp. Eng.* 225:144-153.
- Hutchinson, I.B., Parnell, J., Edwards, H.G.M., Jehlička, J., Marshall, C.P., Harris, L.V. and Ingley, R. (2014a) Potential for analysis of carbonaceous matter on Mars using Raman spectroscopy. *Planet. Space Sci.* 103:184-190.
- Hutchinson, I.B., Ingley, R., Edwards, H.G.M., Harris, L.V., McHugh, M., Malherbe, C. and Parnell, J. (2014b) Raman spectroscopy on Mars: identification of geological and bio-geological signatures in Martian analogues using miniaturized Raman spectrometers. *Phil. Trans. R. Soc. A* 372, doi:10.1098/rsta.2014.0204.
- Jehlička, J. and Oren, A. (2013a) Use of a handheld Raman spectrometer for fast screening of microbial pigments in cultures of halophilic microorganisms and in microbial communities in hypersaline environments in nature. *J. Raman Spectrosc.* 44:1285-1291.
- Jehlička, J. and Oren, A. (2013b) Raman spectroscopy in halophile research. *Front. Microbiol.* 4, doi:10.3389/fmicb.2013.00380.
- Jehlička, J., Edwards, H.G.M. and Oren, A. (2013) Bacterioruberin and salinixanthin carotenoids of extremely halophilic Archaea and Bacteria: a Raman spectroscopic study. *Spectrochim. Acta A* 106:99-103.

- Jehlička, J., Edwards, H.G.M. and Oren, A. (2014) Raman spectroscopy of microbial pigments. *Appl. Environ. Microb.* 80:3286-3295.
- Johnston, C.G. and Vestal, J.R. (1991) Photosynthetic carbon incorporation and turnover in Antarctic cryptoendolithic microbial communities: are they the slowest-growing communities on Earth?. *Appl. Environ. Microbiol.* 57:2308-2311.
- Jorge Villar, S.E. , Edwards, H.G.M. and Cockell, C.S. (2005) Raman spectroscopy of endoliths from Antarctic cold desert environments. *Analyst* 130:156-162.
- Jorge Villar, S.E. and Edwards, H.G.M. (2006) Raman spectroscopy in astrobiology. *Anal. Bioanal. Chem.* 384:100-113.
- Josset, J.L., Westall, F., Hofmann, B.A., Spray, J.G., Cockell, C., Kempe, S., Griffiths, A.D., De Sanctis, M.C., Colangeli, L., Koschny, D. and Pullan, D. (2012) CLUPI, a high-performance imaging system on the ESA-NASA rover of the 2018 ExoMars mission to discover biofabrics on Mars. In *EGU General Assembly Conference Abstracts*, 14:13616.
- Keating, A., Mohammadzadeh, A., Nieminen, P., Maia, D., Coutinho, S., Evans, H., Pimenta, M., Huot, J.P. and Daly, E. (2005) A model for Mars radiation environment characterization. *IEEE T. Nucl. Sci.* 52:2287-2293.
- Kieffer, H.H., Martin, T.Z., Peterfreund, A.R., Jakosky, B.M., Miner, E.D. and Palluconi, F.D. (1977) Thermal and albedo mapping of Mars during the Viking primary mission. *J. Geophys. Res.* 82:4249-4291.
- Kieffer, H.H. and Titus, T.N. (2001) TES mapping of Mars' north seasonal cap. *Icarus* 154:162-180.
- Kingma, K.J. and Hemley, R.J. (1994) Raman spectroscopic study of microcrystalline silica. *Am. Mineral.* 79:269-273.
- Klingelhofer, G., DeGrave, E., Morris, R.V., Van Alboom, A., De Resende, V.G., De Souza Jr., P.A., Rodionov, D., Schröder, C., Ming, D.W. and Yen, A. (2005) Mössbauer spectroscopy on Mars: goethite in the Columbia Hills at Gusev crater. *Hyperfine Interact.* 166:549-554.
- Klein, H.P. (1978) The Viking biological experiments on Mars. *Icarus* 34:666-674.

- Klein, H.P. (1979) The Viking mission and the search for life on Mars. *Rev. Geophys.* 17:1655-1662.
- Kminek, G. and Bada, J.L. (2006) The effect of ionizing radiation on the preservation of amino acids on Mars. *Earth Planet. Sci. Lett.* 245:1-5.
- Knittle, E., Phillips, W. and Williams, Q. (2001) An infrared and Raman spectroscopic study of gypsum at high pressures. *Phys. Chem. Miner.* 28:630-640.
- Köhler, J., Wimmer-Schweingruber, R.F., Appel, J., Ehresmann, B., Zeitlin, C., Hassler, D.M., Reitz, G., Brinza, D.E., Böttcher, S., Böhm, E., Burmeister, S., Guo, J., Harri, A. M., Kahanpää, H., Krauss, J., Lohf, H., Martin, C., Matthä, D., Posner, A. and Rafkin, S. (2016) Electron/positron measurements obtained with the Mars Science Laboratory Radiation Assessment Detector on the surface of Mars. *Ann. Geophys.* 34:133-141.
- Kontoyannis, C.G. and Vagenas, N.V. (2000) Calcium carbonate phase analysis using XRD and FT-Raman spectroscopy. *Analyst* 125:251-255.
- Korablev, O., Trokhimovsky, A., Grigoriev, A.V., Shakun, A., Ivanov, Y.S., Moshkin, B., Anufreychik, K., Timonin, D., Dziuban, I., Kalinnikov, Y.K. and Montmessin, F. (2014) Three infrared spectrometers, an atmospheric chemistry suite for the ExoMars 2016 trace gas orbiter. *J. of Appl. Remote Sens.*, 8, doi:10.1117/1.JRS.8.084983.
- Korablev, O.I., Dobrolensky, Y., Evdokimova, N., Fedorova, A.A., Kuzmin, R.O., Mantsevich, S.N., Cloutis, E.A., Carter, J., Poulet, F., Flahaut, J. and Griffiths, A. (2017) Infrared spectrometer for ExoMars: a mast-mounted instrument for the Rover. *Astrobiology* 17:542-564.
- Krumbein, W.E. and Jens, K. (1981) Biogenic rock varnishes of the Negev Desert (Israel) an ecological study of iron and manganese transformation by cyanobacteria and fungi. *Oecologia* 50:25-38.
- Landsberg, G. and Mandelstam, L. (1928) A new appearance in the light diffusion in crystals. *Naturwissenschaften* 16:772.
- Langevin, Y., Poulet, F., Bibring, J.P. and Gondet, B. (2005) Sulfates in the north polar region of Mars detected by OMEGA/Mars Express. *Science* 307:1584-1586.
- Laudermilk, J.D. (1931) On the origin of desert varnish. *Am. J. Sci.* 21:51-66.

- Leroi, V., Bibring, J.P. and Berthe, M. (2009) Micromega/IR: design and status of a near-infrared spectral microscope for in situ analysis of Mars samples. *Planet. Space Sci.* 57:1068-1075.
- Liu, Y., Wang, A. and Freeman, J.J. (2009). Raman, MIR, and NIR spectroscopic study of calcium sulfates: gypsum, bassanite, and anhydrite. Presented at the 40<sup>th</sup> Lunar and Planetary Science Conference, 23-27 March 2009, The Woodlands, TX, USA.
- Longhi, J., Knittle, E., Holloway, J.R. and Wänke, H. (1992) The bulk composition, mineralogy and internal structure of Mars. In *Mars*, edited by H.H. Kieffer, B.M. Jakosky, C.W. Snyder and M.S. Matthews, The University of Arizona Press, Tucson, AZ, USA, pp 184-208.
- Lopez-Reyes, G., Rull, F., Venegas, G., Westall, F., Foucher, F., Bost, N., Sanz, A., Catalá-Espí, A., Vegas, A., Hermosilla, I., Sansano, A. and Medina, J. (2013) Analysis of the scientific capabilities of the ExoMars Raman Laser Spectrometer instrument. *Eur. J. Mineral.* 25:721-733.
- Lundin, R., Barabash, S., Andersson, H., Holmström, M., Grigoriev, A., Yamauchi, M., Sauvaud, J.-A., Fedorov, A., Budnik, E., Thocaven, J.-J., Winningham, D., Frahm, R., Scherrer, J., Sharber, J., Asamura, K., Hayakawa, H., Coates, A., Linder, D.R., Curtis, C., Hsieh, K.C., Sandel, B.R., Grande, M., Carter, M., Reading, D.H., Koskinen, H., Kallio, E., Riihela, P., Schmidt, W., Säles, T., Kozyra, J., Krupp, N., Woch, J., Luhmann, J., McKenna-Lawler, S., Cerulli-Irelli, R., Orsini, S., Maggi, M., Mura, A., Milillo, A., Roelof, E., Williams, D., Livi, S., Brandt, P., Wurz, P. and Bochsler, P. (2004). Solar wind-induced atmospheric erosion at Mars: First results from ASPERA-3 on Mars Express. *Science* 305:1933-1936.
- Lunine, J., Waite, H., Postberg, F., Spilker, L. and Clark, K. (2015) Enceladus life finder: the search for life in a habitable moon. *Geophys. Res. Abstr.* 17:14923.
- Mahaffy, P.R., Webster, C.R., Atreya, S.K., Franz, H., Wong, M., Conrad, P.G., Harpold, D., Jones, J.J., Leshin, L.A., Manning, H., Owen, T., Pepin, R.O., Squyres, S., Trainer, M. and the MSL Science Team (2013) Abundance and isotopic composition of gases in the martian atmosphere from the Curiosity rover. *Science* 341:263-266.

- Malherbe, C., Ingley, R., Hutchinson, I.B., Edwards, H.G.M., Carr, A.S., Harris, L.V. and Boom, A. (2015) Biogeological Analysis of Desert Varnish Using Portable Raman Spectrometers. *Astrobiology* 15:442-452.
- Mancinelli, R.L. and White, M.R. (1996). Mineralogical analysis of desert varnish by DTA/GC: applicability to the exobiology of Mars. In *27<sup>th</sup> Lunar and Planetary Science Conference*, Lunar and Planetary Institute, Houston, Texas, USA, pp 803-804.
- Mancinelli, R.L., Fahlen, T.F., Landheim, R. and Klovstad, M.R. (2004) Brines and evaporites: analogs for Martian life. *Adv. Space Res.* 33:1244-1246.
- Mangold, S., Valdés, J., Holmes, D.S. and Dopson, M. (2011) Sulfur metabolism in the extreme acidophile *Acidithiobacillus caldus*. *Front. Microbiol.* 2, doi:10.3389/fmicb.2011.00017.
- Mankins, J.C. (1995) Technology readiness levels. *NASA White Paper*. Available online at <https://www.hq.nasa.gov/office/codeq/trl/trl.pdf>
- Marshall, C.P. and Olcott Marshall, A. (2010) The potential of Raman spectroscopy for the analysis of diagenetically transformed carotenoids. *Phil. Trans. R. Soc. A* 368:3137-3144.
- Marshall, C.P. and Olcott Marshall, A. (2011) Hematite and carbonaceous materials in geological samples: a cautionary tale. *Spectrochim. Acta A* 80:133-137.
- Marshall, C.P. and Olcott Marshall, A. (2013) Raman hyperspectral imaging of microfossils: potential pitfalls. *Astrobiology* 13:920-931.
- Marshall, C.P., Leuko, S., Coyle, C.M., Walter, M.R., Burns, B.P. and Neilan, B.A. (2007) Carotenoid analysis of halophilic archaea by resonance Raman spectroscopy. *Astrobiology* 7:631-643.
- Marshall, C.P., Edwards H.G.M. and Jehlička J. (2010) Understanding the application of Raman spectroscopy to the detection of traces of life. *Astrobiology* 10:229-243.
- Marshall, C.P., Emry, J.R. and Olcott Marshall, A. (2011) Haematite pseudomicrofossils present in the 3.5-billion-year-old Apex Chert. *Nat. Geosci.* 4:240-243.

- Matthews, M.J., Pimenta, M.A., Dresselhaus, G., Dresselhaus, M.S. and Endo, M. (1999) Origin of dispersive effects of the Raman D band in carbon materials. *Phys. Rev. B* 59, doi:10.1103/PhysRevB.59.R6585.
- Matthiä, D., Ehresmann, B., Lohf, H., Köhler, J., Zeitlin, C., Appel, J., Sato, T., Slaba, T., Martin, C., Berger, T., Boehm, E., Boettcher, S., Brinza, D.E., Burmeister, S., Guo, J., Hassler, D.M., Posner, A., Rafkin, S.C.R., Reitz, G., Wilson, J.W. and Wimmer-Schweingruber, R.F. (2016) The Martian surface radiation environment a comparison of models and MSL/RAD measurements. *J. Space Weather Space Clim.* 6, doi:10.1051/swsc/2016008.
- Maurice, S., Wiens, R.C., Le Mouélic, S., Anderson, R., Beyssac, O., Bonal, L., Clegg, L., DeFlores, G., Dromart, G., Fischer, W., Forni, O., Gasnault, O., Grotzinger, J.P., Johnson, J., Martinez-Frias, J., Mangold, N., McLennan, S., Montmessin, F., Rull, F., Sharma, S. and the SuperCam team (2015) The SuperCam Instrument for the Mars2020 Rover [abstract 185]. Presented at the *European Planetary Science Congress 2015*, 27 September-2 October 2015, Nantes, France.
- McCarty, K.F. (1988) Inelastic light scattering in  $\alpha$ -Fe<sub>2</sub>O<sub>3</sub>: Phonon vs magnon scattering. *Solid State Commun.* 68:799-802.
- McKay, C.P. (1997) The search for life on Mars. In *Planetary and Interstellar Processes Relevant to the Origins of Life*, edited by D.C.B. Whittet, Springer Netherlands, Dordrecht, Netherlands, pp 263-289.
- McSween Jr., H.Y. and Murchie, S.L. (1999) Rocks at the Mars Pathfinder landing site. *Am. Sci.* 87:36-45.
- Mellon, M.T., Arvidson, R.E., Marlow, J.J., Phillips, R.J. and Asphaug, E. (2008a) Periglacial landforms at the Phoenix landing site and the northern plains of Mars. *J. Geophys. Res.-Planet.* 113, doi:10.1029/2007JE003039.
- Mellon, M.T., Boynton, W.V., Feldman, W.C., Arvidson, R.E., Titus, T.N., Bandfield, J.L., Putzig, N.E. and Sizemore, H.G. (2008) A prelanding assessment of the ice table depth and ground ice characteristics in Martian permafrost at the Phoenix landing site. *J. Geophys. Res.-Planet.* 113, doi:10.1029/2007JE003067.

- Mitrofanov, I., Malakhov, A., Mokrousov, M., Golovin, D., Fedosov, F., Kozyrev, A., Lisov, D., Litvak, M., Nikiforov, S., Sanin, A. and Tret'yakov, V. (2016) FRENDS neutron telescope for mapping the Martian water with fine spatial resolution. In *EGU General Assembly Conference Abstracts* 18:16402.
- Molina-Cuberos, G.J., Stumptner, W., Lammer, H., Kömle, N.I. and O'Brien, K. (2001) Cosmic ray and UV radiation models on the ancient Martian surface. *Icarus* 154:216-222.
- Moral, A.G., Rull, F., Maurice, S., Hutchinson, I.B., Canora, C.P., López, G., Canchal, R., Gallego, P., Seoane, L., Prieto, J.A.R. and Santiago, A. (2016) Raman Laser Spectrometer for 2020 ExoMars Mission [abstract 1980]. Presented at the *3rd International Workshop on Instrumentation for Planetary Missions*, 24-27 October 2017, Pasadena, CA, USA.
- Morthekai, P., Jain, M., Dartnell, L., Murray, A.S., Bøtter Jensen, L. and Desorgher, L. (2007) Modelling of the dose rate variations with depth in the Martian regolith using GEANT4. *Nucl. Instrum. Meth. A* 580:667-670.
- Mouginis-Mark, P.J., Wilson, L. and Zuber, M.T. (1992) The physical volcanology of Mars. In *Mars*, edited by H.H. Kieffer, B.M. Jakosky, C.W. Snyder and M.S. Matthews, The University of Arizona Press, Tucson, AZ, USA, pp 424-452.
- Mutch, T.A., Arvidson, R.E., Binder, A.B., Guinness, E.A. and Morris, E.C. (1977) The geology of the Viking Lander 2 site. *J. Geophys. Res.* 82:4452-4467.
- Navarro-González, R., Vargas, E., de La Rosa, J., Raga, A.C. and McKay, C.P. (2010) Reanalysis of the Viking results suggests perchlorate and organics at midlatitudes on Mars. *J. Geophys. Res.-Planet.* 115, doi:10.1029/2010JE003599.
- Nelson, D.R., Trendall, A.F. and Altermann, W. (1999) Chronological correlations between the Pilbara and Kaapvaal cratons. *Precambrian Res.* 97:165-189.
- Noblet, A., Stalport, F., Guan, Y.Y., Poch, O., Coll, P., Szopa, C., Cloix, M., Macari, F., Raulin, F., Chaput, D. and Cottin, H. (2012) The PROCESS experiment: amino and carboxylic acids under Mars-like surface UV radiation conditions in low-Earth orbit. *Astrobiology* 12:436-444.

- Ojha, L., Wilhelm, M.B., Murchie, S.L., McEwen, A.S., Wray, J.J., Hanley, J., Massé, M. and Chojnacki, M. (2015) Spectral evidence for hydrated salts in recurring slope lineae on Mars. *Nat. Geosci.* 8:829-832.
- Olcott Marshall, A., Emry, J.R. and Marshall, C.P. (2012) Multiple generations of carbon in the Apex chert and implications for preservation of microfossils. *Astrobiology* 12:160-166.
- Olcott Marshall, A., Jehlička, J., Rouzaud, J.N. and Marshall, C.P. (2014) Extensive mixing of carbonaceous material in the Archean and Proterozoic. *Gondwana Res.* 25:284-289.
- Oesterhelt, D. (1998) The structure and mechanism of the family of retinal proteins from halophilic archaea. *Curr. Opin. Struct. Biol.* 8:489-500.
- Oren, A. (2002) Diversity of halophilic microorganisms: environments, phylogeny, physiology, and applications. *J. Ind. Microbiol. Biot.* 28:56-63.
- Palmer, C.A. and Loewen, E.G. (2005) *Diffraction Grating Handbook Sixth Edition*, Newport Corporation, Springfield, OH, USA.
- Parnell, J., Lee, P., Cockell, C.S. and Osinski, G.R. (2004) Microbial colonization in impact-generated hydrothermal sulphate deposits, Haughton impact structure, and implications for sulphates on Mars. *Int. J. Astrobiol.* 3:247-256.
- Parnell, J., McMahon, S., Blamey, N.J., Hutchinson, I.B., Harris, L.V., Ingley, R., Edwards, H.G.M., Lynch E. and Feely, M. (2014) Detection of reduced carbon in a basalt analogue for martian nakhlite: a signpost to habitat on Mars. *Int. J. Astrobiol.* 13:124-131.
- Pasteris, J.D. and Wopenka, B. (1991) Raman-spectra of graphite as indicators of degree of metamorphism. *Can. Mineral.* 29:143-153.
- Pasteris, J.D. and Wopenka, B. (2002) Laser-Raman spectroscopy (Communication arising): Images of the Earth's earliest fossils?. *Nature* 420:476-477.
- Pasteris, J.D. and Wopenka, B. (2003) Necessary, but not sufficient: Raman identification of disordered carbon as a signature of ancient life. *Astrobiology* 3:727-738.

- Patel, M.R., Zarnecki, J.C. and Catling, D.C. (2002) Ultraviolet radiation on the surface of Mars and the Beagle 2 UV sensor. *Planet. Space Sci.* 50:915-927.
- Pavlov, A.K., Blinov, A.V. and Konstantinov, A.N. (2002) Sterilization of Martian surface by cosmic radiation. *Planet. Space Sci.* 50:669-673.
- Perez-de-Tejada, H. (1992) Solar wind erosion of the Mars early atmosphere. *J. Geophys. Res.* 97:3159-3167.
- Perry, R.S., Engel, M.H., Botta, O. and Staley, J.T. (2003) Amino acid analyses of desert varnish from the Sonoran and Mojave Deserts. *Geomicrobiol. J.* 20:427-438.
- Peter, Y.Y. and Shen, Y.R. (1974) Study of Dispersive Raman Modes in Cu<sub>2</sub>O by Resonant Raman Scattering. *Phys. Rev. Lett.* 32, doi:10.1103/PhysRevLett.32.939.
- Phillips, C.B. and Pappalardo, R.T. (2014) Europa Clipper Mission Concept: Exploring Jupiter's Ocean Moon. *Eos, Trans. Amer. Geophys. Union* 95:165-167.
- Poch, O., Noblet, A., Stalport, F., Correia, J.J., Grand, N., Szopa, C. and Coll, P. (2013) Chemical evolution of organic molecules under Mars-like UV radiation conditions simulated in the laboratory with the “Mars organic molecule irradiation and evolution”(MOMIE) setup. *Planet. Space Sci.* 85:188-197.
- Pollack, J.B., Kasting, J.F., Richardson, S.M. and Poliakoff, K. (1987) The case for a wet, warm climate on early Mars. *Icarus* 71:203-224.
- Potter, R.M. and Rossman, G.R. (1979) The manganese-and iron-oxide mineralogy of desert varnish. *Chem. Geol.* 25:79-94.
- Poulet, F., Bibring, J.-P., Mustard, J.F., Gendrin, A., Mangold, N., Langevin, Y., Arvidson, R.E., Gondet, B., Gomez, C. and The Omega Team (2005) Phyllosilicates on Mars and implications for early Martian climate. *Nature* 438:623-627.
- Prawer, S. and Nemanich, R.J. (2004) Raman spectroscopy of diamond and doped diamond. *Phil. Trans. R. Soc. A* 362:2537-2565.
- Pullan, D., Sims, M.R., Wright, I.P., Pillinger, C.T. and Trautner, R. (2004) Beagle 2: the exobiological lander of Mars express. *Eur. Space Agency Spec. Publ.* 1240:165-204.

- Rabbow, E., Horneck, G., Rettberg, P., Schott, J.-U., Panitz, C., L'Afflitto, A., von Heise-Rotenburg, R., Willnecker, R., Baglioni, P., Hatton, J., Dettmann, J., Demets, R. and Reitz, G. (2009) EXPOSE, an astrobiological exposure facility on the international space station—from proposal to flight. *Origins Life Evol. B.* 39:581-598.
- Raman, C.V. (1929) Part II.—The Raman effect. Investigation of molecular structure by light scattering. *J. Chem. Soc. Faraday Trans.* 25:781-792.
- Raman, C.V. and Krishnan, K.S. (1928a) A new type of secondary radiation. *Nature* 121:501-502.
- Raman, C.V. and Krishnan, K.S. (1928b) The optical analogue of the Compton effect. *Nature*, 121:711-711.
- Raman, C.V. and Krishnan, K.S. (1929) The production of new radiations by light scattering. Part I. *Proc. R. Soc. A* 122:23-35.
- Reiff, G.A. (1966) Mariner IV: Developing the Scientific Experiment. *Science*, 151:413-417.
- Rodriguez, I.H., Lopez-Reyes, G., Llanos, D.R. and Perez, F.R. (2014) Automatic Raman Spectra Processing for ExoMars. In *Mathematics of Planet Earth*, edited by E. Pardo-Igúzquiza, C. Guardiola-Albert, J. Heredia, L. Moreno-Merino, J.J. Durán, J.A. Vargas-Guzmán, Springer Verlag GmbH, Heidelberg, Germany, pp 127-130.
- Rothschild, L.J. and Mancinelli, R.L. (2001) Life in extreme environments. *Nature* 409:1092-1101.
- Rull, F., Sansano, A., Díaz, E., Canora, C.P., Moral, A.G., Tato, C., Colombo, M., Belenguer, T., Fernández, M., Manfredi, J.A.R., Canchal, R., Dávila, B., Jiménez, A., Gallego, P., Ibarria, S., Prieto, J.A.R., Santiago, A., Pla, J., Ramos, G., Díaz, C. and González, C. (2011) ExoMars Raman laser spectrometer for Exomars. In *Proc. SPIE 8152, Instruments, Methods, and Missions for Astrobiology XIV*, doi:10.1117/12.896787.
- Rull, F. and the RLS team (2014) The Laser Raman Instrument (RLS) for EXOMARS 2018 Mission and the Scientific Operation on Mars. Presented at the *Eighth International Conference on Mars*, 14-19 March 2014, Pasadena, CA, USA.

- Rull, F., Maurice, S., Hutchinson, I., Moral, A., Perez, C., Diaz, C., Colombo, M., Belenguer, T., Lopez-Reyes, G., Sansano, A., Forni, O., Parot, Y., Striebig, N., Woodward, S., Howe, C., Tarcea, N., Rodriguez, P., Seoane, L., Santiago, A., Rodriguez-Prieto, J.A., Medina, J., Gallego, P., Canchal, R., Santamaría, P., Ramos, G. and Vago, J.L. (2017) The Raman Laser Spectrometer for the ExoMars Rover Mission to Mars. *Astrobiology* 17:627-654.
- Ryan, J.M., Lockwood, J.A. and Debrunner, H. (2000) Solar energetic particles. *Space Sci. Rev.* 93:35-53.
- Saito, R., Jorio, A., Souza Filho, A.G., Grueneis, A., Pimenta, M.A., Dresselhaus, G. and Dresselhaus, M.S. (2002) Dispersive Raman spectra observed in graphite and single wall carbon nanotubes. *Physica B Condens. Matter* 323:100-106.
- Schelble, R.T., McDonald, G.D., Hall, J.A. and Nealson, K.H. (2005) Community structure comparison using FAME analysis of desert varnish and soil, Mojave Desert, California. *Geomicrobiol. J.* 22:353-360.
- Schmidt, R. (2003) Mars Express-ESA's first mission to planet Mars. *Acta Astronaut.* 52:197-202.
- Schneiderman, D. (1967) Mariner Mars 1964 Project report: Spacecraft performance and analysis. JPL Technical Report No. 32-882.
- Schofield, J.T., Barnes, J.R., Crisp, D., Haberle, R.M., Larsen, S., Magalhães, J.A., Murphy, J.R., Seiff, A. and Wilson, G. (1997) The Mars Pathfinder atmospheric structure investigation/meteorology (ASI/MET) experiment. *Science* 278:1752-1758.
- Schopf, J.W. and Packer, B.M. (1987) Early Archean (3.3-billion to 3.5-billion-year-old) microfossils from Warrawoona Group, Australia. *Science* 237:70-73.
- Schulte, W., Widani, C., Hofmann, P., Bönke, T., Re, E. and Baglioni, P. (2008). Design and breadboarding of the sample preparation and distribution system of the ExoMars mission. Presented at the *9th International Symposium on Artificial Intelligence, Robotics and Automation in Space*, 26-29 February 2008, Hollywood, CA, USA.

- Sephton, M.A. (2002) Organic compounds in carbonaceous meteorites. *Nat. Prod. Rep.* 19:292-311.
- Serafim, A., Mallet, R., Pascaretti-Grizon, F., Stancu, I.C. and Chappard, D. (2014) Osteoblast-like cell behavior on porous scaffolds based on poly (styrene) fibers. *BioMed Research International*, doi:10.1155/2014/609319.
- Sharpe, E.N. (1970) An occurrence of pillow lavas in the Ordovician of County Down. *Ir. Nat. J.* 16:299-301.
- Shim, S.H. and Duffy, T.S. (2002) Raman spectroscopy of Fe<sub>2</sub>O<sub>3</sub> to 62 GPa. *Am. Mineral.* 87:318-326.
- Shkrob, I.A., Chemerisov, S.D. and Marin, T.W. (2010) Photocatalytic decomposition of carboxylated molecules on light-exposed martian regolith and its relation to methane production on Mars. *Astrobiology* 10:425-436.
- Shotwell, R. (2005) Phoenix-the first Mars Scout mission. *Acta Astronaut.* 57:121-134.
- Simpson, J.A. (1983) Elemental and isotopic composition of the galactic cosmic rays. *Annu. Rev. Nucl. Part. Sci.* 33:323-382.
- Siscoe, G.L., Davis, L., Coleman, P.J., Smith, E.J. and Jones, D. E. (1968) Power spectra and discontinuities of the interplanetary magnetic field: Mariner 4. *J. Geophys. Res.* 73:61-82.
- Smekal, A. (1923) Zur quantentheorie der dispersion. *Naturwissenschaften* 11:873-875.
- Smith, E. and Dent, G. (2005) *Modern Raman spectroscopy: a practical approach*. Wiley, Hoboken, New Jersey, USA.
- Smith, D.E., Zuber, M.T., Frey, H.V., Garvin, J.B., Head, J.W., Muhleman, D.O., Pettengill, G.H., Phillips, R.J., Solomon, S.C., Zwally, H.J., Banerdt, W.B., Duxbury, T.C., Golombek, M.P., Lemoine, F.G., Neumann, G.A., Rowlands, D.D., Aharonson, O., Ford, P.G., Ivanov, A.B., Johnson, C.L., McGovern, P.J., Abshire, J.B., Afzal, R.S. and Sun, X. (2001) Mars Orbiter Laser Altimeter: Experiment summary after the first year of global mapping of Mars. *J. Geophys. Res.* 106:23689-23722.

Smrekar, S., Catling, D., Lorenz, R., Magalhães, J., Moersch, J., Morgan, P., Murray, B., Presley, M., Yen, A., Zent, A. and Blaney, D. (1999) Deep Space 2: the Mars microprobe mission. *J. Geophys. Res.* 104:27013-27030.

Sobron, P., Sobron, F., Sanz, A. and Rull, F. (2008) Raman signal processing software for automated identification of mineral phases and biosignatures on Mars. *Appl. Spectrosc.* 62:364-370.

Soffen, G.A. and Young, A.T. (1972) The Viking missions to Mars. *Icarus* 16:1-16.

Squyres, S.W., Arvidson, R.E., Baumgartner, E.T., Bell III, J.F., Christensen, P.R., Gorevan, S., Herkenhoff, K.E., Klingelhöfer, G., Madsen, M.B., Morris, R.V., Rieder, R. and Romero, R.A. (2003) Athena Mars rover science investigation. *J. Geophys. Res.-Planet.* 108, doi:10.1029/2003JE002121.

Squyres, S.W., Grotzinger, J.P., Arvidson, R.E., Bell III, J.F., Calvin, W., Christensen, P.R., Clark, B.C., Crisp, J.A., Farrand, W.H., Herkenhoff, K.E., Johnson, J.R., Klingelhöfer, G., Knoll, A.H., McLennan, S.M., McSween Jr., H.Y., Morris, R.V., Rice Jr., J.W., Rieder, R. and Soderblom, L.A. (2004) In situ evidence for an ancient aqueous environment at Meridiani Planum, Mars. *Science* 306:1709-1714.

Stalport, F., Coll, P., Szopa, C. and Raulin, F. (2008) Search for organic molecules at the Mars surface: The “Martian Organic Material Irradiation and Evolution”(MOMIE) project. *Adv. Space Res.* 42:2014-2018.

Stalport, F., Coll, P., Szopa, C., Cottin, H. and Raulin, F. (2009) Investigating the photostability of carboxylic acids exposed to Mars surface ultraviolet radiation conditions. *Astrobiology* 9:543-549.

Stalport, F., Guan, Y.Y., Coll, P., Szopa, C., Macari, F., Raulin, F., Chaput, D. and Cottin, H. (2010) UVolution, a photochemistry experiment in low Earth orbit: investigation of the photostability of carboxylic acids exposed to Mars surface UV radiation conditions. *Astrobiology* 10:449-461.

Steele, A., McCubbin, F.M., Fries, M., Kater, L., Boctor, N.Z., Fogel, M.L., Conrad, P.G., Glamoclija, M., Spencer, M., Morrow, A.L., Hammond, M.R., Zare, R.N., Vicenzi, E.P., Siljeström, S., Bowden, R., Herd, C.D.K., Mysen, B.O., Shirey, S.B.,

Amundsen, H.E.F., Treiman, A.H., Bullock, E.S. and Jull, A.J.T. (2012) A reduced organic carbon component in martian basalts. *Science* 337:212-215.

Stephenson, D.D. and Willenberg, H.J. (2006) Mars ascent vehicle key elements of a Mars Sample Return mission [abstract 1009]. Presented at the *IEEE Aerospace Conference 2006*, 4-11 March 2006, Big Sky, MT, USA.

Stern, J.C., Sutter, B., Freissinet, C., Navarro-González, R., McKay, C.P., Archer Jr., P.D., Buch, A., Brunner, A.E., Coll, P., Eigenbrode, J.L., Fairen, A.G., Franz, H.B., Glavin, D.P., Kashyap, S., McAdam, A.C., Ming, D.W., Steele, A., Szopa, C., Wray, J.J., Martín-Torres, F.J., Zorzano, M.-P., Conrad, P.G., Mahaffy, P.R. and the MSL Science Team (2015). Evidence for indigenous nitrogen in sedimentary and aeolian deposits from the Curiosity rover investigations at Gale crater, Mars. *Proc. Natl. Acad. Sci. U.S.A.* 112:4245-4250.

Stone, H.W. (1996) Mars pathfinder microrover: A low-cost, lowpower spacecraft. Presented at the *1996 AIAA Forum on Advanced Developments in Space Robotics*, August 1996, Madison, WI, USA.

Surkov, Y.A. and Kremnev, R.S. (1998) Mars-96 mission: Mars exploration with the use of penetrators. *Planet. Space Sci.* 46:1689-1696.

Taylor, S.R. and McLennan, S.M. (1985) *The Continental Crust: Its Composition and Evolution*, Blackwell Scientific Publications, Oxford, UK.

ten Kate, I.L., Garry, J.R., Peeters, Z., Foing, B. and Ehrenfreund, P. (2006) The effects of martian near surface conditions on the photochemistry of amino acids. *Planet. Space Sci.* 54:296-302.

Thomas, N., Cremonese, G., Ziethe, R., Gerber, M., Brändli, M., Bruno, G., Erismann, M., Gambicorti, L., Gerber, T., Ghose, K. and Gruber, M. (2017) The Colour and Stereo Surface Imaging System (CaSSIS) for the ExoMars Trace Gas Orbiter. *Space Sci. Rev.*, 212:1897-1944.

Thrower, P.A. (Ed.) (1996) *Chemistry & Physics of Carbon (Volume 25)*, CRC Press, Boca Raton, FL, USA.

- Treiman, A.H. (2005) The nakhlite meteorites: Augite-rich igneous rocks from Mars. *Chem. Erde-Geochem.* 65:203-270.
- Trewin, N.H. (1986) Palaeoecology and sedimentology of the Achanarras fish bed of the Middle Old Red Sandstone, Scotland. *Trans. R. Soc. Edinb.* 77:21-46.
- Tucker, J.M., Dyar, M.D., Schaefer, M.W., Clegg, S.M., Barefield, J.E., Wiens, R.C. and Bishop, J.L. (2008). Laser-induced Breakdown Spectroscopy of Phyllosilicates for ChemCam Calibration [abstract P53A-1429]. Presented at the *AGU Fall Meeting 2008*, 15-19 December 2008, San Francisco, CA, USA.
- Vago, J.L., Witasse, O., Baglioni, P., Haldemann, A., Gianfiglio, G., Blancquaert, T., McCoy, D., de Groot, R., and the ExoMars team (2013) ExoMars, ESA's next step in Mars exploration. *ESA Bull.* 155:12–23.
- Vago, J.L., Witasse, O., Svedhem, H., Baglioni, P., Haldemann, A., Gianfiglio, G., Blancquaert, T., McCoy, D. and de Groot, R. (2015a) ESA ExoMars program: the next step in exploring Mars. *Sol. Syst. Res.* 49:518-528.
- Vago, J.L., Lorenzoni, L., Calantropio, F. and Zashchirinskiy, A.M. (2015b) Selecting a landing site for the ExoMars 2018 mission. *Sol. Syst. Res.* 49:538-542.
- Van Kranendonk, M.J. (2006) Volcanic degassing, hydrothermal circulation and the flourishing of early life on Earth: a review of the evidence from c. 3490–3240 Ma rocks of the Pilbara Supergroup, Pilbara Craton, Western Australia. *Earth-Sci. Rev.* 74:197-240.
- Van Kranendonk, M.J. and Pirajno, F. (2004) Geochemistry of metabasalts and hydrothermal alteration zones associated with c. 3.45 Ga chert and barite deposits: implications for the geological setting of the Warrawoona Group, Pilbara Craton, Australia. *Geochem.-Explor. Env. A.* 4:253-278.
- Van Kranendonk, M.J., Smithies, R.H., Hickman, A.H. and Champion, D.C. (2007) Review: secular tectonic evolution of Archean continental crust: interplay between horizontal and vertical processes in the formation of the Pilbara Craton, Australia. *Terra Nova* 19:1-38.

- Van Kranendonk, M.J., Philippot, P., Lepot, K., Bodorkos, S. and Pirajno, F. (2008) Geological setting of Earth's oldest fossils in the ca. 3.5 Ga Dresser Formation, Pilbara Craton, Western Australia. *Precambrian Res.* 167:93-124.
- Vandaele, A.C., Daerden, F., Drummond, R., Neefs, E., Lopez-Moreno, J.J., Gomez, J.R., Patel, M.R., Bellucci, G. and the NOMAD team (2011) NOMAD, a spectrometer suite for nadir and solar occultation observations on the ExoMars Trace Gas Orbiter. *Mars Atmosphere: Modelling and Observation*, 484-487.
- Vaniman, D.T., Bish, D.L., Ming, D.W., Bristow, T.F., Morris, R.V., Blake, D.F., Chipera, S.J., Morrison, S.M., Treiman, A.H., Rampe, E.B., Rice, M., Achilles, C.N., Grotzinger, J.P., McLennan, S.M., Williams, J., Bell III, J.F., Newsom, H.E., Downs, R.T., Maurice, S., Sarrazin, P., Yen, A.S., Morookian, J.M., Farmer, J.D., Stack, K., Milliken, R.E., Ehlmann, B.L., Sumner, D.Y., Berger, G., Crisp, J.A., Hurowitz, J.A., Anderson, R., Des Marais, D.J., Stolper, E.M., Edgett, K.S., Gupta, S., Spanovich, N. and MSL Science Team (2014) Mineralogy of a mudstone at Yellowknife Bay, Gale crater, Mars. *Science* 343, doi:10.1126/science.1243480.
- Varfolomeyev, T. (1993) The Soviet Mars programme. *Spaceflight* 7:230-231.
- Varnali, T., Edwards, H.G.M. and Hargreaves, M.D. (2009) Scytonemin: molecular structural studies of a key extremophilic biomarker for astrobiology. *Int. J. Astrobiol.*, 8:133-140.
- Vítek, P., Jehlička, J., Edwards, H.G.M., and Osterrothová, K. (2009a) Identification of  $\beta$ -carotene in an evaporitic matrix—evaluation of Raman spectroscopic analysis for astrobiological research on Mars. *Anal. Bioanal. Chem.* 393:1967-1975.
- Vítek, P., Osterrothová, K. and Jehlička, J. (2009b) Beta-carotene—a possible biomarker in the Martian evaporitic environment: Raman micro-spectroscopic study. *Planet. Space Sci.* 57:454-459.
- Vorontsov, V.A., Lokmatova, M.G., Martynov, M.B., Pichkhadze, K.M., Simonov, A.V., Khartov, V.V., Zasova, L.V., Zelenyi, L.M. and Korablev, O.I. (2011) Prospective Spacecraft for Venus Research: Venera-D Design. *Sol. Syst. Res.* 45:710-714.

- Walsh, A.D. (1947) The properties of bonds involving carbon. *Disc. Faraday Soc.* 2:18-25.
- Wang, A., Jolliff, B.L. and Haskin, L.A. (1995) Raman spectroscopy as a method for mineral identification on lunar robotic exploration missions. *J. Geophys. Res.* 100:21189-21199.
- Wang, A., Haskin, L.A., Kuebler, K.E., Jolliff, B.L. and Walsh, M.M. (2001) Raman spectroscopic detection of graphitic carbon of biogenic parentage in an ancient South African chert [abstract 1423]. Presented at the 32<sup>nd</sup> Lunar and Planetary Science Conference, 12-16 January 2001, Houston, TX, USA.
- Wang, A., Haskin, L.A., Lane, A.L., Wdowiak, T.J., Squyres, S.W., Wilson, R.J., Hovland, L.E., Manatt, K.S., Raouf, N. and Smith, C.D. (2003) Development of the Mars microbeam Raman spectrometer (MMRS). *J. Geophys. Res.-Planet.* 108, doi:10.1029/2002JE001902.
- Wang, A., Freeman, J.J., Jolliff, B.L. and Chou, I.M. (2006a) Sulfates on Mars: A systematic Raman spectroscopic study of hydration states of magnesium sulfates. *Geochim. Cosmochim. Ac.* 70:6118-6135.
- Wang, A., Haskin, L.A., Squyres, S.W., Jolliff, B.L., Crumpler, L., Gellert, R., Schröder, C., Herkenhoff, K., Hurowitz, J., Tosca, N.J., Farrand, W.H., Anderson, R. and Knudson, A.T. (2006b) Sulfate deposition in subsurface regolith in Gusev crater, Mars. *J. Geophys. Res.-Planet.* 111, doi:10.1029/2005JE002513.
- Wang, A., Wei, J., Lambert, J.L. and Hutchinson, I.B. (2015). A Compact Integrated Raman Spectrometer, CIRS, for Fine-Scale Definitive Mineralogy in Venus Explorations [abstract 1838]. Presented at the *Venus Science Priorities for Laboratory Measurements and Instrument Definition Workshop*, Hampton, VA, USA.
- Wang, Y., Alsmeyer, D.C. and McCreery, R.L. (1990) Raman spectroscopy of carbon materials: structural basis of observed spectra. *Chem. Mater.* 2:557-563.
- Webster, C.R., Mahaffy, P.R., Atreya, S.K., Flesch, G.J., Mischna, M.A., Meslin, P.-Y., Farley, K.A., Conrad, P.G., Christensen, L.E., Pavlov, A.A., Martín-Torres, J., Zorzano, M.-P., McConnochie, T.H., Owen, T., Eigenbrode, J.L., Glavin, D.P., Steele, A., Malespin, C.A., Archer Jr., P.D., Sutter, B., Coll, P., Freissinet, C., McKay, C.P.,

Moores, J.E., Schwenzer, S.P., Bridges, J.C., Navarro-Gonzalez, R., Gellert, R., Lemmon, M.T. and the MSL Science Team (2015) Mars methane detection and variability at Gale crater. *Science* 347:415-417.

White, C.H. (1924). Desert varnish. *Am. J. Sci.* s5v7:413-420.

Wiens, R.C., Newell, R., Clegg, S.M., Sharma, S.K., Misra, A., Bernardi, P., Maurice, S., McCabe, K. and Cais, P. (2017) The SuperCam Remote Raman Spectrometer for Mars 2020 [abstract 1964]. Presented at the *48th Lunar and Planetary Science Conference*, 20-24 March 2017, The Woodlands, TX, USA.

Wierzchos, J., Ascaso, C. and McKay, C.P. (2006) Endolithic cyanobacteria in halite rocks from the hyperarid core of the Atacama Desert. *Astrobiology* 6:415-422.

Williams, R.M.E., Grotzinger, J.P., Dietrich, W.E., Gupta, S., Sumner, D.Y., Wiens, R.C., Mangold, N., Malin, M.C., Edgett, K.S., Maurice, S., Forni, O., Gasnault, O., Ollila, A., Newsom, H.E., Dromart, G., Palucis, M.C., Yingst, R.A., Anderson, R.B., Herkenhoff, K.E., Le Mouélic, S., Goetz, W., Madsen, M.B., Koefoed, A., Jensen, J.K., Bridges, J.C., Schwenzer, S.P., Lewis, K.W., Stack, K.M., Rubin, D., Kah, L.C., Bell III, J.F., Farmer, J.D., Sullivan, R., Van Beek, T., Blaney, D.L., Pariser, O., Deen, R.G. and the MSL Science Team (2013) Martian fluvial conglomerates at Gale crater. *Science* 340:1068-1072.

Wilson, L. and Head III, J.W. (1994) Mars: Review and analysis of volcanic eruption theory and relationships to observed landforms. *Rev. Geophys.* 32:221-263.

Windscheif, J., Stolz, H. and Von der Osten, W. (1977) Dispersive phonon modes by resonant Raman scattering in AgBr. *Solid State Commun.* 24:607-609.

Wray, J.J., Squyres, S.W., Roach, L.H., Bishop, J.L., Mustard, J.F. and Dobrea, E.Z.N. (2010) Identification of the Ca-sulfate bassanite in Mawrth Vallis, Mars. *Icarus* 209:416-421.

Wynn-Williams, D.D. and Edwards, H.G.M. (2000) Proximal analysis of regolith habitats and protective biomolecules in situ by laser Raman spectroscopy: overview of terrestrial Antarctic habitats and Mars analogs. *Icarus* 144:486-503.

Xin, L. Group theory in action: molecular vibrations. Available online at <http://web.thu.edu.tw/tslim/www/groups5.pdf>

Yang, C., He, Z. and Yu, W. (2009) Comparison of public peak detection algorithms for MALDI mass spectrometry data analysis. *BMC Bioinform.* 10, doi:10.1186/1471-2105-10-4.

Zeitlin, C., Hassler, D.M., Cucinotta, F.A., Ehresmann, B., Wimmer-Schweingruber, R.F., Brinza, D.E., Kang, S., Weigle, G., Böttcher, S., Böhm, E., Burmeister, S., Guo, J., Köhler, J., Martin, C., Posner, A., Rafkin, S. and Reitz, G. (2013) Measurements of energetic particle radiation in transit to Mars on the Mars Science Laboratory. *Science* 340:1080-1084.

Zorzano, M.P., Mateo-Marti, E., Prieto-Ballesteros, O., Osuna, S. and Renno, N. (2009) Stability of liquid saline water on present day Mars. *Geophys. Res. Lett.* 36, doi:10.1029/2009GL040315.

Zuber, M.T., Smith, D.E., Solomon, S.C., Abshire, J.B., Afzal, R.S., Aharonson, O., Fishbaugh, K., Ford, P.G., Frey, H.V., Garvin, J.B., Head, J.W., Ivanov, A.B., Johnson, C.L., Muhleman, D.O., Neumann, G.A., Pettengill, G.H., Phillips, R.J., Sun, X., Zwally, H.J., Banerdt, W.B. and Duxbury, T.C. (1998) Observations of the north polar region of Mars from the Mars Orbiter Laser Altimeter. *Science* 282:2053-2060.

Zuber, M.T., Solomon, S.C., Phillips, R.J., Smith, D.E., Tyler, G.L., Aharonson, O., Balmino, G., Banerdt, W.B., Head, J.W., Johnson, C.L., Lemoine, F.G., McGovern, P.J., Neumann, G.A., Rowlands, D.D. and Zhong, S. (2000) Internal structure and early thermal evolution of Mars from Mars Global Surveyor topography and gravity. *Science* 287:1788-1793.